UNIVERSITÀ
DEGLI STUDI
DI PADOVA

UNIVERSITA’ DEGLI STUDI DI PADOVA

Dipartimento di Ingegneria Industriale DII

Corso di Laurea Magistrale in Ingegneria dei Materiali

Investigation on the stress corrosion cracking susceptibility of an alloy 718 prepared by laser powder bed fusion assessed by microcapillary method

Relatore: Prof. Manuele Dabalà

Correlatore: Arshad Yazdanpanah, Mattia Franceschi

Mattia Venturin 2022861

Anno Accademico 2021/2022

Riassunto

L'indagine svolta in questa tesi mirava a confrontare il comportamento elettrochimico e la suscettibilità alla tensocorrosione della lega 718 lavorata, utilizzando diverse potenze laser, mediante produzione additiva con la lega 718 convenzionale sottoposta ad un trattamento di invecchiamento a due stadi. È stato utilizzato il metodo microcapillare, che ha permesso di indagare le fasi iniziali della comparsa delle cricche da tensocorrosione, ovvero incubazione e nucleazione.

Nello specifico, i campioni sono stati prodotti mediante selective laser melting (SLM). Si è svolta un'analisi dei difetti superficiali, della durezza e della microstruttura dei campioni in esame e si è cercata una correlazione tra questi risultati e quelli ottenuti tramite le indagini elettrochimiche. La superficie lucidata dei campioni è stata osservata al microscopio ottico per la determinazione della porosità, così come la superfice attaccata elettroliticamente per l'osservazione delle pozze di fusione. Le prove di microdurezza sono state svolte con un durometro Vickers.

Le prove di polarizzazione elettrochimica sono state impiegate per valutare la resistenza dello strato passivo sulla superficie del materiale. Sono state eseguite prove di polarizzazione potenziodinamica e galvanostatica, utilizzando il metodo a tre elettrodi. Il campione svolgeva il ruolo dell'elettrodo di lavoro, un filo di platino fungeva da controelettrodo, che chiude il circuito e permette di misurare la corrente, mentre un elettrodo standard al calomelano fungeva da elettrodo di riferimento per la misurazione del potenziale. Le prove si sono svolte sia su campioni non tesi, sia su campioni sotto un sforzo di trazione superiore del 10% allo sforzo di snervamento del materiale. I risultati sono stati confrontati con le controparti prodotte convenzionalmente. La microstruttura e le cricche da tensocorrosione sono state osservate al microscopio elettronico a scansione (SEM).

Le caratteristiche microstrutturali della lega 718 SLM sono strettamente legate al metodo utilizzato per la loro produzione e ai parametri di processo utilizzati. È stato osservato che la dimensione delle pozze di fusione è correlata alla potenza del laser utilizzata. Nel complesso, con l'aumento della potenza del laser, la profondità e la larghezza delle pozze sono aumentate. La potenza del laser di 115W ha permesso di ottenere la combinazione più ottimale delle due proprietà. In effetti, la profondità delle pozze a questa potenza laser è risultata essere la più piccola, pur avendo la larghezza maggiore. Un'altezza troppo grande indurrebbe la formazione di porosità per intrappolamento di gas, mentre una larghezza elevata permette una migliore sovrapposizione delle pozze dello stesso strato, diminuendo la porosità per mancanza di fusione.

La porosità del materiale rispecchiava il comportamento delle pozze di fusione; infatti, la potenza di 115W ha permesso di ottenere un materiale con la densità dei pori più bassa e con pori di dimensione minore. Al contrario, la potenza del laser di 125W è quella che ha mostrato la maggiore densità dei pori, avendo sia un elevato numero di piccoli pori, sia un numero considerevole di grandi pori che seguono lo

schema di scansione. Questo comportamento è dovuto all'eccessiva potenza laser utilizzata che ha aumentato la densità di energia che ha colpito il materiale e ha portato a un gran numero di pori a causa dell'intrappolamento di gas.

La durezza ha seguito l'andamento imposto dalla densità dei pori ma in modo opposto. Infatti, maggiore è la densità dei pori, minore è la durezza del materiale. Quindi questa caratteristica meccanica è stata influenzata anche dalla potenza del laser. Il campione da 115 W ha mostrato la durezza più alta, mentre il campione da 125 W aveva la durezza più bassa. I campioni convenzionali erano quelli che presentavano la maggiore durezza, a causa del trattamento di invecchiamento in due fasi che ha l'obiettivo di aumentare la resistenza meccanica del materiale attraverso la precipitazione di particelle fini nella matrice.

Le prove di polarizzazione potenziodinamica hanno permesso di avere un quadro generale del comportamento alla corrosione dei campioni. I risultati più significativi, tuttavia, sono stati determinati grazie a prove galvanostatiche, che hanno mostrato che, tenuto conto delle condizioni di carico a trazione, sui campioni SLM la comparsa di cricche da tensocorrosione è ritardata rispetto al materiale tradizionale. Ciò indica una migliore resistenza della lega SLM 718 all'incubazione e alla nucleazione delle cricche. Ciò è ulteriormente confermato dall'elevato potenziale di rottura dei campioni SLM.

La resistenza alla corrosione non è direttamente correlata alla durezza e alle dimensioni delle pozze di fusione, poiché i campioni più duri erano anche quelli più soggetti a tensocorrosione. Al contrario, nei campioni SLM sembra che la durezza sia proporzionale alla resistenza alla corrosione, ma ciò è dovuto principalmente alla porosità. Infatti, è proprio questa caratteristica che determina sia la durezza che la resistenza alla corrosione localizzata. I campioni con una densità dei pori inferiore, e quindi una durezza maggiore, hanno la migliore resistenza dello strato passivo alla corrosione. Pertanto, la potenza del laser di 115W è quella che ha prodotto il materiale più resistente, mentre la potenza di 125W è quella che ha prodotto il materiale più attaccabile. I pori si comportano come siti attivi, più soggetti all'attacco di corrosione, per la maggiore facilità di accumulare al loro interno specie aggressive, come gli ioni Cl-. Maggiore è la dimensione dei pori e la loro densità, minore è la resistenza alla corrosione del materiale.

La presenza di uno stato di sollecitazione a trazione è strettamente legata alla resistenza alla corrosione del materiale. Si è infatti rilevato che il carico era essenziale per la comparsa delle cricche e che ciò diminuiva notevolmente il potenziale necessario per la rottura dello strato passivo.

Nei campioni SLM, sono state rilevate crepe nell'area adiacente ai bordi dei sottograni cellulari/colonnari, mentre nei campioni convenzionali appaiono adiacenti ai precipitati, anche all'interno della matrice. Le crepe dei campioni SLM, essendo confinate nei sottograni, erano molto più piccole di quelle del materiale convenzionale. Questa è una conferma visiva della maggiore resistenza alla tensocorrosione del materiale ottenuto mediante produzione additiva.

La particolare nucleazione delle cricche che si è verificata nei campioni SLM è dovuta a diversi fattori. Il bordo del sottograno è arricchito di elementi che ne aumentano la resistenza alla corrosione, come Nb e Mo, al contrario la matrice è impoverita di questi elementi. Ciò ha prodotto un accoppiamento galvanico tra il bordo del sottograno e la matrice adiacente, causando una maggiore dissoluzione del metallo in quella zona. Inoltre, la presenza di una fitta rete di dislocazioni nell'area adiacente ai bordi del sottograno rende quest'area più vulnerabile, per la formazione di un film passivo più difettoso e una maggiore concentrazione dello sforzo di trazione che provoca la rottura del film passivo e l'avanzamento della cricca. In presenza di sollecitazioni di trazione, il micro-accoppiamento galvanico nel sottograno è più favorito rispetto all'accoppiamento tra il fondo del poro e la superficie metallica, a causa della minore distanza che la corrente di elettroni deve percorrere.

Abstract

The study focused on evaluating the stress corrosion cracking (SCC) behaviour of alloy 718 processed by laser powder bed fusion (L-PBF), also called selective laser melting (SLM), with different laser powers, in a solution containing chloride, using the microcapillary method under constant tensile load. An analysis of the surface defects, hardness, and microstructure of the samples under examination was carried out and a correlation was sought between these results and those obtained by electrochemical investigations. The polished surface of the samples was observed under the optical microscope, as was the electro-etched surface. Vickers hardness measurements were carried out. Electrochemical polarization tests were used to evaluate the resistance of the passive layer on the surface of the material. Potentiodynamic and galvanostatic polarization tests were performed. The tests were carried out on as-printed samples and samples under tensile load. The results were compared with conventionally produced counterparts. The microstructure and stress corrosion cracks were observed under the scanning electron microscope (SEM). The 115W laser power produced samples with a lower defect density; therefore, the highest resistance to localized corrosion was found. L-PBF samples under tensile load showed corrosion and SCC resistance superior to that of conventional material. In the L-PBF samples, submicronic cracks were detected adjacent to the boundaries of the subgrain, and the mechanisms that led to their appearance were explained as a synergistic effect of various microstructural factors, specifically, the greater corrosion resistance of the subgrain boundary and the high concentration of dislocations in the adjacent area. The fine microstructure of the L-PBF samples generated much smaller cracks than those observed on the conventional material, which explains the increased resistance to SCC observed in electrochemical tests.

Index

1 Introduction

1.1 Corrosion

1.1.1 Electrochemical reaction

Corrosion has an electrochemical nature that can be illustrated by the attack on zinc by hydrochloric acid. When zinc is placed in dilute hydrochloric acid, a vigorous reaction occurs; hydrogen gas is evolved and the zinc dissolves, forming a solution of zinc chloride, during the reaction, zinc is oxidized to zinc ions and hydrogen ions are reduced to hydrogen (Figure 1.1).

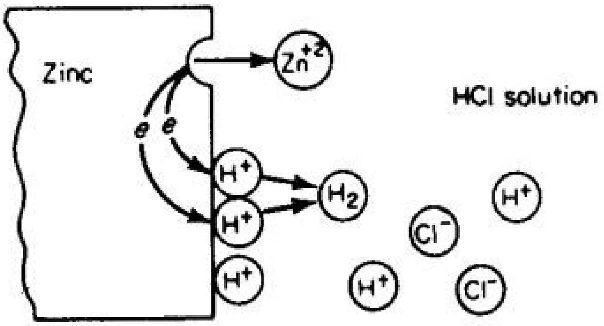

Figure 1.1: Electrochemical reactions occurring during corrosion of zinc in air-free hydrochloric acid.[1]

Oxidation or anodic reaction is indicated by an increase in valence or production of electrons. A decrease in valence charge or the consumption of electrons signifies a reduction or cathodic reaction. Here a zinc atom has been transformed into a zinc ion and two electrons. These electrons, which remain in the metal, are immediately consumed during the reduction of hydrogen ions. During metal corrosion, the oxidation rate equals the reduction rate [1]. The problem of hydrochloric acid corrosion is simplified since in every case the cathodic reaction is the evolution of hydrogen gas. The anodic reaction in every corrosion reaction is the oxidation of the metal to its ion. There are several different cathodic reactions encountered in metallic corrosion, such as hydrogen evolution, oxygen reduction, metal ion reduction, and metal deposition. Oxygen reduction is very common since any aqueous solution in contact with air can produce this reaction. During corrosion, more than one oxidation and one reduction reaction may occur. When an alloy is corroded, its component metals go into solution as their respective ion.

More importantly, more than one reduction reaction can occur during corrosion. Consider the corrosion of zinc in aerated hydrochloric acid. Two cathodic reactions are possible: the evolution of hydrogen and the reduction of oxygen. Since the rates of oxidation and reduction must be equal, increasing the total reduction rate increases the rate of zinc solution. Hence, acid solutions containing dissolved oxygen will be more corrosive than air-free acids.

Since the anodic and cathodic reactions occurring during corrosion are mutually dependent, it is possible to reduce corrosion by reducing the rates of either reaction. If the surface of the metal is coated with paint or another non-conducting film, the rates of both anodic and cathodic reactions will be greatly reduced, and corrosion will be retarded. A corrosion inhibitor is a substance that when added in small amounts to a corrosive reduces its corrosivity. Corrosion inhibitors function by interfering with either the anodic or cathodic reactions or both. Many of these inhibitors are organic compounds; they function by forming an impervious film on the metal surface or by interfering with either the anodic or cathodic reactions[1]. It is possible to increase the electrical resistance of the electrolyte or corrosive and thereby reduce corrosion. The low corrosivity of high-purity water is primarily due to its high electrical resistance.

1.1.2 Thermodynamic-Free energy

The change in free energy ΔG is a direct measure of work capability or maximum electric energy available from the system. If the charge in free energy accompanying the transition of the system from one state to another is negative, this indicates a loss in free energy and also the spontaneous reaction direction of the system. If the change in free energy is positive, this indicates the transition represents an increase in energy, and this requires that additional energy be added to the system. It is not possible to accurately predict the velocity of a reaction from the change in free energy. This parameter reflects only the direction of reaction by its sign.

1.1.3 Cell potentials and the EMF series

The change in free energy accompanying an electrochemical or corrosion reaction can be calculated from a knowledge of the cell potential of the reaction. To illustrate the principle of a reversible cell potential, consider the replacement reaction between copper and zinc occurring at equilibrium. To study the free-energy change associated with the reaction, we can construct an electrochemical cell containing copper and zinc electrodes in equilibrium with their ions separated by a porous membrane to retard mixing, as illustrated in Figure 1.2.

The concentrations of metal ions are maintained at unit activity. Both electrodes must be at equilibrium. That is, the rate of metal dissolution and deposition must be the same; there is no net charge in the system[1]. At certain points on the metal surface, copper atoms are oxidized to cupric ions, and at other points, cupric ions are reduced to metallic copper. Equilibrium conditions dictate that the rates of both reactions be equal. Similar restrictions apply to the zinc electrode. These equilibrium electrodes are called half-cells.

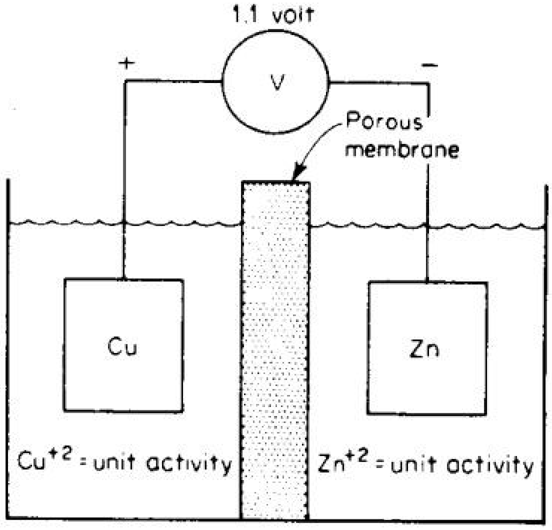

Figure 1.2: Reversible cell containing copper and zinc in equilibrium with their ions. [1]

If a high-resistance voltmeter is connected between the copper and zinc electrodes, a potential difference of approximately 1.1 volts is observed[1]. This is the cell potential that is used in determining the free energy of the overall electrochemical reaction. An arbitrary half-cell reaction is used as a reference by defining its potential as zero, and all other half-cell potentials are calculated concerning this reference. The hydrogen-hydrogen ion reaction is universally used.

Table 1.1: Standard oxidation-reduction potentials, 25°C.[2]

$Au = Au^{3+} + 3e$	+ 1.498
$O_2 + 4H^+ + 4e = 2H_2O$	+ 1.229
$Pt = Pt^{2+} + 2e$	+ 1.2
$Pd = Pd^{2+} + 2e$	+ 0.987
$Ag = Ag^+ + e$	+ 0.799
$2Hg = Hg_2^{2+} + 2e$	+ 0.788
$Fe^{3+} + e = Fe^{2+}$	+ 0.771
$O_2 + 2H_2O + 4e = 4\ OH$	+ 0.401
$Cu = Cu^{2+} + 2e$	+ 0.337
$Sn^{4+} + 2e = Sn^{2+}$	+ 0.15
$2H^+ + 2e = H_2$	0.000
$Pb = Pb^{2+} + 2e$	− 0.126
$Sn = Sn^{2+} + 2e$	− 0.136
$Ni = Ni^{2+} + 2e$	− 0.250
$Co = Co^{2+} + 2e$	− 0.277
$Cd = Cd^{2+} + 2e$	− 0.403
$Fe = Fe^{2+} + 2e$	− 0.440
$Cr = Cr^{3+} + 3e$	− 0.744
$Zn = Zn^{2+} + 2e$	− 0.763
$Al = Al^{3+} + 3e$	− 1.662
$Mg = Mg^{2+} + 2e$	− 2.363
$Na = Na^+ + e$	− 2.714
$K = K^+ + e$	− 2.925

Table 1.1 lists the half-cell potentials for some electrochemical reactions. This table is frequently called the emf series, half-cell, or redox potentials. It is important to note that in all cases these potentials refer

to electrodes in which all reactants are at unit activity and 25 °C. From the data presented in Table 1.1, it is possible to calculate the cell potential for numerous electrochemical reactions. Potentials between metals are determined by taking the absolute differences between their standard emf potentials. To determine the potential of a system in which the reactants are not at unit activity, the Nernst equation can be employed, that is:

$$E = E_0 + 2.3 * \frac{R * T}{n * F} * log \frac{a_{oxid}}{a_{red}}$$

Equation 1.1

Where E is the half-cell potential, E_0 is the standard potential, R is the gas constant, T is the absolute temperature, n is the number of electrons transferred, F is the Faraday constant, and a_{oxid} and a_{red} are the activities of oxidized and reduced species. As indicated in the above equation, half-cell potential becomes more positive as the amount of oxidized species increases.

1.1.4 Applications of thermodynamics to corrosion

There is a define relation between the free-energy change and cell potential of an electrochemical reaction; that is:

$$\Delta G = -n * F * E$$

Equation 1.2

Where ΔG is the free-energy change, n is the number of electrons involved in the reaction, F is the Faraday constant, and E equals the cell potential.

The most important factor is the sign of the free-energy change for a given reaction since this indicates whether or not the reaction is spontaneous. A simple rule derived from Equation 1.2 is used to predict the spontaneous direction of an electrochemical reaction. In any electrochemical reaction, the most negative or active half-cell tends to be oxidized, and the most positive or noble half-cell tends to be reduced[1].

Redox potentials are very useful in predicting corrosion behaviour. From the above rule, it follows that all metals with reversible potentials more active than hydrogen will tend to be corroded by acid solution (for the presence of hydrogen ions). If dissolved oxygen is present, there is a possibility of oxygen reduction.

As the reversible potential of a metal becomes nobler, its tendency to corrode in the presence of oxidizing agents decreases. Hence, the metals at the uppermost part of the redox series are very inert. Since half-cell potentials change with concentration, Nernst calculations must be made before making predictions about spontaneous direction at concentrations other than unit activity.

Half-cell potentials can be used to state a criterion for corrosion. Corrosion will not occur unless the spontaneous direction of the reaction indicates metal oxidation. It is important to remember that although the spontaneous direction of a reaction may be in the direction of metal corrosion, this does not necessarily indicate that corrosion will occur. If the reaction proceeds at a negligible rate, then the metal will be essentially inert[1].

1.1.5 Electrode Kinetics

From an engineering standpoint, the major interest is in the kinetics or rate of corrosion. Corroding systems are not at equilibrium, and therefore thermodynamic calculations cannot be applied. As when cells are short-circuited. In a short-circuited cell with a platinum electrode and a zinc electrode (Figure 1.3): the zinc electrode rapidly dissolves in the solution and simultaneously a rapid evolution of hydrogen is observed at the platinum electrode. Electrons released from the zinc-dissolution reaction are transferred through the connecting wire to the platinum electrode where they are consumed in the hydrogen-reduction reaction[1].

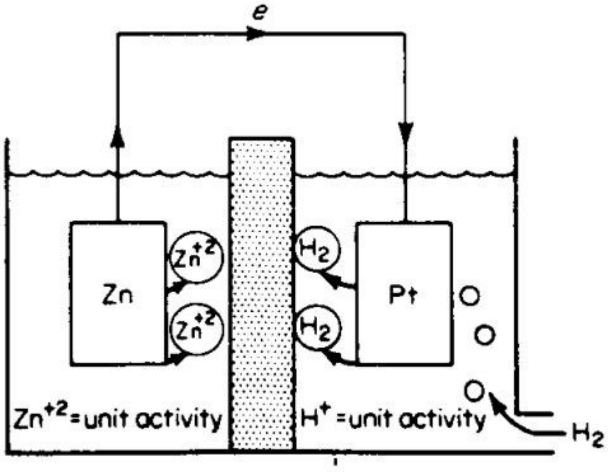

Figure 1.3: Short-circuited cell containing zinc and hydrogen electrodes.[1]

In the cell divided by a selective membrane, the reactions occur on separate electrodes, whereas in a corrosion process these reactions occur on the same metal surface. Anode refers to an electrode at which a net oxidation process occurs, and cathode refers to an electrode at which a net reduction reaction occurs. In this instance, the zinc electrode is the anode, and the platinum or hydrogen electrode is the cathode when the terminals are short-circuited. When a cell is short-circuited and net oxidation and reduction processes occur at the electrode interfaces, the potentials of these electrodes will no longer be at their equilibrium potential. This deviation from equilibrium potential is called polarization. Polarization can be defined as the displacement of electrode potential resulting from the net current. The magnitude of polarization is frequently measured in terms of overvoltage. Overvoltage, usually abbreviated as η, is a measure of polarization concerning the equilibrium potential of an electrode. That is, the equilibrium potential of an electrode is considered zero, and the overvoltage is stated in terms of volts or millivolts plus or minus concerning this zero reference[1].

1.1.6 Exchange current density

At an equilibrium hydrogen electrode, there is a finite rate of interchange between hydrogen molecules and hydrogen ions in solution. By plotting electrode potential versus reaction rate, it is possible to establish a point corresponding to the platinum-hydrogen electrode. This point represents the particular exchange reaction rate of the electrode expressed in terms of moles reacting per square centimetre per second[1]. There is no net reaction since both the oxidation and reduction rates are equal: the exchange reaction rate is equal to the rate of oxidation and reduction. Since two electrons are consumed during the reduction of the two hydrogen ions, and since two electrons are released during the oxidation of the single hydrogen molecule, the reaction rate can be expressed in terms of current density. The relationship between exchange reaction rate and current density can be directly derived from Faraday's law:

$$r_{oxid} = r_{red} = \frac{i_0}{n * F}$$

Equation 1.3

where r_{oxid} and r_{red} are the equilibrium oxidation and reduction rates and i_0 is the exchange current density. Exchange current density i_0 is the rate of oxidation and reduction reactions at an equilibrium electrode expressed in terms of current density. The exchange current density varies depending on the metal electrode. The magnitude of exchange current density is a function of several variables. First, it is a specific function of the particular redox reaction. Further, it is also related to electrode composition[1]. Like reversible potentials, exchange current densities are influenced by the ratio of oxidized and reduced species that are present and by the temperature of the system. The exchange current density for any given system must be determined experimentally. Exchange current density is usually expressed in terms of projected or geometric surface area, and as a consequence, it is dependent on surface roughness.

1.1.7 Activation polarization

Electrochemical polarization is divided into two main types: activation and concentration polarization. Activation polarization refers to electrochemical reactions that are controlled by a slow step in the reaction sequence. This slow step during hydrogen evolution might be the electron-transfer step or the formation of hydrogen molecules: The relationship between reaction rate and overvoltage for activation polarization is:

$$\eta_a = \pm\beta * log\frac{i}{i_0}$$

Equation 1.4

Where η_a is overvoltage, β is a constant, and i is the rate of oxidation or reduction in terms of current density[1]. Equation 1.4 is called the Tafel equation, and β is frequently termed "β slope" or Tafel constant.

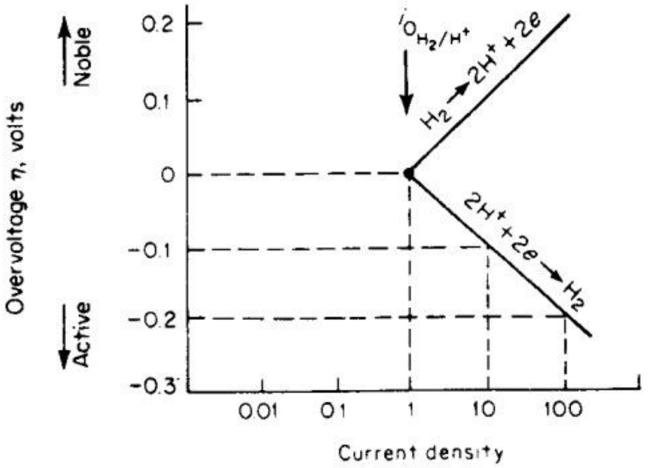

Figure 1.4: Activation-polarization curve of a hydrogen electrode.[1]

If a logarithmic current scale is used, the relationship between overvoltage or potential and current density is a linear function (Figure 1.4). This illustration shows that the reaction rate of an electrochemical reaction is very sensitive to small changes in electrode potential. Further, it can be seen that at all potentials nobler than the reversible potential a net oxidation process occurs and that at all potentials more active or more negative than the reversible potential a net reduction occurs. At the reversible potential or zero overvoltage, there is no net rate of oxidation or reduction since both rates are equal at this intersection point.

1.1.8 Concentration polarization

To illustrate the phenomenon of concentration polarization, we must consider the hydrogen-evolution reaction. At low reduction rates, the distribution of hydrogen ions in the solution adjacent to the electrode surface is relatively uniform. At very high reduction rates the region adjacent to the electrode surface will become depleted of hydrogen ions. If the reduction rate is increased further, a limiting rate will be reached that is determined by the diffusion rate of hydrogen ions to the electrode surface.

This limiting rate is the limiting diffusion current density i_L. It represents the maximum rate of reduction possible for a given system; the equation expressing this parameter is:

$$i_L = \frac{D * n * F * C_B}{x}$$

Equation 1.5

where D is the diffusion coefficient of the reacting ions, C_B is the concentration of the reacting ions in the bulk solution, and x is the thickness of the diffusion layer[1]. There is a linear relationship between the concentration of reactive ions in solution and the limiting diffusion current density. The diffusion layer thickness is influenced by the shape of the particular electrode, the geometry of the system, and by agitation. Agitation tends to decrease the diffusion layer thickness because of convection currents and consequently increases the limiting diffusion current density[1]. i_L is usually only significant during reduction processes and usually negligible during metal-dissolution reactions. The reason for this is that there is an almost unlimited supply of metal atoms for dissolution. Many useful qualitative predictions and correlations can be achieved merely by the knowledge of the relationship between limiting diffusion current density and various other factors of the particular system. The equation for concentration polarization is:

$$\eta_c = 2.3 * \frac{R * T}{n * F} * \log\left(1 - \frac{i}{i_L}\right)$$

Equation 1.6

Concentration polarization does not become apparent until the net reduction current density approaches the limiting diffusion current density. The net reduction current asymptotically approaches i_L. When the net reduction current is equal to the limiting diffusion current, overvoltage is equal to infinity (Figure 1.5). As the solution velocity, concentration, or temperature are increased, limiting diffusion current increases since all of these factors exert an influence.

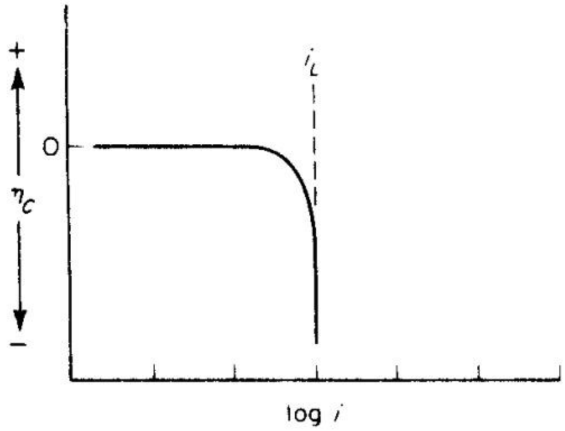

Figure 1.5: Concentration polarization curve (reduction process).[1]

1.1.9 Combined polarization

Both activation and concentration polarization usually occurs at an electrode. At low reaction rates, activation polarization usually controls, whereas at higher reaction rates concentration polarization becomes controlling. The total polarization of an electrode is the sum of the contributions of activation polarization and concentration polarization[1]. During anodic dissolution, concentration polarization is not a factor and the equation for the kinetics of anodic dissolution is given by:

$$\eta_{diss} = \beta * log\frac{i}{i_0}$$

Equation 1.7

During reduction processes such as hydrogen evolution or oxygen reduction, concentration polarization becomes important as the reduction rate approaches the limiting diffusion current density. The overall reaction for a reduction process is given by:

$$\eta_{red} = -\beta * log\frac{i}{i_0} + 2.3 * \frac{R * T}{n * F} * log\left(1 - \frac{i}{i_L}\right)$$

Equation 1.8

They are the basic equations of all electrochemical reactions. Using only three basic parameters, namely, β, i_0, and i_L, the kinetics of virtually every corrosion reaction can be precisely described.

1.1.10 Mixed-Potential Theory

The mixed-potential theory consists of two simple hypotheses: any electrochemical reaction can be divided into two or more partial oxidation and reduction reactions, and there can be no net accumulation of electric charge during an electrochemical reaction[1]. From this, it follows that during the corrosion of an electrically isolated metal sample, the total rate of oxidation must equal the total rate of reduction. The mixed-potential theory, together with the kinetic equations, constitute the basis of modern electrode-kinetics theory.

1.1.11 Mixed Electrodes

A mixed electrode is an electrode or metal sample that is in contact with two or more oxidation-reduction systems. If we consider a zinc electrode in equilibrium with its ions, it would be represented by a reversible potential corresponding to the zinc-zinc-ion electrode reaction, and a corresponding exchange current density. Likewise, if we consider the hydrogen-electrode reaction occurring on a zinc surface under equilibrium conditions, then this particular equilibrium state would be represented by the reversible potential of the hydrogen electrode and the corresponding exchange current density. However, if a piece of zinc is inserted in hydrochloric acid containing some zinc ions, the electrode cannot remain at either of these two reversible potentials but must lie at some other potential (Figure 1.6) [1].

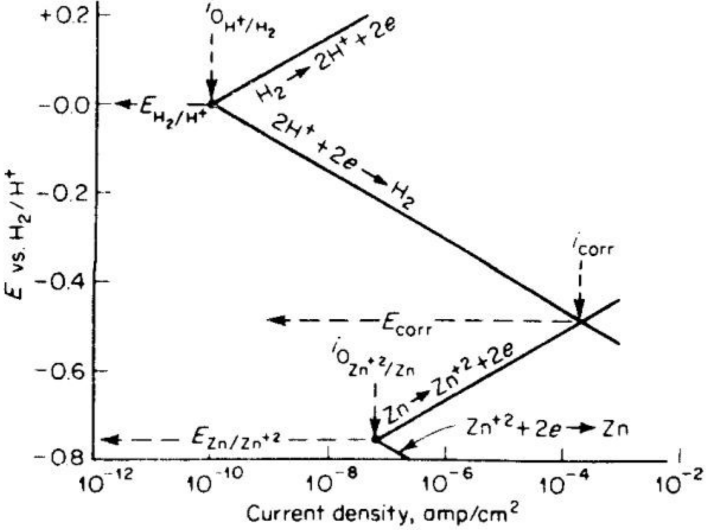

Figure 1.6: Electrode kinetic behaviour of pure zinc in acid solution.[1]

The only point in this system where the total rates of oxidation and reduction are equal is at the intersection represented by a “mixed” or corrosion potential E_{corr}. At this point, the rate of zinc dissolution is equal to the rate of hydrogen evolution expressed in terms of current density. Only at this point is charge conservation maintained. The current density corresponding to this point is usually called corrosion current density, i_{corr}. If the β values and exchange current densities for this system are known, it is possible to predict the corrosion rate of zinc in hydrochloric acid from electrochemical data. The exact relationship between dissolution current density and corrosion rate can be calculated utilizing Faraday’s law. Under many actual corrosion conditions, the environment is more complicated. Consider the corrosion behaviour of a metal M in an acid containing ferric salts (as oxidizers). Reversible potentials are indicated for the three redox Systems, metal-metal ion, hydrogen ion-hydrogen gas, and ferric-ferrous ions. The basic principles of the mixed-potential theory also apply to this more complex system.

To determine steady-state conditions, the total rate of oxidation is determined by summing the individual oxidation currents corresponding to metal dissolution, hydrogen-gas oxidation, and ferrous-ion oxidations at constant potentials. As shown in Figure 1.7, The total rate of oxidation follows the metal-dissolution rate until the reversible hydrogen potential is reached and an increase is noted because of the addition of hydrogen-oxidation currents. Similarly, the total rate of reduction is determined by summing the total reduction currents corresponding to ferric-ion reduction, hydrogen-ion reduction, and metal-ion reduction. The point at which the total rate of oxidation equals the total rate of reduction is the mixed or corrosion potential of this system[1].

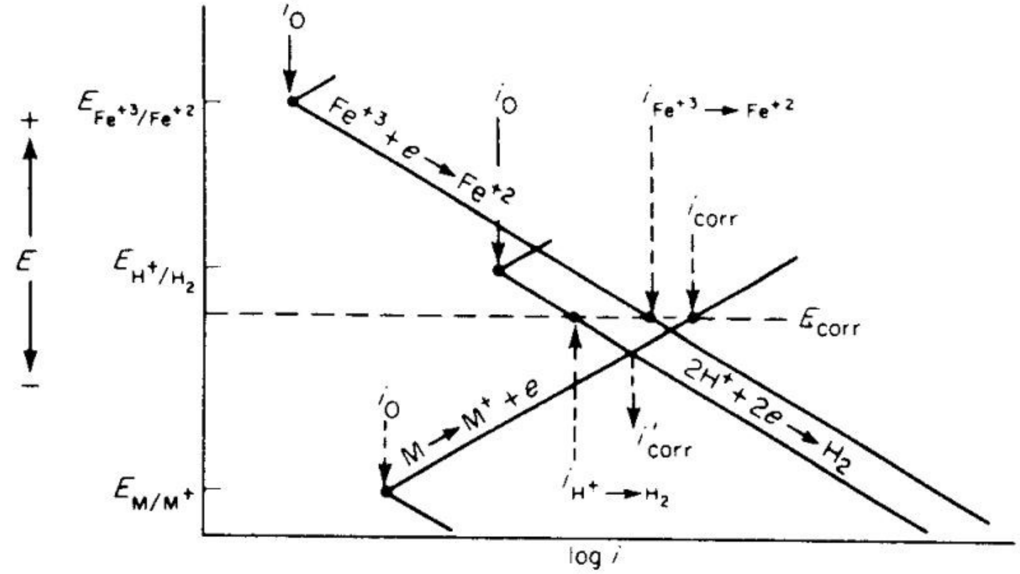

Figure 1.7: Behaviour of metal M in an acid solution containing ferric salts showing the determination of E_{corr}.[1]

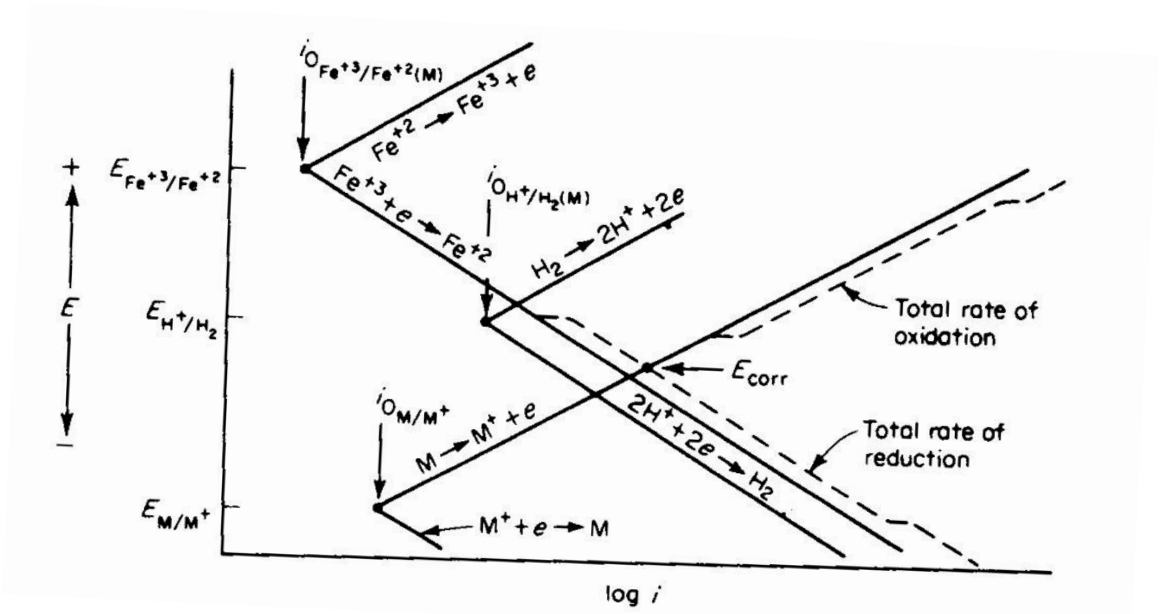

Figure 1.8: Behaviour of metal M in an acid solution containing ferric salts showing the determination of E_{corr}. [1]

A horizontal line is drawn at E_{corr} since the metal is equipotential (Figure 1.8). The rate of metal dissolution or the corrosion current is given by i_{corr}, the rate of ferric-ion reduction is equal to $i_{Fe3+Fe2+}$, and the rate of hydrogen evolution is given by i_{H+H2}. In the absence of oxidizers, the corrosion rate of metal M is given by the intersection of the hydrogen-reduction and metal-dissolution polarization curves. The addition of an oxidizer, such as ferric ions, shifts the corrosion potential to E_{corr} and consequently increases the corrosion rate and decreases hydrogen evolution. In this case, the reduction in hydrogen-evolution rate is a direct result of the shift in corrosion potential. In oxidizer-free acids i_{corr}=rate of H evolution. The effect of an oxidizing agent is dependent both on its redox potential and its particular reduction kinetics. Kinetic factors are very important in determining the effect of an oxidizing-agent condition. If the exchange current density for the ferric-ferrous half-cell on metal M is considered to be very small, the addition of ferric ions produces no change in the corrosion potential and corrosion rate of the system. This example serves to illustrate that not only is the redox potential of a particular oxidizing agent important, but also its exchange current density on the particular metal surface involved[1]. This same kind of analysis can be applied to more complex systems. In all cases, the analysis is the same. The total rates of oxidation and reduction are determined, and the resulting corrosion potential of the system is graphically located. From this, the dissolution rate and the rates of the individual processes can be determined. The same principles can be applied to systems where one or more of the reduction processes are under diffusion control. In this example, the metal M follows the typical anodic dissolution reaction under activation control and the reduction process follows the overall Equation 1.8. Initially, the reduction rate of hydrogen ions is under activation control; at higher reduction currents it is controlled by concentration polarization[1].

1.1.12 Passivity

Passivity is an unusual phenomenon observed during the corrosion of certain metals and alloys. Simply, it can be defined as a loss of chemical reactivity under certain environmental conditions. In the passive state, the corrosion rate of a metal is very low. The passive state often is relatively unstable and subject to damage. Hence, from an engineering viewpoint, passivity offers a unique possibility for reducing corrosion, but it must be used with caution because of the possibility of a transition from the passive to active state. Passivity is the result of a surface film. It is estimated that the film is only approximately 30 angstroms or less in thickness, contains considerable water of hydration, and, is extremely delicate and subject to changes when removed from a metal surface or when the metal is removed from a corrosive environment[1]. Iron, chromium, nickel, titanium, and alloys containing major amounts of these elements demonstrate active-passive transitions. Figure 1.9 schematically illustrates the typical behaviour of an active-passive metal. The metal initially demonstrates behaviour similar to nonpassivating metals. That is, as electrode potential is made more positive, the metal follows typical Tafel behaviour, and the dissolution rate increases exponentially. This is the active region. At more noble potential, the dissolution rate decreases to a very small value and remains essentially independent of potential over a considerable potential region. This is termed the passive region. Finally, at very noble potentials, the dissolution rate again increases with increasing potential in the transpassive region. This behaviour results in the increase of an oxidizer concentration. One of the important characteristics of an active-passive metal is the position of its anodic current density maximum characterized by the primary passive potential E_{pp} and the critical anodic current density for passivity I_c.[1]

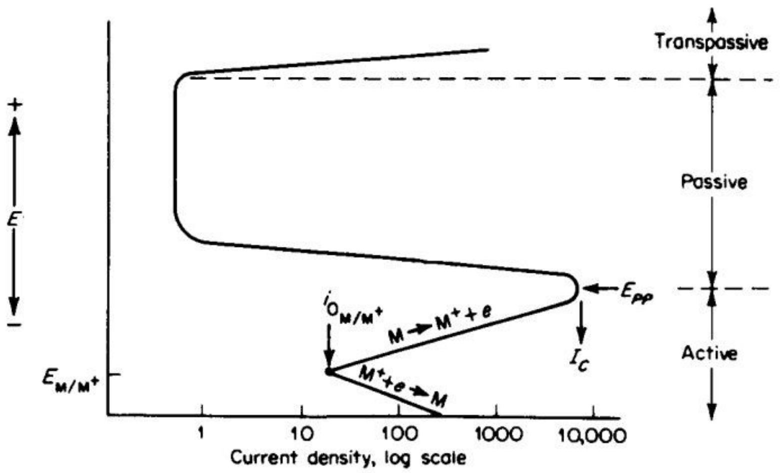

Figure 1.9: Typical anodic dissolution behaviour of an active-passive metal.[1]

The decrease in dissolution rate just above the primary passive potential is the result of film formation at this point. The transpassive region where the dissolution rate again increases with increasing potential is apparently due to the destruction of the passive film at very positive potentials.

Both temperature and hydrogen-ion concentration tend to increase the critical anodic current density and usually have relatively little effect on the primary passive potential and passive dissolution rate. A similar effect is noticed upon increasing chloride additions in the case of stainless steels and other ferrous-base alloys[1]. When considering mixed electrodes involving an active-passive metal, the peculiar S-shaped anodic polarization curves of these metals often lead to unusual results (Figure 1.10).

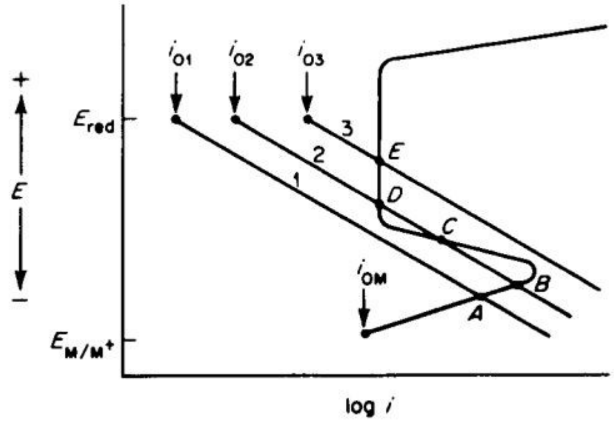

Figure 1.10: Behaviour of an active-passive metal under corrosive conditions.[1]

In case 1 there is only one stable intersection point, point A, which is in the active region, and a high corrosion rate is observed. Case 2 is particularly interesting since there are three possible intersection points at which the total rate of oxidation and total rate of reduction are equal. These are points B, C, and D.

Point C is electrically unstable and, as a consequence, the system cannot exist at this point[1]. Hence, both points B and D are stable; B is in the active region corresponding to a high corrosion rate, while D is in the passive region with a low corrosion rate. This system may exist in either the active or passive state under identical environmental conditions. In case 3 there is only one stable point, in the passive region at point E. For such a system, the metal or alloy will spontaneously passivate and remain passive. From an engineering viewpoint, case 3 is the most desirable. This system will spontaneously passivate and corrode very slowly. In case 2 there could be an unexpected transition from the passive to the active state as a result of surface damage or similar factors. The position of the current maximum or "nose" of the anodic polarization curve is important. Spontaneous passivation only occurs if the cathodic reduction process clears the tip of the nose of the anodic dissolution curve as shown in case 3. More precisely, at the primary passive potential, the cathodic reduction rate must be equal to or greater than the anodic dissolution rate for spontaneous passivation to occur[1]. It follows that a metal or alloy will be more readily passivated if it has a small critical anodic current density and an active primary passive potential.

1.1.13 Effect of temperature

Temperature increases the rate of almost all chemical reactions. There can be a very rapid or exponential rise in corrosion rate with increasing temperature or an almost negligible temperature effect is followed by a very rapid rise in corrosion rate at higher temperatures[1].

1.1.14 Effects of corrosive concentration

Many materials that exhibit passivity effects are only negligibly affected by wide changes in corrosive concentration. Other materials show similar behaviour except at very high corrosive concentrations when the corrosion rate increases rapidly[1]. The behaviour of acids that are soluble in all concentrations of water often yields curves in which, initially, as the concentration of corrosive is increased, the corrosion rate is likewise increased. This is primarily because the number of hydrogen ions, which are the active species, are increased as acid concentration is increased. However, as acid concentration is increased further, the corrosion rate reaches a maximum and then decreases. This is because at very high concentrations of acids ionization is reduced.

1.1.15 Metallic properties

Grain boundaries are high-energy areas and are more active chemically since the most stable configuration of the metal is its particular crystal lattice. Hence, grain boundaries are usually attacked slightly more rapidly than grain faces when exposed to a corrosive. Metallographic etching depends on this difference in chemical reactivity. The grain boundaries appear dark because they have been more severely attacked[1]. Solid-solution alloys are usually more corrosion-resistant than alloys with two phases since galvanic coupling effects are not present. Very pure metals, usually, are more corrosion-resistant than commercial materials.

1.1.16 Galvanic coupling

The galvanic couple between dissimilar metals can be treated by application of the mixed-potential theory. Let us first consider a galvanic couple between a corroding and an inert metal. If a piece of platinum is coupled to zinc corroding in an air-free acid solution, vigorous hydrogen evolution occurs on the platinum surface and the rate of hydrogen evolution on the zinc sample is decreased. Also, the corrosion rate of zinc is greater when coupled with platinum (Figure 1.11). The corrosion rate of zinc in an air-free acid is determined by the intersection between the polarization curves corresponding to the hydrogen evolution and zinc dissolution reactions[1]. When equal areas of platinum and zinc are coupled, the total rate of hydrogen evolution is equal to the sum of the rates of this reaction on both the zinc and platinum surfaces.

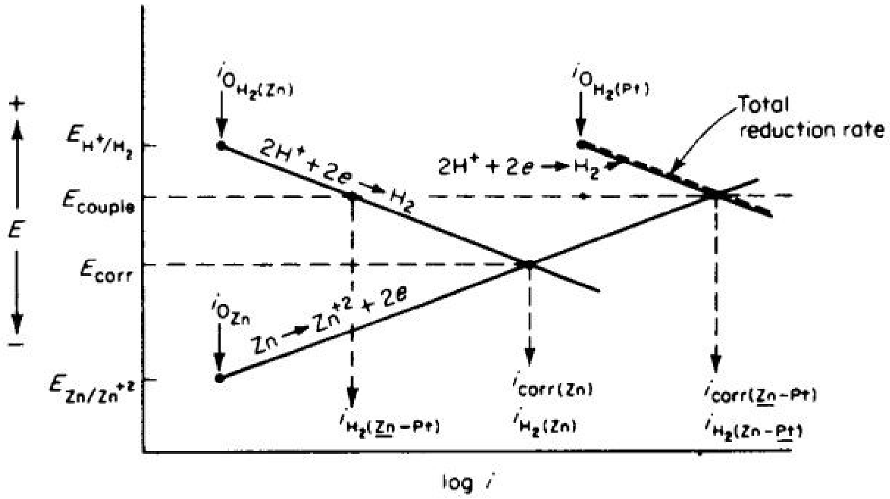

Figure 1.11: Effect of galvanically coupling zinc to platinum.[1]

Since the hydrogen-hydrogen ion exchange current density is very high on platinum and very low on zinc, the total rate of hydrogen evolution is effectively equal to the rate of hydrogen evolution on the platinum surface[1]. Figure 1.11 shows that coupling zinc to platinum shifts the mixed potential from E_{corr} to E_{couple} increases the corrosion rate (i_{corr}), and decreases the rate of hydrogen evolution on the zinc. The increase in the corrosion rate of zinc observed when this metal is coupled to platinum is the result of the higher exchange current density for hydrogen evolution on platinum surfaces. It is not due to the noble reversible potential of the platinum-platinum-ion electrode[1]. Another example, that demonstrates this fact is the effect of coupling zinc to gold. If equal areas of gold and zinc are coupled, the corrosion rate increase is less than that observed if equal areas of zinc and platinum are coupled. The reason why gold produces a less severe galvanic effect is not related to its reversible potential (gold has a reversible potential higher than that of platinum) but rather to the fact that it has a lower hydrogen exchange current density than platinum. A couple between two corroding metals may also be examined by application of mixed-potential principles. Metal M has a relatively noble corrosion potential and a low corrosion rate, while metal N corrodes at a high rate at an active corrosion potential. If equal areas of these two metals are coupled, the resultant mixed potential of this system occurs at the point where the total oxidation rate equals the total reduction rate. The rates of the individual partial processes are determined by this mixed potential. Coupling equal areas of these two metals decrease the corrosion rate of metal M and increase the corrosion rate of metal N[1]. The relative areas of the two electrodes in a galvanic couple also influence galvanic behaviour Increasing the area of an electrode increases its exchange current, which is directly proportional to specimen area. As the size of the cathode in a galvanic couple is increased, the corrosion rate of the anode is increased. If the relative area of the anode electrode in a galvanic couple is increased, its overall corrosion rate is reduced[1]. To sum it up, if two corroding metals are galvanically coupled, the corrosion rate of the metal with the most active corrosion potential is accelerated and that of the other metal is retarded. The metal with the active corrosion potential becomes the anode and the one with the noble corrosion potential, the cathode. Hence, in determining the effect of galvanic coupling, the anode should be defined based on corrosion potential rather than corrosion rate. The corrosion behaviour of a galvanic couple is determined by the reversible electrode potential of the actual processes involved, their exchange current densities and Tafel slopes, and the relative areas of the two metals. Galvanic-corrosion behaviour cannot be predicted accurately based on emf potentials. Galvanic couples containing active-passive metals produce unusual effects under certain conditions[1]. For example, an isolated titanium electrode will corrode in an acid solution in the active state. Upon coupling to an equal area of platinum, the titanium spontaneously passivates, and its corrosion rate decreases. This particular system represents an exception to the general rule that the metal with the most active corrosion potential is accelerated when galvanically coupled. This unusual behaviour only occurs if the passive region of the metal begins at a potential more active than the reversible potential of the redox system[1] (Figure 1.12).

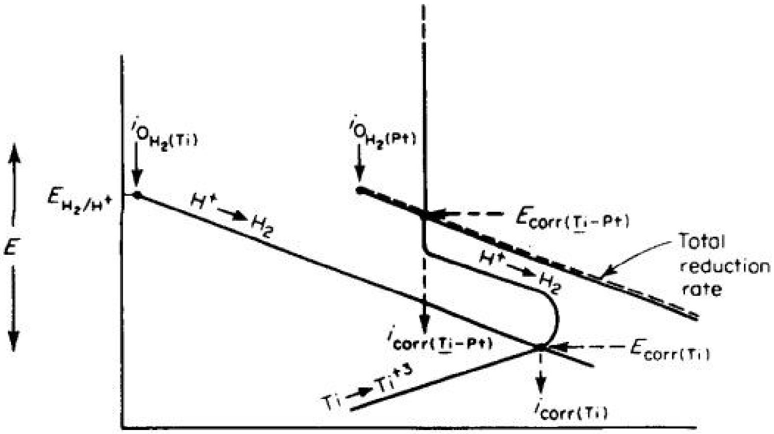

Figure 1.12: Spontaneous passivation of titanium by galvanically coupling to platinum.[1]

If the passive range of metal begins at potentials nobler than the reversible hydrogen potential, coupling to platinum in the absence of oxidizers increases the corrosion rate.

1.1.17 Alloy evaluation

Using mixed-potential theory it is possible to estimate the corrosion behaviour of an alloy from electrochemical data. Many commercial metals and alloys depend on the achievement of passivity for their corrosion resistance, and there are two general ways for achieving passivity. First, the system may be made oxidizing to cause spontaneous passivation, or in special instances, the galvanic coupling can be used to achieve passivity as in the case of titanium[1]. One of the most common oxidizers encountered in practice is oxygen. Oxygen is very slightly soluble in water and aqueous solutions, and, as a result, its reduction is usually under diffusion control. In air-saturated non-agitated solutions, the limiting diffusion current for oxygen reduction is approximately 100 μA/cm^2. If an active-passive metal is exposed to an aerated corrosive medium, it spontaneously passivates if its critical anodic current density is equal to or less than approximately 100 μA/cm^2.

Because of its very large critical anodic density and relatively noble primary passive potential, iron is difficult to passivate in acid solutions. The addition of chromium to iron increases the ease of passivation by reducing critical anodic current density. Although the critical anodic current density of this alloy is too high to be passivated by dissolved oxygen, it is more easily passivated by oxidizing agents than pure iron. The addition of both chromium and nickel to iron markedly increases the ease of passivation. This is the typical 18Cr-8Ni austenitic stainless steel used in the chemical industry, and its critical anodic current density of approximately 100 μA indicates that it will be passivated in aerated acid solutions[1].

1.2 Pitting

Pitting is a form of extremely localized attack that results in holes in the metals. Pits are sometimes isolated or so close together that they look like rough surface. Pitting is particularly vicious because it is a localized and intense form of corrosion. It is often difficult to detect pits because of their small size and because the pits are often covered with corrosion products.

1.2.1 Pit shape and growth

Pits usually grow in the direction of gravity. Pitting usually requires an extended initiation period before visible pits appear. Once started, however, a pit penetrates the metal at an ever-increasing rate. In addition, pits tend to undermine or undercut the surface as they grow[1].

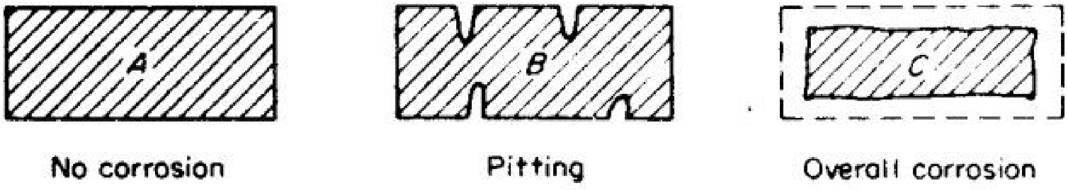

Figure 1.13: Diagrammatic representation of pitting corrosion as an intermediate stage.[1]

Pitting may be considered the intermediate stage between general overall corrosion and complete corrosion resistance. Intense pitting occurred on specimen B at the points of breakthrough. This situation can be readily demonstrated by exposing three identical specimens of 18-8 stainless steel to ferric chloride and increasing the concentration and/or the temperature as we move to the right in Figure 1.13[3].

1.2.2 Autocatalytic nature of pitting

A corrosion pit is a unique type of anodic reaction. It is an autocatalytic process. That is, the corrosion processes within a pit produce conditions that are both stimulating and necessary for the continuing activity of the pit. This is illustrated schematically in Figure 1.14. Here a metal M is being pitted by an aerated sodium chloride solution. Rapid dissolution occurs within the pit, while oxygen reduction takes place on adjacent surfaces. The rapid dissolution of metal within the pit tends to produce an excess of positive charge in this area, resulting in the migration of chloride ions to maintain electroneutrality. Thus, in the pit there is a high concentration of MCl and, as a result of hydrolysis, a high concentration of hydrogen and chloride ions. Both hydrogen and chloride ions stimulate the dissolution of most metals and alloys, and the entire process accelerates with time[1]. Since the solubility of oxygen is virtually zero in concentrated solutions, no oxygen reduction occurs within a pit. The cathodic oxygen reduction on the surfaces adjacent to pits tends to suppress corrosion. In a sense, pits cathodically protect the rest of the metal surface.

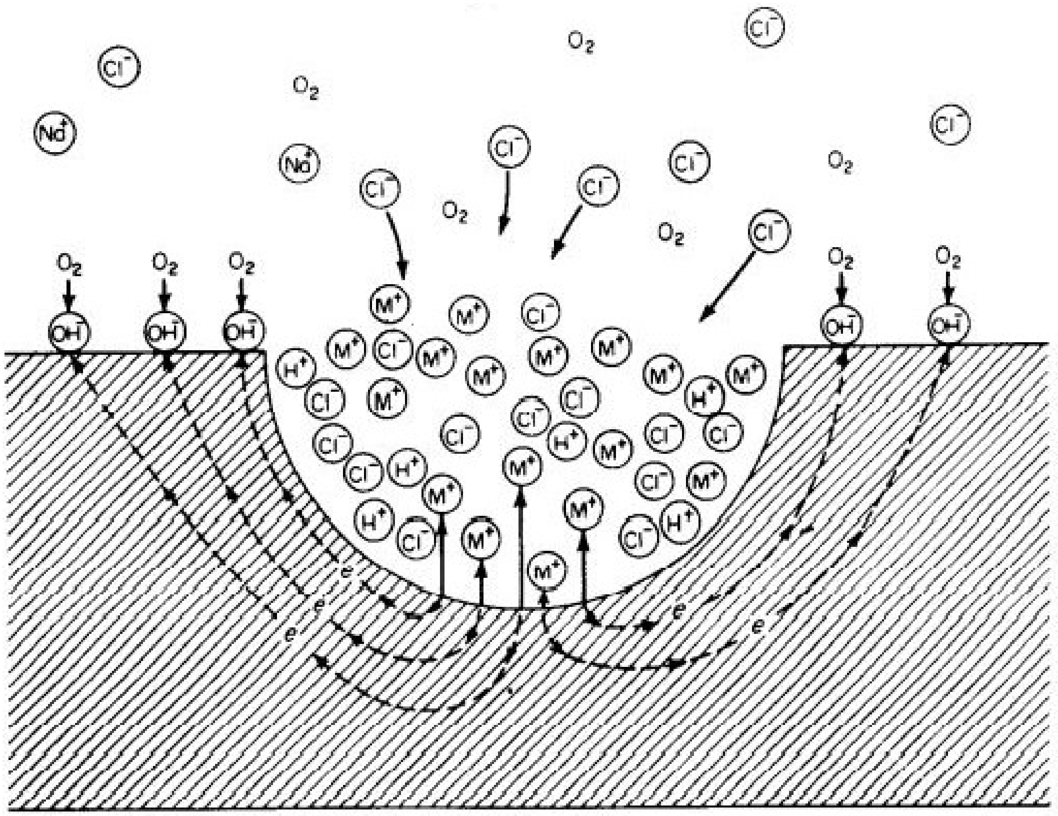

Figure 1.14: Autocatalytic processes occurring in a corrosion pit.[1]

This process is initiated if, for any reason, the rate of metal dissolution is momentarily high at one particular point, so chloride ions will migrate to this point[4]. Since chloride stimulates metal dissolution, this change tends to produce conditions that are favourable to further rapid dissolution at this point. Locally, dissolution may be momentarily high because of a surface scratch, an emerging dislocation or other defects, or random variation in solution composition. The gravity effect mentioned before is a direct result of the autocatalytic nature of pitting. Since the dense, concentrated solution within a pit is necessary for its continuing activity. Pits are most stable when growing in the direction of gravity. Also, pits are generally initiated on the upper surfaces of specimens because chloride ions are more easily retained under these conditions[1].

1.2.3 Solution composition

Most pitting failures are caused by chloride and chlorine-containing ions. Oxidizing metal ions with chlorides are aggressive pitters. Cupric and ferric chlorides do not require the presence of oxygen to promote attack because their cations can be cathodically reduced. This is one reason ferric chloride is widely used in pitting studies[1].

1.2.4 Velocity

Pitting is usually associated with stagnant conditions such as a liquid in a tank or a liquid trapped in a low part of an inactive pipe system. Increasing velocity often decreases pitting attack[1].

1.2.5 Metallurgical variable

As a class, stainless-steel alloys are more susceptible to damage by pitting corrosion than any other group of metals or alloys. Surface finish often has a marked effect on pitting resistance. Pitting and localized corrosion are less likely to occur on polished than on etched or ground surfaces. Generally, the pits that form on a polished surface are larger and penetrate more rapidly than those on rough surfaces[1].

1.3 Stress corrosion cracking

Stress-corrosion cracking (SSC) refers to cracking caused by the simultaneous presence of tensile stress and a specific corrosive medium. During SSC the metal is virtually unattacked over most of its surface, while fine cracks progress through it. This cracking phenomenon has serious consequences since it can occur at stresses within the range of typical design stress[1]. Not all metal-environment combinations are susceptible to cracking. Stainless steels crack in chloride environments but not in an ammonia-containing environment, whereas brasses crack in ammonia-containing environments but not in chlorides. Further, the number of different environments in which a given alloy will crack is generally small. The important variables affecting stress-corrosion cracking are temperature, solution composition, metal composition, stress, and metal structure.

1.3.1 Crack morphology

SC cracks give the appearance of a brittle mechanical fracture, when, indeed, they are the result of local corrosion processes. Both intergranular and transgranular stress-corrosion cracking is observed.

Intergranular cracking proceeds along grain boundaries, while transgranular cracking advances without apparent preference for boundaries[1]. Cracking proceeds generally perpendicular to the applied stress. Cracks are without branches, or they exhibit multibranched patterns, depending on the metal structure and composition and upon the environment composition.

1.3.2 Stress effects

Increasing the stress decreases the time before cracking occurs. There is some conjecture concerning the minimum stress required to prevent cracking. This minimum stress depends on temperature, alloy composition, and environmental composition. For each alloy-environment combination, there is probably an effective minimum, or threshold, stress. The criteria for the stresses are simply that they are tensile and of sufficient magnitude. These stresses may be due to any source: applied, residual, thermal, or welding. Stresses can be generated by corrosion products in constricted regions. The wedging action results in very high stresses at the crack tip because the tip is a sharp notch which is a great stress concentrator[5].

1.3.3 Time for cracking

As SC cracks penetrate the material, the cross-sectional area is reduced and the final cracking failure results entirely from mechanical action. As cracking progresses the cross-sectional area of the specimen decreases and the applied stress increases. The rate of crack movement increases with crack depth until rupture occurs. Immediately preceding rupture, the cross-section of the material is reduced to the point where the applied stress is equal to or greater than the ultimate strength of the metal, and failure occurs by mechanical rupture. During later stages, the crack widens. Before rupture, extensive plastic deformation occurs and a large change in extension is observed[1].

1.3.4 Environmental factors

Stress-corrosion cracking is well known in various aqueous mediums, but it also occurs in certain liquid metals, fused salts, and nonaqueous inorganic liquids. The presence of oxidizers often has a pronounced influence on cracking tendencies[1], indeed, the presence of dissolved oxygen or other oxidizing species is critical to the cracking of austenitic stainless steels in chloride solutions, and if the oxygen is removed, cracking will not occur. It is usually characteristic of crack-producing environments that the alloy is negligibly attacked in the non-stressed condition.

As is the case with most chemical reactions, stress-corrosion cracking is accelerated by increasing temperature. The physical state of the environment is also important. Alloys exposed to single-phase aqueous environments are sometimes less severely attacked than metals at the same temperature and stress when exposed to alternate wetting and drying conditions.

1.3.5 Metallurgical Factors

The susceptibility to stress-corrosion cracking is affected by the average chemical composition, preferential orientation of grains, composition, and distribution of precipitates, dislocation interactions, and progress of the phase transformation[1]. These factors further interact with the environmental composition and stress to affect the time to crack. Ni added to 18 Cr-Fe base shows the effects of alloy composition in austenitic stainless steels. There is a minimum in time to cracking as a function of composition. This observation of a minimum in time to cracking versus composition is a common observation in other alloy systems. While generally, the use of pure metals is often an available avenue for preventing cracking, it should be pursued only with caution. High-strength aluminium alloys exhibit much greater susceptibility to stress-corrosion cracking in directions transverse to the rolling direction than in those parallel to the longitudinal direction. This effect is due to the distribution of precipitates that results from rolling[6].

1.3.6 Mechanism

Corrosion plays an important part in the initiation of cracks. A pit, trench, or other discontinuity on the surface of the metal acts as a stress raiser. Stress concentration at the tip of the notch increases tremendously as the radius of the notch decreases[1]. Stress-corrosion cracks are often observed to start at the base of a pit. Once a crack has started, the tip of the advancing crack has a small radius and the attendant stress concentration is great[7]. Plastic deformation can occur in the region immediately preceding the crack tip. If the alloy is metastable, a phase transformation could occur, and the new phase could have less corrosion resistance. If the alloy is not metastable, the cold-worked region might be less corrosion-resistant than the matrix because of the continuous emergence of slip steps[1].

The role of tensile stress is important in rupturing protective films. Breaks in the passive film or enriched layer on stainless steel allow more rapid corrosion at various points on the surface and thereby initiate cracks. Breaking film ahead of the advancing crack would not permit healing, and propagation would continue[1]. Rapid local dissolution without stifling is required for rapid propagation. In the case of intergranular cracking, the grain-boundary regions could be more anodic, or less corrosion-resistant. because of precipitated phases, depletion, enrichment, or adsorption, thus providing a susceptible path for the crack.

Two basic models for a general mechanism are the dissolution model wherein anodic dissolution occurs at the crack tip because strain ruptures the passive film at the tip, and the mechanical model, wherein specific species adsorb and interact with strained metal bonds and reduce bond strength[1]. In general, susceptibility to cracking increases with strength level. Changes in solution composition or temperature could shift the potential of the system into or out of the danger zone. Inhibitor additions can inhibit cracking.

1.4 Superalloys

Superalloys are classified according to the main alloying elements in the composition, with the three base metals being nickel, cobalt, and iron. The entire superalloy family shares a common basic microstructure, which is a face-centred cubic (fcc) matrix with several dispersed secondary strengthening phases[8].

1.4.1 Nickel-base Superalloys

Nickel-base superalloys achieve the highest temperature/strength combination of all cast and wrought superalloys, making them ideal for turbine blades. Wrought nickel-base superalloys are often used where high toughness is required. Castings are favoured for high strength and creep resistance in high-temperature applications, such as investment-cast turbine blades and wheels, and are alloys such as Inconel alloys 100, 713, and 738[9]. The superior high-temperature capability of nickel-base superalloys is due to the precipitation of high-volume fractions of the γ'-$Ni_3(Al, Ti)$ phase, which requires combined aluminium and titanium contents of at least four to six weight per cent[8]. Some nickel-base alloys do not rely on precipitates for strengthening but rather depend mainly on solid-solution hardening (SSH).

There is a group of superalloys that are produced by pounding in a dry milling process. The mechanically alloyed (MA) materials. The MA process involves a metallic and/or nonmetallic powder charge being worked by a highly energetic ball to produce a composite metal powder. As a result of the repeated welding-fracturing process, the MA powder has a fine lamellar structure and is chemically homogeneous[10]. Mechanically alloyed materials exhibit improved high-temperature strength through the combined effects of γ' strengthening and fine oxide dispersions. The term oxide-dispersion-strengthened (ODS) superalloys is often used to describe MA materials containing oxide dispersions[10]. This oxide addition limits the manufacturing method of these alloys to mechanical alloying of powder materials and subsequent sintering and/or hot isostatic pressing. Melting of these alloys during processing cannot be allowed, because the oxide particles would segregate to the surface of the melt, due to their lower density, and leave the bottom of the casting depleted of the alloy’s principal strengthening phases[8].

Sometimes, powder metallurgy or isothermal forging is necessary to produce the wrought versions of such highly alloyed superalloys as Rene 95, Astroloy, and Inconel 100 due to their high-volume fraction of γ'. Severe dendritic segregation, coarse grain size, and brittle interdendritic phases formed during solidification also make hot working difficult. When γ' volume fractions are higher than 40 to 45 per cent, the gap between the solvus and incipient melting temperature becomes too narrow for practical purposes and limits manufacturing methods to casting or powder metallurgy[8].

1.4.2 Nickel-iron-base alloys

Nickel-iron-base superalloys are characterized by their high toughness and ductility and are used mostly in applications such as turbine discs and forged rotors. Nickel-iron alloys are used only in wrought conditions [11] because this manufacturing method offers a wide variety of mechanisms for controlling grain size and morphology. In addition to their high toughness, another advantage of nickel-iron-base superalloys is their lower cost due to the substantial amount of iron added[11].

There are three groups of nickel-iron-base superalloys: the first is the precipitation-hardened alloys, where γ'-$Ni_3(Al, Ti)$ and/or γ''-Ni_3Nb precipitates form in the fcc γ matrix. The second is the low-coefficient-of-thermal-expansion (CTE) group of alloys. The third group of nickel-iron-base superalloys is the modified stainless steels, primarily strengthened by solid-solution hardening and minor carbide precipitation, such as 19-9DL (18-8 stainless steel with slight chromium and nickel adjustments, additional solution hardeners, and higher carbon) and Inconel-800H (21% Cr and high nickel with small additions of titanium and aluminium, which produce some γ′ phase)[11].

1.4.3 Precipitation-hardened nickel-iron alloys

Some of the alloys that are strengthened through γ′ precipitation are A-286, V-57, Nimonic 901, and Inconel 718. Most nickel-iron-base superalloys rely on titanium additions for hardening through the precipitation of γ′-Ni_3Ti. Long-term exposure above 650 °C tends to cause the γ′ to transform to coarse platelet η phase (a hexagonal-closed-packed Ni_3Ti phase), which results in a considerable decrease in strength[12]. Low levels of aluminium also decrease the environmental resistance of the alloy, because, without sufficient aluminium, the alloy cannot form a protective alumina scale. Another highly effective strengthening precipitate, body-centred tetragonal γ″-Ni_3Nb, forms in alloys that contain niobium. The most widely known such alloy is Inconel 718, a highly weldable superalloy. Some alloys may contain combined aluminium, titanium, and niobium, which could result in dual strengthening by γ′ and γ″, as is the case with Inconel alloys 706, 709, and 718[8].

1.4.4 Strengthening mechanisms

Superalloys are strengthened through three principal mechanisms: solid-solution hardening (SSH), precipitation hardening (PH), and dispersion strengthening. There is usually one dominant mechanism. Further improvement in mechanical properties, such as creep or stress-rupture resistance, is enabled by the control of the grain structure, as in columnar-grained alloys, or by the complete elimination of grain boundaries with the single-crystal superalloys[8].

1.4.4.1 Solid-solution Hardening

Solid-solution hardening is the achievement of an increase in matrix strength by the addition of a different soluble element. The distortion of the atomic lattice caused by the misfit of atomic radius inhibits dislocation movement. Solid-solution hardening increases with the atomic size difference, up to a maximum difference of approximately 10 per cent in atomic size[12]. The use of high-melting-point elements as the solutes provides stronger lattice cohesion and reduces diffusion, particularly at high temperatures. Solid solution hardening also has the effect of decreasing the stacking fault energy (SFE) in the crystal lattice, leading to inhibition of dislocation cross slip, which is the main deformation mode in imperfect crystals at elevated temperatures. A lower SFE makes it more difficult for dislocations to change directions; thus, when a dislocation encounters a barrier, it is more difficult for the dislocation to be able to bypass that barrier by moving onto a new slip plane[11].

In face-centred cubic (fcc) structures, the lowering of SFE leads to three interrelated effects: Dissociation of dislocations into partials. Formation of hexagonally close-packed (hcp) stacking fault ribbons. Increased difficulty of the passage of dislocations from the fcc matrix to the hcp fault.

Atomic clustering or short-range order is another mechanism that contributes to the strength obtained through solid solutions. The effect is related to electronic orbitals[12]. The influence of the clustering effect has been observed in rhenium-modified CMSX-2 by atom probe microanalysis, showing small rhenium atom clusters of approximately 1 nm in size, which significantly impede dislocation movement and thereby improve alloy strength.

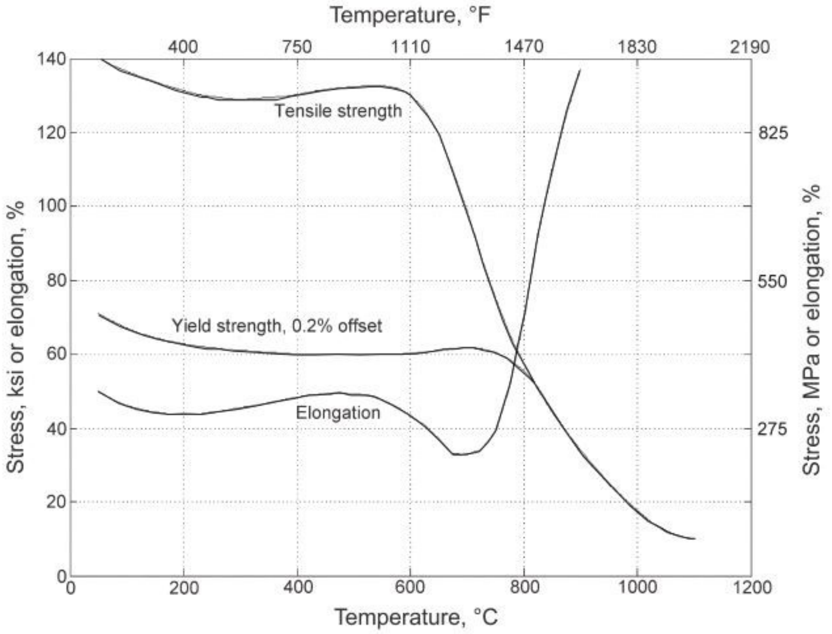

Figure 1.15: Tensile properties of solid-solution-hardened Inconel 625[8].

At temperatures above approximately 0.6 T_M (temperature of melting), creep and strength are strongly influenced by diffusion, which greatly affects SSH alloys, as illustrated in Figure 1.15. SSH only provides strengthening up to approximately 815 °C[13]. Typical elements used in SSH of superalloys are aluminium, iron, titanium, chromium, tungsten, and molybdenum. The use of the more massive elements is desirable because of their lower diffusion rates, but they also increase alloy density and tend to promote the formation of topologically close-packed phases.

1.4.4.2 Precipitation hardening

A considerable increase in the creep strength of alloys for high-temperature applications can be obtained by PH. In the case of nickel-base alloys, this can be achieved using elemental additions such as titanium, aluminium, and niobium. These elements have limited solubility in the alloy matrix, and the solubility is drastically reduced with a decrease in temperature; therefore, finely distributed precipitates can be generated in the matrix from a supersaturated solid solution during heat treatment[11]. The precipitates, which are generally coherent intermetallic compounds such as γ'-$Ni_3(Ti, Al)$ or γ''-Ni_3Nb phase, can inhibit the movement of dislocations. Movement of a dislocation in the matrix containing precipitates can only take place by cutting through or bypassing the particles.

The four factors controlling the effectiveness of PH are:

Coherency strains between the matrix (γ) and the precipitate (γ', γ'') due to the difference in their lattice parameters. Antiphase-boundary (APB) energy in the presence of an ordered precipitate (γ', γ''). The

APB represents the energy needed for the dislocation to cut through the ordered precipitate because cutting could result in disordering between the matrix and precipitate. The volume fraction of the precipitate (γ', γ'') and particle size.

The strengthening achieved through coherent strains and ordering increases with particle size because these two mechanisms require that dislocations cut through the particle. However, this increase in strength with increasing particle size is limited by Orowan bowing, where the dislocation will bypass the particle if it is too large[14]. The strengthening in this case is provided by the extra work needed for the dislocation to alter its path. The morphology of the coherent precipitate in two-phase alloys is strongly influenced both by the elastic strain energy associated with the lattice mismatch between precipitate and matrix and by the interfacial energy of the particle-to-matrix boundary. The elastic strain energy depends on the shape, habit, and volume of the precipitates. Interfacial energy merely depends on the surface area of the particle[15]. For a matrix and precipitate with similar lattice parameters, a spherical precipitate is formed, while for large differences in lattice parameters, an elastically favoured cuboidal precipitate is formed.

1.4.4.3 Carbide hardening

In alloy systems in which SSH elements such as molybdenum and tungsten have limited solubility, carbides are often used to provide high-temperature strengthening[16]. Carbide hardening can be particularly useful for increasing creep strength because under service loads, the high-temperature creep processes mainly take place at the grain boundaries and carbides precipitate preferentially at the grain boundaries. They inhibit grain-boundary slip, transferring creep processes from the grain boundary to the interior of the grain, where diffusion is slower. Small, globular, non-cohesive carbides are best suited for stabilizing grain boundaries. The primary carbides assume the formula of MC and M_6C, with “M” representing molybdenum, tungsten, titanium, and niobium. With prolonged exposure to high temperatures, MC and M_6C carbides tend to transform to $M_{23}C_6$, as do chromium carbides. Because most high-temperature alloys contain high chromium contents for corrosion resistance, the formation of $Cr_{23}C_6$ carbides is unavoidable in alloys with carbon. The formation of chromium carbides depletes the surrounding matrix of chromium, reducing the corrosion resistance of the grain-boundary region, similar to the sensitization phenomenon in stainless steel. The $M_{23}C_6$-type carbides are often cohesive and form along grain boundaries. Because carbides are brittle, these cohesive grain-boundary precipitates represent a preferred path for crack growth, resulting in a decrease in stress-rupture strength and ductility. In contrast, with non-cohesive globular carbides, stresses can be reduced by slight grain-boundary slip, hindering, or preventing the formation of microcracks. At high temperatures, $M_{23}C_6$ carbides also tend to agglomerate, forming fewer but larger carbides on the grain boundary, which could provide crack initiation sites[16]. The carbide-forming elements molybdenum and tungsten can be consumed as carbides at the grain boundaries after long-term exposure to high temperatures. This causes the grain-boundary zones to be depleted of these elements in the solid solution. Although there is a disadvantage associated with the formation of such a depletion zone, the beneficial influence prevails, because the stresses can be dissipated via these "softer" zones adjacent to the grain boundaries and not through the carbide-rich grain boundaries[8].

1.4.5 Phase and microstructure of superalloys

The microstructure of superalloys is highly complex, with a large number of dispersed intermetallics and other phases that modify alloy behaviour through their composition, morphology, and location. The microstructure of a superalloy can be described as a face-centred cubic (fcc) γ-phase matrix that contains several secondary phases.

The morphology of the precipitates is a key factor that determines the properties of the alloy. Continuous grain-boundary carbides render the alloy prone to brittle intergranular fracture; dispersed carbides along the grain boundaries pin the grains against sliding, thus increasing alloy strength. Because maximum strength is achieved with one particular γ′ precipitate morphology, but maximum stress-rupture strength is attained with different morphology, most γ′-strengthened nickel-base superalloys have a bimodal γ′ morphology[8]. The primary process that modifies precipitate morphology is heat treatment.

Grain sizes in superalloys are highly dependent on the manufacturing method. In the 1980s, Howmet Turbine Component Corporation pioneered Grainex, a fine-grained casting technique that uses agitation during solidification to break growing dendrites and promote nucleation. Howmet then developed the Microcast-X process, which involves pouring at a temperature only slightly higher than the liquidus. Because the pour is turbulent and the pouring temperature is low, the alloy solidifies rapidly, producing a uniformly fine-grained casting with a cellular structure[17].

1.4.5.1 Matrix phase

The fcc γ-phase matrix is ideal for high-temperature structural alloys for several reasons:

The fcc matrix has optimal mechanical properties because it has a high modulus and multiple slip systems. The densely packed fcc matrix is ideal for use at high relative temperatures (T/T_M) because of the low diffusivity of alloying elements. The fcc matrix has a broad solubility of secondary elements that permits precipitation of intermetallic compounds, such as γ′ and γ″ for strengthening, and allows the dissolution of high-melting-point refractories[18].

The main element present in the matrix-phase composition is the superalloy base metal, but there is also a high percentage of solid-solution elements, which provide solid-solution hardening to the matrix[19].

1.4.5.2 Geometrically close-packed phases

Geometrically close-packed (GCP) phases are intermetallics with the formula A_3B. They include the principal strengthening phases γ′ (fcc Ni_3Al, Ni_3Ti) and γ″ (body-centred-tetragonal Ni_3Nb) and the closely related η (hexagonally-close-packed Ni_3Ti) and δ (orthorhombic Ni_3Nb) phases. The γ′ phase is the most stable of the GCP phases and is the dominant strengthening phase in superalloys[8].

γ′-$Ni_3(Al,Ti)$:

The γ′-Ni3(Al, Ti) precipitate is undoubtedly the most useful and important strengthening phase in superalloys. Its yield strength increases with temperature up to 800 °C. It is metastable in nickel-iron-base alloys and will transform to η over time in service at high temperatures, which is a drawback to the use of iron as a base element.

Pure Ni_3Al is a superlattice that exhibits a long-range ordered structure up to temperatures near its melting point of 1385 °C. It exists over a fairly limited compositional range, but alloying elements may substitute liberally for either of its constituents to a considerable degree and thereby modify the phase properties. Most nickel-base alloys are strengthened by a γ′ precipitate in which titanium and/or niobium can substitute for up to 60 per cent of the aluminium. Aluminium and titanium are the main alloying additions used to promote the precipitation of γ′[13].

The phase forms as coherent precipitates within the γ matrix. Some of the most representative morphologies are shown in Figure 1.16. Generally, γ′ disperses throughout the γ matrix, but filmlike γ′ can also be formed along the grain boundaries after high-temperature exposure and can be beneficial to creep-rupture properties.

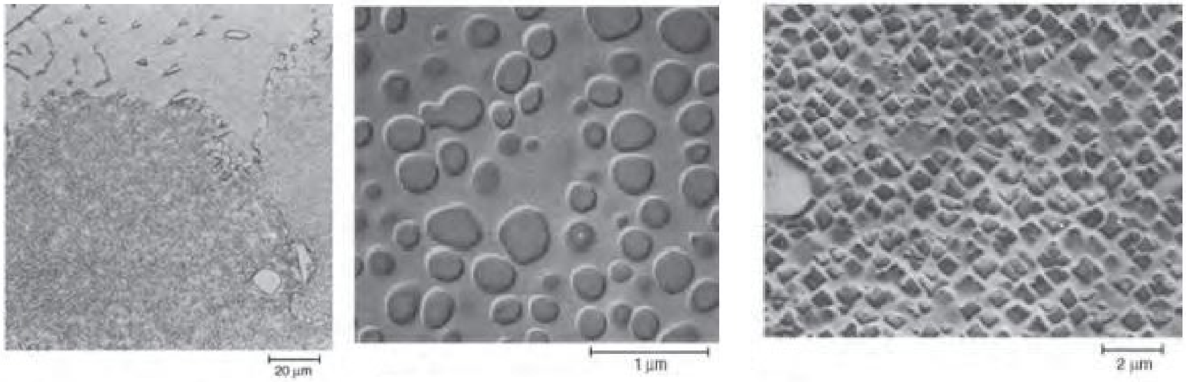

Figure 1.16: Selected morphologies of the γ' phase. (left) B-1900 nickel-base alloy, as cast. Light-etching carbide particles are dispersed in the matrix and at grain boundaries. The fine constituent within grains is γ'. (centre) IN-738 nickel-base alloy casting, after holding at 815 °C for 1000 h. Replica electron micrograph showing structure consisting of rounded γ' particles in γ matrix. (right) IN-738 nickel-base alloy, as cast. Replica electron micrograph showing randomly distributed precipitated γ' Ni_3 (Al, Ti) and a carbide particle (at the left edge) in a matrix of γ solid solution[20].

The coherence between the γ′ phase and fcc γ matrix is maintained by tetragonal distortion. As a result, the nucleation of homogeneous precipitates with low surface energy and extraordinary long-time stability is possible. The presence of such precipitates is particularly useful in alloys intended for high-temperature exposure because it allows the desired microstructure to be retained for a longer time at high temperatures[19].

The compatibility between γ and γ′ is quantified by the lattice mismatch δ. The lattice mismatch is an important factor in determining the morphology of the γ′ precipitate. A lattice mismatch magnitude between 0 and 0.2 per cent produces a spherical precipitate; between 0.5 and 1.0 per cent, a cuboidal precipitate; above 1.25 per cent, a platelike precipitate[19]. The spherical shape minimizes surface energy, but as the lattice mismatch grows larger, the change to cuboidal morphology is driven by the need to minimize elastic energy. The lattice parameter of the γ matrix increases more rapidly with increasing temperature than the lattice parameter of the γ′ precipitate, and as a result, there is an increasingly negative lattice mismatch at elevated temperatures.

The increased lattice mismatch between γ/γ′ improves creep life in single-crystal nickel-base superalloys because the γ/γ′ interface is a barrier to mobile dislocations and a hindrance to plate thickening due to dislocation pile-up at the interface. As the lattice mismatch is further increased, the interfacial dislocations become more closely spaced and act as a strong barrier to mobile dislocations shearing through the interface[21]. So, for alloys with high values of lattice mismatch, the number of interfaces should be maximized to attain optimal properties. The size of the γ′ precipitate is also important in providing effective precipitation hardening because the hardening generally increases with particle size until the particle reaches a critical size. Beyond this size, the dislocation movement mode changes from a cutting mode to a bypassing mode, causing a loss of hardness and strength[8].

At temperatures above approximately 0.6 T_M, γ′ increases in size at a significant rate, facilitating dislocation bypassing. Measures that minimize this effect will help retain long-time creep resistance.

One of the most significant features of the γ′ phase is that its yield strength increases with temperature in the range of −196 to 800 °C. The relationship between yield strength and temperature is also highly dependent on the aluminium content in the γ′ phase, with the magnitude and position of the peak in flow stress being controlled by the presence of such other alloying elements as titanium, chromium, and niobium. Both chromium and titanium raise the temperature of the flow-stress peak, but chromium weakens γ′ at low temperatures while titanium strengthens it[13].

The volume fraction of the γ′ phase is important for determining the strength and creep properties of the alloy and for determining the manufacturing processes that can be used to produce a particular component. Although alloys can be hot worked at low γ′ volume fractions, beyond 40 to 45 per cent volume fraction of γ′ the component must be manufactured by casting[12]. The disadvantage of γ′-strengthened alloys is that the service temperature and life of the component are ultimately limited by the coarsening and dissolution of the γ′ precipitates.

γ″-Ni_3Nb:

The γ″ precipitate is a useful strengthening phase, mainly in nickel-iron-base superalloys. The γ″ precipitate is a coherent bct Ni_3Nb phase with an ordered crystal structure that assumes a disk-shaped morphology. One of the main disadvantages of γ″ as a strengthening phase in comparison to γ′ is its lower solvus temperature. Alloys hardened through γ″ precipitation have a rapid decrease in strength above 650 °C, caused by the loss of the strengthening γ″ phase as it transforms to δ phase[22].

Carbides:

The role of carbides in superalloys is complex; they can either increase or decrease alloy properties, depending on location, composition, and shape. Carbides are present in all superalloy families and tend to locate at grain boundaries. In general, carbides provide a beneficial effect on rupture strength at high temperatures. However, carbides adversely affect the chemical stability of their matrix by locally depleting carbide-forming elements[19]. Cobalt-base superalloys are primarily strengthened through carbide precipitation. Carbides also control grain size during forging, heat treatment, and service exposure[23].

Primary carbides MC (where "M" is tantalum, titanium, zirconium, or tungsten), are formed as discrete blocky particles or as eutectic phases during casting solidification and commonly have an fcc crystal structure. These carbides form during solidification, occurring as discrete particles distributed heterogeneously throughout the alloy, at both intragranular and intergranular locations, and often form between dendrites. These carbides act as a major source of carbon for the alloy during heat treatment and service[19]. Secondary chromium-rich M_7C_3 and $M_{23}C_6$ carbides form mainly on the grain boundaries (Figure 1.17) and usually occur as irregular, discontinuous, blocky particles. The M_6C carbides also precipitate in a blocky form on grain boundaries and can form Widmanstätten structures.

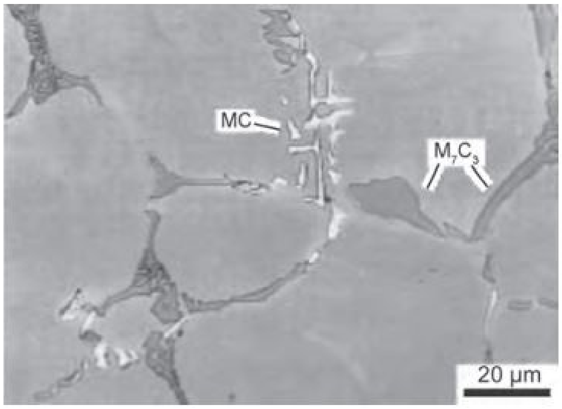

Figure 1.17: Scanning electron micrograph showing carbide distribution in an as-cast cobalt-base superalloy[24].

The $M_{23}C_6$ carbides are profuse in alloys with moderate to high chromium content and are the most common secondary carbides in cobalt-base superalloys.

They form at lower temperatures of 760 to 980 °C than M_6C carbides; however, both types of carbides can form from the degeneration of MC carbides or soluble residual carbon in the alloy matrix. They usually form on grain boundaries, but they can also form along twin boundaries, along stacking faults, and at twin ends. This phase displays a complex cubic structure, which, if the carbon atoms were removed, would closely approximate the structure of the tcp σ phase[10].

The critical location of $M_{23}C_6$ along grain boundaries imparts a significant increase in stress-rupture strength, apparently through inhibition of grain-boundary sliding.

The M_6C carbides tend to be rich in such refractory elements as molybdenum and tungsten. Although like $M_{23}C_6$, they require higher molybdenum + tungsten content to form in nickel-base superalloys (6 to 8 atomic per cent) and cobalt-base superalloys (4 to 6 atomic per cent). In alloys with molybdenum plus tungsten content below these levels, M_6C carbide formation can be induced if the decomposition of primary tungsten-rich MC carbides produces tungsten-rich zones[19,24].

Because of their higher formation temperature in comparison to that of $M_{23}C_6$, M_6C carbides are more beneficial as a grain-boundary precipitate for controlling grain size during the processing of wrought alloys. The mechanical properties most directly affected by carbides are stress-rupture strength and tensile strength. The main benefit of primary MC carbides is indirect in that they provide a relatively stable source of carbon for the precipitation of secondary carbides. However, script-like grain boundary primary MC carbides serve both as crack initiation sites and crack propagation paths and are therefore considered detrimental[25].

In most superalloys, it is the secondary carbides, formed during heat treatment, that provide significant beneficial effects, with the fine secondary carbide dispersions pinning dislocations and hardening the alloy. These carbides stabilize the grain boundaries against excessive shear and thereby improve stress-rupture strength. The amount of carbide at the grain boundaries must be precisely controlled because continuous carbides at the grain boundaries provide easy paths for crack propagation[24].

Carbide dispersions sometimes reduce alloy incipient melting temperature as an indirect effect. The reduced melting temperature is due to the higher carbon contents necessary to form the carbides. When carbide dispersions are formed through mechanical alloying and no precipitation, the incipient melting temperature is observed to increase because of the manufacturing method, which allows residual carbon concentration to be reduced. The disadvantage of adding carbide dispersions through mechanical alloying is the loss of coherency with the γ matrix, which results in lower strengthening effects than would otherwise be achievable[25].

1.4.5.3 Topologically Close-packed phases

Topologically close-packed phases are undesirable. In these phases, the atoms are close-packed in layers that are separated by intervening layers of relatively large atoms. They often form as platelike or needle-like precipitates. The TPC phases include σ-A_xB_y, μ-$A_x' B_y'$, and Laves-A_2B phases, where A is iron, nickel, or cobalt, and B is niobium, molybdenum, tantalum, or chromium. The formation of these phases reduces rupture strength and ductility. The crystal structure of $M_{23}C_6$ carbides is very similar to that of the σ tcp phase, and the M_6C to that of the μ tcp phase, in alloys that contain molybdenum and tungsten[8].

The most detrimental tcp phase is the σ phase, which has hexagonal symmetry. It is characterized by brittleness and a tendency to form plates or needles, which act as crack initiation and propagation sites. The embrittlement effect is particularly strong at low temperatures and high strain rates. The hard tcp precipitates act as barriers to dislocation motion, which lead to dislocation pile-ups at the precipitate interface, causing loss of cohesion at the interface and crack initiation. This effect is exacerbated by the preferential location of the tcp phases along the grain boundaries. The σ phase also contains a high percentage of refractory metal, which depletes the matrix reducing γ-matrix strength. In alloys with high γ′ volume fractions, the σ phase can precipitate at the grain boundaries, where the concentration of molybdenum and chromium is high, or in the dendrite cores, where the concentration of tungsten is high. Commonly, the σ phase precipitates in the Widmanstätten morphology shown in Figure 1.18[12].

To form tcp phases, specific compositions and relatively large amounts of chromium, molybdenum, and tungsten are necessary.

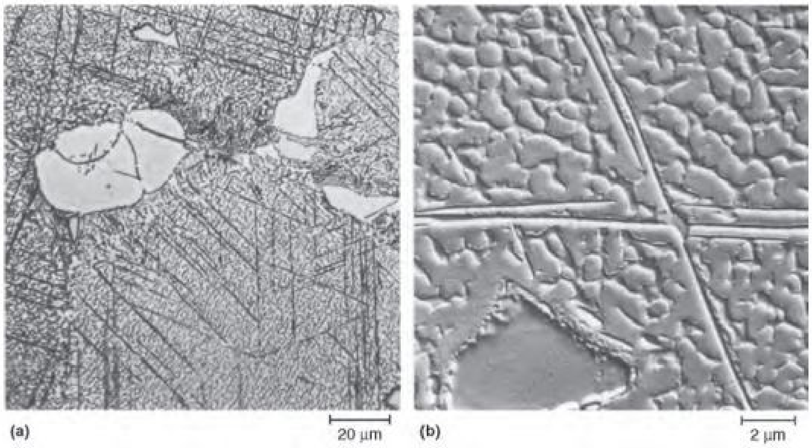

Figure 1.18: IN-100 nickel-base alloy casting, held at 815 °C for 5000 h. (a) The structure consists of massive MC particles, platelets of σ phase, and primary and precipitated γ' in the γ matrix. (b) Replica-electron micrograph shows a massive particle of MC, Widmanstätten platelets of σ phase, and γ' in the γ matrix[12].

Nickel-iron-base alloys have a greater tendency to form tcp phases because the electronic structure of iron has four vacant d sites, and this structure is more likely to form intermetallics with extremely low interatomic distances, for example, the Laves and σ phases. This increased propensity for tcp formation lowers the maximum amount of solid-solution element that can be tolerated in the iron-containing γ matrix and therefore restricts the solid-solution strengthening effect; this restriction is the main drawback to the use of iron in superalloys[19].

1.4.6 Microstructural modifications through heat treatment

Heat treatment is an important method for modifying the morphology of the precipitates in superalloys. Heat treatment has three primary purposes in superalloys: To homogenize the alloy. To dissolve the precipitate in precipitation-hardened alloys. To precipitate secondary phases in a controlled fashion.

Other functions of heat treatment include stress relieving, grain growth, and surface modifications[8]. One goal of homogenization heat treatment is the reduction of compositional gradients. In this process, the alloy is heated to an elevated temperature to increase solid-state diffusion and achieve a more uniform distribution of elements; segregation in cast superalloys can be quite remarkable and can lead to the formation of tcp phases. In wrought solid-solution-hardened alloys, this processing step is called annealing, and although it still reduces compositional gradients, its main goal is to produce complete recrystallization to achieve maximum softness for forging or other shaping processes[8]. For precipitation-hardened alloys, solution heat treatment is performed to dissolve precipitates formed during casting or ageing for the controlled reforming of the precipitates in a precipitation-hardening treatment[15].

In ageing or precipitation hardening, the elements taken into solid solution during solution treatment are precipitated in a favourable type and morphology. This controlled precipitation process is usually a multi-step process that takes place at various temperatures. The γ' and γ'' phases are precipitated in this way. Carbide formation provides strengthening through coherent precipitates and also delays σ-phase formation by consuming significant portions of such σ-forming elements as chromium and molybdenum. Over-aging can produce undesirable precipitate phases and morphologies and should therefore be avoided[26].

1.4.6.1 Rafting

Microstructural changes occur in superalloys during service at elevated temperatures; rafting is one such change. It occurs over time at elevated temperatures under applied stress.

During the rafting, the initially discrete γ' particles coarsen, forming continuous γ' lamellae, or rafts. The lamellae are perpendicular to the direction of applied tensile stress for a negative lattice mismatch between the matrix and the precipitate, which is the case for the typical superalloy matrix and γ' precipitate, and parallel to the direction of applied stress for a positive lattice mismatch. The situation is reversed for applied compressive stress[27].

Rafts can improve the creep resistance of an alloy by providing effective barriers to dislocation motion, effectively forcing a dislocation to shear a γ' lamella to propagate in the perpendicular direction. However, in general, rafting is detrimental to mechanical properties due to the coarseness of the resulting microstructure. Because the shape of the γ' precipitate is dependent on the lattice mismatch δ, it has been found that δ is one of the driving forces of the rafting process, with faster rafting occurring at higher mismatch values[21].

1.4.6.2 Directionally solidified superalloys

In polycrystalline superalloys, diffusion and creep deformation occur preferentially at grain boundaries. These are followed by void formation and eventually by cracking. Also, thermal fatigue cracks initiate from grain boundaries. To prevent such damage, one approach in superalloy development has been the reduction and/or complete removal of grain boundaries. This approach has resulted in the development of directionally solidified (DS) superalloys[8].

In the manufacture of DS alloys, dendrite growth is promoted in a specific direction through the use of a thermal gradient (which can be provided by a chill plate and gradual mould withdrawal), producing a microstructure in which all of the grains are oriented in the same direction. The grain growth direction is deliberately chosen to correspond to the direction in which cubic crystal dendrites grow preferentially, namely the <100> direction. This is typically also the direction of greatest resistance to creep and thermal fatigue because of the low elastic modulus[16].

1.5 Additive Manufacturing

Additive manufacturing, or 3D printing, has been able to respond to the growing demand for greater complexity in the design and more efficient use of raw materials. AM allows the production of complex-shaped metal components in less time and minimizes waste material. This production method makes it possible to use materials that are difficult to work with traditional methods and, in some cases, allows for improvement of their mechanical properties and resistance to corrosion. Metal additive manufacturing is divided into two categories: powder bed fusion (PBF) and direct laser deposition (DLD). PBF processes are divided into selective laser melting (SLM) and electron beam melting (EBM).

The SLM process involves melting a bed of metal powder by the passage of a high-powered laser, following a CAD (Computer Aided Design) model. Once a layer is completed, the building platform is lowered and covered with another layer of powder by an overlay arm. The thickness of the layer can vary from 20 μm to 100 μm. This process is repeated until the complete construction of the component. The chamber in which the process takes place is filled with an inert gas such as argon or nitrogen to avoid oxidation of the molten metal, moreover, to prevent the entry of oxygen, it is kept at positive pressure. The construction resolution is determined by the size of the powder used which commonly has a diameter between 10 μm and 45 μm[28].

The EBM process also involves the fusion of a bed of metal powder which, however, is performed using an electron beam. The chamber in which the process takes place is under vacuum to prevent the electron beam from colliding with the gas molecules and being disturbed. Furthermore, as in the previous case, the state of the chamber avoids contamination and oxidation of the molten metal[28].

The factor that leads to the formation of a certain microstructure is the energy density that hits the dust. This affects the temperature of the melt pool and its size, also determining the cooling rate. All this will determine the resulting microstructure. The process parameters that determine the incident energy density are the power of the laser or electron beam, the size of the impact point, and the scanning speed. The temperature distribution is also affected by the hatch spacing and the scan pattern.

The DLD process does not use a bed of powder but supplies the filler material simultaneously with the emission of energy. The dust is blown out of a nozzle that surrounds the one where the laser beam passes. The system operates on a 5 to 6-axis system. Metal powder with a diameter between 50 μm and 150 μm is used. The inert gas to avoid oxidation of the powder is introduced with the powder itself[28].

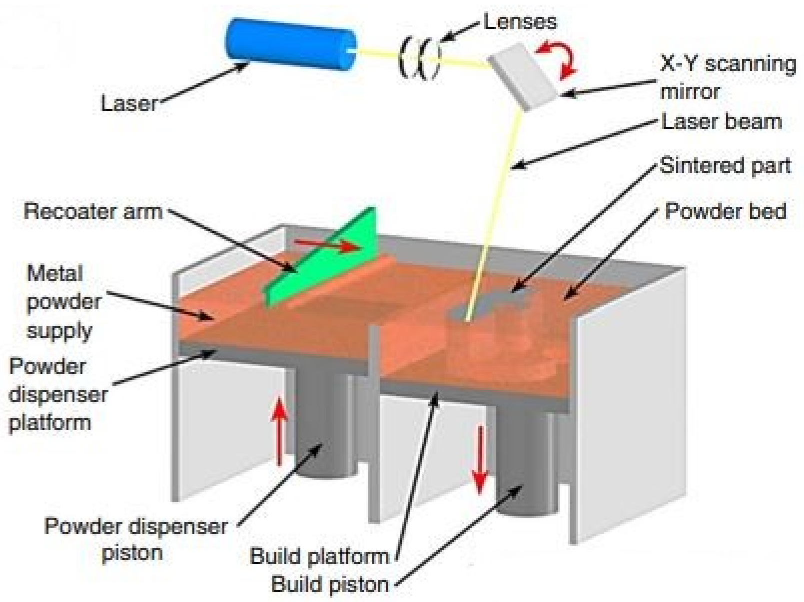

Figure 1.19: Selective Laser Melting machine.[28]

1.6 Model for passivity

The general formula that regulates the growth of a layer that gives the phenomenon of passivation is essentially of two types:

$$L = A + B * \ln(t)$$

Equation 1.9

$$1/L = C - D * \ln(t)$$

Equation 1.10

where L is the film thickness and t is the time. A, B, C, and D are constants. Equation 1.9 is a logarithmic law. While Equation 1.10 is an inverse logarithmic law.

Both of these formulas are equally well represented by the experimental data, indeed, there is not a big difference between the two formulas for very small thickness variations. [29,30]

Since the 1940s, various models have been developed, each of which increasingly fits the experimental data.

1.6.1 Mott-Cabrera model

This model which is essentially the first complex model to determine the growth of the passivating layer has several assumptions: It assumes that the cations travelling to the film/solution interface determine the growth of the film when these come in contact with the solution, they react to form the products that make up the layer. Their movement through the strange is driven by the high electric field that is generated inside the oxide layer and is substantial between one interface and the other (intensity of the field $\varepsilon = -d\Phi/dx$ where Φ is the electric potential and x is the distance); that is, it is equal to the total potential difference that crosses the film (not influenced by the thickness); The slowest step of the process is the transport of the cations from the metal to the film.[31].

1.6.2 Sato and Cohen's model

The mechanism described by this model for the growth of the film is that of the "place exchange". Continuous adsorption of oxygen ions occurs on the surface of the metal, and new sites for absorption are generated by the rotation of the oxide molecules (M - O bond) which leaves new metal uncovered[32].

1.6.3 Fehlner and Mott's model

A different model for the thickening of the passive layer is given by Fehlner and Mort which takes the basis from the Mott-Cabrera model. It is no longer the cations but the anions that, by moving, allow the film to grow. In this case, the anion coming from the solution encounters more difficulties for diffusion at the film/environment interface, and this difficulty is linked to a high activation energy to carry out this action which increases as the thickness of the layer increases[33].

These models are not reliable, each new model discredits the previous one, moreover, even the last one has various problems, indeed, there should be the growth of the passive layer even at low pH, but in these conditions depassivation takes place. Furthermore, the balance at the film/solution interface is very fast and therefore does not represent the rate-limiting step.

1.6.4 PDM-I generation- C. Y. Chao, L. F. Lin, and D. D. Macdonald Model

The Point Defect Model (PDM) is characterized by various assumptions: The passive film can only form if the external potential, V_{ext}, is nobler than Flade's potential; this film is made up of metal oxide ($MO_{x/2}$). The most important feature of this film is that it is very defective, indeed, it is full of punctual defects, that is $V_M^{x'}$ (cation vacancies), $Vo^{\circ\circ}$ (oxygen vacancies), and charged species like e' and h°; The film is intended as an "incipient semiconductor", in fac,t the intensity of the electric field that crosses the passive layer is comparable to that required for breaking the dielectric; The intensity of the field is a function exclusively of the chemical and electrical characteristics of the film (the thickness does not play any role); The electrons (e ') and electron holes (h°) are in an equilibrium state and the speed of the reactions involving them is determined at the metal/film (m/f) or film/solution (f/s) interfaces. The transport speed of the point defects (the vacancies of both cations and anions) determines the growth rate of the passive layer, which reaches its equilibrium at the m/f and f s interfaces.[29].

These reactions occur at the metal/film (m/f) interface:

$$m \rightleftarrows M_M + x/2\, V_O^{\cdot\cdot} + xe'$$

$$m + V_M^{x'} \rightleftarrows M_M + xe'$$

These reactions occur at the film/solution (f/s) interface:

$$V_O^{\cdot\cdot} + H_2O \rightleftarrows 2H^+(aq) + O_O$$

$$M_M \rightleftarrows V_M^{x'} + M^{x+}(aq)$$

The two kinds of point defects in the lattice are generated and diffused oppositely. Oxygen vacancies arise at the m/f interface, travel to the other interface (f/s) and are eliminated. While cationic vacancies arise at the f/s interface they travel up to the m/f interfaces and are then eliminated. The two species are also opposite in their role, the oxygen vacancies ($Vo^{\circ\circ}$) make the passive film grow, while the cationic vacancies ($V_M^{x\,'}$) are responsible for the dissolution of the metal.

The growth rate of the film is therefore determined by the diffusion rate of the oxygen vacancies, it follow the formula:

$$\frac{dL}{dt} = \frac{\Omega}{N_v} * J_{V_{O^{\cdot\cdot}}}$$

Equation 1.11

where dL/dt is the film growth rate, Ω is the molar volume per cation, Nv is Avogadro's number, and $Jvo^{\circ\circ}$ is the flux of $Vo^{\circ\circ}$ per unit area per unit time.

An important hypothesis to add is the dependence of the potential drop at the f/s interface on the pH and the potential applied to the system. The potential drop is always independent of thickness because the f/s interface is polarizable as well as the fact that the growth reaction is an interfacial reaction[29].

1.6.4.1 Film growth due to reprecipitation of the cations from solution

C. Y. Chao, L. F. Lin, and D. D. Macdonald hypothesized that the metal cations (those in the solution and those in the passive film) at the film/solution interface are in their equilibrium state. The metal cations in solution are at a higher concentration and tend to precipitate on the passive layer forming another crystalline layer since this allows them to have a more stable energetic condition. However, this process is quite slow as the new phase has a very regular pattern. This process is independent of the potential and can only take place if the oxidation state of the cation does not change[29].

1.6.4.2 The mechanism for the Breakdown of a Passive Film

Experimental data give some knowledge: Film breakdown occurs only above a critical potential, Vc (the critical breakdown potential); For a specific material, Vc is a function of halide activity; Breakdown occurs at localized sites; Exists an incubation time between the addition of halide and the start of pitting corrosion. This incubation time depends on the potential;[34] Ellipsometric readings for the passive film undergo a sudden change which might be attributed to the incorporation of Cl- anion into the oxide film during the incubation time.

The diffusion of metal cations from the m/f to the f/s interfaces causes the creation of metal vacancies (or "metal holes") at the metal/film interface. These metal "holes" will tend to submerge into the bulk of the metal and will disappear. However, when the cation diffusion rate (i.e., the metal hole production rate) is higher than the "metal hole" submergence rate into the bulk, the metal holes will start piling up and hence will form a void at the metal/film interface (this is the process of pit incubation). When the void grows to a certain critical size, the passive film suffers a local collapse, and the pit incubation period ends. Subsequently, the collapsed site dissolves much faster than any other place on the surface and so pits grow[35].

J_{ca} is the cation diffusion rate in the film. The presence of halide ions greatly enhances J_{ca} and hence accelerates film breakdown.

$$J_{ca} = J^{o} * \left[C_{V_{O^{\cdot\cdot}}}(f/s)\right]^{-x/2}$$

Equation 1.12

Where J° is derived by the change in Gibbs energy for the Schottky-pair reaction, x is the charge on a cation. From this equation results that J_{ca} can be increased by decreasing the concentration of oxide vacancies at the f/s interface ($C_{Vo^{\circ\circ}}$(f/s)). Kruger et al.[34] have shown that Cl- ions can be incorporated into passive films. Can be assumed that this is due to the occupation by Cl- ions of oxygen vacancies. Thus, as the concentration of chloride increases, so does the number of vacancies that are occupied. This results in a concomitant decrease in the $Vo^{\circ\circ}$ concentration at the f/s interface[36].

1.6.4.3 Impedance Response

The point defect model can be used to interpret the impedance response of a passive film. The same assumptions of the point defect model are adopted in this analysis.

The rate-controlling step for an electrochemical reaction involving electrons or electron holes takes place at the metal/film (m/f) or the film/solution (f/s) interfaces. On the contrary, the rate-controlling step for an electrochemical reaction that involves metal cations or oxide anions is the transport of these species across the oxide film. The activity coefficients for point defects are always equal to one.

It is assumed also that the small alternating current (a-c) perturbing potential applied between the metal and the solution, and the resulting a-c current, do not affect the thickness of the passive film[35].

The impedance function, Z, for an electrochemical system is defined as:

$$Z = V_{ac}(\omega)/I_{ac}(\omega)$$

Equation 1.13

where $V_{at}(\omega)$ and $I_{ac}(\omega)$ are the external a-c potential and current, and ω is the frequency.

The total current through the passive film is the sum of four components: electronic current due to the transport of electrons, electronic current due to the diffusion of electron holes, ionic current due to the transport of $Vo^{\circ\circ}$, and ionic current due to the transport of $V_M^{x'}$. The transport of each one of these species is independent.[35]

The total impedance is equal to:

$$\frac{1}{Z_{total}} = \frac{1}{Z_e} + \frac{1}{Z_h} + \frac{1}{Z_O} + \frac{1}{Z_M}$$

Equation 1.14

The rate-controlling step for electrochemical reactions involving electrons is located at an interface, so electron transport across the film is considered to be rapid. Thus, the transport of electrons in the passive film is like that in metals, the passive film is considered a pure resistor for electrons, i.e., Ze = Re.

The impedance for electron holes can also be considered as a resistor, i.e., Zh = Rh.

The rate-controlling step for an electrochemical reaction involving anions is the transport of the anions or anion vacancies across the film. The anions at the metal/film (m/f) and film/solution (f/s) interfaces are assumed to be in their equilibrium states. From this assumption, The concentrations of anions or anion vacancies depend on the potential differences at these interfaces, which in turn depend on the applied potential[35].

The change in the $Vo^{\circ\circ}$ concentrations at the m/f and the f/s interfaces with time results in the redistribution of oxide ion vacancies inside the film and hence in the flow of current. The redistribution of $Vo^{\circ\circ}$ follows Fick's second law[35].

The impedance for anions has the form of a Warburg impedance for a finite-thickness diffusion layer.

1.6.4.4 Experimental Observations for Passivation Electrodes

Considering pure nickel in O.1N Na_2HP0_4 (pH 9.1) and 0.I5N borate buffer (pH 8.7) solutions Chao and Macdonald[37] found that the complex impedance plane for a passivated nickel electrode can be represented by the diagram in Figure 1.20. This diagram is made up of two semicircles at high frequencies and a Warburg-type response at low frequencies. The two semicircles represent the film/solution interfacial impedance. The Warburg-type impedance is associated with vacancy transport across the passive film.

It has been discovered, using ellipsometry and coulometry, that when nickel is passivated, a majority of the electrical charge is stored in the passive film[38]. The primary passive film (which is not precipitated from the solution) can only grow by the diffusion of oxygen anion vacancies. Therefore, the external current measured on a passivated nickel electrode is almost exclusively due to the transport of oxygen anion vacancies and the contribution from the transport of cation vacancies, electrons, or holes is not significant[35]. Considering a type 304 stainless steel in 0.1N Na_2HPO_4 solution (pH 9.1). The complex impedance plane for passivated Type 304SS is like that for nickel. The diagram consists of two semi-circles at high frequencies and a Warburg response at low frequencies. But, for this material, the Warburg coefficient (the slope of the line) increases with increasing (direct current) d-c potential[37].

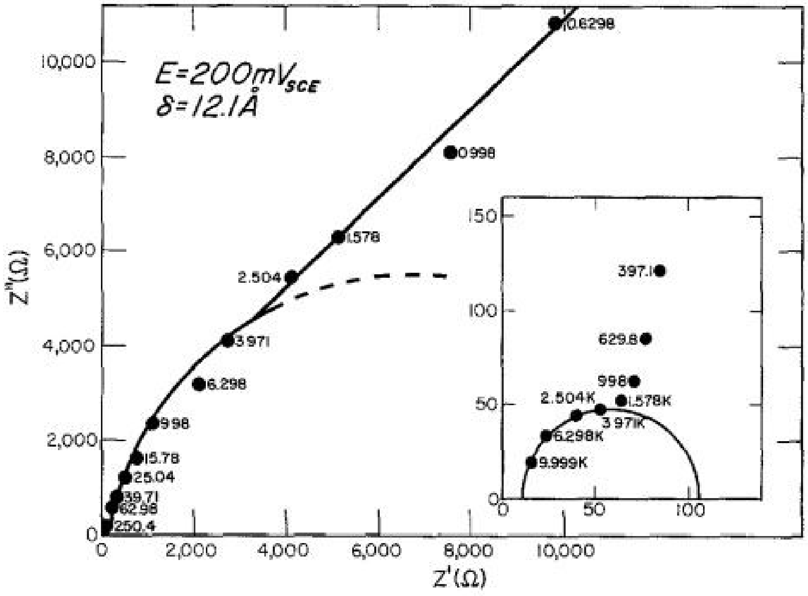

Figure 1.20: Complex impedance plane for passive nickel in phosphate buffer solution; Z' is the real component of the impedance, and Z" is the imaginary component [35].

To summarise: The analysis predicts that a passive film will exhibit a Warburg-type plot in the complex plane at low frequencies, which has the general characteristics of those for a system of finite diffusion length. The theoretical findings fit very well with the experimental impedance data for passivated Ni and Type 304SS in aqueous borate and phosphate solutions[35].

1.6.4.5 Macdonald's considerations

Thanks to the experiments it is known that: Passive films generally form as bilayers composed of a highly disordered "barrier" layer adjacent to the metal and an outer film with a precipitated phase that may incorporate anions and/or cations from the solution. Passivity is observed even in the absence of the outer film, so it is possible to attribute "passivity" to the barrier layer. The steady-state thickness of the barrier layer and the logarithm of the steady-state current vary linearly with the applied voltage, except when a change in the oxidation state of the cation within the film takes place within the passive range. The linear variation of the film thickness with applied voltage results in the fact that the electric space field within the film is also independent of voltage, even under controlled potential conditions[39].

It is assumed that the transmission of ions through the barrier layer occurs by vacancy motion, due to the preponderance of Schottky defects, the reactions that occur at the metal/film and film/solution interfaces are those in Figure 1.21. They are the only possible elementary reactions for vacancy generation and annihilation.

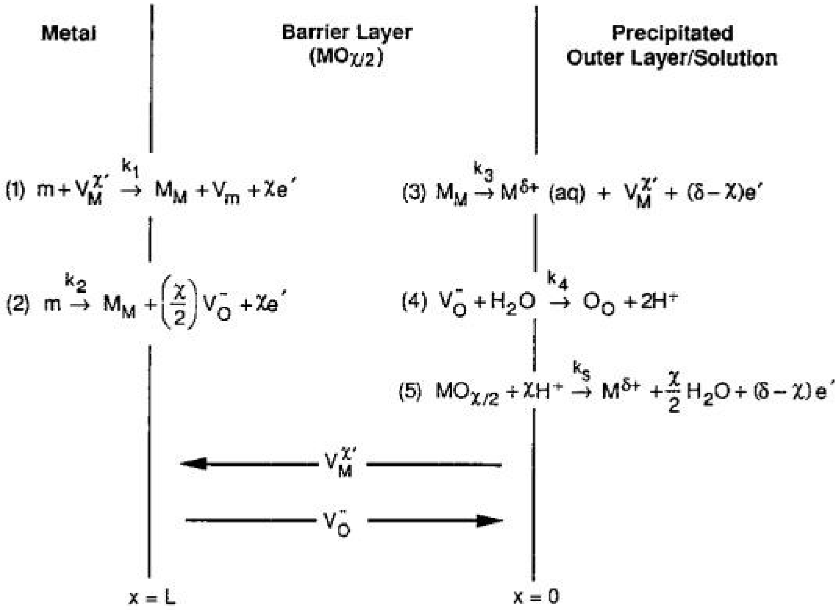

Figure 1.21: Schematic of physicochemical processes that occur within a passive film according to the point defect model[39].

Reactions 1, 3, and 4 conserve the film because they involve the movement of ions across the boundaries. Reaction 2 causes the generation of the film by a fluctuation in electron density around an atom in the metal at the metal/film boundary. The metal atom (m) does not move, but the ions within the film must move to create the oxygen vacancy. Reaction 5 results in the destruction of the film by dissolution, and hence, is also non-conservative[39].

Because the steady state involves two nonconservative reactions the rates of reactions 2 and 5 must be equal. In the steady state, the current is generated by the flux of cation vacancies and by the flux of oxygen vacancies[39].

1.6.4.6 Impedance

Considering the passive film on Ni(III) in phosphate buffer solutions, the PDM fits with the experimental impedance data by regarding various model parameters as variables. These parameters included the interracial rate constants and transfer coefficients, electric field strength, and vacancy diffusivities.

The calculated data were found assuming that cation vacancies alone move through the barrier layer and a single set of kinetic parameters yielded a calculated impedance function that fits very well with the experimental data over wide ranges of voltage and pH. However, the full set of simulations was performed for the two cases in which it is assumed that either cation vacancies or oxygen vacancies within the barrier layer are mobile. Analysis of the two cases (cation vs. anion motion) found that the fits to the cation conducting case were much better than for the oxygen ion conducting case[35]. This finding agrees with the fact that the barrier layer on nickel is a cation conductor. On the contrary, the passive film on tungsten is an oxygen ion conductor and the passive current is dominated by the kinetics of dissolution of the barrier layer (oxygen ion conducting case)[39].

1.6.4.7 Passivity Breakdown and Pit Nucleation

Considering a hydrated chloride ion approaching the film/solution interface of the barrier layer (after passing through the precipitated layer), the barrier layer appears as an undulating surface of charge with positive potentials that take place over cations and negative potentials over anions, with the difference between the peaks depending on the degree of covalent bonding in the lattice (the greater the extent of covalent bonding the lower the difference between peaks). Occasionally, the chloride ion finds vacancies, with cation vacancies appearing as sites of high negative charge and oxygen vacancies appearing as sites of high positive charge. Thus, the chloride ion has several attractive sites to attack[39].

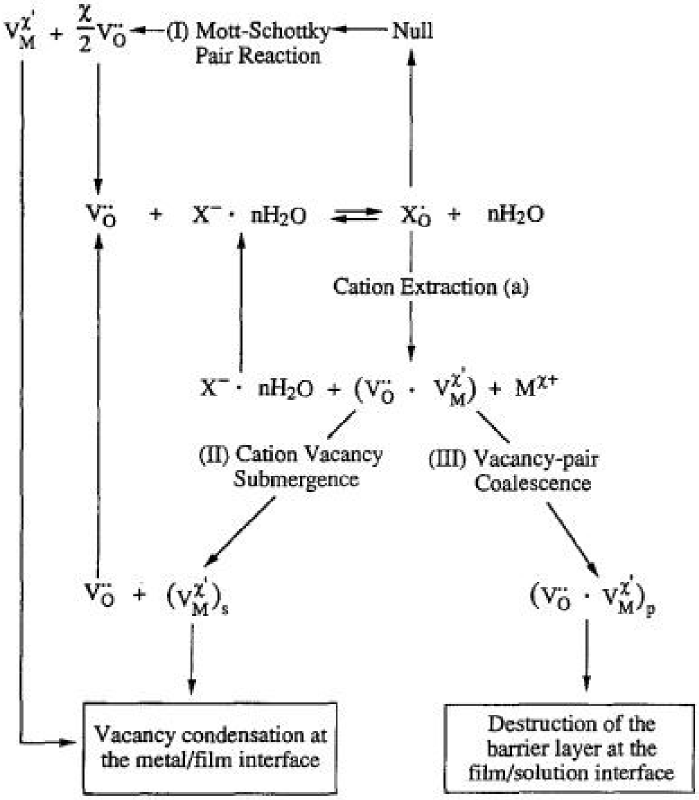

Figure 1.22: Summary of proposed reactions leading to passivity breakdown[39]

In the case in which an anion absorbs into a surface oxygen vacancy, the film may respond in several ways Figure 1.22. In case I, the system responds to the loss of oxygen vacancies by the generation of cation vacancy/oxygen vacancy pairs via a Schottky-pair type of reaction. The oxygen vacancies then react with additional anions (e.g., chloride) at the film/solution interface to generate more cation vacancies. The generation of cation vacancies is autocatalytic, but the film can break down or not, it depends on the relative rates with which the cation vacancies are transported across the barrier layer and are annihilated by the emission of cations from the metal into the film. If the annihilation reaction can't consume the cation vacancies arriving at the metal/film interface, the vacancies will condense and lead to the local detachment of the film from the underlying metal[39].

A cation vacancy-anion vacancy pair can form if an absorbed anion desorbs along with a surface cation [process a]. This process is significant in those cases where the anion tends to complex with the cation (e.g., in the case of iron in chloride solutions), instead of forming an insoluble compound[39].

In case II, the cation vacancy may submerge into the barrier layer by the outward movement of a cation, causing the regeneration of an isolated surface oxygen vacancy. The anion vacancy may then absorb another anion, so this process is autocatalytic and, because X^- is regenerated in reaction “a” the concentration of the absorbed anion may exist in a steady state for any given set of conditions. Reaction II, in this way, leads to the anion-catalyzed generation of cation vacancies at the barrier layer/environment interface and their penetration into the film[39].

Cation vacancies do not submerge into the barrier layer in those films where the cation mobility is very low. In case III, indeed, the pairs may persist at the surface and eventually coalesce to destroy the lattice at the barrier layer/environment interface. Reaction III can be seen as the macroscopic anion-catalyzed dissolution of the film[39].

Regions of the film, where cation mobility is very low promote the destruction of the barrier layer at the film/solution interface by vacancy pair formation. However, it might be thought that the system responds by growing additional film at the metal/film interface. If this process occurs over a localized area, the barrier layer penetrates the metal substrate in like fashion. This may be the mechanism of the formation of porous anodic films on aluminium upon anodizing in acid solutions[39]. Presumably, dissolution takes place at some persistent defect that extends through the barrier layer to the film/solution interface. Destruction of the vacancy pairs by the outward flow of cations is promoted in films or regions where the cation mobility is high, and this leads to the generation of cation vacancy condensates at the metal/film interface. Pits nucleate at points of high disorder where high cation mobility is expected, for this reason, the arguments presented above seem to favour vacancy condensate formation (cases I and II), rather than local film thinning (case III), as the fundamental nucleation event, although local thinning is, in any case, expected to occur[39].

For a film in the steady state, a balance exists between the rate of film formation at the metal/film interface and the rate of dissolution at the film/solution interface, but if the film is detached locally from the metal because cation vacancies condensate, reaction 2 cannot occur and the film ceases to grow into the metal. However, reaction 5 doesn’t stop and the film thins locally until rupture eventually takes place.

To summarise: passivity breakdown occurs at regions of the film that are characterized by high cation vacancy diffusivities; At the beginning there is the condensation of cation vacancies at the metal/film interface, causing local detachment of the film from the metal. Due to the inhibition of the generation of oxygen vacancies at the metal/film interface and the growth of the barrier layer into the metal, the film thins as a result of the continued dissolution of the barrier layer by reaction 5. In the end, rupture occurs because of either complete dissolution or mechanical rupture, which takes place because of residual or induced stresses. The various stages in pit nucleation, according to the above model, are illustrated in Figure 1.23[39].

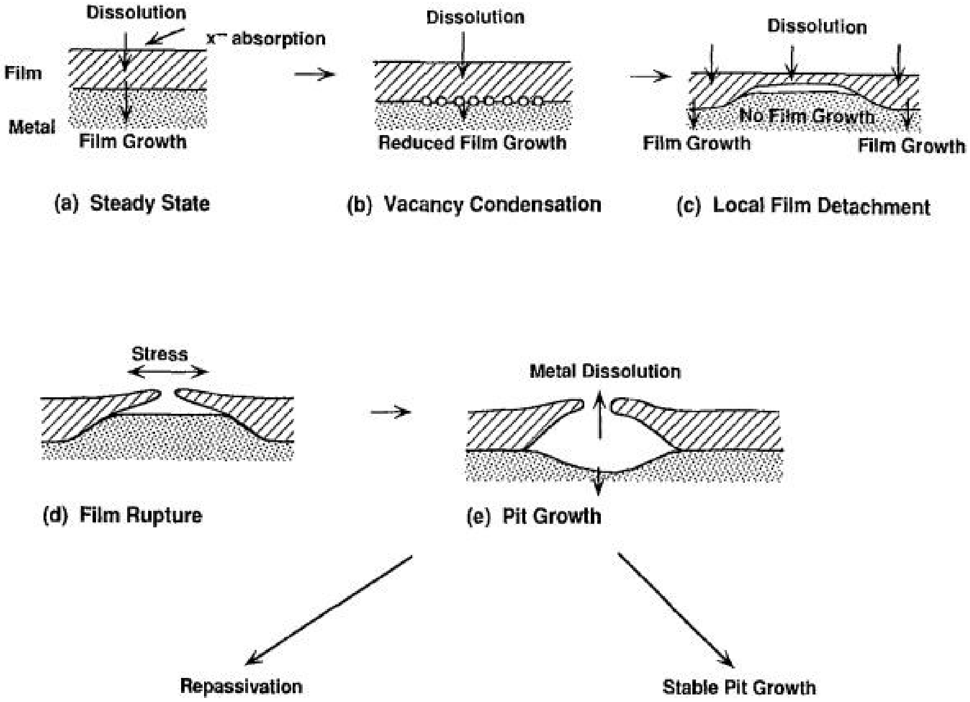

Figure 1.23: Various stages of pit nucleation according to the PDM[39]

Givens et al.[40]found that the nucleation of pits on aluminium in chloride-containing solutions is preceded by the formation of local areas of detached film. These areas are called blisters and they grow with time and at some point emit a fine stream of bubbles (presumably hydrogen) before evident rupture. Chloride penetration can take place via the existing oxygen vacancy structure as Clo° species. However, any movement of chloride through the lattice would necessarily involve unfavourable transport up an electric potential gradient of the order of 106 V/cm because Clo° carries the same sign of charge as Vo°° (the vacancies are ionised). This is a very difficult process, particularly since the flux of oxygen vacancies is irreversibly in the opposite direction[39].

It is possible that chloride ions could move (as anionic species) through channels (grain boundaries and others) in the film to the uncovered metal at the metal/film interface. However, hydroxide ions could move similarly and, because of the much higher concentration of water than chloride at the barrier layer/solution interface, it is much more probable that such channels would passivate[39].

It is assumed that the absorption of an aggressive anion (e.g., Cl-) into a surface oxygen vacancy is the initial event that takes place at the barrier layer/environment interface in passivity breakdown, and it is followed by a Schottky-pair type reaction, (Figure 1.22, Case I).

In this mechanism, anion absorption leads to the generation of cation vacancies at the film/solution interface and, as a consequence, the flux of cation vacancies across the barrier layer increases. The flux of cation vacancies across the barrier layer that results from the increased concentration of vacancies at the film/solution interface, could not be accommodated by reaction 1 (Figure 1.21), so it lead to the formation of a cation vacancy condensate. Once a critical size of the condensate is reached, the dissolution of the film at the film/solution interface and the tensile stresses in the barrier layer induce a mechanical or structural instability, that causes the rupture of the film and a rapid localized attack[36].

A reason why Chloride ion is so effective at inducing passivity breakdown on many metals and alloys can be given by the thermodynamics of the process. The Gibbs energy for the reaction of absorption of X- is composed of two principal components; the dehydration energy ΔGh and the energy required to expand the vacancy to accommodate the ion ΔGe. Thus, from the first halide to the latter of the series F-, CI-, Br-, and I-, ΔGh becomes less positive for the tendency of larger ions to hydrate with less ease but this is compensated by the greater (more positive) energy that is required to expand the vacancy. Cl- has the most favourable Gibbs energy of absorption into an oxygen vacancy, and for this reason is the most dangerous. ΔGe depends on the size of the oxygen vacancy in the surface of the barrier layer; the larger the size, the more favourable the Gibbs energy, and larger anions can be adsorbed. Consequently, other anions may be better able than chloride to induce passivity breakdown on the base of oxygen vacancies size[39].

On any real surface, many potential breakdown sites exist that correspond to a distribution in the properties of the "weak spots." Besides lowering the total number of potential breakdown sites per unit area of the surface, the cation vacancy diffusivity is another parameter that may be manipulated to improve the resistance of a passive film to chemically induced breakdown. A decrease in the cation vacancy diffusivity causes an increase in the "pitting potential" (i.e., Vc), indeed, a higher voltage is required to produce the same flux of cation vacancies across the barrier layer[39].

1.6.4.8 Transpassive dissolution and electropolishing

Film breaking can also occur in the absence of "aggressive" anions because other processes can lead to a sufficiently high cation vacancy generation rate. Indeed, with the increase of the potential, an accelerated expulsion of cations from the film is obtained according to reaction 3 (Figure 1.21).

The rate of this reaction is strongly influenced by the potential. At a sufficiently high potential, the generated cation vacancies cannot be eliminated by reaction 1, the speed of which depends only weakly on the applied voltage. Condensation of cation vacancies at the metal/film interface generally occurs across the surface, and this causes macroscopic decohesion of the barrier layer from the metal. After the breakdown of the layer over large areas, the high dissolution rate (controlled by mass transport) of the substrate will inhibit the formation of the barrier layer although another type of layer, an outer layer, possibly as a "film", may form of salt [41]. Consequently, the system is no longer passive due to the presence of the barrier layer that exists at lower potentials in the passive range, but in any case, the current decreases over time due to the mass transfer through the newly formed outer layer. This is the mechanism proposed by Macdonald for the phenomenon of transpassive dissolution and electropolishing.

1.6.5 PDM-II generation

Figure 1.21 shows the reaction scheme adopted in PDM-I for the generation and elimination of cation vacancies at the m/f and f/s interfaces. Metallic interstitials (point defects) are not considered in these reactions and film dissolution is not described. Furthermore, PDM-I is not considered reliable because it cannot explain the existence of the steady states observed in the passive current density and barrier layer thickness. In many cases, where the film is n-type, only oxygen vacancies cannot explain the current, there must be another mobile donor. That species is precisely the interstitial cation. Finally, PDM-I does not distinguish reactions based on their lattice conservation nature. Thus the development of PDM-II became necessary[42].

1.6.5.1 Specific features and assumptions

PDM-II, to accurately describe the physical-electrochemical processes that occurred at the interface, takes into consideration the dissolution of the barrier layer which occurs at the barrier layer/solution interface (outer layer) by chemical or electrochemical processes; the formation of steady states of thickness and current is verified; It divides the interfacial reactions into conservative and non-conservative reticulum; New point defects are introduced in the barrier layer, i.e. the interstitial ions (donors), which are, in many cases, the dominant defects (Fe, Zn, Pt, stainless steel, alloy 22, etc.). However, many hypotheses of PDM-I are preserved: The fact that the passivating film consists of two layers, the inner layer (barrier) consisting of elements of the metal, indeed, it grows towards the inner surface, and the outer layer also consists of elements of the solution, which precipitate from it; The barrier layer is the one that makes the most significant contribution to the interfacial impedance and consequently to the corrosion rate and the passive current density; The inner layer has a non-perfect point-like crystal lattice structure (nano-crystallites) because various point defects are present, i.e. vacancies of cations (acceptors), interstitial cations (donors) and oxygen vacancies (donors). The electronic character of the film is determined by these defects; The speed is essentially determined at the metal/barrier layer interface, indeed, the intensity of the electric field is independent of the applied voltage; The generation of electron-hole pairs through Esaki tunnelling is the reason why the intensity of the electric field cannot exceed the limit of about 5 MV/cm; The metal layer, the barrier layer and the outer layer (solution) are at different potentials, and in particular, the difference across the barrier layer/solution interface is a linear function of the applied voltage and pH. A Steady state must always be achieved when performing experiments to determine barrier layer thickness and passive current density[42].

PDM-II adds other reactions to the mechanism proposed in PDM-I (Figure 1.24). The exclusive reactions of this model are those for the generation and elimination of interstitials (Reactions (2) and (5), respectively) and the specific one for the dissolution of the barrier layer. Only some of these reactions can change the position of the phase boundary (m/bl or bl/s interface), i.e. those involving the minimum unit of the film ([$M_M(O_O)_{\chi/2}$], [$M_M(V_O)_{\chi/2}$], or [$V_M(O_O)_{\chi/2}$]). Only reactions (3) and (7) meet this prerequisite, they are the only ones that determine the size of the film; indeed, they are defined as non-conservative of the lattice. The remaining reactions are called conservative of the lattice because they do not change its boundaries[42].

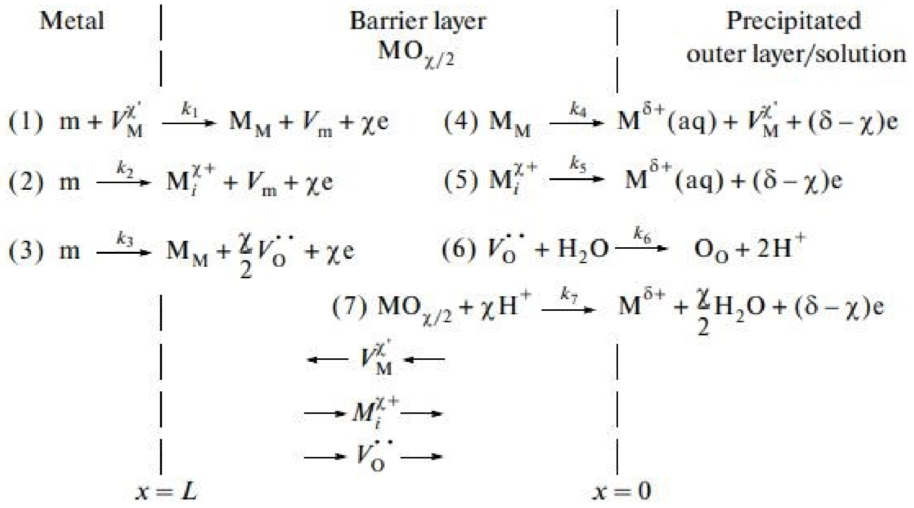

Figure 1.24: Summary of the defect generation and annihilation reactions envisioned to occur at the interfaces of the barrier oxide layer on a metal. $V_M^{x'}$ cation vacancy, M_i^{x+} cation interstitial, $V_O^{\circ\circ}$ oxygen (anion) vacancy, $M^{\delta+}(aq)$ cation in outer layer/solution interface, M_M cation in cation site on the cation sublattice, O_O oxide ion in anion site on the anion sublattice, $MO_{\chi/2}$ stoichiometric barrier layer oxide[42].

The dependence of the steady-state barrier layer thickness concerning voltage and pH is linear. This is an important confirmation of the veracity of the PDM-II.

The growth of the barrier layer occurs due to the formation of oxygen vacancies thanks to the reaction (3) and the elimination of these defects thanks to the reaction (6), which occur at the m/bl interface and the bl/s interface, respectively. The barrier layer grows towards the inside of the metal and not thanks to the precipitation from the solution of other species, only the water participates by providing oxygen. All this agrees with the fact that in the barrier layer no species comes from the solution but only alloying elements and their products. The external layer is the one that instead consists of the cations that cross the barrier layer, hydrolyse themselves, and react with species of the solution, in particular the anions, and then precipitate. The outer layer consists of these products which are essentially oxides, hydroxides and oxyhydroxides, and those specific products of the reaction between cation and anion (e.g. siderite, FeCO3, in carbonated solutions). The outer layer can also be formed by a simple reaction of the barrier layer with the solution, which occurs at the bl/s interface[42].

If the dominant charge transfer process is the movement of the vacancies of the cations, a barrier-like layer of p-type is obtained, if $\delta = \chi$, i.e. no change in the oxidation state of the cation occurs. If it is the transmission of the cationic interstitials and vacancies of oxygen to be dominant, the barrier layer is of n-type. In the first case, the passive current obeys the Tafel relation (Tafel's law) while in the second case the passive current density is independent of the applied voltage. The fluxes of each defect at the two interfaces must be equal to maintain the steady state and therefore dL/dt = 0. All reactions (Figure 1.21) that produce ($\chi > 0$) or consume electrons ($\delta < \chi$) make their contribution to the passive current.[42]

1.6.5.2 The Kinetic Properties of the Passive State

What allows the passive layer to exist is a perfect relationship between the rates of the two non-conservative reactions. Its existence is determined by kinetics and not by equilibrium. If only that were considered, for example in the case of iron, the latter would transform everything into the outer layer (or would go into solution), because the outer layer would be the thermodynamically more stable one. Even iron could convert in the outer layer directly thanks to the reaction:

$$m \longrightarrow M^{\delta+}(aq) + V_m + \delta e' \qquad \text{(Reaction 8)}$$

After the dissolution of the metal in the solution, when the latter reaches saturation, the products that can form the outer layer would precipitate, leading to its generation and growth. If the concentration of metallic ions in the solution were to approach that for equilibrium with the metal, the solution would be supersaturated concerning the barrier and the outer layer, and these phases would tend to precipitate. The net result is that the metal converts into the barrier layer, which in turn converts into the outer layer/solution in an irreversible thermodynamic way. Therefore, to study the passive state it is necessary to use a kinetic point of view. [42].

$$\frac{dL}{dt} = ae^{-bL} - c$$

Equation 1.15

This equation allows relating the growth rate of the barrier layer to the thickness of the barrier layer. L is the independent variable and represents the x-axis while the two terms on the left are plotted as a function of it in the mathematical analysis technique called phase space analysis.[43]. It is assumed that $\delta = \chi$, so that the dissolution term, i.e "c", is not a function of the potential but a constant. (Figure 1.25) A graph is generated consisting of various elements: a horizontal line, which represents the value of c concerning L, (Lines 1 and 2); an exponential decrease representing the relationship between the first term on the right side of the equation and L, the function tends to dL/dt = 0 asymptotically. The condition for which the barrier layer may exist (metastable phase) is that the horizontal line intersects the exponential with positive L values (case: 1 and 3). On the contrary, it does not form a negative L (case: 2 and 3). So the general rule for the existence of the barrier layer is that $(dL/dt)_{L=0} > c$.[42].

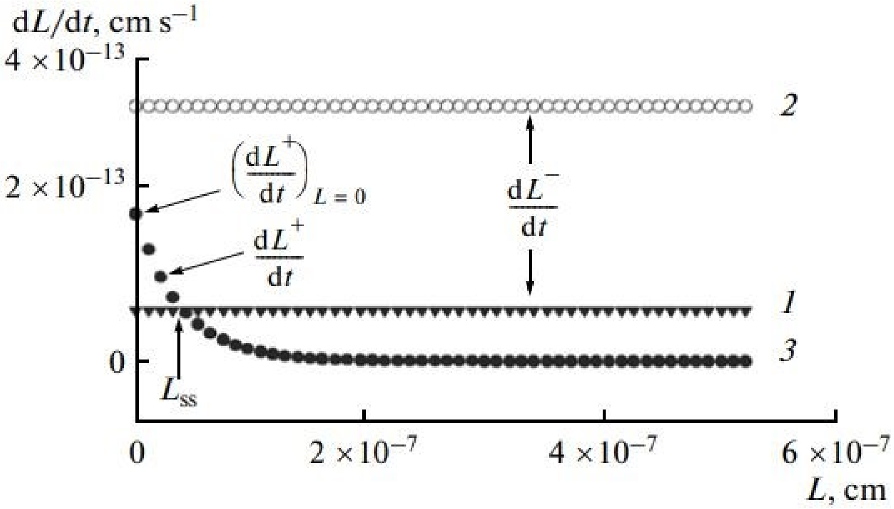

Figure 1.25: Schematic of phase space analysis showing the steady state, passive condition [intersection of filled points, (1) and (3)] and the depassivated condition [filled and open circles, (2) and (3)][43].

The inverse condition [that is, $(dL/dt)_{L=0} < c$] relates to the possibility of having a depassivation of the material. To predict the depassivation of a material, it is possible to directly compare the rate of growth (or decrease) dL/dt with the pH. For example, in depassivation by an acid, the dissolution rate increases as the pH decreases; indeed, the dissolution rate of the barrier layer at the bl/s interface is a positive function of the H + concentration.

An Alloy 22 was analyzed in 6.256 M (sat) of NaCl at a potential of 0.300 V (SHE) and at a temperature of 50 ° C to verify the assumptions of PDM-II, which is further confirmed by the experimental results: The dissolution rate continues to increase until depassivation is reached at lower pH (-1.3), if the pH is further reduced, the passive layer is not even able to form[42]. Below the pH value of 6, the cationic interstitials are the dominant defects in the determination of the total current, while above the pH value of 8, it is the cationic vacancies that dominate the current and the passive film changes from type n to type p; the logarithms of the partial current densities for the oxygen vacancies and the metal interstitial decrease linearly with increasing pH; The partial current due to the movement of the cation vacancies is independent of the pH[44].

1.6.6 PDM-III generation

To further improve PDM, PDM-III has begun to be developed. The focus of this model is the explanation of the fact that in many metals and alloys (Al, Ti, Zr, Nb, W, Ta, and the alloys of these metals after anodization) the interfacial impedance and polarization resistance are dominated by the outer layer and not from the barrier layer; therefore, it is this layer that determines the corrosion rate having a great influence on the current density. Considering the anodized aluminium in H2SO4, the external layer is crossed by a regular and hexagonal series of pores that come out at the bl/ol interface, which place a certain resistance to the transport of water and harmful species towards the innermost and susceptible layer to depassivation (barrier layer), but in any case, better performance is obtained by sealing the pores dissolution and reprecipitation of the external layer by boiling in water[42]. This phenomenon can also occur in other metals, under certain conditions. For example, the formation of FeCO3 on iron in contact with brines of oil fields acidified by CO2.[45].

Therefore the PDM-III has the following characteristic hypotheses: The external layer participates and can also be dominant in the determination of the potential difference across the film and of the passive current density; The outer layer can also have a resistance such as to dominate the impedance and therefore determine the polarization resistance; The IR (I(current)*R(resistance)) potential drop determines the fraction of the applied potential which is responsible only for the growth of the barrier layer, this potential drop is largely determined by the external layer which therefore affects the properties of the barrier layer; The barrier layer can dissolve due to a large drop in IR potential, but passivity is still maintained due to the strength of the outer layer.[42].

For example, in the case of an n-type passive film, the thickness of the barrier layer increases linearly with voltage. The impedance is determined by the barrier layer, when there are low specific resistance values (lower than $3*10^{-7}$ Ω/cm^2), indeed, the passive current density is independent of the voltage. When the specific resistance increases, the impedance is progressively dominated by the outer layer, a phenomenon characterized by an ohmic behaviour of the current.[46].

The thickness of the barrier layer is determined by the outer layer, because the higher its specific resistance, the greater the potential drop across the outer layer and the lower the potential available to drive the growth of the barrier layer. If the specific resistance is very high, the barrier layer can disappear completely.

1.6.6.1 Experimental procedure

Essentially two parameters are required to determine the growth rate of the film, namely the density and diffusivity of the point defects in the passive film. The determination of these parameters is possible through the Mott-Schottky analysis. This analysis was performed on AISI 316L and 321 stainless steel in H2SO4 solutions. Defect concentrations were determined as a function of (passivation) potential and temperature[47]. Samples annealed at 1050 °C of AISI 316L were used. The tests were carried out at 25 °C, 50 °C and 75 °C, in 1 M and 0.5 M sulfuric acid solutions. The electrochemical analysis was performed with the three-electrode technique (a Pt plate as the counter-electrode and a saturated calomel electrode (SCE) as the reference electrode)[47].

1.6.6.2 Potentiodynamic polarization

Figure 1.26 shows the potentiodynamic polarization curves for AISI 316L. These curves show how as the temperature increases; the passivation current also increases. It has been further demonstrated that a steady state is formed upon passivation, indeed, the current density decreases to a constant value.[47].

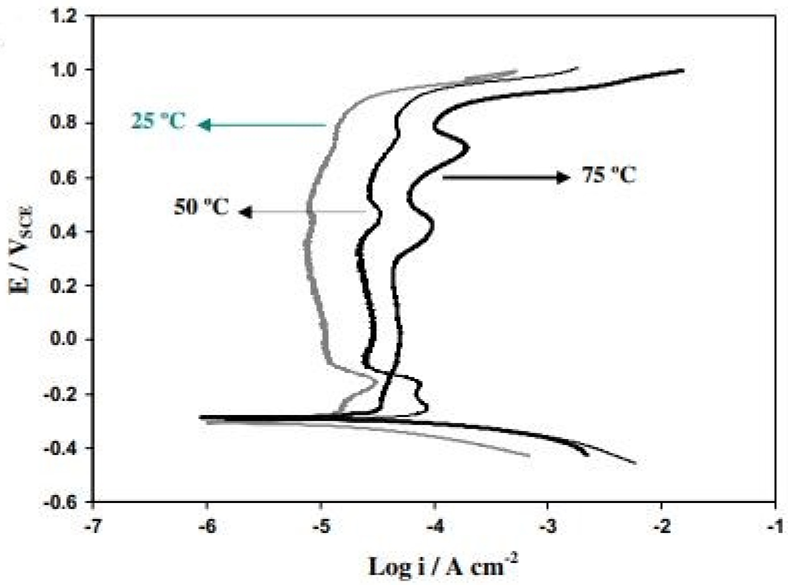

Figure 1.26: Potentiodynamic polarization curves at 1 mV/s for AISI 316L at different temperatures in 1 M H_2SO_4.[47]

1.6.6.3 Mott–Schottky analysis

The formula for determining the capacitance of the electrode C as a function of E (potential), allows to derive the charge distribution thanks to the Mott-Schottky relationship. For an n-type semiconductor we obtain the formula:

$$\frac{1}{C^2} = \frac{2}{\varepsilon\varepsilon_0 e N_D} * \left(E - E_{FB} - \frac{kT}{e}\right)$$

Equation 1.16

where e is the electron charge, N_D is the donor density for an n-type semiconductor, ε is the dielectric constant of the passive film, usually taken as 15.6, ε_0 is the vacuum permittivity, k is the Boltzmann constant, T is the absolute temperature and E_{FB} is the flat band potential[47].

The slope of the experimental graphs C^{-2} to E (Figure 1.27) gives the value of N_D and again thanks to this type of graph E_{FB} is determined by the extrapolation of the linear portion to $C^{-2} = 0$. The greater it is the temperature the higher the slope of the curve. While the increase in potential determines a decrease in the density of donors. In the range 0.1-0.6 VSCE the curves have a slope that represents the type of film on the steel, in this case, being positive the film is of n-type. Instead, a negative slope indicates a p-type film, indeed, the peak indicates the conversion from n-type to p-type[47].

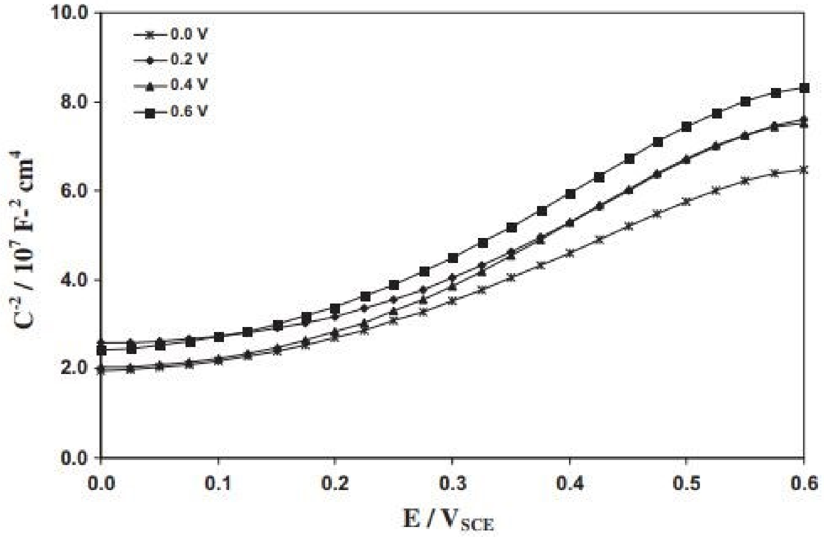

Figure 1.27: Mott–Schottky plots of the capacitance behaviour measured in 0.5 M H_2SO_4 at 25 °C. The electrode is pre-passivated for 1 h at each formation potential.[47]

The relationship between donor density and film formation potential is given by the following formula:

$$N_D = \omega_1 exp(-bE) + \omega_2$$

Equation 1.17

where ω and b are experimental constants.

The combination of the Mott-Schottky analysis and the PDM gives the main result that the effect of an increase in temperature is essentially linearly increasing the density of the donor. This effect can be explained by the fact that increasing the temperature decreases the thickness of the electric double layer (in particular the diffuse layer) that is formed on an electrode immersed in a solution. A lower thickness translates into a steeper drop in the potential which leads to a greater reaction rate of formation of the passive film at the beginning of the process. A greater speed, however, implies a greater density of defects (donors), due to the limited time given to the species to arrange themselves correctly. This higher density of defects will affect the growth of the film since it is their diffusion through the layer that is the determining factor[47]. The formula that relates the film growth rate to the flux of point defects is the following:

$$\frac{dL}{dt} = J * \frac{\Omega}{N_A}$$

Equation 1.18

where L is the thickness of the film, t is the time, Ω the molar volume per cation, N_A Avogadro's number, and J is the flux of the vacancies.

$$J = J_C + J_P$$

Equation 1.19

where J_C and J_P are the flux due to concentration gradient and potential gradient, respectively. The higher donor density will lead to higher J_P and thus higher film growth rate, because the diffusivity don't change enough[47].

1.7 Reasons and objectives of the thesis

The studies that have been performed so far have focused more on the microstructural characteristics and pitting resistance of alloy 718 prepared by additive manufacturing. On the contrary, the stress corrosion study on this alloy was not carried out in depth. The mechanisms for the initiation of cracks and the link of the microstructural characteristics with the susceptibility to localized corrosion of this alloy have not been clarified. Furthermore, there is considerable uncertainty about the performance of the alloy prepared by additive manufacturing compared to its counterpart produced by the conventional method. Conventional methods for studying the initiation of SCC such as compact test (CT) under constant/cyclic loading/displacement, slow strain rate tensile testing (SSRT), and single/double U bend immersion test for an extended time, mainly focus on the propagation phase of the SCC evolution. These methods, bringing the sample to breakage, do not allow an understanding of the mechanism underlying the incubation/nucleation phase of SCCs, which is the most important phase to determine the susceptibility of a material to this phenomenon.

This study aims to clarify the initiation mechanism of SCC using electrochemical analyzes with a microcapillary method, to compare the susceptibility of alloy 718 prepared by additive manufacturing with that of alloy prepared with a traditional method. Furthermore, an investigation on the different localized corrosion resistance of the 718 L-PBF alloy, prepared using different laser powers, correlating the microstructure and surface defects with the different electrochemical responses was performed.

2 Literature review

1) In 2015, Mickaël Payet et al.[48] studied **the corrosion behaviour of Ni-based alloys in supercritical water.** The samples used in the tests were mini-autoclaves made of alloy 690 (Ni-Cr-Fe) subjected to an internal pressure of 25 Mpa and a temperature of 600 ° C, in presence of supercritical water. The samples were kept under these conditions for some time: 335 h, 840 h and 1740 h. Sheets of the same material as the autoclave were suspended inside them before they were polished down to 0.04 µm, while the mini-autoclaves were polished only on the upper surface. Vickers micro-hardness tests were performed on the transverse surfaces. To study the growth of the oxide layer on the sheets, inert gold markers were deposited with the sputtering technique. After the corrosion test, the fluid expelled from the autoclave was analyzed by inductive coupled plasma optical emission spectroscopy (ICP-OES). Field Emission Scanning Gun Electron Microscopy (FEG-SEM), SEM Coupled Energy Dispersive Spectroscopy (EDS), Discharge Optical Light Spectrometry (GDOS), and X-ray diffraction (XRD) to study the oxide layer that has formed.

This procedure led to the following results:

The density of the oxide crystals (1 to 3 µm in size) decreased with increasing exposure time under test conditions. the oxide crystallite structure was more angular at low exposure times. A zone of smaller crystals (200 nm) characterized the grain boundary zone on the surface in both zones. The oxide layer that formed in all the samples consisted of two layers, an external layer with variable thickness and a more homogeneous internal one. In the case of 1740 h, the outer layer has practically disappeared, and the inner layer has remained unchanged. The oxide layer was divided into three zones: the outermost enriched in nickel and iron, an intermediate enriched in manganese (both with a spinel structure), and the innermost enriched in chromium (rhombohedral chroma). The composition of the oxide layer also changes over time. The oxygen profile was more widespread at low exposure times, the spinel structure was predominant at low exposure times, while chromium (predominance of chromia) was more present in the oxide at longer exposure times (in all layers but mostly in the innermost one). There were differences in the structure of the oxide between the polished or simply milled structure. The oxide layer on the milled surface did not differ according to the exposure time, the layer was enriched with manganese only over time. The oxide crystals were smaller on the milled surface, and the oxide layer was much thinner (both outer and inner). The innermost oxide layer was chromium oxide. The metal surface was characterized by a fine grain in proximity to the oxide layer (up to 10 µm) only in the case of the milled surface, due to mechanical processing and followed by recrystallization. The content of iron, nickel and manganese in the water increases with increasing time. Chromium was also present at 1740h. The gold markers were detected only on the intergranular oxidation zone; therefore, an anionic growth is characteristic of the intergranular zone and a cathodic (which covers the markers) is characteristic of the intragranular zone. After 840 h the markers were detected on the whole surface, suggesting that the cathode layer has dissolved (the outer layer has dissolved).

Scholars came to the following conclusions:

Nuclear iron and nickel oxides were mainly above the intragranular zone, and their growth is due to cationic diffusion. Chromium oxide constitutes the innermost layer which nucleates preferably on the edge of the grain by anionic diffusion. The behaviour of the spinel-like layer is reversed (dissolves) at exposure times greater than 335 h, because the chromium oxide layer, increasing in thickness, creates a barrier to the diffusion of cations responsible for the growth of the outer layer. The deformation induced by the milling and subsequent recrystallization causes the formation of an ultrafine structure on the upper layer of the processed metal. This condition is characterized by many grain boundaries, which act as nucleation and growth sites for the chromium oxide layer, emphasizing the behaviour described above. Chromium oxide does not limit the diffusion of manganese or even that of oxygen, which indeed diffuses deeper thanks to the higher concentration of defects.

2) In 1995, H. Bohni et al.[49] studied **localized corrosion on different types of stainless steel**. Samples of various stainless steels with different sulfur content were subjected to microelectrochemical tests. The samples were ground (with a 6 µm abrasive paste). The tests were performed in a microcell consisting of a microelectrode separated from the working electrode by a layer of silicone rubber. The measurements were performed by a high-resolution potentiostat. Potentiodynamic polarization tests were performed in a 1 M Na_2SO_4 solution, in a 1 M NaCl solution and in a 1 M Na_2SO_4 solution with an increasing concentration of chlorine ions. Potentiostatic tests were also performed under the same conditions as potentiodynamic ones. The samples were examined with the scanning tunnelling microscopy (STM) technique before corrosion.

This procedure led to the following results:

In the potentiodynamic tests in sodium sulphate, small pA-current transients were detected in the passive region, undetectable in the measurement with global tests. The transient activity increased with the increase of the sulfur content in the steel in the potentiostatic tests. The MnS inclusions were exposed to the electrolyte, and in this case, a sudden increase in current was noted in a narrow range of potential. The tests carried out in the presence of chlorine ions showed many more current transients, and the presence of a limiting potential for pits growth was found, beyond which pits grow stably. The greater the concentration of chlorine ions, the greater the number of transients and the higher the peak values. The pitting potential decreases as the area of the microelectrode increases (greater presence of inclusions in contact with the solution), while it decreases as the sulfur content in the steel increases.

Scholars came to the following conclusions:

MnS inclusions, in these types of steels, are preferential nucleation sites for pits, these sites can be activated even in the absence of chlorine ions. Not all inclusions are activated, only those of certain dimensions, and in any case, the corrosion of the metal does not begin in the absence of chlorine ions. The chlorides allow the activation of a greater number of nucleation sites (even the smallest inclusions) for the pits (a greater number of transients) and allow the stabilization and growth of existing ones. The chloride ions also trigger the dissolution of the metal, so the transients are larger in size. The pitting potential is related to the size of the largest inclusions present on the sample surface and their distribution, which is related to the sulfur content in the material. The higher the sulfur content, the higher number of inclusions and the lower the pitting potential, the higher corrosion.

3) In 2016, Tanja Trosch et al.[50] studied **microstructure and mechanical properties of selective laser melted Inconel 718**. Cylindrical specimens of the nickel-based alloy Inconel 718 were subjected to uniaxial tensile tests, and produced with three different production methods: SLM, forging, and casting. The tests were carried out at room temperature, 450 ° C and 650 ° C with a deformation rate of $3*10^{-3}$ s^{-1}. The SLM samples were produced with various construction directions, annealed (980 ° C for 1 h) and aged (from 700 ° C to 600 ° C for a total of 16 h). The forged and cast samples were cut from discs that underwent the same heat treatment as the SLM material. The final processing of all the samples was cutting them into a shape suitable for clinging the clamps to the specimen (an elongated shape that narrows in the central area with two triangular shapes at the ends). When the specimens are placed inside the testing machine, they are heated thanks to a short-circuit transformer, and the elongation of the specimen is measured thanks to a video extensometer. To determine the microstructure, the samples (polished and electro-etched) were examined under optical and scanning electron microscopy (SEM) and subjected to energy dispersion X-ray spectroscopy.

This procedure led to the following results:

The SLM samples at room temperature have a higher final tensile strength than the other samples and a lower elongation at break. Among the SLM samples, those built horizontally to the test direction have higher strength and lower elongation than those built vertically, but both have lower strength than those built at 45 ° C. Forged champions have higher strength than cast ones. The fracture surface in the samples has pores and δ-phase particles. At high temperatures, the strength decreases for all samples, although for SLM samples it drops more rapidly above 450 ° C. The same happens to elongation which drastically decreases for SLMs still above 450 ° C. The SLM samples have δ phase particles also within the grain as well as at the grain boundary, unlike the other samples.

Scholars came to the following conclusions:

Vertically constructed SLM specimens have higher ductility for the growth of columnar grains parallel to the load direction, while at 45 ° C the effects of columnar grain and layered structure are combined. It is the large particle size that causes the lower mechanical strength of the cast samples. The drop in resistance of SLM samples at high temperatures is due to the presence of phase δ inside the grains, this is due to the rapid cooling of the melt and the consequent segregation of niobium. Furthermore, even the finest grain size of SLM samples is the cause of the reduced high-temperature resistance. Therefore, to increase the performance of pieces in Inconel 718 produced with SLM, a heat treatment is required that dissolves the δ phase and causes it to precipitate on the grain boundary.

4) In 2020, Mohamed Balbaa et al.[51] studied **properties of selective laser-melted Inconel 718.** The samples were fabricated from Inconel 718 alloy with SLM technology, changing scan speed, laser power, and hatch spacing. Single tracks were fabricated on some supports, and coupons were fabricated with a bidirectional scan with a 90° rotation between each layer. The morphology of the single tracks was examined by SEM, after being polished. The samples were electro-etched and examined under an optical microscope. The density of the coupons was measured using the Archimedes method (measuring the weight of the sample when dry and then immersed in water). Surface roughness was measured with a stylus profilometer. X-ray diffraction tests were used to determine the residual stresses (RS) on the surface of the samples. The tests were performed along the scan tracks and perpendicular to them. Also, Coupons were examined under an optical microscope and SEM to study the melt pools. In addition, a chemical analysis was performed with the inductively coupled plasma (ICP) technique.

This procedure led to the following results:

At SEM the single tracks with a low power/speed ratio showed a discontinuous fusion pool and the phenomenon of balling. The same happened for the tracks produced either with low power or with high speed, only when the power counterbalanced the speed and vice versa this phenomenon was avoided. Observing the transverse surface, it was noted that the depth of the melt pool is reduced by increasing the transfer rate. Beyond 220W of laser power, at low speeds, a serious "keyhole" phenomenon occurred which led to an excessively deep melt pool. It has been noted that the width and depth of the pools decrease with increasing speed and decreasing power. In general, it was noted that the relative density increased with increasing speed, but at low power (170W) and high speeds (1200 mm/s), there was a substantial decrease in density (the density from 98% reaches up to 93%). The highest relative density was recorded at 270 W and 700 mm/s with 0.1 mm hatch spacing (in general, the highest densities were noted at 0.1 mm spacing). The surface roughness decreased with increasing laser power up to 370W of power. On the contrary, with increasing speed the roughness also increased. Above 800 mm/s the roughness increased dramatically. By increasing the hatch spacing, minimal roughness was achieved at slower speeds. The RS decreased with the scanning speed up to 800 mm/s and then increased, in the case of 0.08 mm of spacing. A similar situation occurs also for the other spacings, but an opposite situation is detected at the lowest and highest power. The increase in laser power leads to a decrease in the RS. The RS were all traction with a higher value in the direction of the scan. The depth and width of the melt pool decreased with increasing hatch spacing. At low spacing and a speed of 800 mm/s, columnar grains were present in the microstructure, along the scan direction, while at wider spacings the grain size became mixed, with shorter columnar grains.

Scholars came to the following conclusions:
These are the surface forces that allow the melt pool to have a regular structure, if asymmetrical perturbations occur, the pool is destabilized, and constrictions and widenings are formed which if they are beyond a critical size cause the pool to be divided into balls (balling) due to the high surface energy. Both the intensity of the laser beam and the temperature of the pool have a Gaussian distribution and for this reason, the pool has a parabolic shape (with a peak in the centre). If the ratio between the depth of the pool and half of its width is more than 1, the shape of the pool becomes a keyhole. This form of melt pool can deliver porosity if the ablation pressure (that generated by the evaporating metal) is needed at the tension greater than the surface pressure. The pool opens and then closes forming a pore. This occurs at high laser powers. Porosity arises from non-melting at powers as low as 320 W and high scanning speeds. At high powers and low speeds, the large energy density can lead to the dust surrounding the pool being thrown away from it. This causes a lack of dust for subsequent laser passes, causing porosity. The surface roughness consists of the adjacent scan tracks. High laser power and low scanning speed allow the newly formed melt pool to wet adjacent tracks well, creating a more uniform surface. A slower speed leads to a larger pool which cools down more slowly and has time to even out. The increase in the spacing of the hatch reduces the roughness because it allows for avoiding the throwing of dust away from the newly formed melt pool. The RS present in the material is mainly due to the difference in thermal expansion rates during heating and the difference in shrinkage rates during cooling. This happens in the area adjacent to the melt pool. When the material encounters resistance in expanding or retracting, tensions are generated which are maintained after the material has cooled due to the rapid rate of cooling and the plastic deformations that have been generated. The process parameters affect the size of the melt pool, the increase in the size of the pool leads to greater shrinkage during cooling and a greater surrounding area affected by the heat of the pool. This leads to higher RSs that oppose this narrowing. The melt pool has increased in width and depth passing from single track to coupon because the material has undergone multiple thermal cycles with the overlapping of the various layers. The microstructure was determined by the temperature gradient. A steep temperature gradient (high energy density) led to the growth of columnar grains. At speeds below 600 mm/s, the microstructure is equiaxed because the greater abundance of γ "phase inhibits the growth of the grains.

5) In 2004, A. Machet et al.[52] studied **the growth and structure of passive films in high-temperature water on a nickel-base alloy.** The samples were made of nickel-based alloy 600 in two different forms, one polycrystalline and one monocrystalline. Polycrystalline samples were polished up to 1 μm finish, while monocrystalline samples were polished up to 0.25 μm and then electrochemically polished and then annealed at 1020 ° C for 24 h. The samples were subjected to a temperature of 325 ° C and a pressure of 155 bar in water in a mini autoclave to be in the conditions of PWR unsaturated primary water (for different times). The solution contained 2 mg/L of Li and 1200 mg/L of B and was at pH 7.1. The surfaces

were analyzed using X-ray photoelectron spectroscopy (XPS) and scanning tunnelling microscopy (STM).

This procedure led to the following results:

The XPS analysis shows that there is a small shift in the binding energy (BE) of Cr 2p3/2 after 8.2 minutes. At low BE the signal intensity decreases with increasing time, while at higher BE a component of the signal disappears (577.9 ± 0.1 eV) after 1.2 minutes and the one at 577.2 ± 0.5 eV increases. As for the spectrum of Ni 2p3 / 2, it is divided into a metal component and a bond component. Under 1.2 minutes the metal component prevails while after 8 minutes the bond component is the most intense (attributed to $Ni(OH)_2$). The core level spectra of the two metals indicate oxide formation on the metal. As regards the spectrum of O 1s, it has an intense peak at 533.1 ± 0.5 eV corresponding to B_2O_3 (due to the presence of dehydrated boric acid). The Fe 2p3/2 spectrum does not show significant peaks due to the low iron concentration. The XPS analysis at different angles (90 ° and 45 °) made it possible to highlight that the intensity of the hydroxyl groups is greater than the oxygen intensity in the oxide at a more grazing take-off angle. That is, the hydroxide is found more on the surface than the oxide. The data concerning the monocrystalline alloy do not vary much from those of the polycrystalline alloy. The STM analysis of the single crystal after 1 minute under aggressive conditions provides a surface topography consisting of narrow terraces (70nm) alternating with larger terraces (200nm) and is characteristic of the metal substrate. The surface is covered with platelets, mostly present on the narrow terraces, which represent the growth of the oxide layer. These platelets also have a nano-terraced surface, which represents a crystalline structure of the oxide. The height of these platelets is 0.23 ± 0.01nm, by the lattice distance of the chromium oxide. The surface of the monocrystalline sample is homogeneously coated with platelets after 3 minutes, with thicker platelets scattered over the surface, coinciding with the formation of nickel hydroxide islands.

Scholars came to the following conclusions:

The mechanism of formation of the passive layer seems to start with the formation of oxide (inner layer) and chromium hydroxide (outer layer), these grow in equal proportions for up to 4 minutes. After 4 minutes, the chromium hydroxide oxidizes, thickening the oxide layer, at the same time increasing the amount of nickel hydroxide on the outer layer. After 8 minutes the film is formed by a layer of chromium oxide with islands of nickel hydroxide on the surface. The innermost layer consists of stacked hexagonal layers with an FCC structure. it is the initial dissolution of nickel that leads to the surface enrichment of chromium and therefore to the nucleation and growth of chromium oxide islands. These islands coalesce and form a continuous oxide layer covered with chromium hydroxide, which will then oxidize to oxide. The nickel hydroxide on the surface is generated through the reaction of the Ni diffused through the oxide layer with the solution. Part of the nickel remains in the solution and with it also the iron which, however, does not precipitate again.

6) In 2022, Arshad Yazdanpanah et al.[53] studied **stress corrosion cracking susceptibility of selective laser melted 316L stainless steel under the individual effect of surface residual stresses**. The samples used in this article are made of 316L austenitic stainless steel, they were produced through SLM technology using different laser powers. The specimens were ground to two depths of cut, i.e. 20 µm and 50 µm. Other samples were polished down to 0.02 µm in a colloidal silica suspension. X-ray diffraction (XRD) was used to determine the residual stress on the surface of the samples, both in the longitudinal and transverse directions. Electrochemical tests were performed by immersing the sample in a 3.5% sodium chloride solution at room temperature. Potentiodynamic analysis was performed with the three-electrode method (saturated calomel electrode (SCE) as the reference electrode and platinum cage as the counter electrode), and the area in contact with the solution was a 6 mm circle. Galvanostatic analysis was also performed at a current density of 5 * 10-4 mA*cm^{-2}. The exposure time to the tests was 60 minutes. The samples were cut transversely to the processing direction and subjected to microstructural analyzes using the field emission gun scanning electron microscope (FEG-SEM) and the scanning electron microscope (SEM), in particular, to determine the average pore surface area (PSA) and columnar sub-grain width (CSW). The electro-etching technique was used to highlight the boundaries of the various phases and the boundaries of the fusion pool. For the surface characteristics, EBSD analysis was used, and the images were processed with the "ImageJ" software.

This procedure led to the following results:

The fine columnar grain structure was detected in all the samples, showing no variations with the variation of the laser power. The presence of segregations of alloy elements such as Cr, Ni and Mo at the grain boundaries was detected. The fusion pools increased their width as the laser power increased. PSA decreased as laser power increased to 120W, while it increased to 135W. CSW increased at 90W and then decreased at 135W. Residual stresses (RS) were found to be higher on samples with a higher depth of cut. During potentiodynamic analysis, the breakdown potential (E break) decreased dramatically with a laser power of 135W, it was found that the breakdown potential is more sensitive to PSA while the breakdown current density is more sensitive to CSW. E break decreases as the PSA increases. When the RS was lower, the breakdown potential decreased more than in all other cases for a power of 75 W. While with high RS, all the samples showed a continuous increase in current as the potential increased after a narrow transpassive region. In this case, E_{break} was greatly decreased for all samples regardless of laser power. During the galvanostatic tests, a more noble potential was detected for the samples with smaller CSW for 75W and 120W. For low RS, the drop in potential to stable values was less steep in the 120W and 75W samples. At low RS, a low CSW resulted in higher corrosion resistance than a low PSA. At high RS values, the 120W samples were those that had greater potential and duration, having low PSA and CSW values. However, at high RS, the dominant parameter that determined the breakdown of the passive layer was PSA and RS. In the polished samples, the dominant flaw was the pits, especially for the samples with laser power of 90W and 105W. As the residual stresses increased, the samples at each laser power showed the onset of SCC (stress corrosion cracks) that originated from defects in the material (porosity, fusion pool, grain boundaries), at high RS the cracks were propagated through the sub-grains. Scholars came to the following conclusions:

There seems to be a critical PSA that determines the increase in the corrosion rate. The size of the pores necessary for this phenomenon decreases as the residual stresses increase because the traction causes the activation of the smallest pores as nucleation sites. Larger pores allow the migration and accumulation of aggressive ions that weaken the passive layer. A finer grain size (CSW) allows the formation of a more intact passive layer that resists better the stresses given by the RS and places obstacles to the propagation of the SCC. Residual stresses have a great influence on corrosion resistance, leading to the breakdown of the passive layer and the nucleation and propagation of pitting and/or SCC. The greater their magnitude the greater this effect. Surface defects such as fusion pools and sub-grain boundaries are active sites for the nucleation of SCCs. RS causes a decrease in the level of compression of the passive layer, this effect induces the formation of a more defective passive layer and therefore more subject to attack by aggressive species (pitting). Another mechanism for the initiation and propagation of SCCs is that, once the sites most sensitive to attack by aggressive species have been corroded to a critical passive film thickness, mechanical traction causes the film to break. Large pores, more subject to the accumulation of aggressive species, can be one of these active sites.

7) In 2020, Arshad Yazdanpanah et al.[54] studied **the role of grinding-induced surface residual stress on the probability of stress corrosion cracks initiation in 316L austenitic stainless steel.** The samples were made from 316L austenitic stainless steel. After being cut, the samples were annealed at 1050 ° C for 30 minutes and air quenched, mounted in phenolic resin, and ground. The samples were ground with different depths of cut, from 10 to 50 μm to give different values of RS (residual stress). An XRD analysis was performed to determine the RS, along the longitudinal direction and the direction transverse to the machining direction. The samples were subjected to potentiodynamic and galvanostatic analysis in a 3.5% sodium chloride solution in distilled water and at room temperature, the contact surface with the solution was a 6 mm diameter circle. The current density used in the galvanostatic analysis was 0.001 mA. Before and after the galvanostatic tests, the samples were observed under an optical microscope with a maximum magnification of 1000× and a scanning electron microscope (SEM), on the surface and along the cross-section, to observe the damage caused by corrosion. For the surface analysis, the samples were polished with a 3μm suspension. Microscopic examination was performed during the drop in potential and 15 minutes after the start of the test.

This procedure led to the following results:

The RS were in traction and were larger in the centre of the samples and smaller in the sides. Potentiodynamic tests provide lower pitting potential values for higher RS. The amplitude of the passive region is reduced as the RS increases, almost disappearing at high RS values. Above 300 Mpa of RS, the drop in pitting potential was drastic. Furthermore, the current density at the same potential value was higher for the samples with high RS. In the galvanostatic tests, the potential started at a high value and then had a sudden decrease, after which it stabilized at a certain value. The higher the RS, the shorter the time for the potential fall. At the time of the drop in potential, pits but not SCC (stress corrosion cracks) were detected. For low RS values, the samples were attacked along the grain boundaries while at high RS the corrosion was more distributed. The number of pits and their depth also increased with increasing RS. No SCC was detected even after 15 minutes on all samples.

Scholars came to the following conclusions:

The RS reduces the corrosion resistance of the samples, and the greater its magnitude, the greater the effect on resistance. The signs of workmanship and other defects act as active sites for the corrosive attack as well as act as sites of stress concentration. The film naturally dissolves up to a critical thickness at which a mechanical break occurs. The greater the RS the greater the thickness considered critical. The RS accelerates the formation of pits. The corrosion potential was the same for all samples as the surface roughness was the same. Only when the passive layer breaks down is the behaviour affected by the RS. Samples with compressive RS, on the other hand, have better corrosion resistance, because when the film breaks due to dissolution in an aggressive environment, the compressive forces lead to self-repair of the surface by covering the uncovered points of the metal. After reaching the stable potential, and hence the stable pitting, all the samples had comparable potential. Therefore, the RS no longer had an influence on the corrosion rate after the breaking of the film because the depth of the pits exceeded that subject to the action of the RS. No SCC was found, probably because the RS level was not high enough and the environment was not excessively aggressive to cause its onset.

8) In 2021, Arshad Yazdanpanah et al.[55] studied **Stress Corrosion Cracking probability of selective laser melted 316L austenitic stainless steel under the effect of grinding-induced residual stresses**. The samples are made of 316L steel, are produced using SLM (selective laser manufacturing) technology, have been annealed at 1050 ◦C for 30 minutes, and have been ground to various grit sizes, i.e., 30, 60 and 90 μm. Other samples were also annealed after mechanical processing. To measure the residual stress on the surface of the samples, the X-ray diffraction (XRD) method was used after electropolishing, the measurements were made along the direction parallel to the machining marks. In a 3.5% sodium chloride solution in distilled water at room temperature, a potentiodynamic analysis was carried out using the three-electrode method (platinum net as the counter electrode and saturated calomel electrode (SCE) as the reference electrode). A galvanostatic analysis was also performed with a current of 0.001 mA (over an area of 6mm) and for different times. Subsequently, the samples were also analyzed with the scanning electron microscope (SEM) and with the X-ray energy dispersion microanalysis (EDX), cutting the samples crosswise. An optical microscope was also used for the microstructural analysis, roughness, and porosity before the electrochemical tests.

This procedure led to the following results:

Grinding introduced tensile stresses on the surface of the samples, the residual stresses are greater on the samples with a greater depth of cut. In the potentiodynamic analysis, the pitting potential was found to be lower for samples with higher residual stresses (RS). The passivation region was very unstable for this type of sample, indeed, the current density underwent strong fluctuations, and this phenomenon was also greater for samples with higher RS. In the galvanostatic analysis, the maximum potential was lower for samples with higher RS. The potential decreased after an incubation time; this time was shorter for samples with higher RS (incubation region). For the samples with higher RS, that is 460 Mpa, the potential continued to have fluctuations (metastable region), reaching lower values compared to the other samples, while for the others it stabilized after a further decrease (stable region). Pits are formed preferably along the grinding direction and their density is higher in samples with higher RS. While in the annealed samples the pits are generated in specific sites. The SEM analysis found that SCC (stress corrosion cracks) were formed for samples above 310 Mpa of RS. At 310 MPa the cracks originated from the pores and followed the boundaries of the melt pool. At 460 Mpa the cracks were more and originated from all the defects that characterize the sample (pool boundaries, transgranular cracks, and even pores just below the surface). Crack propagation occurred along the boundaries of the melt pool and the longitudinal direction of the surface. For the samples with RS of 460 Mpa cracks also propagated through the grains, rather than along the boundaries. EDX analysis shows that Mo undergoes reverse segregation along the fusion pool.

Scholars came to the following conclusions:

The lower corrosion resistance (lower pitting potential) of the samples with higher RS is given by the fact that higher tensile stresses cause the passive film to break at a critical value of greater thickness (thickness reached through normal dissolution), thus making more vulnerable the sample surface at a lower corrosion rate. Samples with higher RS have a shorter incubation time because the film needs to thin less than less stressed samples to cause mechanical breakage. the combination of pitting and SCC propagation is the reason for the existence of the metastable region. In the stable region, the film is now dissolved in the most stressed or sensitive points and the corrosion continues at a constant speed. The pores represent stress concentration sites which therefore tend to cause cracks. The greater the initial (RS) stress the more intense the concentrated stress. Due to the extreme heating and cooling conditions, many dislocations are formed along the boundaries of the fusion pool which is therefore more likely to generate cracks and is a preferential path for their propagation. Furthermore, due to the grinding, a martensitic structure with the nanocrystalline grain is formed on the surface which is more brittle than the normal passive layer, and this causes it to break at lower stress values. Higher RS also cause the activation of nucleation sites that are more difficult to activate. Molybdenum segregation leads to a reduction in corrosion resistance along the boundaries of the melt pool, this element being largely responsible for corrosion resistance. The cracks that are generated on the samples with the highest RS are propagated in a transgranular way because, given the presence of fine columnar grains, much more energy would be required to follow the boundary of the grains than to pass through them.

9) In 2019, Baicheng Zhanga et al.[56] studied **pitting corrosion of SLM Inconel 718**. The samples used were made of alloy Inconel 718, produced with the SLM (selective laser melting) technique in a rectangular shape. The samples were examined as-printed or after heat treatment at various temperatures (annealing at a temperature of 1040 ° C (H1040), 1100 ° C (H1100) or 1200 ° C (H1200) for 2 hours, always followed by ageing at 720 ° C for 8 hours and at 620 ° C for 10 hours.). The samples were electrochemically polished. The corrosion tests were conducted with the three-electrode technique in an electrochemical cell. The reference electrode was a saturated calomel electrode (SCE) and the counter electrode was a high-density graphite rod. The working electrode was the sample fixed on resin immersed in a 1.0 M NaBr solution. The metallographic characterization of the samples was performed under the optical microscope, the scanning electron microscope (SEM), the energy dispersion X-ray technique (EDX) and through electron backscatter diffraction (EBSD).

This procedure led to the following results:

Under the optical microscope, the edges of the melt pools could be seen in the as-printed sample. By increasing the temperature of the thermal treatment, the edges of the pools disappeared, and the crystalline grain increased in size. At SEM, a fine dendritic structure could be recognized in the as-printed sample. Interdendritic segregations were present which were eliminated after the various heat treatments, and the matrix after the treatment was smooth with the presence of a particle structure. Following the potentiodynamic tests, the as-printed sample showed the lowest corrosion current of 0.33 $\mu A/cm^2$. As the temperature of the heat treatment increased, the corrosion current also increased. The corrosion potential did not undergo significant variations between the various samples. The pitting potential is very low for the H1200 sample (5 mV_{SCE}) while it is very high for the electropolished sample only (840 mV_{SCE}). Under the microscope, the surface of the various samples after the corrosion tests showed several micrometric pits, relatively larger on the H1200 and as-printed samples, while on the polished sample the pits had an irregular shape.

Scholars came to the following conclusions:

The SLM technique, due to the rapid cooling rate, leads to the formation of an oversaturated γ-phase and precipitates of the Laves phase. After 1040 ° C segregation on the grain boundary continues and the Laves phase begins to dissolve. The Laves phase has completely disappeared at 1100 ° C and the previously present carbides, distributed in the matrix, swell. The granulometry increases in size with increasing temperature and at 1200 ° C the columnar grains thicken a lot due to the reaching of the recrystallization temperature. From the potentiodynamic results, it is found that the heat treatments increase the corrosion rate of the material. The low corrosion rate of the as-printed sample is due to the presence of residual stresses after the rapid heating and cooling rates due to manufacturing with SLM.

Residual stress is relaxed more and more with increasing treatment temperature, causing an increase in the corrosion rate. The precipitation of γ ′/γ ″phases at the grain boundary and the presence of increasingly larger carbides with increasing temperature could lead to the generation of a galvanic effect which reduces the corrosion resistance at the grain boundary, but this effect is counterbalanced by an increase in grain size which leads to a decrease in the grain boundary area. At 1200 ° C, however, the dominant precipitates are large carbides which cause the depletion of Cr and Mo in the surrounding areas, weakening the passive layer that forms and also causing a severe galvanic effect. The high pitting resistance of the electropolished sample appears to be due to the presence of a 1.5 µm thick layer of oxide on the surface.

10) In 2015, Xingying Tang et al.[57] studied **the corrosion behaviour of nickel base alloys, stainless steel and titanium alloy in supercritical water.** To test the corrosion resistance of different materials in supercritical water conditions (400 ° C and 25MPa) during an oxidation treatment of organic waste, different solutions were used containing hydrogen peroxide as an oxidizing agent and sodium chloride as corrosive species at different concentrations. and sodium triphosphate. Experiment 1 with sodium chloride and hydrogen peroxide; experiment 2 with peroxide and sodium triphosphate; experiment 3 with peroxide, chloride and triphosphate; experiment 4 with chloride and triphosphate. Tests were performed in an autoclave on samples of 316 SS, Inconel 600, Inconel 625, Hastelloy C-276 and TA10, cut into coupon shapes. The samples were polished to 2000 grit and cleaned thoroughly. The samples after corrosion were examined by scanning electron microscope (SEM), energy diffraction spectrometer (EDS), X-ray diffraction technology (XRD), and X-ray photoelectric spectrometer (XPS).
This procedure led to the following results:
316 stainless steel had the greatest mass loss compared to the other alloys in Experiment 1, and Inconel 600 gained much more mass than the other samples in Experiment 2. The TA10 underwent the least mass change during all experiments. The 316 SS showed the most severe oxide scales spallation, and the Inconel 600 showed the most severe pitting corrosion after Experiment 1. Nickel alloys suffered the most corrosion during Experiment 1 compared to the other conditions. While the greatest corrosion resistance was observed during the experiment with triphosphate and oxygen. 316 SS suffered severe pitting corrosion even in the presence of triphosphate. On the surface of the nickel alloys, amorphous oxides were observed while on TA10 the oxide was uniform. In each experiment containing phosphate, the presence of phosphorus was detected on the surface of the samples, this amount was greater after experiment 2. On the 316 SS, it was detected in small quantities due to the large spallation of the oxide. On the TA10 the phosphorus was in lower quantity than in the other samples. A large amount of oxygen was detected in the samples after all the experiments that contained the oxidizing species. In nickel alloys, molybdenum was more present on the outer layer in the presence of chlorine only. Stable Cr_2O_3 and Fe_2O_3 bones were observed on 316 SS in the presence of oxygen alone. The phosphate ion formed stable

compounds with the alloy cations on the surface. The passive layer of 316 SS was made up of $(Fe, Cr)_2O_3$ / $(Fe, Cr)_3O_4$ / Cr_2O_3 and matrix enriched with Ni from the outside to the inside. On the Hastelloy C-276, on the other hand, Cr_2O_3, $NiCr_2O_4$, NiO and MoO_2 were detected. On the surface of TA10: Ti_2O_3, TiO_2, Ti_2O, $(TiO)_2P_2O_7$ and $NiMoO_4$ were detected. A triplex layer of TiO_2 / Ti_2O_3 / TiO has formed on the TA10 from the outside to the inside. On the Inconel 625 alloy, a greater loss of nickel was detected in experiment 1 compared to experiment 2, the same applies to the oxygen penetration depth, greater in the first experiment.

Scholars came to the following conclusions:

On the 316 SS, the outer oxide layer was rich in iron and the oxides present were dissolved under the highly aggressive conditions of supercritical water. the spallation of the remaining oxide layer occurred which causes the metal to be exposed to the corrosive medium, increasing the corrosion rate. 316 SS is highly susceptible to attack by chlorine and even more in the presence of oxidants. The phosphate can increase the corrosion resistance of all alloys by reacting with the metal ions and forming a very resistant and insoluble passive layer. Only on the 316 SS, the phosphate was not able to increase the corrosion resistance since the spallation of the oxide also causes the spallation of the phosphate layer that could form. On nickel alloys, the phosphate film allows reducing the dissolution of this element. Chromium and molybdenum oxide were the main reason for the corrosion resistance in the environment with chloride and oxygen. The TA10 showed the best corrosion resistance due to the presence of a compact film made up of very stable oxides. The 316 SS is the one with the worst performance due mainly to the low percentage of molybdenum. Chlorine is the most aggressive agent. The action of the SCW was to increase the penetration of aggressive species between the oxide flakes due to its intermediate state between vapour and liquid.

11) In 2020, J.P. Oliveira et al.[58] made a review of **processing parameters in laser powder bed fusion metal additive manufacturing.** In this work, the influence of the various parameters of the L-PBF production process (laser-based powder bed melting technology) on the characteristics of the finished metal product was discussed, and an appropriate compromise was also sought between the various parameters to optimize the properties of the product. Scholars, by gathering information from various scientific papers, came to the following conclusions:

Porosity: An excessive energy density of the laser leads to the vaporization of the metal, the vapour is trapped as a result of the solidification of the melt pool, forming pores. A low energy density leads to the lack of melting of the metal and thus to the formation of pores between the pools and the unmelted powder. To avoid the porosity linked to the keyhole phenomenon (the one that occurs at a high energy density) it is necessary to decrease the laser power and increase the scanning speed. it is necessary to avoid the permanence of the laser in a specific point for too long, this is linked to a scanning strategy that forces the laser to often change direction and therefore to slow down in some points. To avoid porosity due to the lack of fusion the melt pools must overlap without leaving spaces between them. Depending on the size of the melt pool, there is a minimum overlap depth. The hatch spacing determines the maximum thickness of the molten layer (the greater the spacing, the smaller the layer thickness) and this must be less than the minimum overlap depth.

Preferential evaporation: At high energy densities, the preferential evaporation of some elements of the alloy may occur. For example, in Ti-Al-V alloys, aluminium is preferentially evaporated, as is chromium in the Inconel 718 alloy. By reducing the linear energy density to the minimum possible, this phenomenon is reduced. The spacing of the hatch greatly influences this phenomenon, the reduction of the spacing, indeed, increases the preferential evaporation of a given element.

Residual stresses: In materials produced with AM technology there are residual stresses due to the high thermal gradients that are formed in the material due to rapid heating and cooling. These temperature variations cause expansions and shrinkages to which the material not affected by the high thermal gradient opposes. This opposition generates residual stresses, which can be of such a high entity as to generate distortion of the piece. The only way to eliminate this phenomenon seems to be post-construction heat treatment. In any case, the shorter the length of the scan lines, the lower the magnitude of residual stresses. The material, under construction, can be pre-heated or post-heated using a second lower-power heat source (laser).

Rapid solidification microstructure: Using AM technology, cellular, columnar or equiaxial structures are often obtained due to the high rate of solidification and a moderate temperature gradient. The high solidification rate leads to very fine grain size. Large columnar grains (a few millimetres long) are observed when both the laser power and the scanning speed are high. The micro-segregation that occurs in some alloys causes high constitutional undercooling that causes the formation of equiaxed grains. To avoid this phenomenon, a higher laser power (higher thermal gradient) or a higher scanning speed is required. Increasing the scanning speed increases the solidification rate and a columnar structure is favoured. Increasing the laser power increases the temperature gradient and columnar grains are favoured. The fact that the material undergoes multiple melting and solidification cycles as it passes through the laser makes predicting the microstructure more complicated.

Micro-segregation: After the manufacturing of the piece, the presence of phases and precipitates can be found that are deleterious to the properties of the material. For example, the δ phase formation in Inconel 718. This appearance is due to the micro-segregation of niobium in the interdendritic zones. The formation of this phase can also occur as a result of post-construction heat treatments. The formation of unwanted phases is strongly linked to the composition of the alloy which must be adapted to the process conditions to which it is subjected during AM. Each alloy has a liquid diffusivity value and an equilibrium solute partition coefficient. A low liquid diffusivity leads to more probable segregation because the species struggle to arrange themselves to have an equilibrium composition. Increasing the solidification rate to very high values can prevent the solute from being expelled from the growing solid phase, leading to less segregation. This is possible at high scanning speeds. With speed, the laser power must also increase to avoid the formation of defects.

12) In 2021, Shuwei Guoa et al.[59] made a review of **corrosion characteristics and mechanisms of typical Ni-based in sub- and supercritical water.** In this work, the corrosion behaviour of Ni-Fe-Cr alloys and Ni-Fe-Cr-Mo-Cu alloys in subcritical and supercritical water environments (T = 374 ° C, p = 22.1 MPa) is presented. Scholars, by gathering information from various scientific papers, came to the following conclusions:

Corrosion weight change: Ni-Fe-Cr alloys show an increase in weight following the onset of corrosion, this increase has a parabolic trend and reaches a stable value after a certain period. The weight gain is greater the higher the operating temperature. An increase in oxygen content causes greater weight gain. On Incoloy 800H alloy, grain boundary engineering treatment causes an increase in corrosion weight, while shot peening causes less weight gain compared to untreated material. Hence shot peening increases the corrosion resistance of the material.

Oxides: Ni-Fe-Cr alloys, following corrosion in SCW, show the formation of a double-layer oxide film, with the inner layer consisting of chromium oxides and the outer layer consisting mainly of iron oxides. Nickel hardly reacts with oxygen because it is present in fewer quantities than other alloys and that iron reacts preferentially. Shot peening generates an ultra-fine microstructure of the outermost part of the oxide layer. A fine austenitic microstructure helps to increase the formation of chromium oxides and therefore to increase the corrosion resistance.

Surface treatment processes: Shot peening causes a reduction in the size of the crystalline grain on the sample surface, increasing the grain boundaries and thus promoting chromium diffusion. This facilitates the formation of protective chromium oxides. The grain boundary engineering facilitates the formation of chromium oxide and reduces the exfoliation of the film thanks to the serrated interface located between the layers of the film (observed on Incoloy 800 at 500 ° C in SCW for 503 h). A more homogeneous and compact oxide film is obtained.

A comparison: Incoloy 800H nickel alloy is much more resistant than 316L stainless steel. Incoloy 800H forms a thinner and more stable oxide film, due to the greater presence of Cr, the better particle size, and the high nickel content. In any case, since they do not contain molybdenum, Ni-Fe-Cr alloys have a lower corrosion resistance than Ni-Cr-Mo or Ni-Fe-Cr-Mo-Cu alloys. Ni-Fe-Cr-Mo-Cu alloys have a high resistance to corrosion by acid attack thanks to their high concentration of copper, as well as having good resistance to corrosion in general. The oxides on the surface of nickel-based alloys have a coarse structure on the outside, while the further you go inside, the finer and more compact the structure becomes. In general, the higher the chromium content of a nickel-based alloy, the higher its resistance to corrosion because a compact layer of protective chromium oxide is formed. Molybdenum-free alloys, such as

Inconel 600, exhibit poorer pitting resistance. Inconel 625 and Hastelloy C-276 have the lowest corrosion rates of the most widely used alloys in many environments.

Corrosion mechanisms: The solid-state growth mechanism of the oxide film involves transfers of charged species across the interfaces and across the oxide layer itself. The inner layer of the film is formed by the transfer of oxygen ions towards the metal/oxide interface while the outer layer is generated by the transport of metal cations towards the oxide/solution interface. Depending on the composition of the alloy, the cations of the solutes which are in substitutional positions in the substrate of the barrier layer can reduce the diffusivity of the defects that allow the growth of the oxide layer. Elements with low diffusivity tend to accumulate in the outer layer of the film while the others manage to migrate to the outer layer. The mixed growth mechanism implies that the outer layer is generated by the reaction between the metal cations and the species present in solution (such as OH-), the ions are first dissolved in solution and after the reaction precipitate on the surface of the barrier layer. For example, in the case of the alloy Inconel 690 in SCW, chromium is an easily oxidizable element which however has a reduced diffusivity and therefore constitutes the inner layer of the film, while nickel and iron have a higher diffusivity and constitute the layer. external. Oxygen ions (or oxygen vacancies in the opposite direction) move towards the metal substrate by increasing the thickness of the chromium oxide layer, while metal cations move outward due to diffusion in the opposite direction of the cationic vacancies or through the mechanism of interstitials. Thus, the nickel diffuses to the outside and reacts with the solution generating nickel oxide, and so does the iron. As corrosion progresses, the oxides react with each other generating NiFe2O4 on the outer layer and NiCr2O4 on the inner layer. After long periods of exposure to the corrosive environment, the inner layer is thick enough to hinder the transfer of iron and nickel to the strange outside, inhibiting its growth and bringing the layer close to dissolution. The breakage of the passivating film is given by the generation of cationic vacancies at the outer layer/solution interface, which condense at the metal/inner layer interface and cause the decohesion of the film. The presence of chlorine and oxygen in supercritical water leads to greater corrosion of the metal material, while the presence of phosphate generates a very resistant external passivating layer.

13) In 2020, J.P. Oliveira et al.[60] made a review about **the revisitation of fundamental welding concepts to improve additive manufacturing.** Scholars, by gathering information from various scientific papers, came to the following conclusions:

A great similarity is evident between electron beam or laser welding processes and additive manufacturing that uses the same basic technology. The high solidification speed and the repeated thermal cycles that the welded material undergoes are important points in common combined with the resulting microstructure and therefore the properties associated with it. The cooling rate is the fundamental aspect that allows you to determine the transformations that the material undergoes in the solid state. The heat input to the material is given by the relationship between the welding power and the welding speed, it is a factor that allows you to determine the shape of the melt pool, the extension of the area affected by heat as well as its cooling rate. In electron beam and laser welding, an important parameter is the energy density. The peak temperature and the cooling rate determine the microstructure of the material. The temperature gradient in the area adjacent to the molten material causes differential expansions and contractions that cause residual stresses to arise when the material cools. If excessive, these stresses generate permanent deformations in the area affected by the weld. Heat treatments can reduce or eliminate the extent of these stresses. Multi-pass welding allows, through the multiple passages of the heat source on the area to be welded, to perform heat treatment on the piece at the same time as the welding. The steps following the first allow to partially re-melt the previously solidified metal and generate a heat gradient that is not too high which allows the material to be re-cooked, generating a finer grain and with less residual stresses (reducing the cooling rate).

In the thermal analysis of additive manufacturing, the most important parameter is the energy density per unit of volume, which represents the heat input supplied to the material. The energy density, therefore, determines the phase transformations that occur in the metal, such as the formation of precipitates or the transformation of the phases according to the equilibrium diagram or the generation of metastable phases due to rapid cooling. Proper control of the energy density leads to the formation of a fine-grained microstructure. A great advantage of additive manufacturing is precisely the control of the microstructure based on the appropriate choice of process parameters. The defects that may arise during AM are mainly: The porosity given by the vaporization of the metal and the entrapment of these vapours; The presence of unfused areas, and the presence of residual stresses that can cause delamination. The pores can be eliminated by hot isostatic pressing, while the stresses by heat treatment.

The development of a large columnar grain microstructure is one of the biggest problems in welding processes. This causes anisotropy of the material and lowers mechanical resistance. Various techniques can regulate the growth of the microstructure as desired. One technique is the modulation of the heat source which is performed by modulating the pulse current. The modulation of the pulses in arc welding allows to perform the transfer of the material but with an average welding current lower than that which should be used at constant voltage, avoiding excessive heating of the material. Another improvement is given by high-frequency pulses which allow to have a shorter arc and therefore a more localized melting zone, but this causes a coarser microstructure given by the low cooling rate. The pulsation allows to have supercooled areas of the melt that allow the growth of heterogeneous nuclei and therefore refining of the crystalline grain. The continuous change of direction of the maximum thermal gradient also limits the growth of the grain. This technique can be used in electric arc additive manufacturing but also with techniques that use electron beams and lasers. In these latter processes, the modulation of the pulses is more useful in reducing porosity since the microstructure is already very fine due to the high cooling rate.

The reduction of porosity is obtained when the power of the beam is modulated at the same frequency as the oscillation of the melt pool. The segregation of alloying elements can also be reduced through this technique by using a near-continuous wave laser source that allows a higher cooling rate, for example in the case of niobium in nickel-based Inconel alloys.

In processes based on the electric arc, it is possible to manipulate the heat source through magnetic oscillation, making the arc oscillate in different directions that have a different impact on the microstructure that will be formed. This technique allows you to change the orientation of the grains as well as refine them. At high frequency, the longitudinal oscillation is more effective while at low frequency the circular or transverse oscillation, concerning the direction of advancement, is more effective. The movement allows the detachment of pieces of dendrites that will act as nuclei for the growth of grains, refining the microstructure.

A high heat input causes a large melt pool and a large area affected by heat, this causes a lower cooling rate and therefore a coarser microstructure as well as causing greater residual stresses. The control of heat input is essential to avoid the phenomenon of hot cracking and liquefaction cracking. Adequate heat input in multipass welding is important to obtain an adequate interpass temperature to heat treat the previously deposited material, the same is true for additive manufacturing. Adequate shielding gas is also important, as it allows for a plasma beam that creates a wider and deeper melt pool, reducing the amount of heat needed.

For aluminium alloys, it was found that at low scanning speeds the cracking phenomenon was reduced but there was a risk of grain enlargement and therefore it was necessary to introduce elements into the alloy that would promote refining. A reduced heat input on Inconel alloys produced lower residual stresses and therefore avoided the phenomenon of cracking. Less heat input promotes the refining of the crystalline grain. It has been observed that an increase in the incident angle of the laser beam causes an increase in the lateral temperature gradient, favouring the growth of secondary dendrites and eliminating the liquefaction crack. A greater heat input increases the wettability of the melt and allows for a less wavy surface. The shielding gas flow must be intense enough to remove the fumes produced by the laser process to avoid their interaction with the beam. The use of carbon dioxide mixed with an inert gas allows for a reduction in process costs while maintaining an excellent quality of the piece produced in alloys not too susceptible to oxidation.

In welding, it is possible to introduce crystalline grain refiners into the filler material. They act as pre-existing nuclei in the spindle through the phenomenon of heterogeneous nucleation. On these nuclei, the growth of grain occurs thanks to the fact that they reduce the free energy necessary for the formation of the latter, as there is a pre-existing surface.

In additive manufacturing, crystal grain refiners such as titanium and aluminium can be added to nickel alloys, they favour γ' phase precipitation, but they also increase the risk of hot cracking and therefore to overcome this problem particles are added to the fusion pool to increase the heat resistance of the material. The addition of TiC and TiB_2 nanometric particles increases the strength and hardness of the as-built material.

The electromagnetic agitation of the melt pool takes place by applying a magnetic field parallel to the axis of the welding arc. The molten metal undergoes annular motion, and the agitation allows the homogenization of the solute (and therefore avoids segregation) and the reduction of porosity. The agitation allows the reduction of the temperature gradient and the solidification speed, reducing residual stresses. Agitation promotes the refining of the crystalline grain through the scattering of the pieces of the dendrites, and through the reduction of the temperature gradient that promotes nucleation. The magnetic field must be of low frequency to avoid inertia effects on the flow of molten metal. Ultrasonic stirring of the bath can also be a means to refine the microstructure.

In additive manufacturing, the hatch distance is essential to obtain melt pools that join each other without leaving gaps between them. It must not be excessive because it would lead to a failure to melt, and it must not be too short because it would lead to an excessive temperature gradient. The hatch distance can be determined by knowing the laser power, the scanning speed, and the thickness of the layer to be melted. The thickness of the layer to be melted must include the layer of powder and part of the underlying layer previously melted. Using these data, it is possible to determine an h max below which there will be more molten material (in excess) and beyond which there will be a lack of fusion.

The powders must not have an excessive diameter which would lead to a lack of fusion between them, furthermore, powders with an irregular shape will lead to a different heat conduction which should be considered.

14) In 2019, Dafan Dua et al.[61] studied the **influence of build orientation on microstructure, mechanical and corrosion behaviour of SLM Inconel 718**. Inconel 718 was used to fabricate laminar-shaped samples with selective laser melting (SLM) manufacturing technology. The samples were fabricated with different angles of inclination of the construction direction, ranging from 0 ° to 45 °. For the tensile tests, the samples were cut in the shape of a dog bone, the test was performed at a speed of 0.6 mm/min. The microstructure was studied under an optical microscope, SEM scanning electron microscope with backscattered electron diffraction (EBSD) detector. Electrochemical corrosion tests were performed with the three-electrode method in a 3.5% NaCl solution at 30 ° C. The counter electrode was a platinum electrode, and the reference electrode was a saturated calomel electrode. Electrochemical impedance spectroscopy and potentiodynamic polarization tests were performed.

This procedure led to the following results:

Increasing the angle of inclination increases the roughness on one side of the sample (the one that represents the smallest face of the perpendicular faces oriented with the determined angle of construction). As the angle increases, the Laves phase goes from scattered precipitates to a continuous network. This phase also increases in volume with the increase of the angle. The columnar grains show a texture index of 15 along the <001> direction in the vertical sample but in the 45 ° tilted sample there is a 3.02 texture index in the <001> direction that occurs parallel to the construction direction. Increasing the angle increases the number of grains in directions <011> and <111>. The increase in the degree of inclination increases the tensile strength of the samples. The elongation does not show variations. The final fracture occurs ductile. The dimples present on the fracture surface develop in all directions in the 45 ° specimen, while for the 0 ° specimen they lie in one direction only. The corrosion potential increases towards more positive values as the angle of inclination increases. On the contrary, the corrosion current density decreases as the angle increases. Therefore, the more inclined samples are the ones more resistant to corrosion.

Scholars came to the following conclusions:

The increase in the angle of inclination causes an increase in the exposure time of the layer of material to the heat source. The laser beam at greater inclinations will tend to hit a part of the dust free from obstacles and another part of the dust that is resting on a previously melted layer. The already solidified part dissipates the heat more easily. The part of dust close to the previously melted part decreases with increasing angle and this causes a decrease in heat dissipation. The thermal gradient decreases as the angle increases, and this causes the growth of the Laves phase. A larger angle of inclination increases the tensile strength of the material. This is due to the orientation of the grains in the material in conjunction with the increase in the Laves phase which, however, is more fragile. The corrosion resistance of the samples increases with the increase in the angle of inclination. The greater the angle, the greater the density of the grain boundary length. In addition, the texture of the crystalline grain changes from <001> to <111> at greater inclination angles. This new direction has a lower surface energy and therefore provides better corrosion resistance.

15) In 2014, Qingbo Jia et al.[62] studied **densification, microstructure and properties of selective laser melting additive manufactured Inconel 718 superalloy parts**. Inconel 718 was used to produce rectangular samples with selective laser melting (SLM) manufacturing technology. To determine the influence of the process parameters on the microstructure and the final properties of the piece, samples with different energy densities were produced, i.e. the laser power and the scanning speed were varied. The microstructural analysis was performed using XRD, optical microscope, and SEM scanning electron microscope. The samples were cut and polished, and also etched for SEM analysis. The chemical analysis was performed via EDX. Vickers micro-hardness tests were carried out with a load of 100 g for 10 s. The density of the sample was determined by the Archimedes method. Mechanical wear tests were performed in a sphere tribometer. Hot oxidation tests were performed in an oven at 1123 K on polished samples.

This procedure led to the following results:

The microstructure consisted of a γ matrix with γ’ phase precipitates consistent with the matrix. In the XRD test, the diffraction peaks of the two phases widened and the intensity decreased when the energy density was increased. At low energy densities (180 J/m) discontinuous tracks bordered by large pores were found. By increasing the energy density, the tracks were continuous and regular with a decrease in porosity, up to the maximum density value of 300 J/m. The surface roughness also decreased with the increase in energy density. A coarse columnar dendritic structure was observed at low energy densities (high scan rates). Cracks were found along both the longitudinal and transverse directions of the grains. This structure was refined with the increase in energy density (higher laser power and slower scanning speed), with the grains growing along the direction of construction. The micro-hardness increased with the increase in energy density, and it was also more homogeneous throughout the entire piece. The wear rate of the material decreased with the increase in energy density. The wear surface at 180 J/m was rough and with granular debris, characteristic of adhesive wear. By increasing the energy density, the wear surface was much smoother. At 330 J/m the surface was completely smooth and compact with the formation of a tribolayer. The weight gain trends followed a parabolic law for all samples during oxidation in the oven. In any case, however, at 180 J/m the weight gain was greater with a very steep increase at the beginning of the process which then stabilizes. In the high cases, the increase was much smaller, and the oxide mass was almost constant after a brief increase in the initial phase.

Scholars came to the following conclusions:

With the increase in energy density, X-ray diffraction shows that the peaks widen and decrease in intensity, this is due to a smaller size of the crystalline grains, and therefore to a more refined structure. At low energy densities and therefore at high scanning speeds the laser remains less in a specific point and therefore the temperature is lower than when there is a high energy density. The viscosity increases and the liquid is not distributed adequately, forming pores, which reduce the density of the piece, and surface roughness. At low energy densities, the effect of balling occurs which is due to the instability of the liquid cylinder which divides into spheres to reduce its surface energy. The coarser morphology at low energy density is because a high scan rate causes high dendrite tip growth. This high speed causes the grain to swell. In addition, thermal stresses remain in the workpiece, causing the cooling to form cracks between the dendrites and within them. With a low scanning speed and high laser power, a higher temperature melt is obtained with a longer cooling time. The high energy supplied allows the nucleation and epitaxial growth of the dendrites, obtaining fine columnar grains. The micro-hardness was higher in the samples produced with higher energy density because the microstructure was more homogeneous, the crystalline grain finer and the density of the piece higher. The presence of a finely dispersed γ’ phase is a further reason for the higher hardness. This phase was formed thanks to the fact that the lower layers underwent an ageing process due to the passage of the laser on the upper layer which also supplied heat to the lower ones. The higher hardness and finer crystalline grain of the material that has undergone a higher energy density are the reason for its lower wear rate. At high energy densities, the alloy had the best oxidation resistance. Oxidation begins with the surface chemical reaction between the metal and oxygen, this process is rapid, and this causes the sudden mass increase of the sample. The oxide layer continues to grow until the oxidation is controlled by the diffusion of oxygen which must pass the surface layer to come into contact with the metal. When the oxide layer reaches a critical thickness, oxidation is practically prevented. At low energy density, the coarse and non-uniform microstructure generates an easily breakable oxide film that detaches whenever it reaches a certain thickness and allows further oxidation of the underlying metal, causing much greater oxidation of the piece.

16) In 2017, Luying Wang et al.[63] studied **the effect of sodium chloride on the electrochemical corrosion of Inconel 625 at high temperatures and pressure.** The alloy Inconel 625 samples were placed in an autoclave immersed in a NaCl solution. Corrosion tests were performed at high temperatures and high pressure (300 °C and 16 MPa). Potentiodynamic polarization tests were performed with the three-electrode method. The working electrode was the sample that was polished up to a grit of 7000. The counter electrode was a platinum electrode, while the reference electrode was an Ag/AgCl electrode. The tests were performed at various concentrations of the NaCl solution (0 mol/L, 0.025 mol/L, 0.05 mol/L, 0.1 mol/L and 0.2 mol/L). Electrochemical impedance measurements were also performed. The structural analysis of the oxide layer was performed with the SEM scanning electron microscope, and the chemical composition was analyzed with energy dispersion X-ray spectroscopy (EDS).
This procedure led to the following results:
The anode current density was found to be constant during the test performed without NaCl. The anode current density increased with increasing concentration of NaCl. The corrosion potential became more positive as the NaCl concentration increased and the passive region shrank in extent. Following the electrochemical impedance measurements, Nyquist plots composed of three depressed capacitive rings were detected. One at high frequencies, one at medium frequencies, and one at low frequencies. Resistance to ion transfer through the internal oxide layer, the external oxide layer, and the double layer decreased with increasing NaCl concentration. As the NaCl concentration increases, increasingly larger pits have formed on the surface of the samples. There was a surface depletion of nickel, chromium and molybdenum and an enrichment of oxygen, magnesium, and aluminium. This behaviour increased with the increase in the NaCl concentration.
Scholars came to the following conclusions:
The constant current density in the absence of chloride ions is due to the formation of a stable oxide layer. The oxide film is formed by an outer layer of nickel oxide and hydroxide, while the inner layer is mainly made up of chromium oxide. Nickel having a higher diffusivity than chromium formed the outer layer. With the addition of chloride ions, the oxide film is destabilized. The dissolution of nickel and its oxide increased with the concentration of chloride ions, the same happened for chromium oxide. This caused the oxide film to break. Following this process, another film was formed consisting of aluminium

and magnesium oxides which replace the internal layer of chromium oxide, while the external layer rich in nickel persists, being more compact. In the end, the corrosion rate increased with the increase in the NaCl concentration. The high-frequency capacitive loop is due to the external oxide layer. The medium frequency capacitive loop is due to the inner layer. The third low-frequency loop is due to the double layer between the surface and the outer Helmholtz plane. The lower charge transfer resistances indicated that they moved more easily through the layers and thus that corrosion was favoured. The small radius of Cl- and the easier dissolution of the outer layer caused the drastic drop in resistance to charge transfer through the outer layer. The higher concentration of O, Mg and Al on the surface is due to their precipitation. While Ni and Cr are dissolved in the solution. The solubility of these metals increases with the concentration of chloride ion which penetrates through the oxide layer.

17) In 2020, Huihui Yang et al.[64] studied **microstructural evolution and mechanical performances of selective laser melting Inconel 718 from low to high laser power.** Inconel 718 was used to produce cuboidal-shaped samples thanks to the SLM (Selective laser melting) manufacturing method. The samples were produced using different laser powers (500 W, 800 W, 1200 W, 1500 W, 1800 W e 2000 W) and different scanning speeds. The density was calculated by processing the cross-sectional images under a light microscope. The samples to be submitted to the microstructural analysis were polished and electro-etched in a solution of H_3PO_4 at 70% by volume at 5 V for 90 s. The samples were subjected to X-ray diffraction (XRD) analysis. They were observed under an SEM scanning electron microscope and TEM transmission electron microscope. Chemical analyzes were performed with an electronic probe micro-analyzer (EPMA) and the grains were analyzed with an EBSD probe. Samples produced in the shape of dog bone were subjected to tensile tests with a drawing speed of 2 mm / s.
This procedure led to the following results:
As the laser power increases, it becomes more and more difficult to find a scanning speed and a hatch spacing that allows the obtaining of a high relative density of the material. In any case, the scanning speed must increase to counterbalance the effect of higher laser power. With the increase in laser power, the presence of micropores increases. A higher power, however, allows for a higher energy density and above all a higher construction speed. The microstructure of the samples under XRD analysis consists of a matrix with fcc-structure. The presence of the Laves phase is not detected. The intensity of the diffraction peaks decreases as the laser power increases. The width of the melt pools has a minimum of 800 W and then increases to higher powers. The aspect ratio of the pools remains below 0.5 in all cases. The 500 W sample has a large columnar crystal grain. With the increase in power, on the other hand, there is a decrease in the size of the columnar grains and the increasing presence of equiaxial grains. The spacing between the arms of the dendrites increases with the laser power and the presence of the interdendritic Laves phase also increases. The segregation of Nb, Mo and Ti increases with the laser power, they constitute the Laves phase. The crystallographic texture is weaker at 800 W with scattered

polar points. The strongest texture is found at 500W. Tensile strength, yield strength and elongation increase with decreasing laser power. Samples manufactured at 500W, 800W, and 1200W have higher mechanical properties than cast samples. The 500 W, 800 W and 1500 W samples show a ductile rupture with the evident presence of dimples on the fracture surface. The 1200 W and 1800 W samples exhibit ductile-brittle rupture. At 2000 W, a completely brittle rupture occurs.

Scholars came to the following conclusions:

The cooling speed decreases with increasing energy density and therefore with increasing laser power. The spacing between the arms of the dendrites increases as the cooling rate decreases. The slower cooling rate allows the atoms to diffuse and segregate, leading to the formation of the Laves phase in the interdendritic zones. Cellular dendrites grow along the direction of deposition. Based on the angle present between the dendrites, a sub-grainy or columnar-grained structure is obtained (as the angle increases). The heat flow is given by the Marangoni convection, where the flow of molten metal goes from the centre of the pool towards the outside, in a circular motion. At the edges, the metal flows from top to bottom. A greater flow of heat, given by greater laser power, leads to a larger melt pool. A greater convective flow causes a greater dispersion of the growth angle of the dendrites, and this allows the growth of finer columnar grains. The best mechanical properties of the samples manufactured at lower powers are due to the finer dendritic structure, the absence of the Laves phase and the higher relative density of the piece. The porosity, the presence of the Laves brittle phase and the coarser dendrites lead to a lower resistance of the samples manufactured at higher powers. With high power, the low relative density dominates the strengthening effect deriving from the fine columnar grain. The maximum elongation is obtained from an optimal number of grain boundaries.

18) In 2018, G.H. Cao et al.[65] studied **γ′, γ″ and δ precipitates in heat-treated alloy Inconel 718 fabricated by selective laser melting**. Inconel 718 was used to fabricate cylindrical samples with selective laser melting (SLM) technology. The samples were heat treated at 1065 °C for 1 h, and then aged at 760 ° C for 10 h and then at 650 ° C for 8 h. A cubic sample was produced by electric discharge machining (EDM) and polished up to 1 μm. The sample was electropolished and electro-etched in a solution of H_3PO_4 at 70% by volume at 5 V. The cube sample was examined under the SEM scanning electron microscope and underwent an X-ray diffraction analysis. disc-shaped, polished, electropolished and electro-etched with 10 vol% perchloric acid and methanol at 25 V and a temperature of -25 °C. The discs were examined under the TEM transmission electron microscope and by selected area electron diffraction (SAED).

This procedure led to the following results:

From the SEM were noted short and thick platelets which are identifiable as the δ phase. Acicular-shaped precipitates representing the γ" phase with bct structure, cuboidal and circular precipitates which are the γ" and γ′ phase respectively were noted. The matrix γ fcc has a cellular substructure. The precipitates were found inside the grains and along the edges. From the TEM, reflections of the superlattice (100), (010) and (110) are detected. The precipitates γ′ cause reflections in (100) and (010), while those in (110) are due to both γ′ and γ". The possible three variants of γ′ and γ" result in SAED models superimposed on some specific guidelines. The acicular precipitates consist of two variants of γ" of [100] and [010]. Globular precipitates with orthorhombic structure have been detected within the grain and along the grain boundaries representing the δ phase.

Scholars came to the following conclusions:

The general microstructure consisted of very fine cellular grains obtained thanks to the high cooling rate typical of the SLM production process. The δ-Ni3Nb phase was present as coarse platelet-shaped precipitates both in the grain and at the grain boundary. The γ "phase was present as discoidal and acicular precipitates inside the grains, while the coarser acicular precipitates characterized the grain boundaries. The γ ′ phase appeared as precipitates with a round shape. The nanometric precipitates allow the maintenance of the fine cellular microstructure even after heat treatment. The lattices of the γ" and δ phases in the [100] directions are superimposed on the lattices of the γ phase in the [001] and [011] directions. The orientation relations of γ" with γ and of δ with γ are (001) [100] γ" // (100) [001] γ and (010) [100] δ // (111) [011] γ, producing small lattice misalignments.

19) In 2018, Tyler Moss et al.[66] made a review about **stress corrosion crack initiation in Alloy 690 in high-temperature water.** Scholars, by gathering information from various scientific papers, came to the following conclusions:

The constant deflection technique implies that the sample, in the shape of a sheet or tube, is bent into a U-shape or a C-shape and held in this position. The tension generated in the workpiece relaxes over time at a high temperature. The tests to detect the formation of SCC (stress corrosion cracks) on the alloy Inconel 690 and, as a reference, on the alloy Inconel 600 were performed in water at temperatures higher than 320 °C and a pressure of 14.2 Mpa. Alloy 690 showed no cracks while alloy 600 was heavily impacted. Only tests performed at high strains such as that performed by Smith et al. with a C deflection of the samples produced SCC at 340 ° C after 1800 h also on alloy 690. Even from constant load tests, alloy 690 was very resistant to SCC nucleation. No SCC was detected except for the test performed by Boursier et al., where the alloy showed small cracks after 11000 h at 360 ° C and was subjected to 90% of its tensile strength. Cracks have been found to propagate intergranularly on pre-cracked samples. Samples at 360 °C and subjected to slow loading and fast loading cycles showed intergranular cavities after 9000 h of exposure. This only happens with very cold worked alloy 690. Tensile tests at constant extension speed allowed the detection of intergranular cracks on alloy 690 samples by conducting the tests at $5*10^{-8}$ / s in primary water at 360 °C. These cracks did not occur in the other types of tests. The cold-worked samples showed a degree of cracking that increased with the increasing speed of extension. The crack is generated in the area of the Cr-depleted grain boundary.

A mechanism that explains the initiation of the crack on a reference alloy 600 is Selective oxidation. That is, the material preferably oxidizes on the surfaces of the grain boundaries and in front of the tip of an already existing crack. The oxide film that forms on the surface of the metal consists of an internal layer of chromium oxide and an external layer of NiO and $NiFe_2O_4$ particles formed by precipitation. The inner layer of alloy 690 is richer in chromium than that of alloy 600. Chromium oxide on the surface is possible due to migration through the grain boundaries of the Cr, once the oxide state is formed the grain boundaries also if they are depleted of Cr they are protected from further oxidation, and this confers high resistance to SCC. The formation of the SCC takes place as a result of numerous breaking cycles (caused by the stress imposed on the piece) and the formation of the oxide layer that exhausts the chromium available on the grain boundary and does not allow the further formation of the protective layer, exposing the grain boundary to the corrosive attack and allowing the nucleation of an SCC.

The oxidation of alloy 690 was studied by placing electro-polished coupons in hydrogenated supercritical water at 360 °C and 400 °C. Chromium oxide and nickel oxide platelets were observed which represented internal oxidation while a layer of chromium oxide was present on the surface of the metal. The grain boundary has undergone a migration due to the diffusion of Cr which has depleted the adjacent area. The depletion, however, is much less marked compared to that suffered by the alloy 600 in the same conditions.

Crack nucleation occurs as a result of deep oxidation of the grain boundaries. Oxidation causes a reduction in the tensile strength of the grain boundaries, which, when subjected to sufficient stress, fracture and separate. The walls of the crack are covered with nickel oxide and chromium oxide, which also extends beyond the tip of the crack due to the oxidation of the grain boundary.

At the high temperatures to which alloy 690 is exposed and if the material is subjected to a sufficient load, the formation of cracks due to the phenomenon of creep is very likely. In addition to the dynamic deformation, also that due to creep favours the onset of SCC. A sufficiently large deformation or a load imposed for a sufficient time causes the rupture of the protective oxide layer. The thicker the layer, the more deformation or time it takes. The presence of carbides in the metal favours the formation of the protective chromium oxide layer and slows down the growth of the crack towards the inside of the piece.

20) In 2019, K. Lutton Cwalina et al.[67] made a review about **the effects of molybdenum and tungsten alloying on the corrosion behaviour of nickel-chromium alloys in aqueous corrosion**. Scholars, by gathering information from various scientific papers, came to the following conclusions:

Ni is a very suitable metal for the solubilization of Mo and Cr due to its ionic radius and electron configuration which allow these large elements to be placed in the lattice. Nickel alloys are divided into precipitation-hardened alloys (suitable for high temperatures) and solid solution-hardened alloys (suitable for low temperatures). Chromium allows the creation of a passive layer resistant to reducing acids, hot gases, and solutions containing chloride. Molybdenum and tungsten increase the resistance of the passive film to oxidizing and reducing acids and chlorides. They are also useful for promoting the hardening of the alloy by solid solution. Considering the Ni-Cr-Mo alloys, the solid solution is maintained thanks to the rapid quenching that the alloy undergoes. The carbon content is minimized to minimize the formation of carbides.

As the concentration of Cr, Mo and W increases, the passivation current is reduced and the passivation potential drops towards more negative potentials. The combination of Mo and W also increases the breaking potential of the passive film.

The oxide film increases in thickness with increasing exposure time to the corrosive environment until it reaches a maximum, at which growth is counterbalanced by dissolution. Even as the potential increases, the film thickness increases until the dissolution potential of the film is reached, after which the thickness decreases. A higher amount of Cr and W results in a higher film thickness. In an environment rich in chloride, the corrosion resistance is higher with the grain oriented in the direction (110) after the formation of the oxide film. Mo and W favour the re-passivation of the film and the time required for pitting corrosion increases.

In general, the growth of the passive film is driven by the formation of the most thermodynamically favoured oxide of each alloying element. Or oxides are formed with the most favourable kinetics. The Pourbaix diagram allows knowing the stability regions of the various oxides based on pH and potential. The oxide film generally consists of an internal layer of Cr_2O_3 or $Cr\ (OH)_3$ and an external layer of NiO or $Ni\ (OH)_2$. At the oxide/solution interface there is an accumulation of Mo^{6+} and/or Mo^{5+} ions. In Ni-Cr-Mo alloys there is the presence of an oxide with the structure of rock salt containing Ni, Cr and Mo which with the continuation of oxidation becomes an oxide with the structure of corundum. Molybdenum allows the oxide to reduce the coalescence of vacancies; indeed, even in an aqueous environment, Mo reduces the mobility of cationic vacancies through electrostatic interactions. Molybdenum promotes the adsorption of oxygen and the oxidation of Ni and Cr, promoting passivation.

Molybdenum which replaces Cr or Ni in the crystal lattice of the respective oxides causes an excess of positive charge which is filled with the capture of the negatively charged cationic vacancies. This allows them to be blocked and prevents their coalescence which would cause the nucleation of pits. The same effect is produced by tungsten.

The aggressive action of chloride ions is given by their adsorption on the surface of the film which causes the dissolution of the cations in solution and the formation of cationic vacancies which, if coalesced, would lead to the formation of large voids which would cause sufficient stresses to break the passivating film. Mo prevents this phenomenon and promotes the adsorption of oxygen instead of chloride. Mo and W concentrate in the crevices where corrosion is localized and form species that inhibit or slow down the dissolution kinetics.

21) In 2012, K.N. Amato et al.[68] studied **microstructures and mechanical behaviour of Inconel 718 fabricated by selective laser melting**. Pre-alloyed powder of Inconel 718 (of composition 53.5Ni-19Cr-18.3Fe-5Nb-3Mo-1Ti-0.43Al) was used to fabricate cylindrical samples using selective laser melting (SLM) additive manufacturing technology. The cylinders were built with the main axis parallel to the laser beam or perpendicular to it, producing specimens constructed vertically or horizontally. The cylinders underwent heat treatment at 982 ° C for half an hour and then hot isostatic pressing (HIP) at 1163 ° C and 0.1 GPa. Some comparison cylinders were only annealed at 1160 ° C for 4 hours. The cylinders were cut into coupons both vertically and horizontally. The coupons were polished and electro-etched in a 70% solution of sulfuric acid at 5V between 5 and 102 seconds. Later, they were observed under the optical microscope, SEM scanning electron microscope equipped with an X-ray spectrometry (EDS) system. An XRD analysis was performed on the samples. Coupons were observed at TEM, after being electro-polished. Microhardness (Vickers) and macro hardness (Rockwell C) measurements were performed by a durometer. Furthermore, the cylinders were machined to perform tensile tests at a strain rate of 10^{-3} s^{-1}.

This procedure led to the following results:

Observing the samples under an optical microscope, the melt pools and the presence of columnar grains inside them that grow following the direction of construction were observed. Samples that have undergone HIP treatment exhibit a much more regular columnar grain structure than as-build samples. There are recrystallized areas in which the precipitates are finely dispersed. The XRD spectra showed mixed texture peaks (111) and (200) in the reference planes of the vertical and horizontal cylinders (cross-section). Dense precipitates forming columnar arrays were observed at TEM. In the matrix and at the boundaries, ellipsoidal precipitates are observed. Elongated precipitates (100) grow along the construction direction. HIP led to the predominance of precipitates with a texture (200). The ellipsoidal precipitates are stacked in columns and have the main axis coinciding with the plane (100) of the matrix. These precipitates constitute the γ "phase. There are also precipitates scattered within the matrix. The annealed samples show similar spectra to the other samples but also show a new peak (004) of the γ” phase and a peak (201) for the orthorhombic δ-Ni3Nb phase. The δ phase is located at the boundaries of the recrystallization grains. The highest hardness (HV) was found after the HIP treatment (5.7 GPa) while the as-build component had the lowest hardness (3.9 GPa). The annealed sample was in the middle (4.6 GPa). The tensile strength was greater than 6% in the samples with the construction direction parallel to the traction axis (z).

Scholars came to the following conclusions:

The columnar structure is made up of Ni3Nb precipitates which constitute the γ "phase with a body-centred tetragonal structure (bct). The strong texture (200) corresponds to the growth of the grains of the γ matrix along the construction direction. The diffraction spectra of the precipitates γ "and γ’ coincide with the spectra of the matrix and therefore TEM analysis is required to distinguish them. The SLM manufacturing technology generates a columnar grain structure that grows along the construction direction. The stacks of ellipsoidal precipitates are generated by the formation of subsequent melt pools which cause this phenomenon in the previous pools. The HIP samples showed a dense distribution of precipitates in the recrystallized zones, while the annealed samples were characterized by a larger but less dense recrystallized zone of precipitates. The precipitates present in the recrystallized matrix are cuboidal or spherical. The greater resistance of the sample constructed along the z-axis is due to the favourable orientation of the precipitates of the γ” phase along the traction direction.

22) In 2018, Dongyun Zhanga et al.[69] studied **the thermofluid field of the molten pool and its effects during selective laser melting (SLM) of Inconel 718 alloy**. A finite element mathematical model of the thermofluid field of the melt pools, generated by the passage of the laser of the SLM machine on a powder bed of Inconel 718 alloy, was simulated with the COMSOL Multiphysics TM 5.0 software characterized by coupling with a multiphysics field comprising the flow of molten metal, temperature distribution and heat flow. The size of the mesh grows from the point of impact of the heat source towards the solid substrate. The ideal packaging model of the powders is used to simplify the simulation and the metal particles are all considered spherical and of equal size. The porosity of the powder bed is 45%. The laser source is considered a Gaussian. The gaps between the particles affect the absorption of energy by the bed. The laser light penetrates the dust layer thanks to multiple reflections. Most of the energy is absorbed by the dust and a smaller part is absorbed by the substrate. About 80% of the energy is absorbed and 20% reflected, of this 20% that hits other particles, 80% is absorbed and 20% reflected, and so on. It is considered that part of the energy is dissipated to the external environment. The molten metal convention due to the Marangoni effect is a fundamental phenomenon that affects heat transfer and the size of the melt pool and is therefore considered. The thermal conductivity of the powder bed is much less than the thermal conductivity of the maximum material Inconel 718 due to the gaps between the particles. The heat capacity of the material, on the other hand, remains unaltered. Given the high heating and cooling speed, numerical simulation is the only way to accurately investigate the effect of Marangoni convection on the SLM process. To simplify the simulation, the heat source is considered to be at a fixed point, to determine the effect of different Marangoni coefficients. While the Marangoni effect on the shape of the melt pools was studied considering a moving heat source. The Inconel 718 alloy samples were produced using a powder bed SLM machine in a chamber with argon gas to avoid oxidation of the material. The samples were polished and electro-etched and then observed with an optical microscope.
This procedure led to the following results:
The molten metal in the centre of the pool flows from the bottom of the pool to the surface, and on the surface flows from the centre to the edges. The molten metal present on the edges flows from the surface towards the bottom of the pool. All this happens with circular motions. This model is called outward convection and was observed with a negative Marangoni coefficient of $-4*10^{-4}$ N/(mK). Inward

convection is characterized by inverse motions to these and is observed with a positive Marangoni coefficient of $4*10^{-4}$ N/(mK). The fastest flows are in the centre and on the surface of the pool. As the Marangoni coefficient increases, the depth of the pool has increased, while its width has decreased, causing the depth-width ratio to increase. The depth and width of the melt pools increase with increasing laser passages. The width is greater where more heat accumulates, i.e., where more tracks meet. The convective heat flow is an order of magnitude greater than the conductive heat flow, and both increase thanks to the action of multiple passages.

Scholars came to the following conclusions:

With a negative Marangoni coefficient, the surface tension of the melt decreases with increasing temperature, and since the melt is warmer in the centre where the heat source is, the fluid is pushed towards the edge. With a positive Marangoni coefficient, the surface tension increases with increasing temperature and the reverse effect occurs. The oxygen and sulfur content can cause the transition from a negative to a positive Marangoni coefficient. The ideal state for SLM manufacturing is outward convection. Outward convection promotes lateral heat conduction, and this generates a higher lateral fusion rate, while downward fusion is slowed down. Hence, the depth-to-width ratio decreases. Inward convection causes the opposite phenomenon. And the depth-to-width ratio is greater than that of the non-convection situation. The movement of the heat source and its multiple passages causes an accumulation of heat in the previously formed melt pools. The molten metal is just hit by the laser and the metal left behind has a higher temperature than the metal before the laser. This causes increased conductivity and a flow of heat preferably towards the metal that the laser leaves behind. Thus, a comet-tailed temperature gradient is obtained. The convective heat flow makes the melt pool wider, and the conductive heat flow makes the melt pool deeper.

23) In 2017, Xiaoqing Wang et al.[70] studied **the effects of thermal cycles on the microstructure evolution of Inconel 718 during the selective laser melting process**. SLM additive manufacturing technology was used to produce Inconel 718 alloy samples. Three-step stairs-shaped samples were fabricated. The steps had a height of 3, 60 and 90 mm starting from the lowest. The scan pattern used was the checkerboard one, consisting of square islands. The scan speed was 600mm/s and the beam scan spacing was 105μm. Coupons were cut in each step, polished and electro-etched. The coupons were observed under a digital microscope, optical microscope, and SEM scanning electron microscope. Back electron diffusion detection (EBSD) was performed. The porosity analysis was performed using the ImageJ software.

This procedure led to the following results:

An equiaxial microstructure was found in the Z plane (parallel to the upper surface of the steps). On the Y plane (parallel to the lateral surface of the steps) the melt pools were detected and inside them, there was a columnar microstructure. Elongated dendrites grow along the Z-axis and pass-through various layers. The melt pools appeared in two modes, one deeper than the other one. At SEM, interconnected precipitates were observed in the interdendritic regions which can be classified as the Laves phase. The columnar microstructure exhibited cellular morphology when cut transversely. In the lower layers, it has been observed that cellular dendrites grow in several directions, while at ever greater heights (along the Z axis) the dendrites grow more and more regularly upwards, reaching to cross more layers. Cellular structures increase in thickness with increasing height. The presence of the Laves phase also increases with the sampling height. Dendrites grow more easily along the main thermal gradient if they undergo multiple thermal cycles. The Laves phase passes from a coarse and interconnected structure to a particle structure when it undergoes multiple thermal cycles. In addition, the volumetric fraction of the Laves phase also decreases with increasing thermal cycles which causes its dissolution. Equiaxial grains with texture [001] were observed in the Z plane through the EBSD tests. On the Y plane, columnar grains were found with a peripheral orientation of <101> concerning the Y direction. It has been observed that the strongest texture on the Y plane is on the middle step, while the weakest texture is on the lower step. The same happens on the Z plane. As the thermal cycles increase, the intensity of the textures on the Z plane and on the Y plane increases. The material has been observed to be characterized by small spherical pores and large spherical or irregularly shaped pores. The surface porosity is 0.2%. There was no change in porosity with increasing thermal cycles or height.

Scholars came to the following conclusions:

The vertical growth of the dendrites is caused by the vertical heat flow concerning the steel substrate which is determined by the series of passages of the laser one over the other. The deeper melt pools were at the turning points of the laser beam where the most heat accumulated. The presence of the Laves phase is determined by the segregation of the alloying elements, especially niobium. Initially, the dendrites nucleated heterogeneously and grow following the temperature gradient. As the heat is dissipated in various directions, the dendrites grow less regularly. As the thickness of the solidified layer increases, peripheral heat loss decreases and the lower layers act as a substrate for the growth of dendrites in an epitaxial way. The predominant thermal gradient is from bottom to top, so the dendrites grow regularly along the vertical direction. The increase in thickness of the dendrites is due to a decrease in the cooling rate with the increase in the thickness of the piece. A slower solidification rate allows the solute to have more time to diffuse and accumulate, causing the Laves phase to precipitate. The increase in texture intensity is due to the progressive preferential orientation of the dendrites in the vertical direction and the progressive increase in the size of the dendrites, which increase up to a maximum and then decrease going towards the upper surface. The small pores are gas bubbles trapped in the molten metal. While large irregular pores are characteristic of suboptimal process parameters.

24) In 2019, Shuncun Luo et al.[71] studied **microstructural evolution and corrosion behaviours of Inconel 718 alloy produced by selective laser melting following different heat treatments.** Cubic

samples of Inconel 718 alloy were produced with SLM additive manufacturing technology. The process parameters were a laser power of 350 W, a scan rate of 800 mm / s, a hatch spacing of 120µm and a layer thickness of 40 µm. The samples were annealed at 500 °C for 3 h. The samples underwent various heat treatments: The ST1 sample was brought to 940 °C × 1 h, the ST2 sample was brought to 980 °C × 1 h, the ST3 sample was brought to 1020 °C × 1 h, while the SA sample underwent heating at 980 °C × 1 h +720 °C × 8 h (cooling in the oven at 50 ° C / h) + 620 °C × 8 h. A hot rolled sample at 980 °C was used as the comparison sample. The samples were all polished. The corrosion tests were performed with a three-electrode system: a calomel electrode saturated with KCL as a reference electrode, a platinum electrode as a counter electrode, and the cubic sample as a working electrode considering a surface of 1 cm^2. Potentiodynamic polarization tests and electrochemical impedance spectroscopy (EIS) tests were performed in a 3.5% by-weight NaCl solution. The samples underwent an X-ray diffraction analysis and an EPMA microanalysis with an electronic probe. The polished samples were electro-etched in a 10% by-volume perchloric acid solution. Subsequently, the samples were observed under the SEM scanning electron microscope and underwent an energy dispersion spectroscopy (EDS) and an electron back-scattering diffraction analysis (EBSD). Samples were cut into thin films, electro-etched and examined under the TEM transmission electron microscope.

This procedure led to the following results:

The diffraction peaks of the γ phase overlapped the diffraction peaks of the γ 'and γ" phases making them indistinguishable. Diffraction on the (211) plane, in the SLM + ST1 and SLM + SA samples, represents the precipitation of the δ phase. Carbides are detected in all samples. There are no peaks relating to the Laves phase. Through SEM observation, cell dendrites and columnar dendrites that grow upwards are detected on the XY plane (parallel to the scan direction), and the columnar dendrites grow towards the centre of the melt pool in the overlapping area of two pools. The Laves phase is present in the interdendritic region. There are NbC carbide particles in the interdendritic region. Nb is very present in interdendritic regions while Fe is very present in dendrites. After annealing at low temperatures, the presence of recrystallized equiaxed grains is detected but they do not have a uniform size. KAM (Kernel average misorientation) values are lower in recrystallized grains, which indicates the release of residual stresses in the grains. By increasing the temperature, the recrystallized grains increase and take on a uniform size. At 1020 ° C the grains swell. The Laves phase is greatly reduced with annealing. The δ phase precipitates with a needle-like and platelet morphology at 940 °C. At 1020 °C the δ phase is greatly reduced and is present as scattered platelets. The carbides do not undergo significant variations. After the SA treatment, the presence of block-shaped precipitates is detected in the interdendritic region, recognized as the residual Laves phase. Needle-like and platelet-shaped particles precipitate around these blocks. At TEM it is observed that spherical and disc-shaped precipitates are uniformly distributed in the matrix, which constitute the dispersed γ 'and γ" phases. The corrosion potential follows this order: SLM <ST1 <rolled <ST2 <ST3 <SA. Corrosion current density is much higher for SLM, ST1 and rolled

samples. Sample ST3 has the lowest corrosion current density. The corrosion rate follows this order: SLM> rolled> ST1> SA> ST2> ST3. The passive potential order is SLM> SA> ST1> ST2> ST3> rolled. ST3 and rolled samples have the lowest passive current. The pitting potential follows this order: rolled> ST3> ST2> ST1> SA> SLM. The diameter of the Nyquist diagram of the rolled sample is larger than that of the ST3 sample. The charge transfer resistance in the bilayer, and the charge transfer resistance in the diffusion layer, are greater for the rolled sample than for the ST3 sample. On the SLM, SA and rolled samples there are cracks on the surface of the passive film. The SA sample shows an exfoliation of the film. Pits are observed on the ST1~ST3 samples. The pits are fewer on the ST3 sample. On the ST1 ~ ST2 samples there are cracks between the precipitated phases and the matrix. The passive film on the rolled sample is the most compact and smooth.

Scholars came to the following conclusions:

The Laves phase present in the interdendritic region is due to the segregation of niobium which leads to the formation of nucleation sites of this phase. Only the Nb is affected by the phenomenon of micro-segregation, the other elements are uniformly distributed thanks to the high speed of solidification. At low annealing temperatures, an incomplete recrystallization of the grains is obtained. Recrystallization is driven by the presence of lattice distortions due to the accumulation of dislocations on the solidification defects maintained in the material due to the rapid solidification speed. Complete recrystallization is achieved at 980 °C. At 1020 °C the solvus temperature of phase δ is exceeded, which is about 1010 °C. The disappearance of phase δ contributes to the enlargement of the grains. The annealing before the double ageing allows the dissolution of the Laves phase and the release of Nb which will form the dispersed phases in the matrix. The rolled sample forms the passive film more easily than the other samples. Among the samples produced using SLM, the ST3 sample is the one with the most pitting-resistant passive film. Corrosion resistance follows this order: rolled> ST3> ST2> ST1> SA> SLM. The higher bilayer charge transfer resistance for the rolled sample implies that corrosion dissolution of the passive surface film is more difficult. On SLM samples, the attack of chlorine ions generates pits or cracks on the passive layer. The chlorine ions are thus able to penetrate the film and reach the metal leading to severe corrosion aggravated by the galvanic effect between the matrix (anode) and precipitates (cathode). Numerous Laves' phase-rich grain boundaries cause an intense galvanic effect leading to severe corrosion of the as-built SLM sample. Residual stress contributes to the formation of cracks. The heat treatments allow the relaxation of residual stresses and the reduction of the Laves phase. The interface between the matrix and phase δ is inconsistent and this causes lattice mismatches that accelerate the anodic dissolution. With the increase in temperature, the δ phase dissolves and the number of grain boundaries is reduced, this decreases the risk of cracking. This is why the ST3 sample is the most resistant. The rolled sample, however, has a coarser and more homogeneous grain, the corrosion attack will thus be uniform over the entire surface and therefore less severe. With the SA heat treatment, fine precipitates dispersed in the matrix are obtained, which cause numerous galvanic effects, in addition, they distort the lattice which aggravates corrosion.

25) In 1998, P. Kritzer et al.[72] studied **Corrosion of Alloy 625 in Aqueous Solutions Containing Chloride and Oxygen.** The Inconel 625 alloy samples were 1 m long annealed tubes with an external diameter of 14.3 mm and an internal diameter of 8.5 mm. The tubes were thoroughly cleaned with acetone, a sample was also polished up to 0.3 μm of grit. Coupons were manufactured of the same material as the pipes that were exposed to the corrosive environment inside the pipes themselves. The temperature profile inside the tubes ranged from room temperature at the ends to reach 500 °C in the central area. The internal pressure reached a maximum of 38 Mpa. The corrosive solutions pumped in the various tests had different compositions. The main components were HCl, and H_2O_2 for the acid solutions, while H_2O_2, NaCl and NaOH were present in the alkaline solutions. The oxygen in the solution was obtained from the decomposition of hydrogen peroxide with a platinum catalyst. In some experiments, the temperature was kept below the critical water temperature. The thickness of the samples was measured with an ultrasonic device. The samples were observed with endoscopes. Subsequently, the tubes were mounted in resin, cut along the longitudinal direction, and observed using a scanning electron microscope (SEM) with an energy dispersion X-ray analyzer (EDX). The surface of the samples underwent secondary neutral mass spectrometry, X-ray diffraction analysis and infrared (IR) spectrometry. The solution after corrosion was analyzed by atomic emission spectrometry, while the solid corrosion products were analyzed by the X-ray fluorescence technique.

This procedure led to the following results:

The pitting appeared starting from 130 °C in an acid solution. With increasing temperature, the density of the pits increased. While decreasing the temperature the pits were deeper. In the neutral solution, the pits appeared starting from 210 °C. The same happened for the polished tube, also in the acid solution. Pitting corrosion did not manifest itself in oxygen-free HCl and alkali chloride solution. The corrosion products in the pits consisted of Cr, Mo and Nb oxides, nickel was absent. In the subcritical region, outside the pits, scale-shaped chromium-rich products (CrOOH) were found. The coupons showed a passive film rich in Cr and Mo, a large amount of titanium was present at the oxide/metal interface, and Ni was dissolved in the solution. The film increased in thickness with increasing temperature. Above 240 °C, the depth of the pits is reduced. Slight intergranular corrosion occurred at the edge of the pits. The whole surface was affected by this phenomenon. At 24 Mpa, above 360 °C, pitting has stopped. General corrosion occurred above 240 °C in solutions rich in HCl or NaCl and oxygen. The highest corrosion rate occurred in the transition region between the area under the critical temperature and the super-critical area of the water. Increasing the concentration of HCl and O_2 decreased the temperature at which the most severe corrosion occurred (with a high reduction in the thickness of the pipe), and the maximum corrosion rate was observed at 350 °C. The concentration of metals in the solution increases as the concentration of oxygen and HCl increases. The concentration of dissolved metals increased with decreasing pH, especially in the case of Ni. The concentration of $CrO_4{}^{2-}$ increased with pH. $NiCl_2*6H_2O$ precipitates were found in the supercritical region. In the supercritical region, intergranular corrosion was predominant. The high pressure favoured the penetration of corrosive species through grain boundaries. Stress corrosion cracks (SCC) were detected in high-pressure experiments, where they originated from intergranular cracks at the bottom of the pits, at high oxygen concentrations the cracks were shorter and took longer to manifest.

Scholars came to the following conclusions:

Pitting occurs at the breakpoints of the passive layer because of Cl^- ions. The underlying metal corrodes, dissolving and generating positively charged species that attract other Cl^- ions which accelerate corrosion, forming a pit. Pitting occurs at lower temperatures if the concentration of aggressive species is higher but also if the surface has more sites where Cl^- ions can accumulate, as in the case of unpolished surfaces. At higher temperatures, general corrosion occurs due to the reaching of the transpassive region of Cr and Mo with the generation of compounds that are soluble in the solution. Reaching the solubility limit of these products generated a saline film on the surface consisting of nickel chloride and nickel dichromate. This generates an electro-polishing effect at the film/metal interface. Inside the pits, this causes intergranular corrosion. The SCCs occurred at high pressures where the high mechanical stresses favoured this phenomenon. Furthermore, the sample was on the borderline between the passivity and trans-passivity region. The cracks were generated on the bottoms of the pits. In the low-density supercritical regions only, intergranular corrosion was detected and, in any case, to a lesser extent than in the subcritical regions. Poor corrosion is due to the presence of undissociated HCl. With increasing pressure, the dissociated HCl increased and therefore a more severe intergranular corrosion occurred. The opposite happened in high temperatures. Compounds of Cr are more soluble under supercritical conditions than those of Ni. So only the nickel oxides were responsible for the passivation which further reduced corrosion.

26) In 1992, J.T. Ho et al.[73] studied **Pitting Corrosion of Inconel 600 in Chloride and Thiosulfate Anion Solutions at Low Temperatures.** The samples used in the study were cylindrical in shape and were made of Inconel 600 alloy, polished with 600 grit silicon carbide paper, thoroughly cleaned with ultrasound in water and then cleaned with acetone. Aggressive solutions were composed of NaCl and $Na_2S_2O_2$ in various concentrations. A case with the deoxygenated solution, a case at a temperature above room temperature, and a case at 3 pH were examined. Furthermore, the cases of room temperature, neutral pH and the solution saturated with oxygen were mainly examined. Electrochemical tests were conducted using a saturated calomel electrode as the reference electrode. Through the potentiodynamic anodic polarization tests, the corrosion potential and the pitting potential were measured in a scanning range between -100 mV (vs Ecorr) and 1200 mV (vs SCE) and the scanning speed was 1 mV/s. The

sample was immersed in chloride and thiosulfate solutions with concentrations from 0.1 to 0.0001 M. Potentiostatic polarization tests were also performed. The corrosion surfaces and products were analyzed using a scanning electron microscope (SEM) and an energy dispersion spectrometer (EDS). Open circuit tests with external potential equal to 0 were carried out to compare the results with those of polarization under accelerated conditions. The surfaces were examined under an optical microscope. The samples were immersed for about 30-60 minutes in a solution containing 20% of NaOH and 3% of $KMnO_4$ at 100 ° C and then immersed for five minutes in a solution of disodium dishydrogen disogenous ethylenediaminotetraacetate (EDTA) at 100 ° C, to uncover the bottoms of the pits. The depth of the pits and their density were measured by observation under an optical microscope.
This procedure led to the following results:
As the concentration of thiosulfate increases, the corrosion potential shifts to less negative potentials. As the chloride concentration increases, the pitting potential shifts towards less noble values. Low concentrations of thiosulfate (0.001, 0.0001 M) shift the pitting potential towards more active potentials, while higher concentrations (0.1, 0.01 M) shift the pitting potential towards more noble values. Deoxygenation causes the pitting potential to shift to more active potentials than in an air-saturated solution. The pitting potentials in solutions with 3 pH are nobler than those with neutral pH. At 70 °C the pitting potential is more active than that at room temperature. The size of the pits is greater as the chloride concentration increases with the presence of thiosulfate concentrations. From the open circuit tests, it can be seen that the pitting resistance of alloy 600 in the solution with [Cl–] = 10^{-1} M and [$S_2O_3^{2}$] = 10^{-4} M is the worst, with many pits of large dimensions, while the resistance to pitting in the solution with [Cl^-] = 10^{-1} M and [$S_2O_3^{2-}$] = 10^{-1} M is the best. Corrosion got worse over time. In the solution with [Cl^-] = 10 ^ -1 M there are more pits than in the solution with [Cl^-] = 10^{-1} M and pH = 3 but the size of the pits is greater in the latter case. The depth and density of the pits increase with increasing chloride concentration and temperature. The density of the pits increases as the thiosulfate concentration decreases. The depth of the pit increases with increasing thiosulfate concentration.
Scholars came to the following conclusions:
Thiosulfate promotes pitting corrosion if present in low concentrations, while at concentrations above 0.001 M it inhibits this phenomenon. At high concentrations of thiosulfate, these ions compete with chloride ions for adsorption sites on the surface of the passive film, reducing the aggressiveness of the attack. The higher the chloride concentration, the higher the thiosulfate concentration needed to inhibit pitting. At low concentrations of chloride and thiosulfate, the latter is not able to inhibit corrosion, on the contrary, it locally increases the ionic conductivity and promotes the degradation of the passive film. The absence of oxygen adsorbed on the surface of the passive film favours the adsorption of chloride ions and therefore the degradation of the film by pitting. A low pH is necessary for the thiosulfate consumption reaction with the liberation of sulfur to take place. Decreasing the thiosulfate concentration below 0.0001 M allows reduction of its influence on the decrease of the pitting potential. H + ions are also consumed

and the acidification of the solution in the pits is reduced. An increase in temperature leads to the most severe decrease in the pitting potential.

27) In 1970, W. D. France JR. [74] studied the **Effects of Stress and Plastic Deformation on the Corrosion of Steel.** Wire-shaped AISI 1008 steel samples were annealed at 870 ° C for 1-2 hours and cooled in the oven. Torsional deformation was applied by placing the samples on a lathe and twisting them a set number of times. While tensile stresses were applied by hanging a load on the sample. The samples were abraded using 600-grit silicon carbide paper and ultrasonically cleaned. An area of 1 cm^2 was exposed to aggressive 0.6 M ammonium nitrate NH_4NO_3 solutions. Corrosion tests were performed in a multi-neck polarization cell. A saturated calomel electrode (SCE) was used as the reference electrode. Potentiodynamic anodic polarization tests and controlled potential tests (i.e kept constant) were performed. The corrosion rate was measured by weight loss.
This procedure led to the following results and scholars came to the following conclusions:
The corrosion rates for the samples that underwent torsional deformations were higher than those of the simply annealed sample. The corrosion rate increased as the number of twistings that the sample had undergone increased. The open circuit corrosion potentials increased (became more positive) with increasing torsional deformation, but after a certain period the reverse trend occurred, due to the increase in the pH of the solution. In the polarization curves it has been noted that after the current peak linked to the primary passive potential, in the case of the samples that have undergone a torsional deformation, there was a decrease in the current with a second peak in the passive region, which does not occur in the non-deformed samples. The current density of the deformed samples was up to 400 times higher than that of the undeformed samples. Tensile strain samples showed similar but less pronounced behaviour. The passive potential range can increase as deformation increases. By varying the pH of the solution in the range of 1.85-7.9, it was noted that at the extremes of this range the anodic polarization curves of the deformed and non-deformed samples are almost identical. While, in the range of 3-6, the effect of the deformation is evident. The presence of chloride ions in the solution generated an increase in current density after a critical passive potential of about 0.1 V in both annealed and deformed samples. The deformed sample showed current peaks even in the passivity range, and also had a more active critical potential than the annealed sample. It has been noted that deformation further accelerates corrosion in cracks, where it is already favoured.

28) In 2016, Hiroyuki Miyamoto[75] made a review about the **Corrosion of Ultrafine Grained Materials by Severe Plastic Deformation.** The scholar, by gathering information from various scientific papers, came to the following conclusions:

The general corrosion rate increases as the grain size decrease, while the local corrosion rate increases as the grain size increases. Nano-crystalline materials have lower corrosion resistance in the active state but, in the passive state, pitting is suppressed.

The SPD (Severe Plastic Deformation) treatment performed on pure metals (type A) causes the simple refinement of the grains. The greater density of grain boundaries can cause a higher rate of corrosion because grain boundaries are more susceptible to attack by aggressive species, due to their greater energy and the greater presence of defects. However, the greater number of grain boundaries provides greater nucleation sites for the passivating film, the dissolution of the film is therefore inhibited. The adhesion of the oxide film is increased through the anchoring mechanism.

An ultra-fine grain size in a solid solution alloy below the solution limit (Type B) can lead to the surface enrichment of the solute which guarantees greater passivity and resistance to pitting, as in the case of Fe-Cr alloys.

SPD treatment is performed on solid solution alloys beyond the solution limit (Type C) only after annealing and is followed by ageing. In aluminium alloys, it has been observed that the formation of precipitates is much faster in fine-grained systems than in coarse-grained systems at the same temperature. Due to the greater number of grain boundaries and the shorter diffusion distance that the elements have to travel, the solute-depleted zones near the grain boundaries are very small, leading to an increase in corrosion resistance.

In two-phase or multiphase materials (Type D), the SPD treatment causes fragmentation and dispersion of the precipitates, generating finer precipitates. When the second phase is nobler than the matrix, its dispersion can increase the potential for breaking passivity.

UFG (Ultrafine grain) aluminium alloys have a higher corrosion resistance given by a higher breakdown potential of the passive film. For example, in biphasic alloys, the reduction of the size of the precipitates below a critical value avoids the nucleation of the pits. The solute-depleted areas are less marked. Some studies show instead that the increase in the extension of the metal/precipitate interface causes greater nucleation of the pits.

The hydroxides and oxides that form on the surface of magnesium alloys are unstable and time-dependent. The high temperatures at which the SPD has performed cause a dynamic recrystallization that can lead to an uneven microstructure, leading to lower corrosion resistance.

UFG copper has a higher corrosion resistance than coarse-grained pure copper. This is due to the presence of microcells between the grain boundary and the inside of the grain. A finer grain allows for areas for cathode sites of insufficient size for rapid degradation.

UFG mild steels have a stronger passive film, due to the many nucleation sites of the film. These steels have a higher pitting potential in 0.9 $NaOH^+$ Cl^- solutions.

Stainless steels that undergo SPD have a lower passive current and a higher breakdown potential in solutions containing Cl^-. In nano-crystalline stainless steels, the surface is more enriched with Cr due to the presence of more grain boundaries that act as corridors for its diffusion.

Materials treated with the SPD technique have high internal stress caused by the presence of non-equilibrium grain boundaries characterized by a large presence of dislocations and therefore have great energy. The atoms on the surface have a high free energy and a low electron work function. This facilitates the formation of the passivating film. The stresses are relaxed through a heat treatment that does not change the microstructure, passing to a condition of equilibrium. However, this can reduce corrosion resistance.

29) In 2013, S.M. Bruemmer[76] studied **Stress Corrosion Cracking of Cold-Rolled Alloy 690 in Pressurized Water Reactor Primary Water.** The samples examined were components made of alloy 690: a tubing heat treated thermally at 1.122 °C, water quench + 716 °C to 725 °C / 10.5 h, air cool; a bar heat treated thermally at 1.038 ° C for 2 h, air cool; and a plate heat treated thermally at 996 ° C for 0.33 h, air cool. The samples were polished and examined under the SEM scanning electron microscope using backscatter electron imaging (BSE). Samples were prepared by focused ion beam (FIB) milling for observation under the field emission gun transmission electron microscope (TEM). The samples underwent energy-dispersive X-ray spectroscopy (EDS). The composition of the grain boundaries was achieved by the scanning transmission mode (STEM). The tests to detect the Stress Corrosion Cracking phenomenon were performed at 360 ° C in simulated PWR primary water with 1,000 ppm of boron and 2 ppm of lithium, with a quantity of dissolved hydrogen equal to 25 cc/kg. The standard stress intensity (K) used for the tests was 30 MPa√m.

This procedure led to the following results:

The as-received tubing had an equiaxial grain microstructure (100 μm in diameter). A semi-continuous distribution of $M_{23}C_6$ precipitates was present at the grain boundaries, along with titanium nitride particles. TiN larger particles were present in the matrix. The tubing was annealed at 1,100 ° C for 1 hour and then quenched in water. This led to the elimination of the $M_{23}C_6$ precipitates. The plate had a similar microstructure to that of the tubing but featured banded regions with small grains and dense precipitation aligned with the rolling direction. The bar had a high density of transgranular $M_{23}C_6$ precipitates, very rare at the grain boundary. The tubings were cold rolled at reductions of 17% (as-received) and 31% (annealed). the 17% tubing was annealed for 1 hour at 700 ° C. The bar was cold-rolled at a 20% reduction, while the plate was rolled at a 26% reduction. A large number of small voids and cracked precipitates were detected at the grain boundaries. The highest damage was found on the plate. The density of the dislocations and the hardness of the material increase as the degree of reduction increases. The annealed tubing and the bar which had few carbides at the grain boundary suffered the least serious damage (few cracked precipitates) even if they had a high density of dislocations and a high hardness.

Thermally treated tubing has a crack growth rate up to 20 times greater than solution-annealed tubing. The crack growth rate for cold-rolled (31%) and then annealed tubing at 700 ° C for 1 hour was 25 times lower than the thermally-treated and cold-rolled as-received material (31%). Materials 31% showed a high mean misorientation around the grain boundaries. Local strains increased as the grain boundaries were approached. The recovery annealing led to a lowering of the average misorientation. The preferred path of the SCCs was the grain boundaries even when there were voids or cracked precipitates. The cracks appear to be blunt and limited when encountering a cracked carbide. A phenomenon that occurred mostly on the plate. The cracks generated by lamination are perpendicular to the direction of intergranular growth and therefore can hinder the propagation of SCC. At TEM, Ni/Fe-rich spinel loose crystallites were detected in open cracks; fine polycrystalline spinel Ni / Cr / Fe and/or oxide of MO structure (not rich in Cr) on the crack walls; penetrative oxidation filaments (Cr_2O_3 and Cr-rich MO) in the Alloy 690 matrix on the crack walls. The area of the tip of the crack had a high density of dislocations. The cracks often ended with a grain-bound carbide.

Scholars came to the following conclusions:

The damage generated by cold rolling does not seem to favour the growth of SCC, indeed in some cases, it seems to hinder it. SCCs propagate along grain boundaries that have migrated as a result of heat treatments and avoid cracked precipitates. Cracks end with cracked carbides. It is the localized stresses generated by cold working that favour the growth of intergranular SCCs. The regions depleted of Cr were not oxidized preferentially, rather the walls of the crack were. Hence the growth of the SCC is not promoted by an oxidative mechanism. The formation/growth of sliding cavities does not occur in front of the crack.

30) In 2014, Koji Arioka[77] studied **Intergranular Stress Corrosion Cracking Growth Behaviour of Ni-Cr-Fe Alloys in Pressurized Water Reactor Primary Water.** A plate of Alloy 800 was produced and then heat treated at 980 ° C for 1 hour in air and water-cooled. Other samples were produced with increasing nickel concentration (16, 20, 25, 32, 40, 50 and 60% of Ni). The plates were heat treated at about 1,030 ° C for 1 hour with air and water cooled. Samples were reduced by 20% by cold rolling them. The samples were pre-cracked and subjected to constant load tests in simulated primary water, which contained boric acid (H_3BO_3, 500ppm as B), lithium hydroxide (LiOH, 2ppm as Li) and dissolved hydrogen (30 cc STP H_2 / kg H_2O) in the temperature range between 290 ° C and 360 ° C. The samples were subjected to tests between 721 hours and 6,903 hours. The initial K values of the test were approximately 30 MPa m ^ 1/2. The surface and cross-section of the samples were examined by SEM and the growth rate of the stress corrosion crack (SCC) was calculated using the equation: IGSCC growth rate (mm/s) = IGSCC maximum depth (mm) / Exposure time (s). The samples were prepared by sputtering gallium ions in a focused ion beam (FIB) apparatus and were subjected to AES (Auger electron spectroscopy) measurements to determine the composition near the intergranular attack zone.

This procedure led to the following results:

On alloy 800 the presence of SCC was detected only after 6,903 hours of exposure at 320 °C. The crack growth rate increases as the temperature decreases, which is the opposite behaviour of the other materials. Deep intergranular cracks were observed on Ni-16% Cr-Fe alloys with a nickel concentration above 60% Ni and on alloys with a nickel concentration below 20% Ni. At the other concentrations, no cracks were detected at 360 °C. The crack growth rate decreased with increasing nickel concentration in the range of 10% -32%, while the growth rate increased with increasing nickel concentration in the 40% -75% range. Deep cracks were observed on all materials at 290 °C. At 290 ° C and 320 °C, there is no clear dependence of the growth rate on the nickel concentration. Growth rate peaks of IGSCC were observed in the temperature range between 320 °C and 340 °C in 60% Ni and 50% Ni alloys. Growth rate peaks of IGSCC were observed around 320 °C on 40% Ni-16% Cr-Fe and 32% Ni-16% Cr-Fe alloys. On the alloys 25% Ni-16% Cr-Fe, 20% Ni-16% Cr-Fe and 16% Ni-16% Cr-Fe, no growth peaks were detected in the test temperature range.

Scholars came to the following conclusions:

Alloy 800 20% CW (cold worked) has the greatest resistance to SCC compared to 316 stainless steel, alloy 600 and alloy 690 in the same conditions and at the same reduction percentage (20%). Alloy 800 could have a maximum crack growth rate at 360 °C when comparing its behaviour with that of other materials. Only alloy 600 (mill-annealed) exhibits a linear growth rate versus temperature trend. The addition of chromium has a beneficial effect only at a certain temperature which differs according to the type of alloy. The solubility of chromium oxide present in the intergranular attacked area increases with increasing temperature and this seems to be linked to the effectiveness of adding chromium to the alloy. As the concentration of nickel increases, the temperature, at which the peak of the growth rate of the crack appears, increases.

31) In 2021, Yanbing Tang et al.[78] studied the **Corrosion Behaviour of a Selective Laser Melted Inconel 718 Alloy in a 3.5 wt.% NaCl Solution.** The materials used for the tests were made of Alloy Inconel 718. A sample was produced with the selective laser melting (SLM) additive manufacturing technique with a power of 138 W, a scanning speed of 429 mm/s and a thickness of the 0.04 mm material plate, while the other sample was produced via commercial rolling. The samples were cylindrical in shape, embedded in resin leaving an exposed surface of 0.785 cm^2, polished with SiC papers up to 1000 grit, and carefully cleaned with ethanol. The electrochemical tests were carried out in a 3.5% by weight NaCl solution at 25 ° C. Potentiostatic polarization tests were performed at a scan rate of 0.1667 mV/s from 250 mV_{SCE} to 1100 mV_{SCE}, while potentiostatic polarization tests were performed at 0.4 V_{SCE} for 1 hour. Electrochemical Impedance Spectroscopy (EIS) measurements were performed. Mott-Schottky tests were performed at an alternating current (AC) amplitude of 10 mV within an applied potential range of 600 mV_{SCE} to 1200 mV_{SCE} in a subsequent 20 mV step after the potentiostatic test. The phases present

on the surface of the materials were examined using X-ray diffraction (XRD). The samples were examined using X-ray photoelectron spectroscopy (XPS). After being corroded for 24 hours, the samples were examined by atomic force microscopy (AFM).

This procedure led to the following results and scholars came to the following conclusions:

The open circuit tests showed that the potential grew over time until it reached its steady state, this indicates the spontaneous generation of the passive film. The steady-state potentials of the two materials were -0.19 V_{SCE} and -0.13 V_{SCE} (SLM and Rolled respectively). The SLM sample had a higher passive current density, correlated with a higher dissolution rate. The corrosion resistance of the SLM sample was lower than the R (rolled) sample. The passive film impedance on the SLM was lower than that on the R, indicating that the SLM had lower corrosion resistance. The electrical resistance of the passive layer of the R sample was much higher than that of the SLM 718, indicating that the passive film of the SLM sample had a lower protective capacity. Through the potentiostatic test it was noted that the current densities have a drastic drop and stabilize at $1.21 \pm 0.09 * 10^{-7}$ and $1.04 \pm 0.08 * 10^{-7}$ A/cm^2 for the SLM sample and the R sample respectively. From the higher current density of the SLM sample, it can be deduced that the passive film is more easily corrodible. The slopes (k) of the curves (in logarithmic scale) for SLM and R were 0.88 and 0.91, respectively. A k closer to 1 indicates a more compact passive film. From the Mott-Schottky graphs (reciprocal of the squared space charge capacitance v.s potential) it can be seen that the passive films acted as a p-type semiconductor (negative slope) at a potential less than 0.1 VSCE due to the presence of Cr_2O_3 and NiO. However, they showed typical n-type semiconductor behaviour (positive slope) at a potential greater than 0.1 V_{SCE} due to the presence of Fe_2O_3. The SLM sample had higher values of donors and acceptors than R, indicating greater defectiveness of the passive film. The passive films on the two samples were composed of Cr_2O_3, Fe_2O_3, NiO, MoO_3, Nb_2O_5 and NbO. The passive film formed on SLM contained more NiO, which made it more porous and therefore less resistant. The corrosion surface on the SLM sample was wavy and more rugged, due to the presence of traces of melting.

32) In 2020, Shuwei Guo et al.[79] made a review of the **Corrosion Characteristics of Typical Ni−Cr Alloys and Ni−Cr−Mo Alloys in Supercritical Water.** Scholars, by gathering information from various scientific papers, came to the following conclusions:

Ni-Cr alloys show an increase in weight during the first corrosion phase, but if they are exposed for a long time to an aggressive environment like SCW (supercritical water) they show a decrease in weight. Only Inconel 690 alloy exhibits weight decrease which progresses with exposure time in SCW at 600 °C, 25 MPa and 8 ppm oxygen content. Increasing the temperature increases the corrosion rate of the material. The lower the Cr content in the alloy, the lower the oxygen content necessary to have the maximum weight increase. The passive film that is generated on the surface of the Ni-Cr alloys in SCW consists of a compact inner layer of Cr_2O_3 and $NiCr_2O_4$, and a porous outer layer of NiFe2O4, NiO and

$Ni(OH)_2$. If organic sulphides are present, NiS deposition occurs on the outer layer. Severe surface plastic deformation due to mechanical processing can lead to the formation of a thinner chromium oxide layer. On Inconel 690 in the hydrogenated SCW at 600 °C, 25 MPa for 335 h it is noted that the outer layer tends to exfoliate, after 1740 h the outer layer has disappeared. The presence of intergranular carbides reduces the resistance to stress corrosion cracking in CW Inconel 690. The edges of the grains are corridors for the diffusion of oxygen within the metal, therefore microstructural optimization is important to increase the corrosion resistance of the material.

Ni-Cr-Mo alloys have improved resistance to pitting corrosion, crevice corrosion and corrosion to non-oxidizing acids. The higher the Mo content the higher the resistance. Incoloy X-750 is the least resistant alloy due to the lack of Mo and the low Cr content. The two most commonly used $Ni - Cr - Mo$ alloys are Hastelloy C-276 (high Mo content) and Inconel 625 (medium Mo content). The weight increase due to corrosion in SCW follows a parabolic trend, first increases (due to the formation of the oxide) and after a long period it decreases (due to the exfoliation of the oxide). The increase in temperature and pressure causes an increase in the corrosion rate and an increase in the thickness of the oxide layer which tends to exfoliate more easily. The higher the oxygen content, the greater the increase in weight. Hastelloy C-276 in SCW at 600 °C and 25 MPa for 1000 h features a passive film with a double-layer structure. The inner layer is made up of Cr2O3 / NiCr2O4 while the outer layer is made up of NiO. In the SCWG (Supercritical water gasification) environment at 500 °C and 25 Mpa, a small amount of MoO_3 is also present in the inner layer, and the Ni oxide and hydroxide disappear on the outer layer, due to the higher concentration of hydrogen in the solution. As the temperature increases, the crystalline dimension of the surface oxides also increases. External oxides are the most unstable and do not make a great contribution to corrosion resistance.

33) In 2019, Parag M. Ahmedabadi et al.[80] studied the **Effect of Plastic Deformation on Passivation Characteristics of Type 304 Stainless Steel.** The material examined was austenitic 304 stainless steel. Sheets were used that have undergone different degrees of reduction (20% -40% -60%) by cold rolling, and therefore have a different degree of plastic deformation. The material was mill-annealed (MA). A sample was annealed (SA) at 1035 °C for 0.5 hours. The samples were ground with SiC paper up to 1200 grit and then polished with diamond paste up to 0.5 μm. The samples were electro-polished in a 10% solution of perchloric acid at a potential of 30 V. The electro-etched samples were observed under an optical microscope. A hardness test was performed on each sample using 500 gf with a residence time of 15 s. The stain-induced martensite content was estimated using a ferritoscope. XRD analysis was performed to determine the phases present. The electrochemical tests used were the potentiodynamic polarization and the double loop potentiokinetic electrochemical reactivation (EPR) (DL-EPR) in solutions with different concentrations of H_2SO_4 and KSCN. The solutions used are the following: 1.0 M H_2SO_4 + 0.01 M KSCN (S1); 0.5 M H_2SO_4 + 0.01 M KSCN (S2); 0.25 M H_2SO_4 + 0.01 M KSCN

(S3); 0.5 M H_2SO_4 + 0.005 M KSCN (S4) and 0.1 M H_2SO_4 + 0.001 M KSCN (S5). The system used consisted of three electrodes, the reference electrode was the saturated calomel electrode (SCE) and the counter-electrode was a platinum disk. The potentiodynamic test was performed at a rate of 2 mV/s from open circuit potential (OCP) to 1.2 V_{SCE}. The EPR was performed by scanning the potential from OCP to 0.3 VSCE and back to OCP with a scan rate of 2 mV/s.

This procedure led to the following results:

Under the optical microscope, linear structures were noted within the grains of the MA0% sample matrix, which turned into intersected structures and non-linear structures in the MA20% sample and the MA60% sample. The hardness of the sample and the martensite content increased as the degree of reduction that the material underwent increased. The XRD peaks corresponding to martensite increased in intensity with increasing plastic deformation. The passive current density increased with increasing plastic deformation. The current density reached a minimum at the Flade potential and then gradually increased and then peaked. For the MA60% sample, the current increased steadily after the Flade potential. The critical current density was the highest in the S1 solution for all samples. In this solution, the critical current increased with increasing plastic deformation. The corrosive attack on the MA0 and MA20 samples appeared with a linear shape, while on the more deformed samples the attack was more generalized, and pits were detected on the MA60 sample in S2. The DL-EPR values were calculated by dividing the reactivation cycle current by the activation cycle current and multiplying the result by one hundred. The DL-EPR values of MA60 were the highest, and in general, the values increased with the increase in plastic deformation. The peak reactivation was observed around the potential 0.27 V_{SCE}. The current density decreased after reaching the peak potential of +0.3 V_{SCE}. The current density of the MA60 sample followed the same trend during both scans.

Scholars came to the following conclusions:

The linear structures visible on the sample surface are given by the deformation regions characterized by the presence of the dislocations on the {111} plane. An increase in plastic deformation leads to a cross-sliding of the dislocations. More intense peaks of martensite indicate a greater quantity, and larger peaks of austenite indicate a greater density of dislocations. This causes an increase in the hardness of the deformed material. In potentiodynamic tests, the plastic deformation is not related to the degree of uniform corrosion. The critical current density decreased as the concentration of the solution decreased because the electrical resistance of the solution increased. For the MA60 sample, the reduction of the passive current density decreased with the reduction of the solution concentration, this implies that the oxide film did not offer good resistance to ion migration. The DL-EPR values are well correlated to the plastic deformation, an increase in the values means that there is greater corrosion, and this happens with an increase in the plastic deformation. The attacks occur in the weakest regions of the film, that is, in tension regions within the matrix. The greater the deformation, the wider these regions are. The greater the deformation, the greater the number of defects in the film and the less resistant it is to dissolution.

34) In 2020, Lin Liu et al.[81] made a review about **Nickel-Based Superalloys.** Scholars, by gathering information from various scientific papers, came to the following conclusions:

Nickel-based superalloys must contain at least 50% by weight of Nickel. The γ matrix has an FCC structure. The reinforcement phase γ' is an intermetallic phase consistent with the matrix based on Ni3 (Al, Ti, Ta) and has an FCC L12 structure. The γ" strengthening phase consists of Ni_3Nb with a body-centred tetragonal structure (BCT) D022. This phase precipitates in the form of discs. Carbon is present in small quantities (up to 0.2%) but allows the formation of carbides which, after heat treatment, decompose into $M_{23}C_6$ and M_6C at the grain boundary. There may be other phases called topologically close together (TCP) such as μ, σ, P and Laves.

Nickel-based alloys can be made more resistant by solid solution hardening. Certain elements such as chromium, tungsten, cobalt, molybdenum, rhenium, and ruthenium cause the distortion of the matrix lattice and inhibit the movement of dislocations and inhibit dislocation cross-slip. The greater the atomic radius of the added metal, the greater the hardening effect.

The γ 'and γ" phases allow obtaining a considerable mechanical resistance at high temperatures thanks to their precipitation. The precipitate has a reinforcing effect given by the lattice mismatch. The presence of the ordered precipitates causes the increase of the energy necessary for the dislocation to cut the precipitate since this would cause disorders in the reticular structure. The dislocation bypass mechanism implies that a dislocation surrounds the precipitate and generates equidistant rings that interfere with the motion of the other dislocations. The greater the volumetric fraction of the γ' phase, the greater the reinforcement effect, without exceeding 75% after which there is a decline in performance. A correct particle size leads the dislocations to have to cut the precipitates, implying a greater sliding force.

The presence of precipitates at the grain boundaries hinders the grain sliding and therefore strengthens the material. Compounds $M_{23}C_6$ and M_6C have this effect.

The vacuum induction melting technique allows the reduction of the concentration of nitrogen and oxygen in the alloy and therefore prevents the oxidation of the more reactive elements. The vacuum also allows the extraction of low-melting contaminants. Vacuum arc remelting (VAR) and electromagnetic remelting (ESR) enhance these beneficial effects on the alloy.

Powder metallurgy applied to Nickel-based superalloys consists in reducing the alloy to a spherical powder and then producing the piece or ingot by hot isostatic pressing. This technique allows for a more homogeneous composition, finer grain sizes and reduced segregations. However, there is the possibility that the boundaries between the particles remain evident, showing a network of carbides in the microstructure.

Investment casting consists in producing a ceramic mould from a previous wax draft of the piece, finally, the molten metal is poured into the mould. This technique allows the production of pieces with directionally solidified structures or single crystal pieces.

Directional growth is possible by creating a strong thermal gradient along the growth direction. In the Bridman process, the bottom of the mould is cooled, and the heating element is gradually removed along the desired direction of growth. On the other hand, in the LMC (liquid metal cooling) process the cooling takes place in a low melting point liquid metal bath.

To obtain a single crystal mould there is a spiral shrinkage that selects only one grain, which will grow into the molten metal present beyond the sorter.

The heat treatment of superalloys allows the obtaining of the desired microstructure, in particular in precipitation-hardened superalloys, it is divided into solution heat treatment and ageing heat treatment. it is possible to perform a solution treatment at a higher temperature than the solvus temperature of the γ 'phase to obtain a coarser microstructure and eliminate the primary γ' phase. Instead, thermal treatment at temperatures lower than that of solvus of γ' implies a finer microstructure.

The as-cast alloys show a severe segregation phenomenon between the dendrite core and the interdendritic region. To solve this problem a solution heat treatment (solubilization of the precipitates) is used. Subsequently, the ageing treatment is carried out to re-precipitate the γ’ phase in the desired way. Ageing is performed at a temperature lower than that of solvus (close to 750 ° C) to precipitate the γ 'phase as fine and uniform precipitates in the matrix.

Additive manufacturing makes it possible to obtain parts with complex shapes that are difficult to obtain with traditional methods. This manufacturing method consists of constructing three-dimensional (3D) parts by progressively adding thin layers of materials following a digital model. In the selective laser melting (SLM) or selective electron beam melting (SEBM) method, a powder bed is used as a substrate that will be melted by the laser or electron beam and trace after trace will build the piece. The high cooling rate allows the obtaining of a very fine microstructure.

Thermal barrier coatings allow superalloys to withstand temperatures above their incipient melting temperature. The coating consists of an outer ceramic layer and a metal bond layer and an oxide layer. The bond coating allows the ceramic layer to adhere to the metal substrate and hinders the oxidation of the alloy. The ceramic layer acts as a thermal barrier and commonly consists of yttria-stabilized zirconia. Nickel-based superalloys combine high strength, oxidation, and corrosion resistance during service at elevated temperatures.

35) In 2017, Helmuth Sarmiento Klapper et al.[82] studied **Critical Factors Affecting the Pitting Corrosion Resistance of Additively Manufactured Nickel Alloy in Chloride Containing Environments.** L-shaped samples were cut from a 718 Nickel-based alloy bar which was annealed and aged. L-shaped samples were produced using selective laser manufacturing (SLM) technology with a laser power of 400 W. The samples were constructed with different orientations (0 °; 45 °; 90 °) relative to the carrier plate. The samples were polished with SiC paper up to 600 grit. Electrochemical tests of cyclic potentiodynamic polarization and open-circuit potential (OCP) were performed. The samples had

an exposed surface of 845 mm^2. The tests were performed with a three-electrode system, the reference electrode was an Ag / AgCl electrode saturated with KCl, and the counter electrode was a Ti electrode covered by TiO_2. There were two test solutions: a 13% by weight deaerated NaCl solution of almost neutral pH at 80 ° C and a 21% aerated NaCl solution with a pH of 2.3 adjusted by additions of 0.1 N HCl at 90 °C. The polarization scan started at -100 mV from the OCP and was then increased in the anodic direction to 0.2 mV/s. After reaching a current density of 0.1 mA/cm^2 (at which the pitting potential was measured), the polarization switched to the cathodic direction to evaluate the repassivation behaviour of the material. The repassivation potential was defined as the potential needed to reduce the current density below 0.1 mA/cm^2.

This procedure led to the following results and scholars came to the following conclusions:

For the bulk sample in the deaerated solution, an average pitting corrosion potential (Epit) of 416 ± 10 mV_{SHE} was measured, higher than the OCP after one hour (68 ± 42 mV_{SHE}), and a repassivation potential (E_{rp}) of 260 ± 4 mV_{SHE}, lower than the E_{pit}. This implies a good resistance to starting the pits and a good repassivation ability. The SLM samples had a passive region of 200 mV followed by the breakdown potential at values above 400 mV_{SHE} and repassivation potentials around 250 mV_{SHE}. The samples showed a metastable pitting region starting at a potential of 250 mV_{SHE}. Repassivation occurred immediately below 0.1 mA/cm_2. The results of the SLM samples were in agreement with those of the bulk samples, indicating a repassivation ability not affected by defects caused by the SLM manufacturing method. Some SLM samples showed a lower pitting potential, while others showed a rapid increase in current density during anodic polarization. This behaviour is probably due to the presence of surface defects and localized corrosion points. The print orientation did not affect the results. During the OCP tests, electrochemical activity was noted on the samples that had shown a rapid increase in current density. This behaviour is probably due to the activation and repassivation of surface defects. A sudden drop in OCP at electrochemical potentials close to 150 mV_{SHE} observed on samples with surface defects was noted in the aerated solution, confirming their role as preferred sites for localized corrosion.

36) In 1983, M. C. Chaturvedi et al.[83] studied **Strengthening mechanisms in Inconel 718 superalloy.** The samples were obtained from a 5 mm thick sheet of Inconel 718. The sheet was cold rolled and annealed at 1473 K. Tensile test specimens and thin films for thin film analysis under an electron microscope were made. The initial speed in the tensile tests was 4.16 x 10^{-4} s^{-1}. The samples were solution annealed for 1 hour at 1473 K and quenched in ice water, then they were aged for different periods at 973, 998 and 1023 K. The thin films were prepared by electro-polishing using a bath of 85% methanol and 15% perchloric acid at 223-233 K. The samples were deformed by 3-5% before being observed under the electron microscope.

This procedure led to the following results:

The presence of the y" phase was observed in the form of disc-shaped precipitates coherent with the {100} planes of the matrix. The y 'phase was present as spherical precipitates. With increasing ageing time, it was observed the increase in the volumetric fraction of the precipitates which reach a constant value over time. The lower the temperature, the longer the time needed to reach the maximum volumetric fraction. The volumetric ratio between the y "and y' phases was equal to 3. As the ageing temperature increases, the maximum yield strength and the time required to reach it decrease. By testing the specimens at different temperatures (77, 183 and 293 K) it was noted that the component of the yield point due to hardening by precipitation decreases by decreasing the test temperature. A high level of coherence strain around the precipitate particles was observed which masked the dislocation contrast. This effect is less pronounced as the ageing time decreases. The dislocations were observed to move in pairs. When an ordered particle is sheared by a glide dislocation, an antiphase boundary is created within the particle. This causes a second dislocation to be pulled forward removing the disorder within the particle. This explains the pairs of dislocations, and thus the deformation of the aged samples occurs by cutting the ordered precipitated particle by glide dislocations.

Scholars came to the following conclusions:

During the ageing process, the γ" phase is the main one. The deformation occurs due to the motion of pairs of glide dislocations which shear the ordered precipitate particles. The strengthening given by the presence of the γ" and γ'phases is due to the strengthening mechanism of the order or coherence. The contributions of the two mechanisms to the resolved critical shear stress (CRSS) $\Delta\tau$ are compared to each other, to determine the dominant mechanism. The observed values of $\Delta\tau$ were plotted against the theoretical values due to the strengthening of the order for both phases. If the order strengthening mechanism were dominant, the graph would be a straight line with a slope of 1.0 and would have to pass through the origin. The slope of the best line was found to be 1.290 and the y-intercept value was 19.15 MN m^{-2}. The total theoretical values of the CRSS due to the coherence strengthening mechanism were obtained with the mean square law method, they were plotted against the observed values. If the coherence-strengthening mechanism were dominant the graph would be a straight line with a slope of 1.0 and would have to pass through the origin. The slope of the best line was found to be 1.005 and the y-intercept value was 1.79 MN m^{-2}. These values indicate a good agreement between the theoretical and observed values so the dominant mechanism of strengthening is that of the coherence deformation. It has been observed that the theoretical values of the CRSS predicted by a combination of order strengthening by y 'and coherence strengthening by y "are also in excellent agreement with the observed values. Therefore, both possibilities are likely.

37) In 2013, Xingying Tang et al.[84] studied the **Corrosion Behaviour of Ni-Based Alloys in Supercritical Water Containing High Concentrations of Salt and Oxygen.** Incoloy 800, Incoloy 825, Inconel 625, and Hastelloy C-276 were the four nickel-based alloys tested. The test solutions to which

the alloys were subjected consisted of wastewater from pesticide production and contained Cl^-, Br^-, SO_4 $^{2-}$, Na^+ and K^+ ions. The oxidizing agent used was hydrogen peroxide. Coupons of the various alloys were produced, polished to a finish of 1600 and carefully cleaned with acetone. The coupons were placed in autoclave reactors made of Hastelloy C-276 alloy. The supercritical water oxidation test was performed up to a temperature of 550 °C and a pressure of 32 Mpa, the exposure time was 60 hours. The results were obtained both in subcritical conditions (350 °C and 25 MPa) without oxygen and in supercritical conditions (450 °C and 25 MPa) with oxygen. The values of COD, ammonium, and Cl- were monitored with a multiparameter water analyzer. The pH and conductivity of the liquid were measured. A gravimetric method was employed to determine the amount of salt. Post-corrosion coupons were examined under a scanning electron microscope (SEM). The composition of the surface film was obtained by energy diffraction spectroscopy, X-ray photoelectric spectrometry, and X-ray diffraction technique.

This procedure led to the following results and scholars came to the following conclusions:

Under supercritical water conditions and in contact with the most concentrated solution of salt and oxygen, the most severe general and pitting corrosion was observed on all alloys. With little oxygen dissolved in the solution, a homogeneous oxide film was formed on all alloys. The oxide film on Incoloy 825 alloy has undergone spallation under all conditions. The alloys exhibited excellent corrosion resistance in the presence of high dissolved oxygen and low Cl- (excluding Incoloy 800 alloy). Incoloy 825 showed the lowest corrosion resistance, and it was noted that the combined effect of oxygen and chlorine led to the most severe attack on all alloys. On Incoloy 825 the growth of platelet-shaped oxide crystals was observed under conditions of oxidizing supercritical water. Corrosion in supercritical water was less severe due to the lower solubility of the corrosion products under these conditions. Corrosion products have deposited on the surface of the metal, protecting it. The combined presence of oxidant and Cl- leads to greater corrosion due to the weakening of the oxide layer by the Cl- ions and this allows oxygen to penetrate deeper. Hastelloy C-276 exhibited de-alloying corrosion and stress corrosion cracking in the presence of chloride and supercritical water. Under subcritical water conditions, Incoloy 800 exhibited the most severe pitting corrosion in the presence of high chloride and low oxygen. Incoloy 800 alloy is the least resistant due to the lack of molybdenum. Due to the large decrease in the ion product constant, corrosion by aggressive ions will be more severe under subcritical conditions. On the other hand, at high temperatures and in supercritical conditions the alloys are more prone to de-alloying corrosion.

From the chemical analysis, it was observed that Nickel is the element that was most dissolved in solution, therefore, its products were easily soluble in supercritical conditions. The metal surface was contaminated with carbon due to the decomposition of organic substances present in the wastewater. Iron was dissolved less than nickel in the presence of oxygen, indicating that a stable and insoluble iron oxide was produced. The high presence of oxygen on the metal surface indicates the presence of a stable oxide layer. The oxide layer consisted of Cr_2O_3, $NiCr_2O_4$ and NiO in the presence of oxygen alone. Fe_3O4, $Ni(OH)_2$ and MoO_2 were found in Incoloy 825, Inconel 625 and Hastelloy C-276 respectively. All XRD peaks (except MoO_2) were less intense under conditions of a solution rich in oxygen and chloride. Hastelloy C-276 has an oxide film consisting of an outer layer of NiO and a mixed inner layer of Cr_2O_3 / $NiCr_2O_4$. The solubility of chromium oxide is lower than that of iron and nickel oxides. Inconel 625 showed the highest corrosion resistance in the presence of oxygen and chloride ions in supercritical water. Hastelloy C-276 showed the best corrosion resistance in the presence of little oxygen but a lot of chloride. Incoloy 825 had the lowest corrosion resistance under all conditions, due to its low molybdenum content. The most aggressive conditions were those of the experiment with a high concentration of oxygen and CL-.

38) In 2018, Le Zhou et al.[85] studied **Microstructure, precipitates and mechanical properties of powder bed fused Inconel 718 before and after heat treatment.** A rectangular block made of Inconel 718 alloy was produced using the SLM (selective laser manufacturing) additive manufacturing technique. The block was cut into several slices using a diamond saw. One sample was kept in as-built condition. Two samples were subjected to solution heat treatment (SHT) at 980 °C below the solvus temperature of phase δ followed by water quenching, and one of these two samples was aged in two phases, which consisted of annealing at 720 °C for 8 hours, cooling of the oven at 620 °C and maintenance for 8 hours at 620 °C, followed by air cooling. Two other samples were solution thermally treated at 1065 °C above the temperature of the δ phase solvus and quenched in water. One of these two samples was aged in two stages, which consisted of annealing at 720 °C for 8 hours, cooling the oven to 620 °C and holding for 8 hours at 620 °C, followed by air cooling. One sample directly underwent the ageing treatment. The cross-section of the samples was examined through X-ray diffraction (XRD). The samples were mounted in epoxy resin, polished up to 0.25 μm and etched in a solution of HCl, acetic acid and HNO3 with a volume ratio of 3:2:1. The samples were examined using an optical microscope and a field emission scanning electron microscope (FE-SEM) equipped with an X-ray energy dispersive spectroscope (XEDS). The grain structure was examined using electron scattering diffraction (EBSD, EDAX). After obtaining thin films from the sample, a transmission electron microscope (TEM) was used for the analysis of the precipitates. The samples were subjected to hardness tests using a Vickers hardness tester with a load of 10 kgf and a residence time of 10 s.

This procedure led to the following results:

X-ray diffraction, performed on the cross-section perpendicular to the construction direction, detected an intense peak (200) relative to the γ matrix due to growth along the construction direction. The XRD model of the samples that have undergone annealing at 980 °C shows a peak (111) of comparable intensity to that (200) probably caused by the recrystallization of the grains. Small peaks were detected between the two main ones, indicators of the presence of the δ phase. Samples annealed at 1065 ° C show a peak (111) more intense than the peak (200) indicating recrystallization. The XY cross-section of the as-built sample showed columnar patterns while the XZ cross-section showed fish scale patterns. Cellular and columnar dendritic microstructures were detected in both sections. The thickness of these structures was very small (<1μm). The dendrites spanned multiple melt pools and thus exhibited epitaxial growth on already solidified grains. The segregation of heavy elements in the interdendritic region was evident. The grains exhibited an irregular elongated shape and could extend across multiple melt pools. The Laves phase was detected along the cell boundary. The presence of carbides was detected in the interdendritic region. Solution heat treatment at 980 °C eliminated as-build patterns on the cross-section. Plaque-shaped δ-Ni3Nb precipitates are visible inside and at the grain boundaries. The grains were still elongated. The cell structure has become enlarged. Needle-shaped precipitates identifiable as γ"-phase were also detected. The heat treatment at 1065 °C led to the elimination of segregation and the disappearance of the melt pools. Annealing Twins were observed inside the grains and cubic precipitates (Nb, Ti)C along the grain boundaries. The precipitates of γ' had a cuboidal shape with an ordered crystal structure L12 and a general formula of $Ni_3(Al, Ti)$, while the precipitates of γ" had an elliptical shape and a body-centred-tetragonal DO22 structure with a general formula of $Ni_3(Nb, Ti)$. Phase γ" was observed at grain boundaries in directly aged samples. In the annealed and then aged samples, the γ" phase was homogeneously distributed. The solution thermal treatment led to a decrease in Young's modulus, which, after ageing, increased again due to the presence of γ" and γ' precipitates. From 208 GPa of the as-built sample, Young's modulus increased to 226 GPa after ageing. Hardness followed the same trend.

Scholars came to the following conclusions:

The arm spacing of the dendrite in the as-built IN718 was in the range of 0.5-1.5 μm which corresponds to a cooling rate of $4*10^4$ and $4*10^6$ K/s respectively. The thermal gradient would therefore have an approximate magnitude of 104-106 K/m. These high values ensure a fine columnar microstructure. Despite the high speed of solidification, the Laves phase was still present. The direct ageing heat treatment was unable to dissolve the carbides and the Laves phase due to the low temperatures. The treatment at 980 °C allowed the dissolution of the Laves phase and formed the δ phase. At 1065 °C both the Laves phase and the δ phase dissolved. Phase γ" was observed at grain boundaries in directly aged samples. In the annealed and then aged samples, the γ" phase was homogeneously distributed. The annealing treatment leads to the reduction of the dislocation density and the reduction of the residual stress which therefore leads to a lower hardness of the material. The formation of γ" precipitates after ageing leads to an increase in the hardness of the material. The sample annealed at 1065 ° C and aged has the maximum hardness because it has the greatest amount of γ" phase with a more homogeneous distribution. This is due to the solubilization of the Laves and δ phases, freeing Nb, which, following ageing, allows the reprecipitation of the intermetallic compounds in the form of a reinforcement phase.

39) In 2017, Helmuth Sarmiento Klapper et al.[86] made a review of the **Localized Corrosion Characteristics of Nickel Alloys.** Scholars, by gathering information from various scientific papers, came to the following conclusions:

In nickel-based alloys, this element must be present at least 50% by weight. Another important element is chromium which allows the formation of a superficial oxide film that protects the alloy from the attack of the aggressive environment. Elements that increase the corrosion resistance of the alloy are molybdenum and tungsten, especially the resistance to acids and chlorides. Ni-based alloys are very resistant to stress corrosion cracking (SCC).

Localized corrosion occurs by breaking the passive oxide film. Pitting corrosion generates pits, while crevice corrosion generates cracks on the surface of the alloy. Pitting Resistance Equivalent (PRE) is a parameter used to compare the localized corrosion resistance of various Ni-based alloys. Cr contributes to the formation of the oxide film (passivation), while Mo and W contribute to the repassivation of the alloy after the formation of the pits. A higher Mo content leads to a faster repassivation and therefore greater resistance to localized corrosion (a higher PRE). The low copper content in the UNS N06200 alloy resulted in a delay in the initiation of the crevice. Critical pitting and crevice temperatures are other parameters for comparing the localized corrosion resistance of Ni-based alloys. They represent the minimum temperature for localized corrosion to occur and are different for each alloy. From these values in various test environments, it can be seen that the critical crevice temperature is always lower than the pitting one, therefore it is the most critical case of corrosion. A higher delta phase content leads to higher localized corrosion.

40) In 2008, K.V.U. Praveen et al.[87] studied **Work-Hardening Behaviour of the Ni-Fe Based Superalloy IN718.** The as-received material was IN718 bars (Ni-Fe based alloy) heat treated at 980 ° C for 1.5 hours and cooled in air. The samples were subjected to various heat treatments. One sample underwent solution treatment (ST); one sample underwent peak ageing (PA); one sample was overaged (OA), and one sample was extra overaged (OA100). Disc-shaped thin films of 3 mm in diameter were prepared from polished coupons up to 0.025 mm. The discs were electro-polished in a 10 pct perchloric acid electrolyte in glacial acetic acid at a potential of 25 V. The films were examined by transmission electron microscope (TEM). Tensile test specimens were produced, and the tests were performed at a constant strain rate of $5*10^{-4}$ s^{-1}. Some samples have also undergone cold rolling and have been re-examined.

This procedure led to the following results:

The microstructure of the sample solution-treated does not show precipitates in the matrix. The peak-aged sample shows precipitates γ '' and γ’ uniformly distributed. The γ ''precipitates are disc-shaped and the γ’ precipitates are round-shaped. The OA sample shows a uniform distribution of γ” precipitates in the γ matrix. The OA100 sample has long δ-phase particles along the grain boundaries. The extent of the work hardening follows this trend: ST> OA100> OA> PA. PA material shows the best combination of strength and ductility. The three phases of work hardening are: (1) the initial portion of the transitory stage, in which $\theta = \delta\sigma / \delta\varepsilon$ decreases rapidly; (2) a stage where θ gradually increases with ε to a maximum; and (3) a stage where θ decreases due to the initiation of dynamic recovery. TEM examining the samples after undergoing one-third and two-thirds of the total elongation it was noted that the ST sample showed distinct slip bands, parallel to each other. At 1/3 the deformation was limited to just two sets of slip systems. At 2/3 the slip is entirely concentrated in two series of separate slip systems that intersect with each other. The PA 2/3 material shows the formation of persistent slip bands (PSB) and the shearing of precipitates. Also, in the other samples, the deformation was limited to only two sets of slip systems. In the OA100 samples, it is noted that with the accumulation of deformation the slip bands become wider. The yield stress and tensile strength decrease with increasing temperature. The mechanical properties of the PA alloy improve with cold rolling but the deviation from the as-aged properties decreases with increasing test temperature. The difference disappears around 700 °C.

Scholars came to the following conclusions:

Alloy 718 exhibits nonlinear log σ vs log ε plots under all different heat-treated conditions. The working hardening rate increases in phase II of the θ vs ε plot for the ST and OA samples; instead, it remains nearly constant for the OA100 sample and gradually decreases for the PA sample. In the transient phase, and with increased stress, both the dislocation rate and the mobile dislocation density increase, leading to a rapid increase in the deformation rate of the plastic immediately after the elastic limit. The free path for the movement of dislocations increases in order from PA to OA, OA100 and ST. Stage II is activated at a critical rate of stress and strain. The difficulty of cross-slip and multiple slips leads to an increase in the work hardening rate. The dominant recovery regime (stage III) is due to recovery processes such as a large cross-slip of dislocations at low temperatures and an increase in dislocations at high temperatures. This results in a decrease in the work hardening rate. The deformation in these materials is initially limited to a single slip system; however, with an increase in tension, an additional slip system is activated. The resistance increased as the degree of cold reduction increased. Residual tensile stresses cause a decrease in tensile properties, while compressive stresses lead to an increase in strength levels.

Table 2-1: Most important results of the articles presented in chapter 2.

Article N°	Year	Authors	Object	Results
1	2015	Mickaël Payet et al.	Impact of plastic deformation on the corrosion mechanism of a Ni-based alloy in supercritical water	The oxide crystals were smaller on the milled surface compared to those on the polished surface, and the oxide layer was much thinner. The many grain boundaries act as nucleation and growth sites for the chromium oxide layer.
2	1995	H. Bohni et al.	Studying Localized corrosion on different types of stainless steel with Microtechnology	The current transient activity increased with the increase of the sulfur content in the steel. The greater the concentration of chlorine ions, the greater the number of transients and the higher the peak values. The pitting potential decreases as the sulfur content in the steel increases.
3	2016	Tanja Trosch et al.	Microstructure and mechanical properties of selective laser melted Inconel 718 compared to forging and casting	The SLM samples at room temperature have the highest final tensile strength and lower elongation at break. Vertically constructed SLM specimens have the highest ductility (columnar grains parallel to the load direction). The SLM samples have a drop in resistance at high temperatures (presence of phase δ inside the grains and finest grain size).
4	2020	Mohamed Balbaa et al.	Densification, surface roughness, and residual stresses of selective laser melted Inconel 718	The width and depth of the pools decreased with increasing speed and decreasing power. They decreased with increasing hatch spacing. The relative density increased with increasing speed. The surface roughness decreased with increasing laser power. On the contrary, with increasing speed the roughness also increased. The (residual stress) RS decreased with the scanning speed. The increase in laser power leads to a decrease in the RS. The RS were all traction with a higher value in the direction of the scan.
5	2004	A. Machet et al.	Growth and structure of	Formation of oxide (inner layer) and chromium hydroxide (outer layer). Then, the chromium hydroxide oxidizes, thickening the oxide layer, at

			passive films in high-temperature water on a nickel-base alloy	the same time increasing the amount of nickel hydroxide on the outer layer. After 8 minutes the film is formed by a layer of chromium oxide with islands of nickel hydroxide on the surface. Surface topography consists of narrow terraces (70nm) alternating with larger terraces (200nm). The surface is covered with platelets. These platelets also have a nano-terraced surface.
6	2022	Arshad Yazdanpanah et al.	Stress corrosion cracking susceptibility of selective laser melted 316L stainless steel under the individual effect of surface residual stresses	RS were found to be higher on samples with a higher depth of cut. With high RS, all the samples showed a continuous increase in current as the potential increased after a narrow transpassive region. low RS and low CSW (columnar sub-grain width) resulted in higher corrosion resistance. At high RS, the dominant parameter was PSA and RS. At high RS appeared SCC from defects in the material. The cracks were propagated through the sub-grains
7	2020	Arshad Yazdanpanah et al.	The role of grinding-induced surface residual stress on probability of stress corrosion cracks initiation in 316L austenitic stainless steel	The RS were in traction. Lower pitting potential values for higher RS. The amplitude of the passive region is reduced as the RS increases. The current density was higher for high RS. The higher the RS, the shorter the time for the potential fall. For low RS values, the samples were attacked along the grain boundaries while at high RS the corrosion was more distributed. The number of pits and their depth also increased with increasing RS.
8	2021	Arshad Yazdanpanah et al.	Stress Corrosion Cracking probability of selective laser melted 316L austenitic stainless steel under the effect of grinding	Grinding introduced tensile stresses on the surface of the samples, the residual stresses are greater on the samples with a greater depth of cut. Lower pitting potential with higher residual stresses (RS). Current density fluctuations are greater for higher RS. Pits are formed preferably along the grinding direction and their density is higher in samples with higher RS. At 310 Mpa The cracks originated from the pores and followed the boundaries of the melt pool. At 460 Mpa the cracks were more and originated from all the defects that characterize the sample.

			induced residual stresses	
9	2019	Baicheng Zhanga et al.	Pitting corrosion of SLM Inconel 718 sample under surface and heat treatments	The as-printed sample showed the lowest corrosion current of 0.33 μA/cm^2. As the temperature of the heat treatment increased, the corrosion current also increased. The pitting potential is very high for the electropolished sample (840 mV$_{SCE}$).
10	2015	Xingying Tang et al.	The corrosion behaviour of nickel base alloys, stainless steel and titanium alloy in supercritical water	On the 316 SS, the outer oxide layer was rich in iron and the oxides present were dissolved under the highly aggressive conditions of supercritical water. Spallation of the remaining oxide layer increases the corrosion rate. The phosphate can increase the corrosion resistance of all alloys by the formation of a very resistant and insoluble passive layer. The action of the supercritical water was to increase the penetration of aggressive species between the oxide flakes due to its intermediate state between vapour and liquid.
11	2020	J.P. Oliveira et al.	Processing parameters in laser powder bed fusion metal additive manufacturing	To avoid the keyhole phenomenon, it is necessary to decrease the laser power and increase the scanning speed. Increasing the scanning speed increases the solidification rate and a columnar structure is favoured. Increasing the laser power increases the temperature gradient and columnar grains are favoured. High scanning speed leads to less segregation.
12	2021	Shuwei Guoa et al.	Corrosion characteristics and mechanisms of typical Ni-based in sub- and supercritical water	Ni-Fe-Cr alloys show the formation of a double-layer oxide film, with the inner layer consisting of chromium oxides and the outer layer consisting mainly of iron oxides. Shot peening causes a reduction in the size of the crystalline grain. The oxides on the surface of nickel-based alloys have a coarse structure on the outside, and a fine structure on the inside. The higher the chromium content the higher the corrosion resistance.
13	2020	J.P. Oliveira et al.	Fundamental welding concepts to improve additive manufacturing	The reduction of porosity and alloying elements segregation is obtained when the power of the beam is modulated at the same frequency as the oscillation of the melt pool. Less heat input promotes the refining of the crystalline grain. Magnetic agitation promotes the refining of the crystalline grain through the scattering of the pieces of the dendrites.
14	2019	Dafan Dua et al.	Influence of build orientation	Increasing the angle of inclination increases the roughness on one side. As the angle increases, the Laves phase goes from scattered precipitates

			on microstructure, mechanical and corrosion behaviour of SLM Inconel 718	to a continuous network and increases in quantity. The increase in the degree of inclination increases the tensile strength. The corrosion potential increases as the angle increases. On the contrary, the corrosion current density decreases as the angle increases.
15	2014	Qingbo Jia et al.	Densification, microstructure, and properties of selective laser melting additive manufactured Inconel 718 superalloy parts	At low energy densities (180 J/m) discontinuous tracks bordered by large pores were found. The surface roughness decreased with the increase in energy density. The columnar dendritic microstructure was refined with the increase in energy density. The micro-hardness increased with the increase in energy density. At 180 J/m the weight gain was greater with a very steep increase.
16	2017	Luying Wang et al.	The effect of sodium chloride on the electrochemical corrosion of Inconel 625 at high temperature and pressure	The anode current density increased with increasing concentration of NaCl. The corrosion potential became more positive as the NaCl concentration increased. Resistance to ion transfer decreased with increasing NaCl concentration. As the NaCl concentration increases, increasingly larger pits have formed on the surface of the samples. There was a surface depletion of nickel, chromium and molybdenum with the increase in the NaCl concentration.
17	2020	Huihui Yang et al.	Microstructural evolution and mechanical performances of selective laser melting Inconel 718 from low to high laser power	With the increase in laser power, the presence of micropores increases. The width of the melt pools increases with the increasing power. High power, the small size of the columnar grains and the increasing presence of equiaxial grains. The presence of the interdendritic Laves phase also increases with power. Tensile strength, yield strength and elongation increase with decreasing laser power.
18	2018	G.H. Cao et al.	γ′, γ″ and δ precipitates in heat-treated Inconel 718 alloy fabricated	Short and thick platelets are identifiable as the δ phase. Acicular-shaped precipitates representing the γ "phase with bct structure, cuboidal and circular precipitates which are the γ" and γ′ phase. The matrix γ fcc has a cellular substructure. The precipitates were found inside the grains and along the edges. The acicular precipitates consist of two variants of γ".

			by selective laser melting	Globular precipitates with orthorhombic structure have been detected within the grain and along the grain boundaries representing the δ phase.
19	2018	Tyler Moss et al.	Stress corrosion crack initiation in Alloy 690 in high-temperature water	Only tests performed at high strains produced SCC at 340 °C after 1800 h also on alloy 690. In constant load tests, alloy 690 was very resistant to SCC nucleation. The alloy showed small cracks after 11000 h at 360 °C and was subjected to 90% of its tensile strength. Cracks have been found to propagate intergranularly. The crack is generated in the area of the Cr-depleted grain boundary.
20	2019	K. Lutton Cwalina et al.	The effects of molybdenum and tungsten alloying on corrosion behaviour of nickel-chromium alloys in aqueous corrosion	Molybdenum and tungsten increase the resistance of the passive film to oxidizing and reducing acids and chlorides. As the concentration of Cr, Mo and W increases, the passivation current is reduced and the passivation potential drops towards more negative potentials. The breaking potential and the thickness of the film increase. Mo and W favour the re-passivation of the film. At the oxide/solution interface there is an accumulation of Mo^{6+} and/or Mo^{5+} ions.
21	2012	K.N. Amato et al.	Microstructures and mechanical behaviour of Inconel 718 fabricated by selective laser melting	Samples that have undergone HIP (hot isostatic pressing) treatment exhibit a much more regular columnar grain structure than as-build samples. In the matrix and at the boundaries, ellipsoidal precipitates are observed. Elongated precipitates grow along the construction direction. The ellipsoidal precipitates, γ" phase, are stacked in columns and have the main axis coinciding with the plane (100) of the matrix. The δ phase is located at the boundaries of the recrystallization grains.
22	2018	Dongyun Zhanga et al.	The thermofluid field of molten pool and its effects during selective laser melting (SLM) of Inconel 718 alloy	The molten metal in the centre of the pool flows from the bottom of the pool to the surface, and on the surface flows from the centre to the edges. The molten metal present on the edges flows from the surface towards the bottom of the pool. All this happens with circular motions. Inward convection is characterized by inverse motions to these. The fastest flows are in the centre and on the surface of the pool. As the Marangoni coefficient increases, the depth of the pool has increased, while its width has decreased, causing the depth-width ratio to increase.
23	2017	Xiaoqing Wang et al.	The effects of thermal cycles on the	On the Y plane, the melt pools were detected and inside them, there was a columnar microstructure. Elongated dendrites grow along the Z-axis and pass-through various layers. Interconnected precipitates, the Laves

			microstructure evolution of Inconel 718 during selective laser melting process	phase, were observed in the interdendritic regions. Cellular structures increase in thickness with increasing height and the Laves phase also increases. The Laves phase passes from a coarse and interconnected structure to a particle structure when it undergoes multiple thermal cycles. The volumetric fraction of the Laves phase also decreases with increasing thermal cycles, because they cause its dissolution.
24	2019	Shuncun Luo et al.	Microstructural evolution and corrosion behaviours of Inconel 718 alloy produced by selective laser melting following different heat treatments	The Laves phase is greatly reduced with annealing and remains as block-shaped precipitates in the interdendritic region. At 1020 °C the δ phase is greatly reduced. Needle-like and platelet-shaped particles precipitate around these blocks-spherical and disc-shaped precipitates are uniformly distributed in the matrix, and they constitute the dispersed γ’ and γ" phases. The corrosion potential follows this order: SLM<rolled <SA. The corrosion rate follows this order: SLM> rolled>SA. The passive potential follows this order: SLM> SA> rolled. The pitting potential follows this order: rolled> SA> SLM. On the SLM, SA and rolled samples there are cracks on the surface of the passive film. The passive film on the rolled sample is the most compact and smooth.
25	1998	P. Kritzer et al.	Corrosion of Alloy 625 in Aqueous Solutions Containing Chloride and Oxygen	With increasing temperature, the density of the pits increased. The film increased in thickness with increasing temperature. The highest corrosion rate occurred in the transition region between the area under the critical temperature and the super-critical area of the water. Increasing the concentration of HCl and O_2 decreased the temperature at which the most severe corrosion occurred. Stress corrosion cracks (SCC) were detected at the bottom of the pits.
26	1992	J.T. Ho et al.	Pitting Corrosion of Inconel 600 in Chloride and Thiosulfate Anion Solutions at Low Temperature	Low concentrations of thiosulfate (0.001, 0.0001 M) shift the pitting potential towards more active potentials, while higher concentrations (0.1, 0.01 M) shift the pitting potential towards more noble values. The density of the pits increases as the thiosulfate concentration decreases. The depth of the pit increases with increasing thiosulfate concentration.
27	1970	W. D. France JR	Effects of Stress and Plastic Deformation on	The corrosion rates for the samples that underwent torsional deformations were higher than those of the simply annealed sample. The corrosion rate increased as the number of twistings that the sample had undergone increased. After the current peak linked to the primary

			the Corrosion of Steel	passive potential, there was a second peak in the passive region, in the deformed samples.
28	2016	Hiroyuki Miyamoto	Corrosion of Ultrafine-Grained Materials by Severe Plastic Deformation	The general corrosion rate increases as the grain size decrease, while the local corrosion rate increases as the grain size increases. Nano-crystalline materials have lower corrosion resistance in the active state but, in the passive state, pitting is suppressed. In nano-crystalline stainless steels, the surface is more enriched with Cr.
29	2013	S.M. Bruemmer	Stress Corrosion Cracking of Cold-Rolled Alloy 690 in Pressurized Water Reactor Primary Water	A large number of small voids and cracked precipitates were detected at the grain boundaries. Thermally treated tubing has a crack growth rate up to 20 times greater than solution-annealed tubing. The preferred path of the SCCs was the grain boundaries even when there were voids or cracked precipitates. The cracks appear to be blunt and limited when encountering a cracked carbide.
30	2014	Koji Arioka	Intergranular Stress Corrosion Cracking Growth Behaviour of Ni-Cr-Fe Alloys in Pressurized Water Reactor Primary Water	The crack growth rate increases as the temperature decreases. The crack growth rate decreased with increasing nickel concentration in the range of 10%-32%, while the growth rate increased with increasing nickel concentration in the 40%-75% range.
31	2021	Yanbing Tang et al.	Corrosion Behaviour of a Selective Laser Melted Inconel 718 Alloy in a 3.5 wt.% NaCl Solution	The steady-state potentials of the two materials were -0.19 V_{SCE} and -0.13 V_{SCE} (SLM and Rolled respectively). The SLM sample had a higher passive current density. The passive film impedance on the SLM was lower than that on the rolled one (R). The passive films on the two samples were composed of Cr_2O_3, Fe_2O_3, NiO, MoO_3, Nb_2O_5 and NbO. The passive film formed on SLM contained more NiO.
32	2020	Shuwei Guo et al.	Corrosion Characteristics of Typical Ni−Cr Alloys and Ni−Cr−Mo	Ni-Cr alloys show an increase in weight during the first corrosion phase, but if they are exposed for a long time to an aggressive environment like SCW (supercritical water) they show a decrease in weight. The lower the Cr content in the alloy, the lower the oxygen content necessary to have the maximum weight increase. Ni-Cr-Mo alloys have improved

			Alloys in Supercritical Water	resistance to pitting corrosion, crevice corrosion and corrosion to non-oxidizing acids. The higher the Mo content the higher the resistance.
33	2019	Parag M. Ahmedabadi et al.	Effect of Plastic Deformation on Passivation Characteristics of Type 304 Stainless Steel	Linear structures were noted within the grains of the MA0% (percentage of deformation) sample matrix, which turned into intersected structures and non-linear structures in the MA20% sample and the MA60% sample. The passive current density increased with increasing plastic deformation. In this solution, the critical current increased with increasing plastic deformation
34	2020	Lin Liu et al.	Nickel-Based Superalloys	The γ matrix has an FCC structure. The reinforcement phase γ 'is an intermetallic phase consistent with the matrix based on Ni_3(Al, Ti, Ta) and has an FCC L12 structure. The γ” strengthening phase consists of Ni_3Nb with a body-centred tetragonal structure (BCT) D022. This phase precipitates in the form of discs. There may be other phases called topologically close together (TCP) such as μ, σ, P and Laves. The presence of precipitates $M_{23}C_6$ and M_6C at the grain boundaries hinders the grain sliding.
35	2017	Helmuth Sarmiento Klapper et al.	Critical Factors Affecting the Pitting Corrosion Resistance of Additively Manufactured Nickel Alloy in Chloride-Containing Environments	The SLM samples had a passive region of 200 mV followed by the breakdown potential at values above 400 mV$_{SHE}$ and repassivation potentials around 250 mV$_{SHE}$. The samples showed a metastable pitting region starting at a potential of 250 mV$_{SHE}$. Repassivation occurred immediately below 0.1 mA/cm^2. A sudden drop in OCP at electrochemical potentials close to 150 mV$_{SHE}$ observed on samples with surface defects was noted in the aerated solution.
36	1983	M. C. Chaturvedi et al.	Strengthening mechanisms in Inconel 718 superalloy	The presence of the y" phase was observed in the form of disc-shaped precipitates coherent with the {100} planes of the matrix. The y' phase was present as spherical precipitates. The volumetric ratio between the y "and y’ phases was equal to 3. The component of the yield point due to hardening by precipitation decreases by decreasing the test temperature.
37	2013	Xingying Tang et al.	Corrosion Behaviour of Ni-	The combined effect of oxygen and chlorine led to the most severe attack on all alloys. On Incoloy 825, growth of platelet-shaped oxide crystals.

			Based Alloys in Supercritical Water Containing High Concentrations of Salt and Oxygen	Hastelloy C-276 exhibited de-alloying corrosion and stress corrosion cracking in the presence of chloride. Incoloy 800 exhibited the most severe pitting corrosion in the presence of high chloride and low oxygen. Nickel is the element that was most dissolved in the solution. The oxide layer consisted of Cr_2O_3, $NiCr_2O_4$ and NiO in the presence of oxygen alone. Fe_3O_4, Ni $(OH)_2$ and MoO_2 were found in Incoloy 825, Inconel 625 and Hastelloy C-276 respectively.
38	2018	Le Zhou et al.	Microstructure, precipitates, and mechanical properties of powder bed fused Inconel 718 before and after heat treatment	Annealing at 980 °C shows recrystallization. Annealing at 1065 °C shows recrystallization. Cellular and columnar dendritic microstructures. The Laves phase was detected along the cell boundary. Carbides in the interdendritic region. At 980 °C, as-build patterns were eliminated. Plaque-shaped δ-Ni_3Nb precipitates are visible inside and at the grain boundaries. A needle-shaped γ”-phase was also detected. At 1065 °C, segregation and melt pools disappeared.
39	2017	Helmuth Sarmiento Klapper et al.	Localized Corrosion Characteristics of Nickel Alloys	Chromium allows the formation of a superficial oxide film that protects the alloy from the attack of the aggressive environment. Elements that increase the corrosion resistance of the alloy are molybdenum and tungsten, especially the resistance to acids and chlorides. Cr contributes to the formation of the oxide film (passivation), while Mo and W contribute to the repassivation of the alloy after the formation of the pits.
40	2008	K.V.U. Praveen et al.	Work-Hardening Behaviour of the Ni-Fe-Based Superalloy IN718	At 1/3 the deformation was limited to just two sets of slip systems. At 2/3 the slip is entirely concentrated in two series of separate slip systems that intersect with each other. The PA 2/3 material shows the formation of persistent slip bands (PSB) and the shearing of precipitates. In the OA100 samples, it is noted that with the accumulation of deformation the slip bands become wider.

3 Experimental procedure

3.1 Material production

The gas-atomised powder of alloy UNS-N07718 (identified by ASTM F3055–14a) with a particle size distribution of 10–45 µm, was used for the fabrication of parallelepiped-shaped samples. The laser machine for metal melting SISMA 100 (SISMA Italy) was used, equipped with a 200 W fibre laser with the laser diameter spot setting at 30 µm. The SLM process was conducted in an argon-controlled atmosphere with an oxygen level below 200 ppm (to minimize the oxidation effect and the formation of unwanted phases), employing a bidirectional alternating checkerboard scanning strategy. The process parameters used are as follows: layer thickness at 20 µm, hatch spacing at 70 µm, scanning speed at 750 mm/s and laser power of 105W, 115W and 125W.

Table 3.1: Chemical composition of alloy 718 powder.

Element	Ni	Cr	Fe	Nb	Mo	Ti	Al
% by weight	53.70	17.93	18.17	5.20	2.96	0.95	0.48

Element	Co	Si	Mn	Cu	C	P	N	B
% by weight	0.33	0.08	0.08	0.05	0.025	0.009	0.004	0.0025

3.2 Porosity analysis

3.2.1 Sample preparation

The bars were cut using an ATA BRILLANT 210, an automatic cutting machine with a disc suitable for hard metal, to obtain the samples used in the following operative procedures. The parameters set in the machine were: 2500 rpm as the disc rotation speed, 0.01 mm/s as the feed rate, a movement of 20 mm along the vertical axis of the arm that supported the piece to be cut, and a thickness of the cut piece of 1.2 mm. Five rectangular-shaped samples were cut for each type of alloy.

The samples were embedded in resin, with the greater surface (the surface on which the melt pools can be seen from above) kept free. The resin support is useful for handling the sample and allowing easy polishing. The sample was put on a plate that go down and enter the machine, and then two spoons of resin powder were poured into the cavity. The hole was closed, and the machine was started. This process is carried out in a STRUERS LaboPress-3 machine, setting 7 minutes of heating to melt the resin and 7 minutes for cooling it.

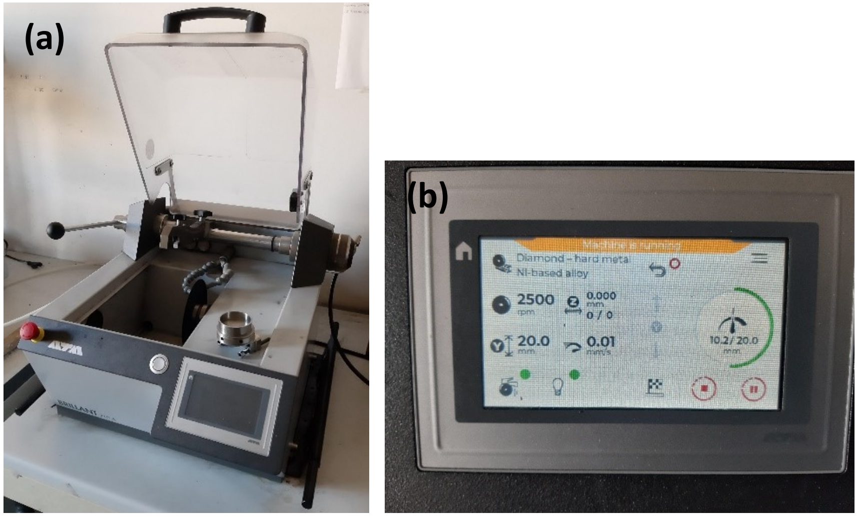

Machine is running
Diamond – hard meta
NI-based alloy
2500 rpm
0.000 mm
0 / 0
20.0 mm
0.01 mm/s
10.2 / 20.0 mm

Figure 3.1: (a) Cutting machine; (b) Cutting parameter.

Figure 3.2: Machine to mount the sample in resin support.

The samples were ground using a REMET LS 2 grinding machine, using rotating 800, 1200 and 4000 grit abrasive discs. Water was poured continuously on the discs to reduce friction and avoid overheating of the sample, which could change the surface properties of the material. The samples were lapped using a STRUERS LaboPol-21 polishing machine. Lapping permitted the elimination of all the scratches on the surface, and in this way, the surface was visible under the microscope with only the material's defects. Lapping was performed by spraying diamond particles suspended in alcoholic solutions on the surface of rotating cloths. Three solutions with different suspended particle sizes were used. 6 μm particles were sprayed on the first cloth, 3 μm particles on the second cloth, and 1 μm particles on the third cloth. When the sample had to pass to the next cloth it was necessary to wash it with water and ethanol, to avoid contamination of coarser particles on the next cloth. During lapping, water was sprayed frequently to avoid excessive friction.

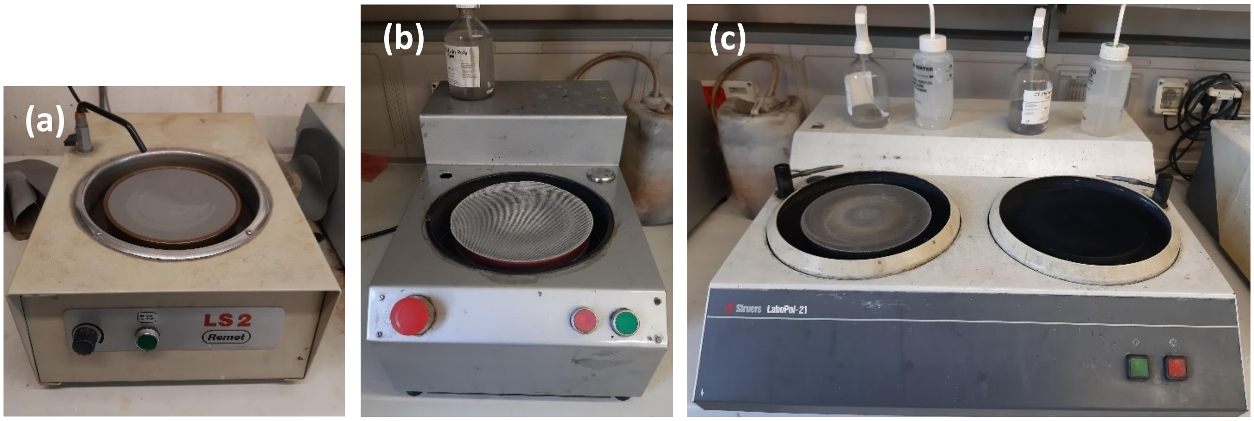

Figure 3.3: (a) Grinding machine; (b) polishing machine for 6 µm particles, (c) polishing machine for 3 µm (left cloth) and 1 µm (right cloth) particles.

The same procedure was performed on samples obtained from pieces produced by traditional processes, which represent the reference samples, i.e., the bulk material. Alloy 718 (according to 2.4668 / UNS-N07718) was used as the representative material for precipitation hardened double ageing conventional material.

Figure 3.4: Mounted and polished sample.

3.2.2 Observation under the optical microscope

For the analysis of the porosity of the materials, the samples were observed under a LEICA DM RE optical microscope, equipped with a camera connected to a computer. The samples were observed at the following magnifications: 5x, 10x, and 20x. At each magnification, 10 images of the surface were captured randomly, in black and white.

3.2.3 Image processing

The images were processed with ImageJ software to determine the area of the pores and their density on the surface, increasing the contrast between pores and metal surface.

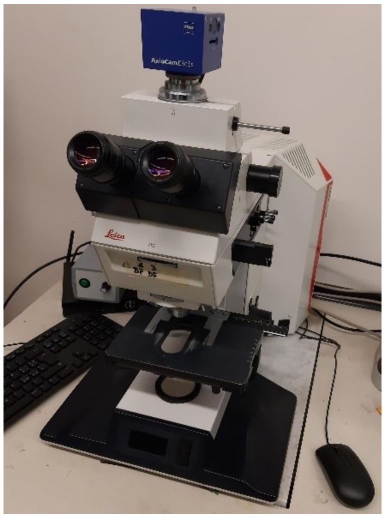

Figure 3.5: Optical Microscope LEICA DM RE.

3.3 Determination of hardness

3.3.1 Sample preparation

The samples used for porosity analysis were used to determine the hardness of the various materials.

3.3.2 Microhardness test

The samples were subjected to Vickers micro-hardness tests in a Leitz Wetzlar Germany 112444 micro-durometer. A 200 g weight was used. Indentations were performed starting from the centre of the sample and scanning the horizontal direction and the vertical direction of the surface. Impressions were made at a distance of 1 mm from each other in the horizontal direction (the longest side of the sample), while at 0.5 mm in the vertical direction (the shortest side of the sample), to have about 20 values of hardness in every direction.

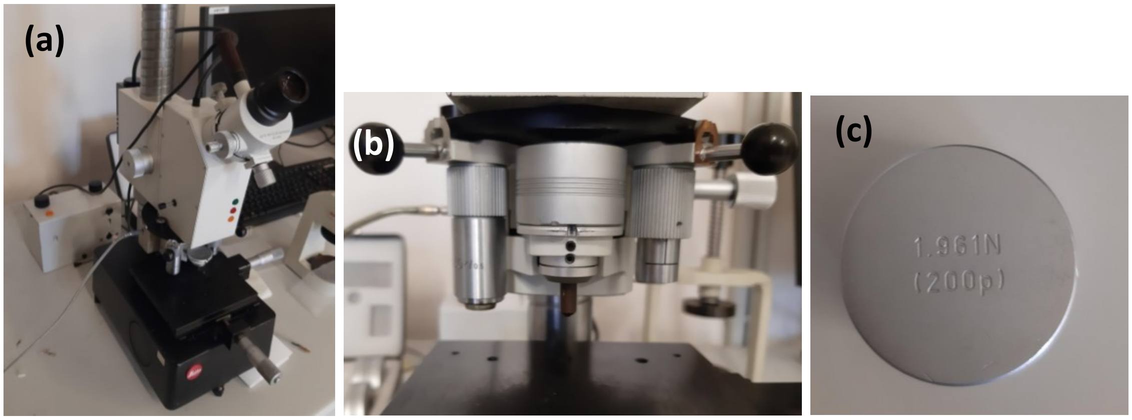

Figure 3.6: (a) Micro-durometer Leitz Wetzlar Germany 112444; (b) The tip of the durometer; (c) Weight of 200 g.

3.3.3 Observation under the optical microscope

The indented specimens were observed under the LEICA DM RE optical microscope, at a magnification of 50x. Black and white images of the prints left by the micro-durometer were captured, which diagonal was measured of using the software of the camera connected to the microscope.

3.3.4 Data processing

The values obtained from the measurements of the diagonals of the impressions were converted into hardness values using the conversion tables supplied with the micro-durometer.

3.4 Analysis of melt pools and the microstructure

3.4.1 Sample preparation

The samples used for the micro-hardness tests were polished again to eliminate any surface imperfections left by the tests and handling. Furthermore, a sample was also incorporated in the resin, for each type of alloy, which had the cross section (the smallest surface of the parallelepiped) kept free from resin. The cross-section was polished like the other samples up to 1 μm.

3.4.2 Electro-etching

A sample of the longitudinal section and a sample of the cross-section, of each type of alloy, after being carefully polished, were cleaned with extreme care with ethanol. Then they were electro-etched using a STRUERS LectroPol-5 Version 1.12 electro-polisher. An adhesive tape was placed in the centre of the sample to delimit the part that will be corroded. The samples were immersed half of their surface in a 10% oxalic acid solution. The samples were held with a metal clamp in direct contact with the free surface of the sample and, through an electric cable, connected to the electro-polisher. The bowl in which the solution was contained was also made of metal and connected via an electrical cable to the device. Electro-etching was performed by passing a current through the circuit closed immersing the sample in the solution. A voltage of 6.0 V was set, and the sample was kept in the solution for 7 seconds. The sample was extracted and cleaned thoroughly with water and ethanol.

Figure 3.7: Electro-polishing machine.

3.4.3 Manual etching

Bulk samples were etched using the etchant Kalling. Two etchant drops were poured on the metal surface using a pipette, and after thirty seconds the sample was observed under the optical microscope to see if the microstructure was in evidence. The procedure was repeated until it was possible to see the microstructure. The bulk sample underwent evident corrosion after 2 minutes.

3.4.4 Observation under the optical microscope

The electro-etched surfaces of the samples were observed under the LEICA DM RE optical microscope. The largest surface, in which the melt pools can be observed from the top, was observed at 5x, 10x, 20x, and 50x magnification. Five images were captured for each magnification. The cross-section was observed at 10x and 20x magnification, paying attention to observe the melt pools with the base of the cone facing upwards. As many images as possible were captured to have a lot of data to process and therefore reduce the error.

3.4.5 Image processing

The cross-sectional images were processed with ImageJ software which made it possible to measure the width of the melt pools and their height.

3.5 Statistical analysis

The measures of pore area, pore density, hardness, and the melt pools dimension, using the software Origin, were analysed statically. From the analysis of the values, we also obtain the following data: N° total, Mean, Standard Deviation, Sum, Minimum, 1st Quartile (Q1), Median, 3rd Quartile (Q3), Maximum, Interquartile Range (Q3 - Q1), Range (Maximum - Minimum). The most important data are the mean and the median of the values and the interquartile.

With these data, we can make a comparison between the different laser powers.

3.6 Corrosion tests

3.6.1 Sample preparation

The samples used for the corrosion analysis underwent the same polishing treatment as the samples for the porosity analysis but were not incorporated, they were simply glued to support. After detaching the sample from the support, the central surface is divided into quadrants of equal area, engraving lines with the tip of a calliper. A thorough cleaning is performed by immersing it in a solution of water and alcohol and placing it in an ultrasonic bath. Both as-received specimens and specimens to which a constant deformation is imposed (corresponding to tensile stress 10% higher than yield stress) are tested.

3.6.2 Experimental method

The electrochemical tests used to determine the resistance of the passive layer of the material were potentiodynamic polarization and galvanostatic polarization. The experiments were carried out in a 3.5% sodium chloride solution in distilled and deionized water and the solution was bubbled with argon gas for 5 minutes before measurements to have almost the same level of dissolved oxygen for all experiments. Three measurements were performed in the central area of the sample to maintain the same residual and applied stress conditions.

The microcapillary method implements the standard three-electrode method, which consists in using the sample, on which the measurements are carried out, as a working electrode and together with it a reference electrode is used for potential measurements. A counter electrode is used to close the circuit and measure the current passing through the system. The substantial difference between this method and the traditional method of analysis is the fact that the solution was in contact with the surface of the material using a capillary with a diameter of 500 μm, normally, however, the sample is totally immersed in the solution. Inside the capillary, there was a platinum wire with a diameter of 100 μm that played the role of the counter electrode and allowed the closure of the circuit together with the surface of the sample. A standard calomel electrode (SCE) was used as the reference electrode. The distance between the counter electrode and the capillary tip was maintained at 3 mm from the surface of the sample. A silicone gel was applied around the tip of the capillary to avoid corrosion localized on the surface directly below the edge of the capillary. The tests are performed by connecting the electrodes to a GAMRY Interface 1010E potentiostat/galvanostat.

Potentiodynamic tests were performed at a scan rate of 1mV/s. The potential range in which they were performed was from -250 to 1500 mV according to open circuit potential measured for 60 min before the measurements. The galvanostatic tests were performed using a fixed current 10% higher than the breakdown current density obtained from potentiodynamic polarization results. The samples were kept in contact with the solution for 30 minutes and the tests lasted a further 30 minutes.

The implementation of the microcapillary method allows the performing of polarization measurements on an extremely small surface, allowing to have a high sensitivity and detecting the beginning of the nucleation of the SCCs (stress corrosion cracks) with extreme precision, avoiding the nucleation and propagation phase overlapping [88].

3.7 Characterization of stress corrosion cracks

3.7.1 Observation under the scanning electron microscope

Following the electro-etching of the SLM and the manual-etching of the conventional samples, a scanning electron microscope (SEM) microstructure analysis was performed using the Leica Cambridge LEO 440 microscope with an accelerating voltage of 15 keV and maintaining the working distance at 10 mm for all specimens. Several images of the surface of the samples were captured following the galvanostatic test under as-received conditions after 5 minutes from the breakdown potential. The same was done for samples corroded under tensile stress, to observe the appearance of cracks and compare them with those of the conventional sample.

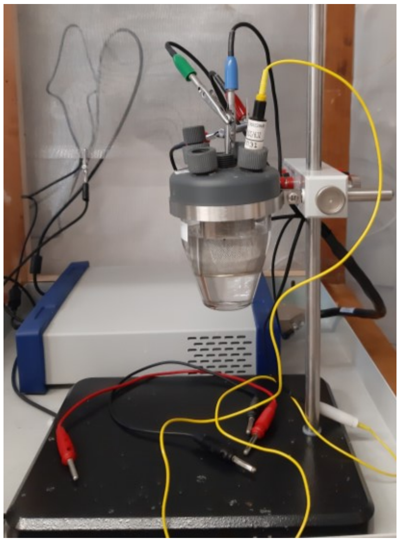

Figure 3.8: Traditional three-electrode implant; Platinum net as counter-electrode, sample as working electrode, saturated calomel electrode (SCE) as the reference electrode.

Figure 3.9: Leica Cambridge LEO 440 scanning electron microscope.

4 Results

4.1 Porosity

Pore area:

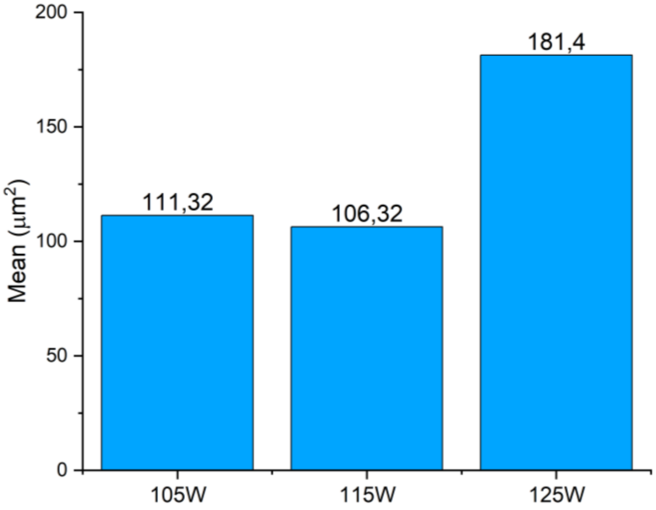

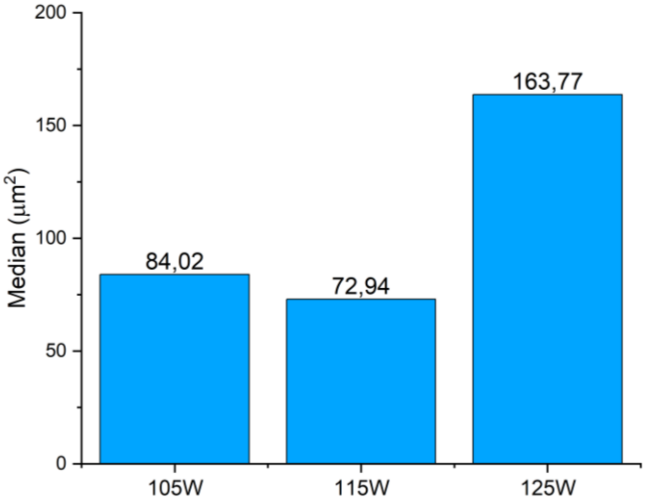

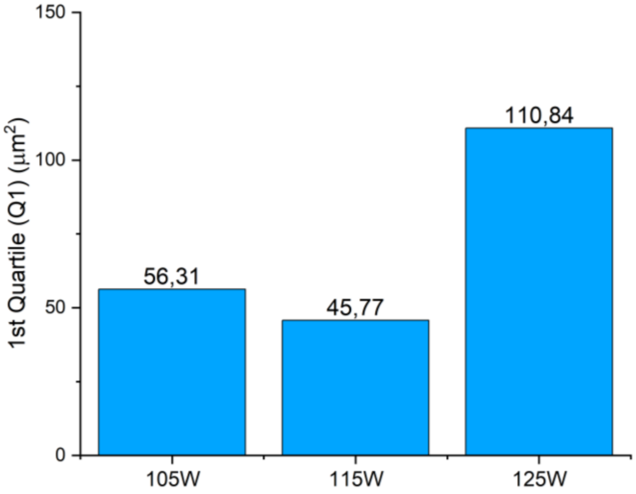

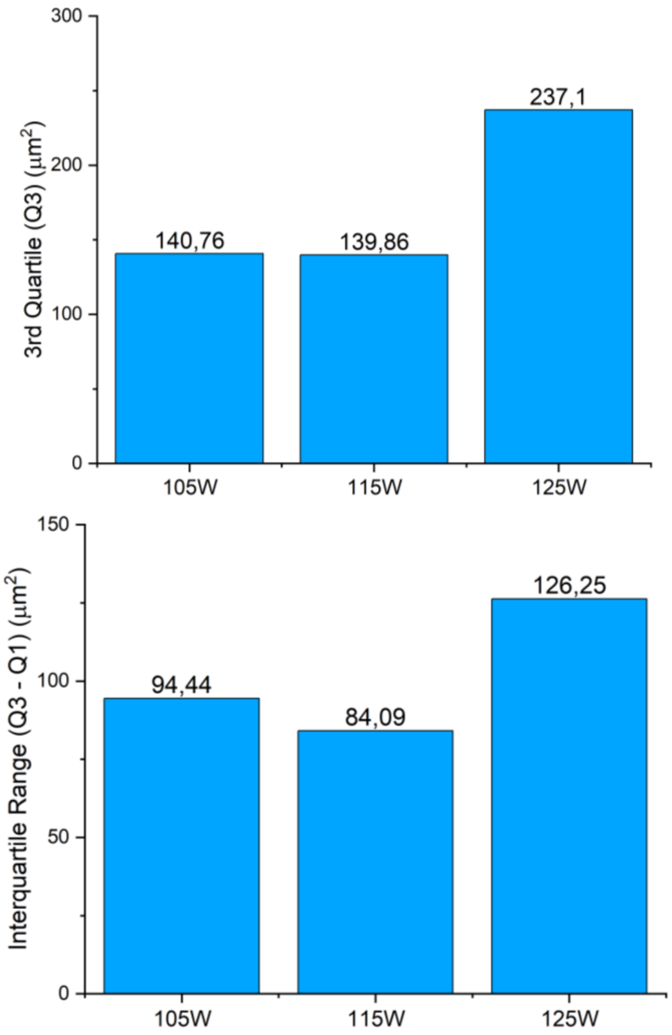

Figure 4.1: Comparison of the pore area data of the samples produced with different laser power.

Table 4.1: Data relating to the pore area of the samples produced with different laser power and their statistical analysis.

Data	N° measurements	Mean	Standard Deviation	Sum	Minimum
		μm²	μm²	μm²	μm²
105W_5x&10x&20x	558	111,32	74,86	62119,26	39,5
115W_5x&10x&20x	608	106,32	83,60	64643,50	29,26
125W_5x&10x&20x	247	181,40	85,17	44807,80	73,66

Data	1st Quartile (Q1)	Median	3rd Quartile (Q3)	Maximum	Interquartile Range (Q3 - Q1)	Range (Maximum - Minimum)
	μm²	μm²	μm²	μm²	μm²	μm²
105W_5x&10x&20x	56,31	84,02	140,76	387,81	84,44	348,31
115W_5x&10x&20x	45,77	72,94	139,86	393,33	94,09	364,06
125W_5x&10x&20x	110,84	163,77	237,10	390,47	126,25	316,81

Pore density:

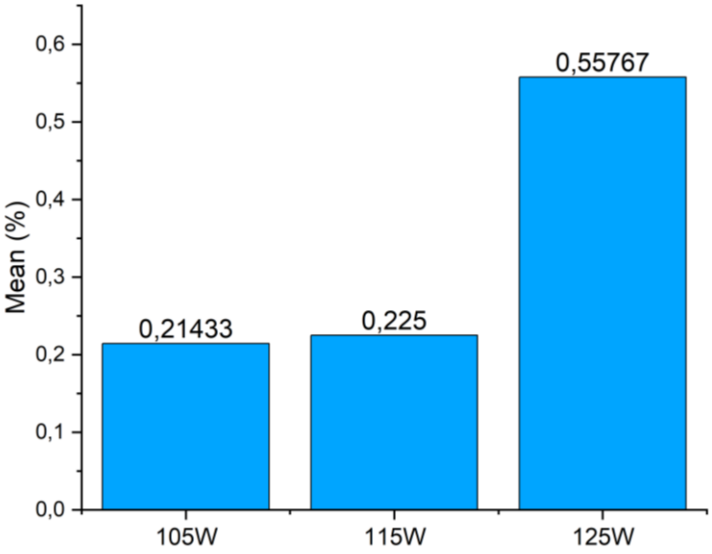

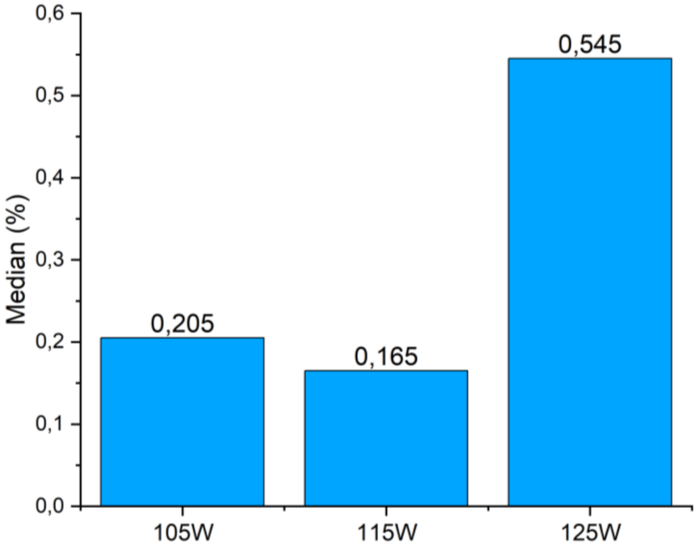

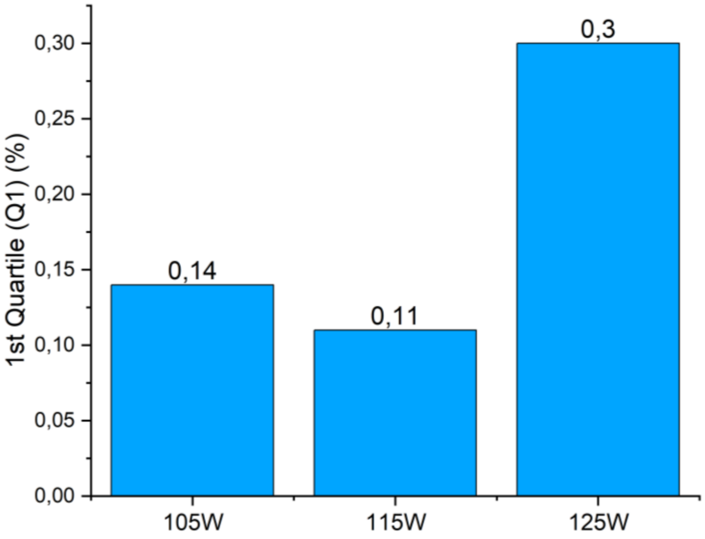

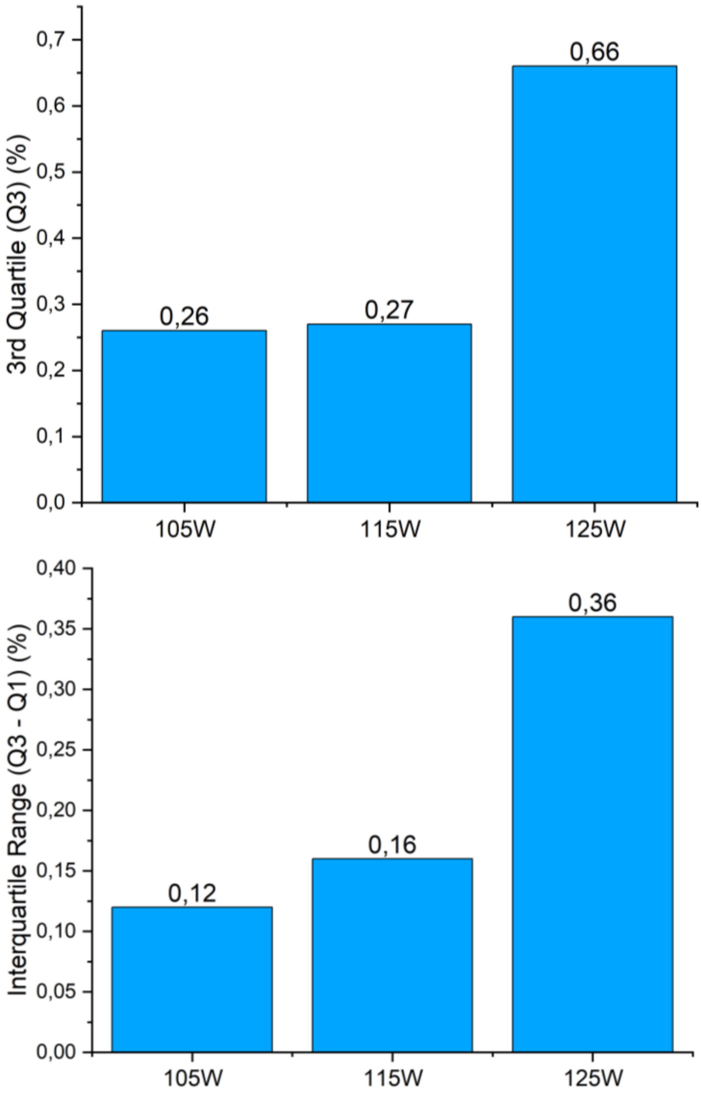

Figure 4.2: Comparison of the pore density (expressed as the percentage of the surface occupied by the pores) data of the samples produced with different laser power.

Table 4.2: Data relating to the pore density of the samples produced with different laser power and their statistical analysis.

Data	N° measurements	Mean	Standard Deviation	Sum	Minimum
105W_5x&10x&20x	30	0,21433	0,11104	6,43	0,02
115W_5x&10x&20x	28	0,225	0,20299	6,3	0,03
125W_5x&10x&20x	30	0,55767	0,38849	16,73	0,08

Data	1st Quartile (Q1)	Median	3rd Quartile (Q3)	Maximum	Interquartile Range (Q3 - Q1)	Range (Maximum - Minimum)
105W_5x&10x&20x	0,14	0,205	0,26	0,56	0,12	0,54
115W_5x&10x&20x	0,11	0,165	0,27	0,92	0,16	0,89
125W_5x&10x&20x	0,3	0,545	0,66	1,9	0,36	1,82

The pores are divided into trapped-gas pores and lack-of-fusion pores. Trapped-gas pores appear because during the transit of the laser the molten metal releases part of the gas trapped inside the metal powder and, given the rapid solidification speed typical of the SLM process, this gas (or the inert gas present in the machine chamber) is trapped in the form of bubbles inside the solidified pools. A high energy density and therefore a high laser power can cause the vaporization of part of the metal and therefore part of the pores can be due to the trapping of these vapours. Furthermore, a high energy density can cause the metal powder adjacent to the melt pool to move away from it, preventing the next melt pool from having enough material to cover the space needed for densification. The lack-of-fusion pores appear because the power of the laser is too low and the laser, passing over the powder bed, doesn't melt it completely. A low laser power leads to a small melt pool that does not allow overlapping with the others and therefore between one pool and the other some not completely melted powder remains. The edges of the unfused powder grains are thus comparable to cracks or pores[89].

An incorrect combination of low laser power and high scanning speed causes the formation of melt pools that have an uneven width along the laser track. This is caused by the fact that the molten material is insufficient to counteract the surface tension which causes the pool to form spheres along its path. This situation causes an uneven overlap of the melt pools and therefore a lack of fusion.

A high laser power produces keyhole melt pools that are characterized by a height/half-width ratio greater than one. Keyhole pools with a height/half-width ratio much greater than 1 are characterized by the formation of trapped-gas pores. This is because the high energy density leads to a significant evaporation rate of the metal, as more heat is absorbed due to the Inverse Bremsstrahlung effect, which increases the diameter and depth of the vapour column formed. When the vapour column exceeds the diameter of the laser beam, there is a drop in ablation pressure (linked to evaporation) which is overcome by the capillary pressure of the pool, leading to its closure. Due to the depth being much greater than the width, the molten metal can exhibit instabilities that lead to the closure of the pool at various heights, trapping the metal vapour inside and generating porosity[51].

105W:

The sample shows a low porosity, the dominant porosity is the trapped-gas porosity. Considering the median and the mean of the values of the pore area, the result is comparable to that of the 115W sample. Considering the median of the pore density, discarding values that are too far from the centre of the distribution, it can be seen that the 105W sample has a higher porosity than the 115W sample.

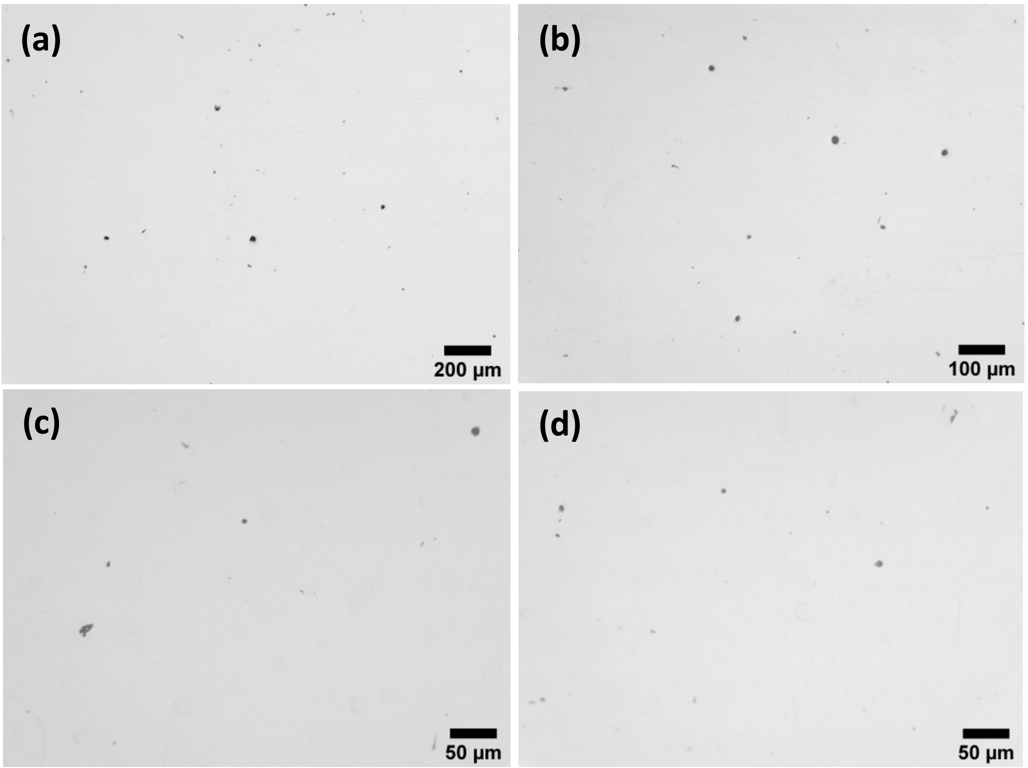

Figure 4.3: Pictures of the metal surface of the 105W sample, under the optical microscope; (a) 5x magnification, (b) 10x magnification, (c) and (d) 20x magnification.

115W:

The 115W sample shows a small pore area when the mean and the median of the values are considered. These values are the lowest respect to that of the other samples. When the median of the pore density values is considered, the 115W sample shows the lowest pore density of all the samples. This means that by discarding the values that repeat with little constancy, i.e. few large pores, the 115W sample is the best of all. There are mainly trapped-gas pores, but some big lack-of-fusion pores are also present.

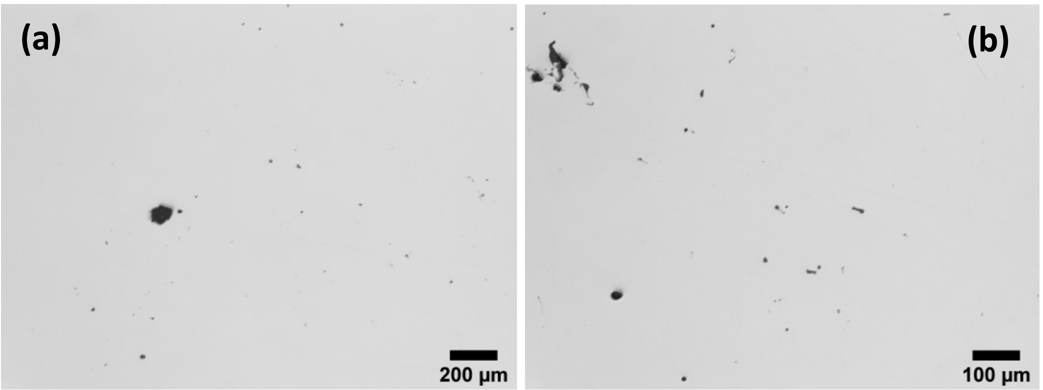

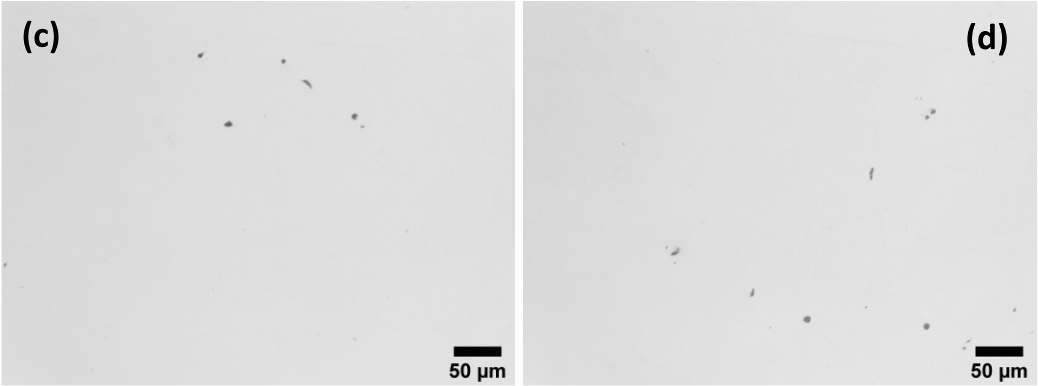

Figure 4.4: Pictures of the metal surface of the 115W sample, under the optical microscope; (a) 5x magnification, (b) 10x magnification, (c) and (d) 20x magnification.

125W:

The 125W sample shows a high density of large pores. Looking at the median of the pore area, the value of this sample is the greatest compared to the others. On the other hand, the 125W sample shows a much higher pore density than the others, especially if the median is considered. The larger pores follow the traces of the pools of fusion and therefore, even if circular in shape, they can be lack-of-fusion. But, much more likely, due to the high laser power, they are gas pores anyway. They are mostly found at the boundary of the squares that form the chessboard which is the path followed by the laser to produce the pieces. At that point, the laser beam has to change direction and slow down. This causes a high energy density in a confined space, and therefore higher quantities of gas are more likely to be generated. Even if there are many large pores, small pores reduce their impact on the average pore area value. But this does not mean that they will not have a great impact on corrosion resistance, indeed, the large presence of these pores is visible to the naked eye. The high percentage of pores present on the surface indicates that also the largest pores, even if outnumbered, are repeated in considerable numbers.

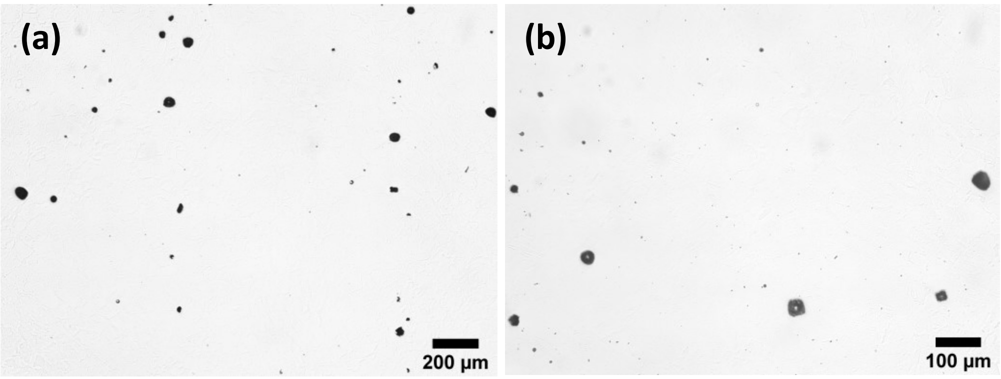

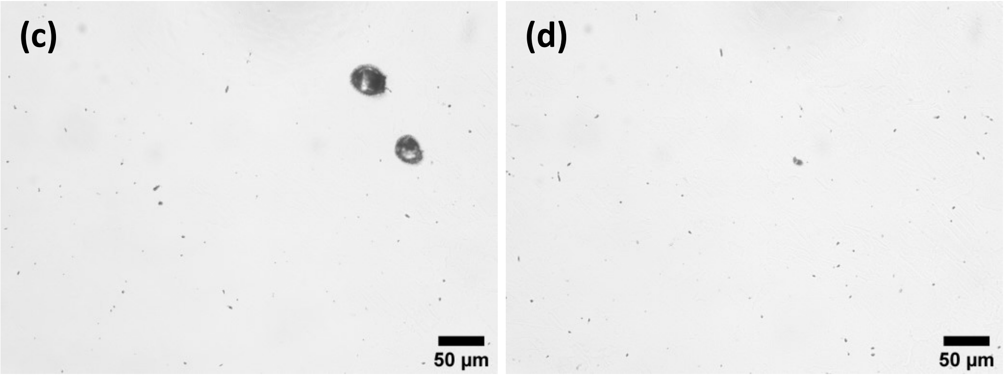

Figure 4.5: Pictures of the metal surface of the 125W sample, under the optical microscope; (a) 5x magnification, (b) 10x magnification, (c) and (d) 20x magnification.

The optimal laser power seems to be 115 W since it allows the obtaining of a material with few pores and rarely of considerable size. The power of 125W produced a sample with a high percentage of large pores, presenting itself as the worst balance between laser power and scanning speed.

As for the pore area, the 125W sample is the one with the highest interquartile range. This indicates that in the sample the pores are present with a high dimensional distribution. The 115W and 105W samples have a less size distribution.

Referring to the pore density, the 125W sample is the one with the greatest variability demonstrated by the high interquartile range. Following 115W sample. The sample with a smaller porosity distribution is 105W.

Box charts:

Pore area:

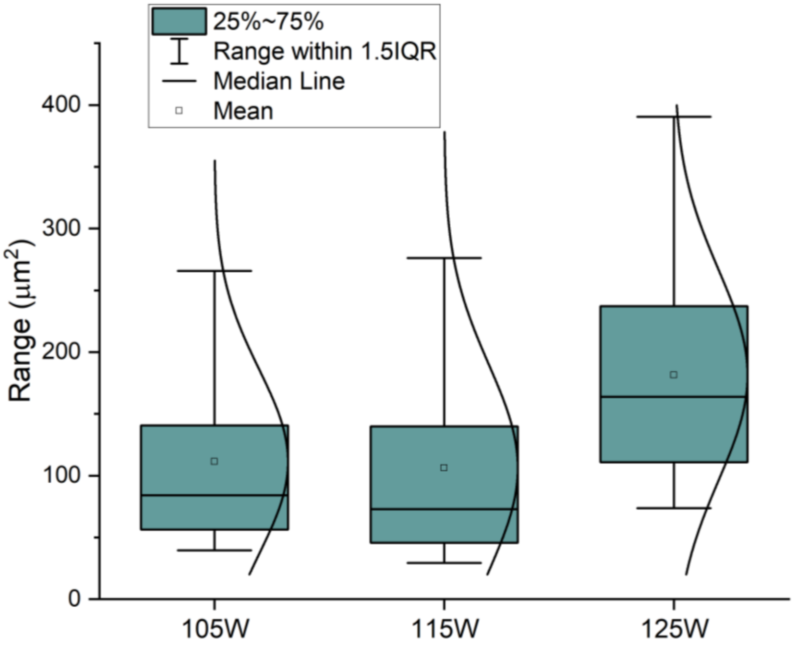

*Figure 4.6: Box chart showing the comparison of the pore area data of the samples produced with different laser power; the small square represents the mean, the line in the grey area represents the median, the grey area represents values in the range 25%~75%, the range delimited by the vertical line passing through the grey area contains the values within 1.5*Interquartile range.*

Pore percentage:

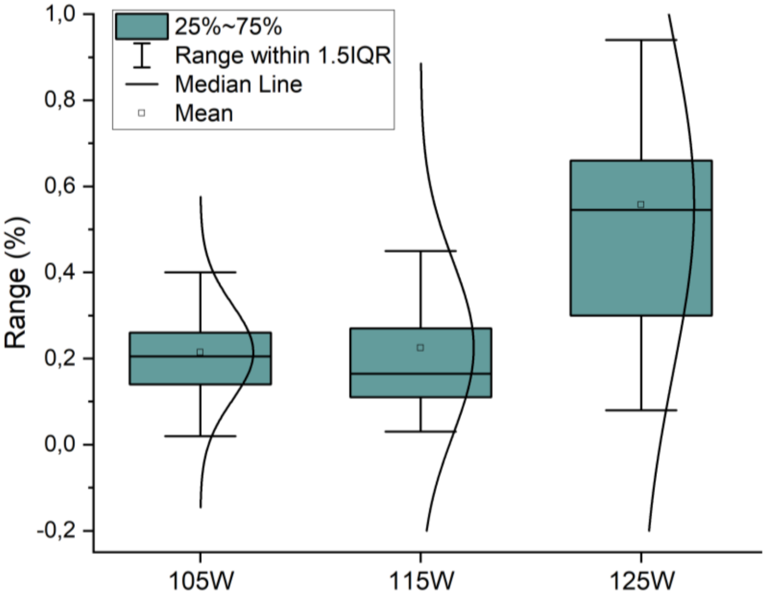

Figure 4.7: Box chart showing the comparison of the pore density data of the samples produced with different laser power; the small square represents the mean, the line in the grey area represents the median, the grey area represents values in the range 25%~75%, the range delimited by the vertical line passing through the grey area contains the values within 1.5*Interquartile range.

4.2 Melt pools and microstructure

Melt pool width:

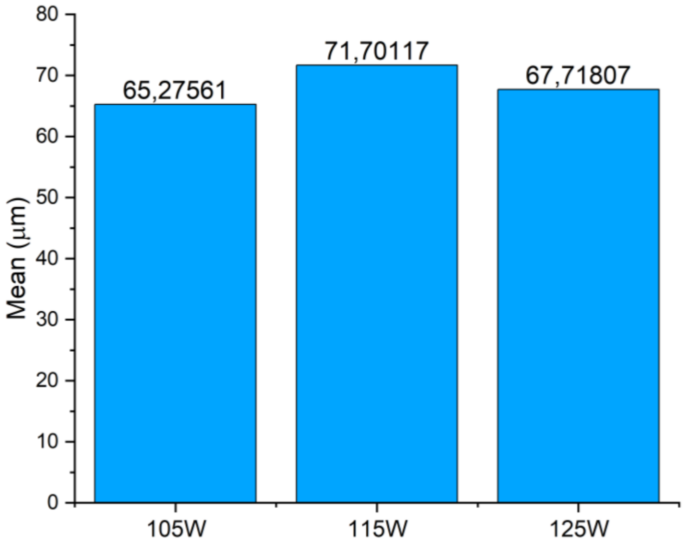

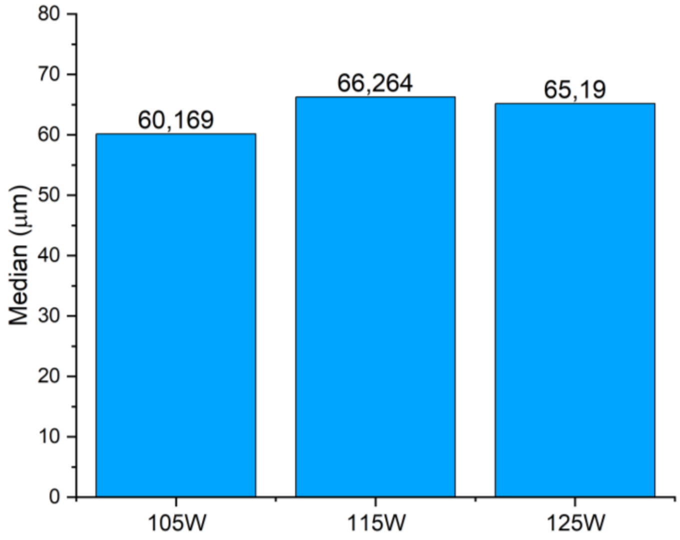

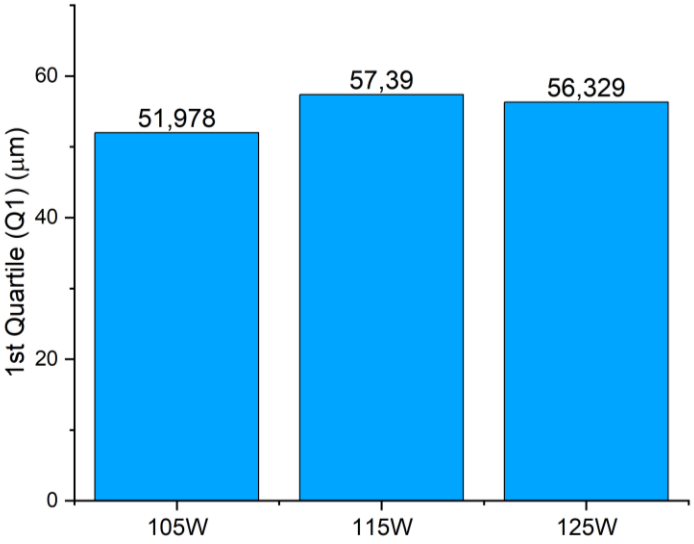

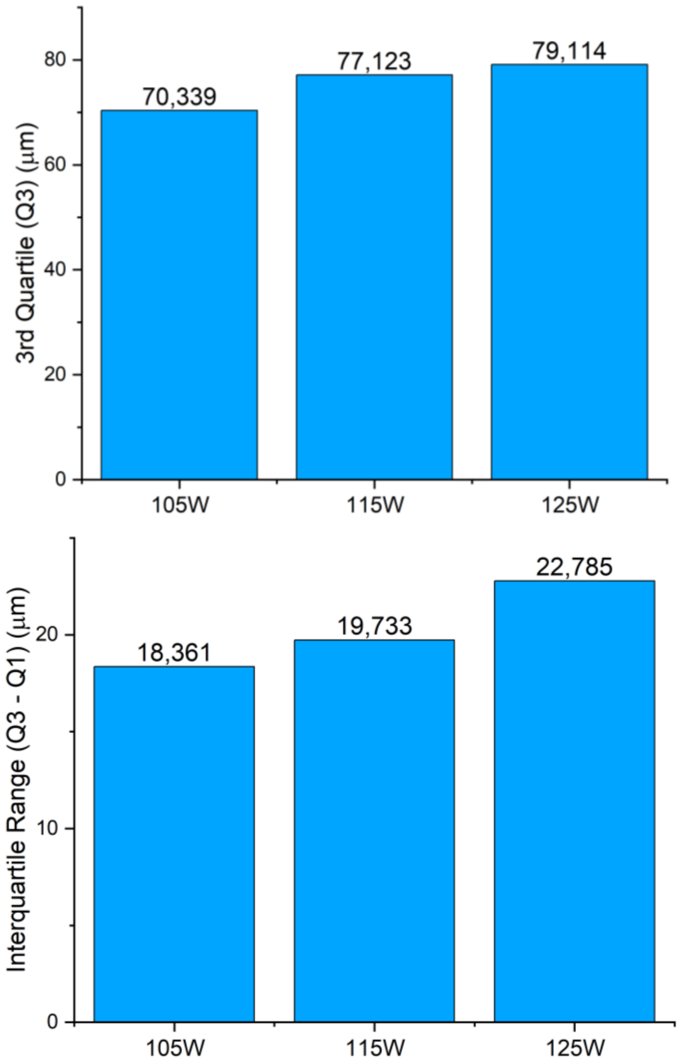

Figure 4.8: Comparison of the melt pool width data of the samples produced with different laser power.

Table 4.3: Data relating to the melt pool width of the samples produced with different laser power and their statistical analysis.

Data	N° measurement	Mean	Standard Deviation	Sum	Minimum
		µm	µm	µm	µm
105W_10x&20x_width	2001	65,27561	24,82064	130616,494	26,174
115W_10x&20x_width	1005	71,70117	24,66371	72059,675	16,056
125W_10x&20x_width	1231	67,71807	19,28148	83360,95	15,823

Data	1st Quartile (Q1)	Median	3rd Quartile (Q3)	Maximum	Interquartile Range (Q3 - Q1)	Range (Maximum - Minimum)
	µm	µm	µm	µm	µm	µm
105W_10x&20x_width	51,978	60,169	70,339	256,78	18,361	230,606
115W_10x&20x_width	57,39	66,264	77,123	245,243	19,733	229,187
125W_10x&20x_width	56,329	65,19	79,114	305,707	22,785	289,884

Melt pool height:

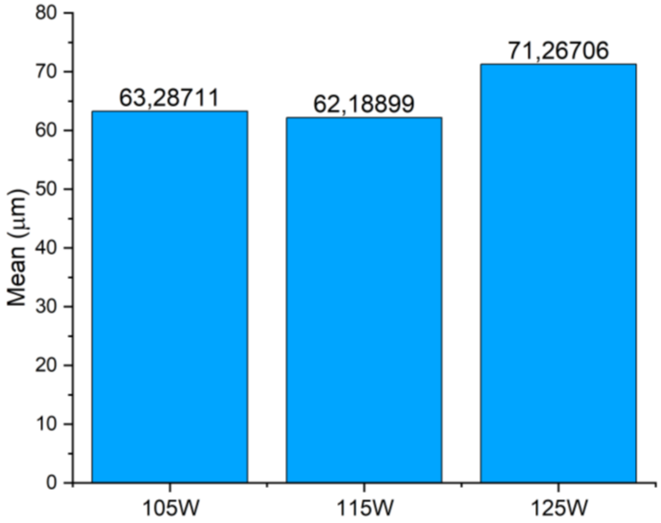

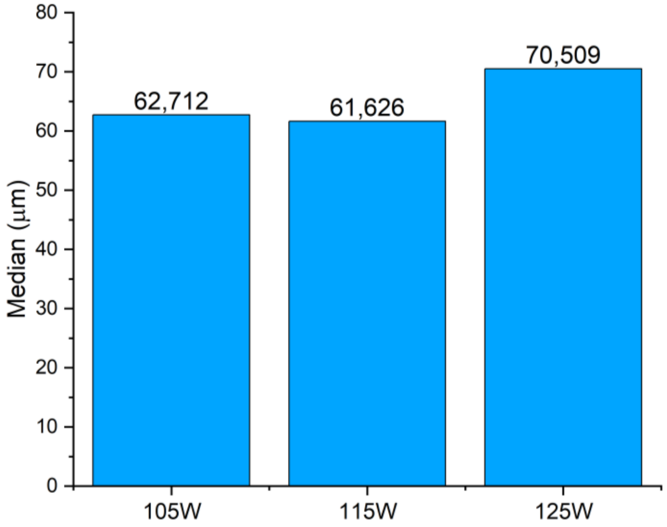

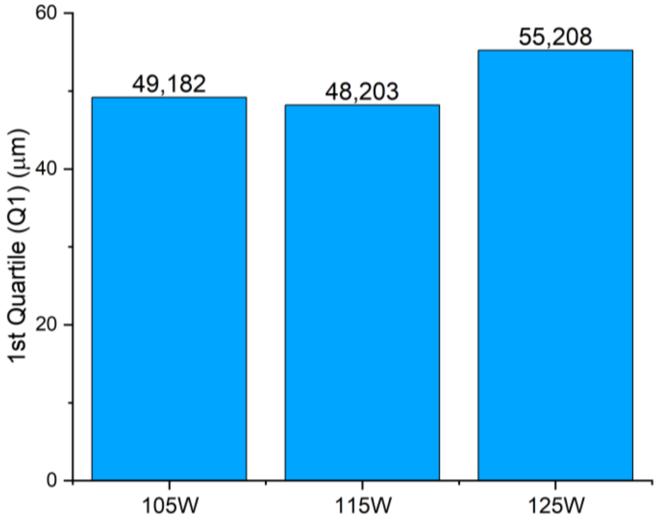

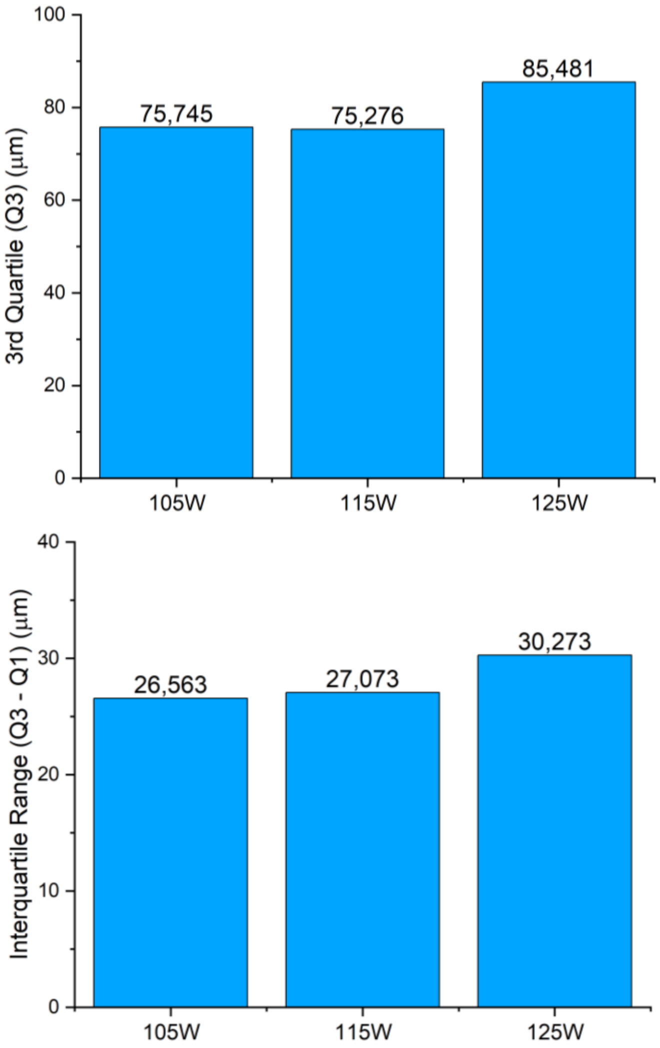

Figure 4.9: Comparison of the melt pool height data of the samples produced with different laser power.

Table 4.4: Data relating to the melt pool height of the samples produced with different laser power and their statistical analysis.

Data	N° measurements	Mean	Standard Deviation	Sum	Minimum
		µm	µm	µm	µm
105W_10x&20x_height	2001	63,28711	19,86912	126637,514	9,321
115W_10x&20x_height	1005	62,18899	20,72294	62499,939	8,606
125W_10x&20x_height	1231	71,26706	23,92392	87729,751	12,025

Data	1st Quartile (Q1)	Median	3rd Quartile (Q3)	Maximum	Interquartile Range (Q3 - Q1)	Range (Maximum - Minimum)
	µm	µm	µm	µm	µm	µm
105W_10x&20x_height	49,182	62,712	75,745	157,807	26,563	148,486
115W_10x&20x_height	48,203	61,626	75,276	145,454	27,073	136,848
125W_10x&20x_height	55,208	70,509	85,481	170,905	30,273	158,88

105W:

The sample shows a structure made up of linear melt pools with lower width and a height comparable to that of the 115W sample.

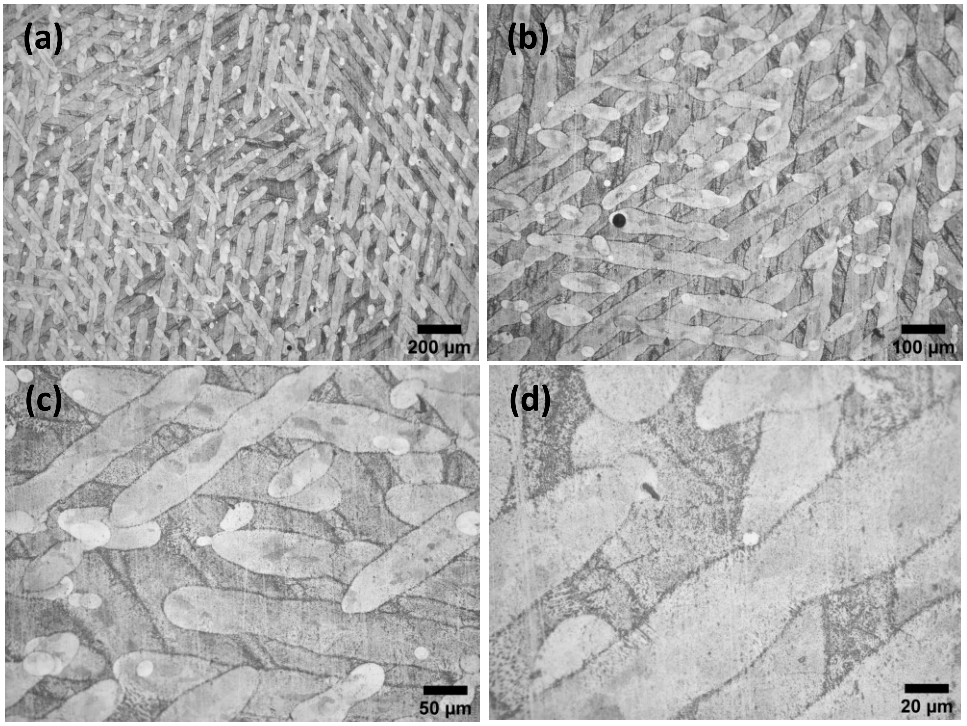

Figure 4.10: Pictures of the etched surface of the 105W sample, where the melt pools can be seen from above, under the optical microscope; (a) 5x magnification, (b) 10x magnification, (c) 20x magnification, (d) 50x magnification.

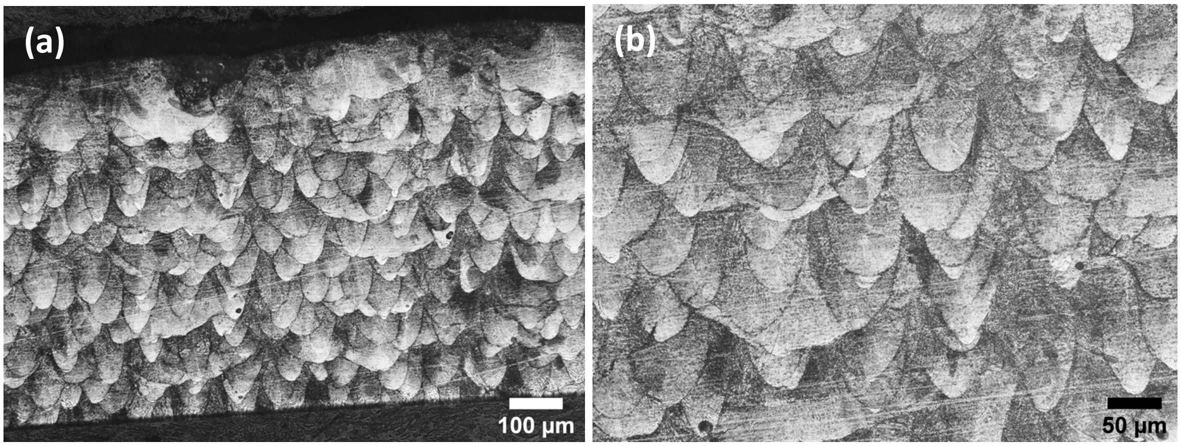

Figure 4.11: Pictures of the etched cross-section of the 105W sample, where the melt pools can be seen from the side, under the optical microscope; (a) 10x magnification, (b) 20x magnification.

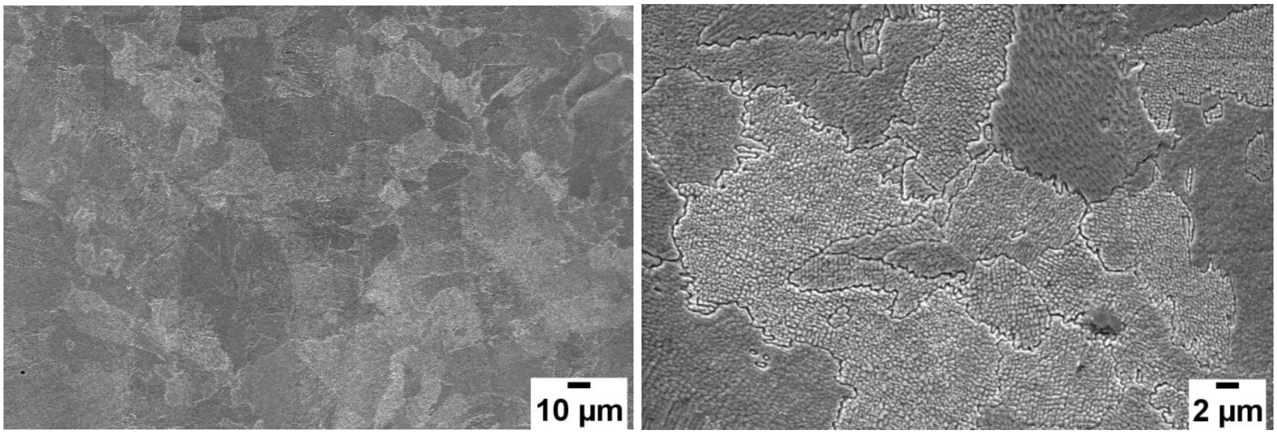

Figure 4.12: Pictures of the etched surface of the 105W sample, under the scanning electron microscope.

115W:

The sample has a structure made up of melt pools whit a greater width and a height comparable to that of the 105W sample.

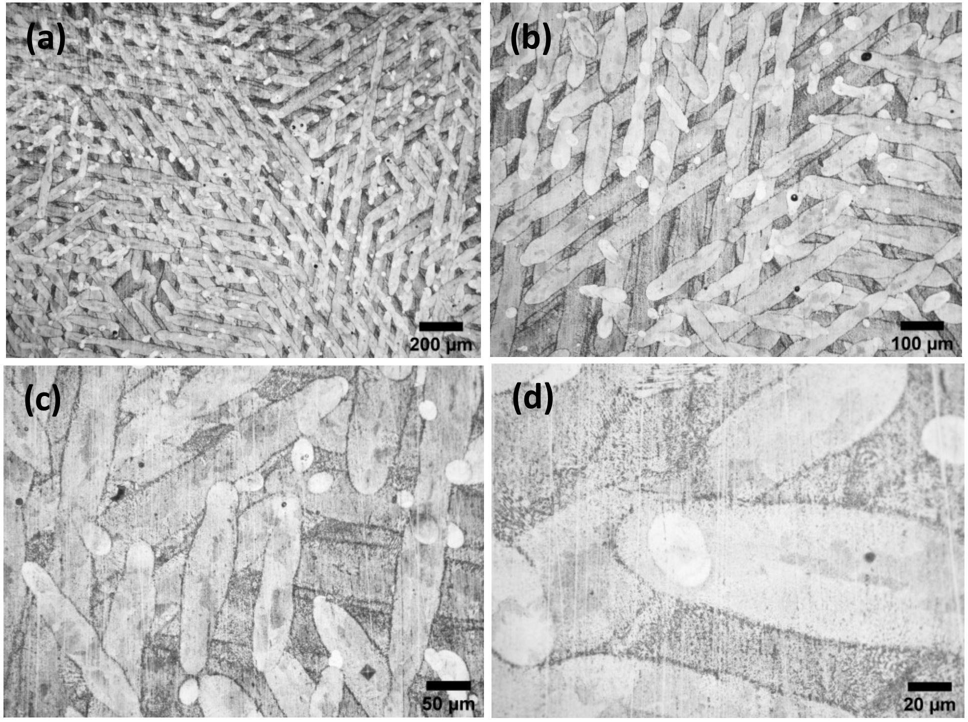

Figure 4.13: Pictures of the etched surface of the 115W sample, where the melt pools can be seen from above, under the optical microscope; (a) 5x magnification, (b) 10x magnification, (c) 20x magnification, (d) 50x magnification.

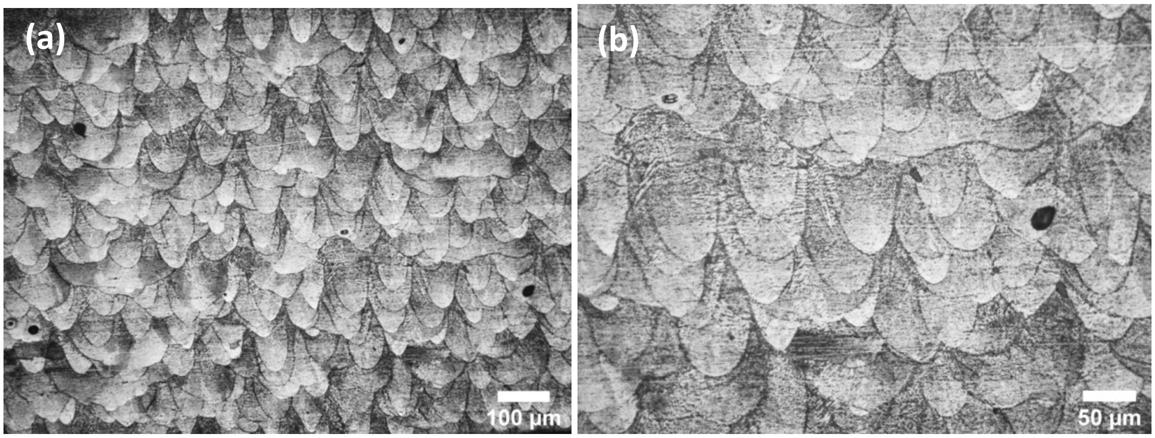

Figure 4.14: Pictures of the etched cross-section of the 115W sample, where the melt pools can be seen from the side, under the optical microscope; (a) 10x magnification, (b) 20x magnification

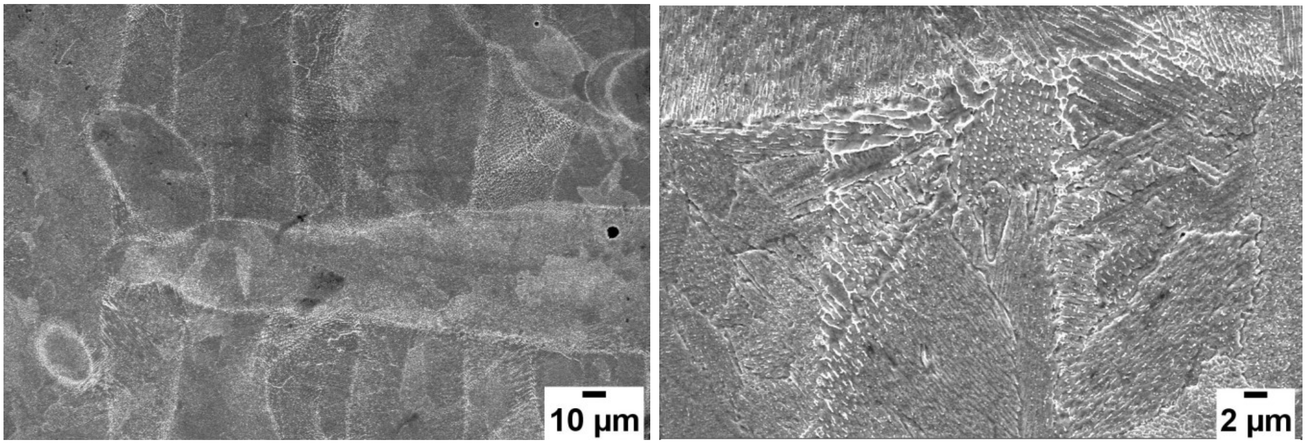

Figure 4.15: Pictures of the etched surface of the 115W sample, under the scanning electron microscope.

125W:

The sample shows the greatest melt pool height and a smaller width compared to that of the 115W sample.

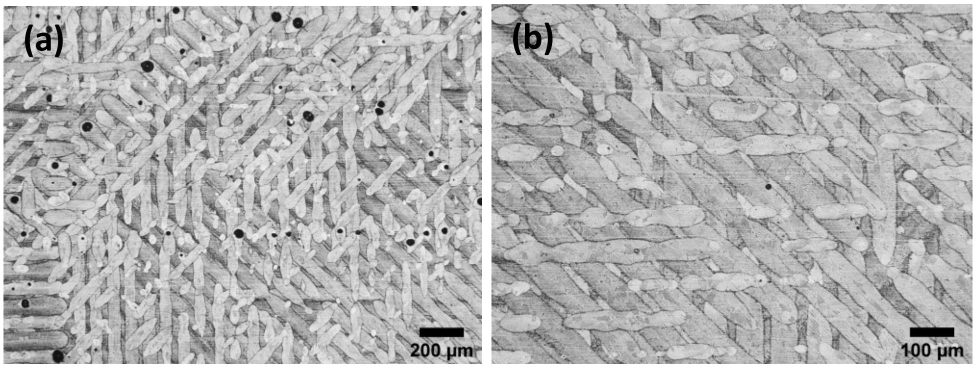

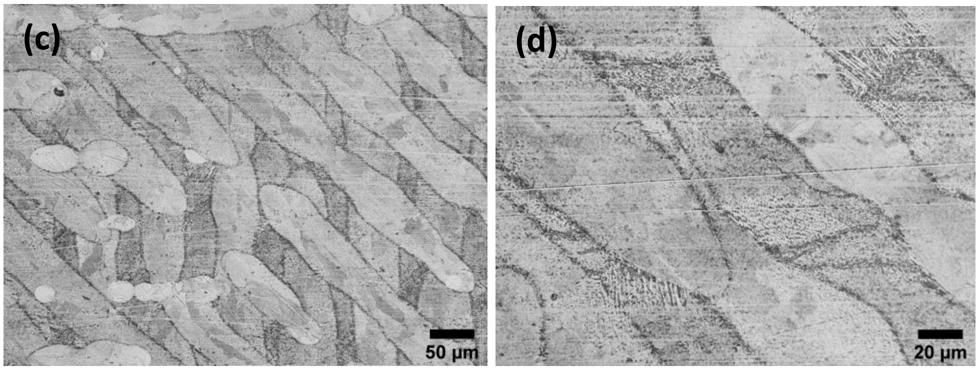

Figure 4.16: Pictures of the etched surface of the 125W sample, where the melt pools can be seen from above, under the optical microscope; (a) 5x magnification, (b) 10x magnification, (c) 20x magnification, (d) 50x magnification.

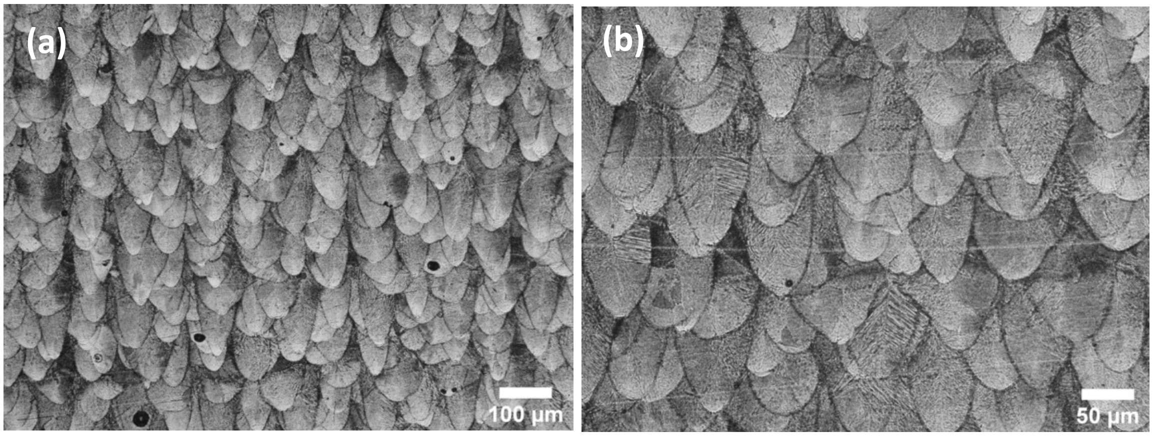

Figure 4.17: Pictures of the etched cross-section of the 125W sample, where the melt pools can be seen from the side, under the optical microscope; (a) 10x magnification, (b) 20x magnification.

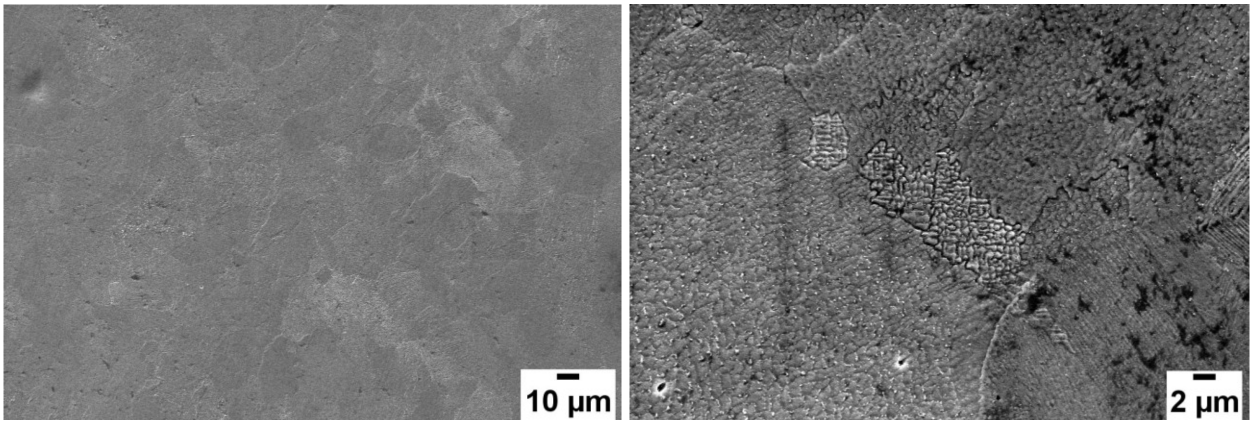

Figure 4.18: Pictures of the etched surface of the 105W sample, under the scanning electron microscope.

All samples show the typical structure of the selective laser melting technique, consisting of linear melt pools, the cross-section of which is conical. The conical shape is the result of the Gaussian distribution of the laser energy intensity, which manifests itself on the impact surface and propagates in the underlying layers. The pattern used for the laser scanning was in the shape of a checkerboard with an angle between the melt pools of the adjacent squares equal to 90 °. Between one layer and another, the orientation has been shifted by 90 °. The pattern described is recognizable in the images of the upper surface under the optical microscope.

From above, in the melt pools, the presence of grains is recognizable, and they are characterized by a colour that varies from darker to lighter shades, indicating a different crystallographic orientation. In the literature, it is possible to note that the prevailing microstructure of the Inconel 718 alloy produced with the SLM technique is the columnar grain one, even if at certain combinations of laser power and scanning speed the appearance of equiaxed grains is noted. The grains are oriented along the construction direction, guided by the thermal gradient that goes upwards due to the continuous passage of the laser layer by layer and the dispersion of heat downwards, where the support of the piece is present[51].

From the images of the cross-section under the optical microscope and better from the images of the surface under SEM, it is possible to notice the presence of thin and elongated structures inside the observable grains. These columnar structures are the cellular dendrites that develop during the solidification process of the melt pools. Cellular dendrites with a very fine thickness grow thanks to the high thermal gradient and the high cooling rate that develops inside the melting pool after the passage of the laser[85].

The dendrites as well as the grain boundaries and the melt pools are delimited by the presence of precipitates highlighted by the black colour (OM), or by white colour (SEM). These precipitates, which take on an elongated shape between one dendrite and the other, have been recognized in the literature as the Laves phase and consist of the stacking of irregular-shaped particles[90].

It seems that by increasing the laser power we pass from a situation in which the melt pools have a small width and a small height, to a situation in which the width reaches a maximum at the power of 115W and the height reaches a minimum. After the peaks, the width decreases again, while the height increases.

The increase in width of the melt pool due to the increase in laser power is attributable to the higher energy density that is supplied to the metal. More heat spreads to the dust surrounding the point of impact and therefore more metal melts. This happens to the detriment of the depth of the pool because the surface is the area where the convective flows of the molten metal converge and, rubbing on the side surface of the pool, it cause it to widen. The flow of molten metal starts from the centre and goes towards the sides and starts from the surface to go towards the bottom of the pool. This happens with a circular motion[51].

This situation is reversed when the energy density reaches very high values that cause the accumulation of a large amount of heat in a narrow area causing the dizzying increase in the depth of the melt pool at the expense of its width. In this case, the heat conduction towards the sides is irrelevant. This is what could have happened to the 125W sample.

The power of 115 W made it possible to obtain the best combination of height and width, indeed, the greater the width of the pool, the greater the overlap with the adjacent pools and therefore the fewer lack of fusion pores appear in the final product.

The dispersion of the height and thickness values of the melt pools, indicated by the interquartile value, follows the trend imposed by the mean and the median. The greater the value of the mean and median, the greater the dispersion of the data.

Box charts:

Melt pool width:

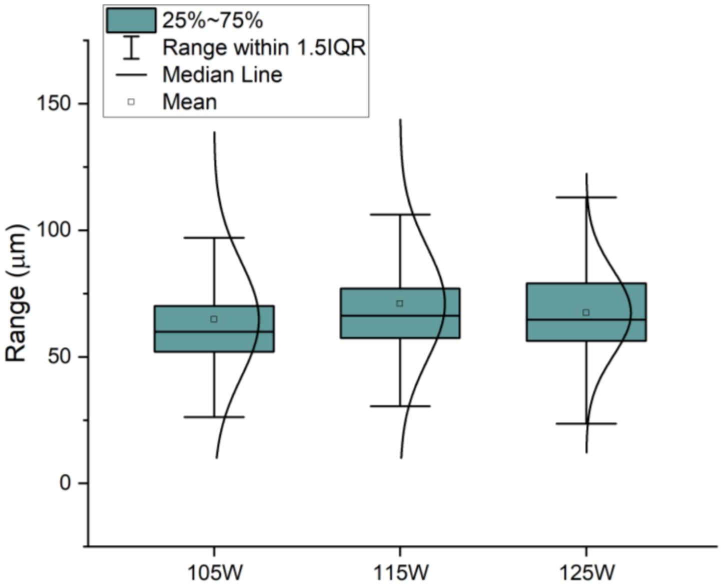

*Figure 4.19: Box chart showing the comparison of the melt pool width data of the samples produced with different laser power; the small square represents the mean, the line in the grey area represents the median, the grey area represents values in the range 25%~75%, the range delimited by the vertical line passing through the grey area contains the values within 1.5*Interquartile range.*

Melt pool height:

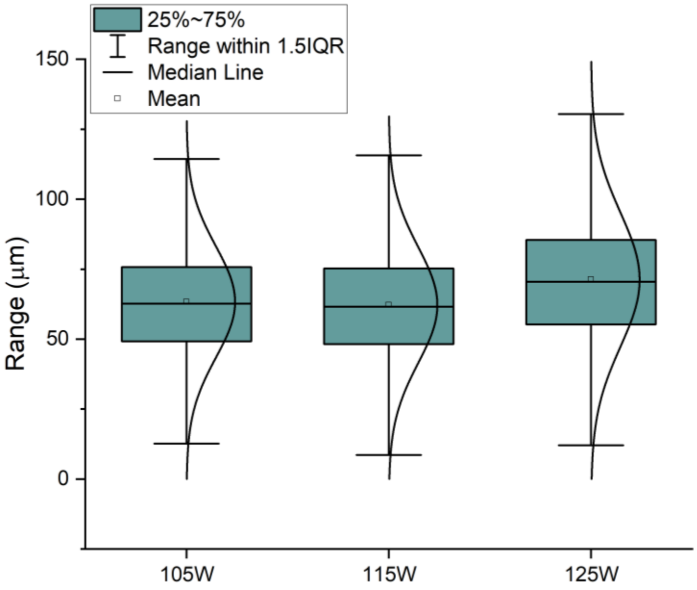

*Figure 4.20: Box chart showing the comparison of the melt pool height data of the samples produced with different laser power; the small square represents the mean, the line in the grey area represents the median, the grey area represents values in the range 25%~75%, the range delimited by the vertical line passing through the grey area contains the values within 1.5*Interquartile range.*

Conventional alloy 718:

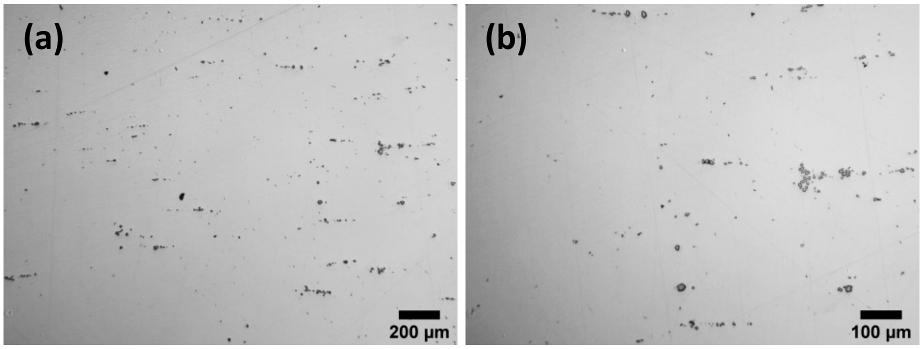

Figure 4.21: Pictures of the metal surface of the Bulk sample, under the optical microscope; (a) 5x magnification, (b) 10x magnification.

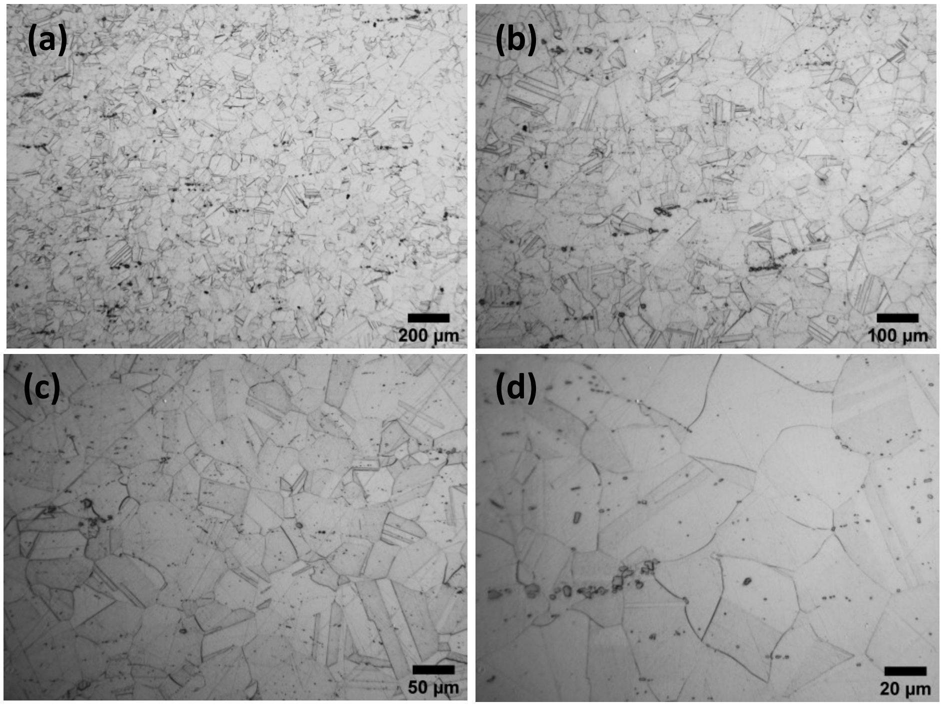

Figure 4.22: Pictures of the etched surface of the Bulk sample, under the optical microscope; (a) 5x magnification, (b) 10x magnification, (c) 20x magnification, (d) 50x magnification.

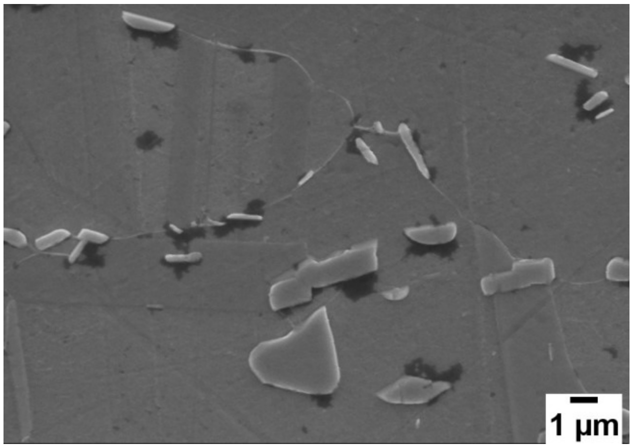

Figure 4.23: Pictures of the etched surface of the Bulk sample, under the scanning electron microscope.

In the Bulk sample an equiaxed grain microstructure of irregular shape, rich in twin crystals, was observed. Even without etching the surface, MC carbides are visible, not to be confused with surface porosity. At higher magnifications it is possible to notice small particles scattered in the grains, representing γ' and γ" reinforcement phases. It is noted that the grain boundaries are also highlighted by the precipitated phase. The plate-shaped precipitates at the grain boundary can be recognized as the δ phase, an undesirable phase. The precipitates are a direct consequence of the ageing process undergone by conventional materials.

4.3 Hardness

Vertical hardness:

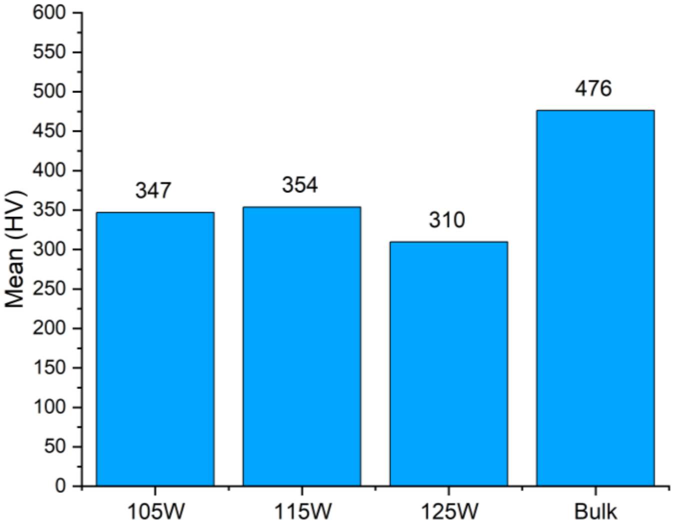

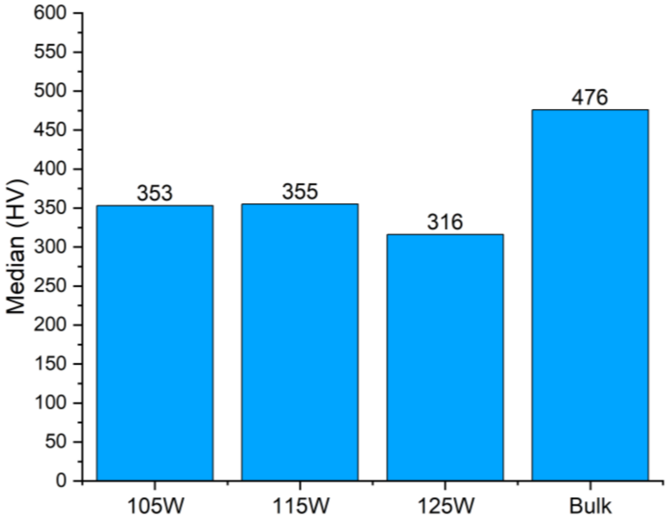

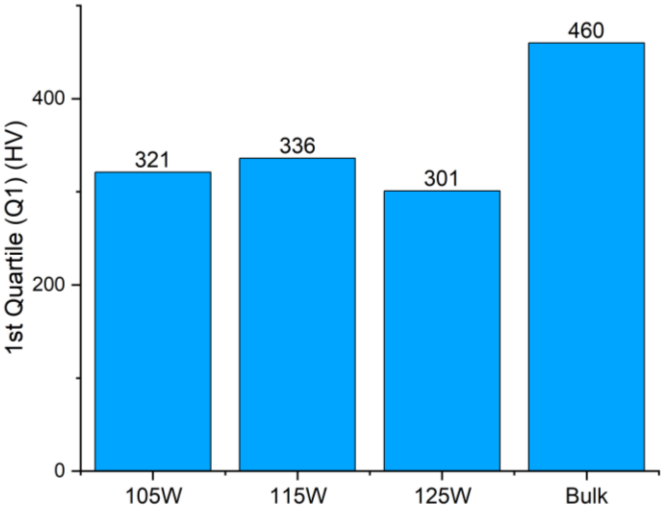

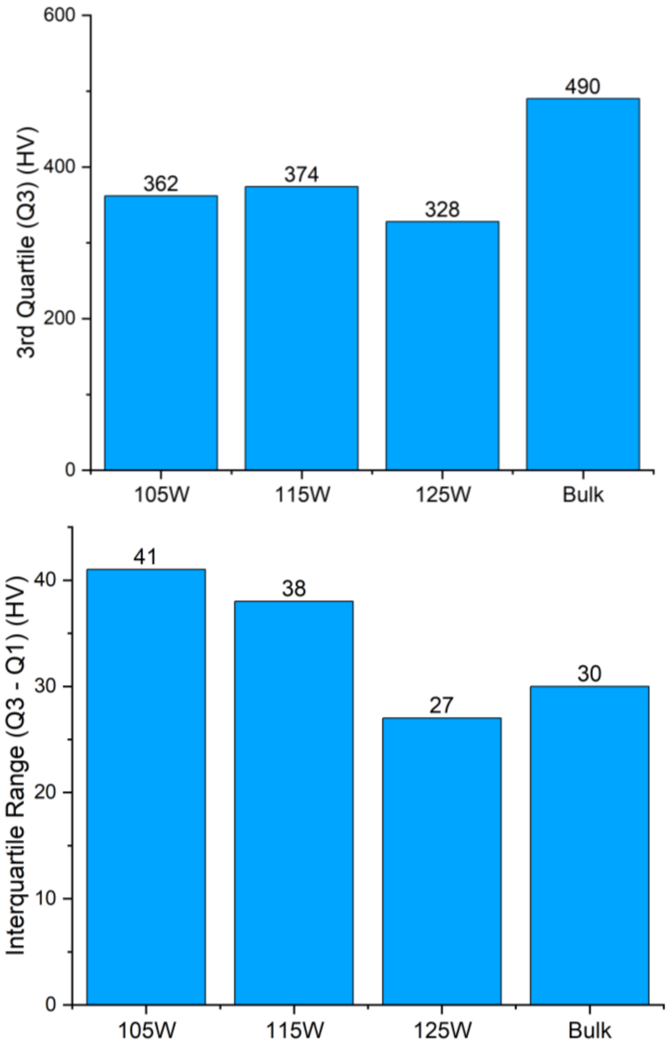

Figure 4.24: Comparison of the vertical hardness data of the samples produced with different laser power.

Table 4.5: Data relating to the vertical hardness of the samples produced with different laser power and their statistical analysis.

Data	N° measurements	Mean	Standard Deviation	Sum	Minimum
		HV	HV	HV	HV
Bulk_vertical hardness	26	476,15385	20,37389	12380	429
105W_vertical hardness	19	346,78947	26,69702	6589	286
115W_vertical hardness	19	353,78947	25,50943	6722	294
125W_vertical hardness	20	309,55	32,79357	6191	232

Data	1st Quartile (Q1)	Median	3rd Quartile (Q3)	Maximum	Interquartile Range (Q3 - Q1)	Range (Maximum - Minimum)
	HV	HV	HV	HV	HV	HV
Bulk_vertical hardness	460	476	490	520	30	91
105W_vertical hardness	321	353	362	394	41	108
115W_vertical hardness	336	355	374	386	38	92
125W_vertical hardness	301	316	328	351	27	119

Horizontal hardness:

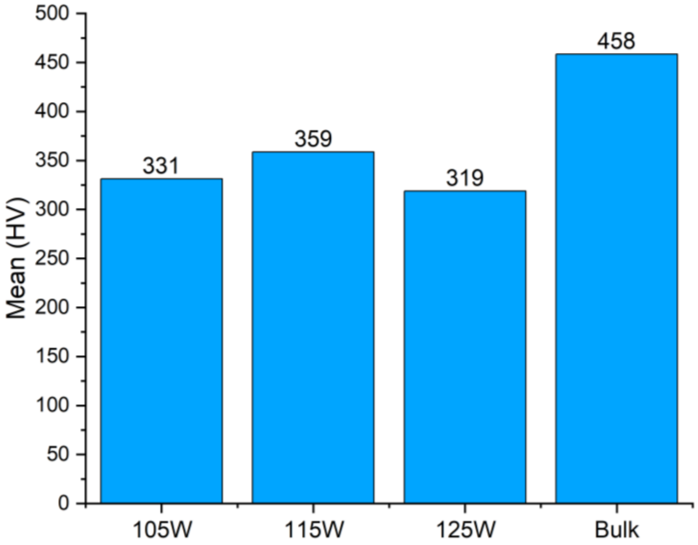

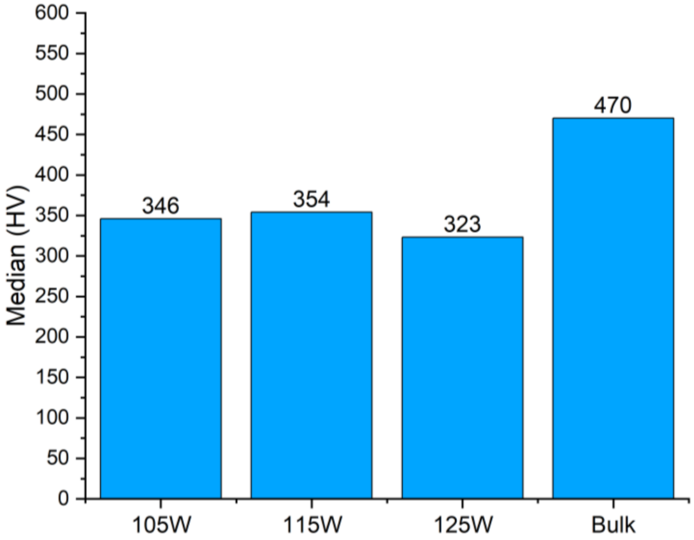

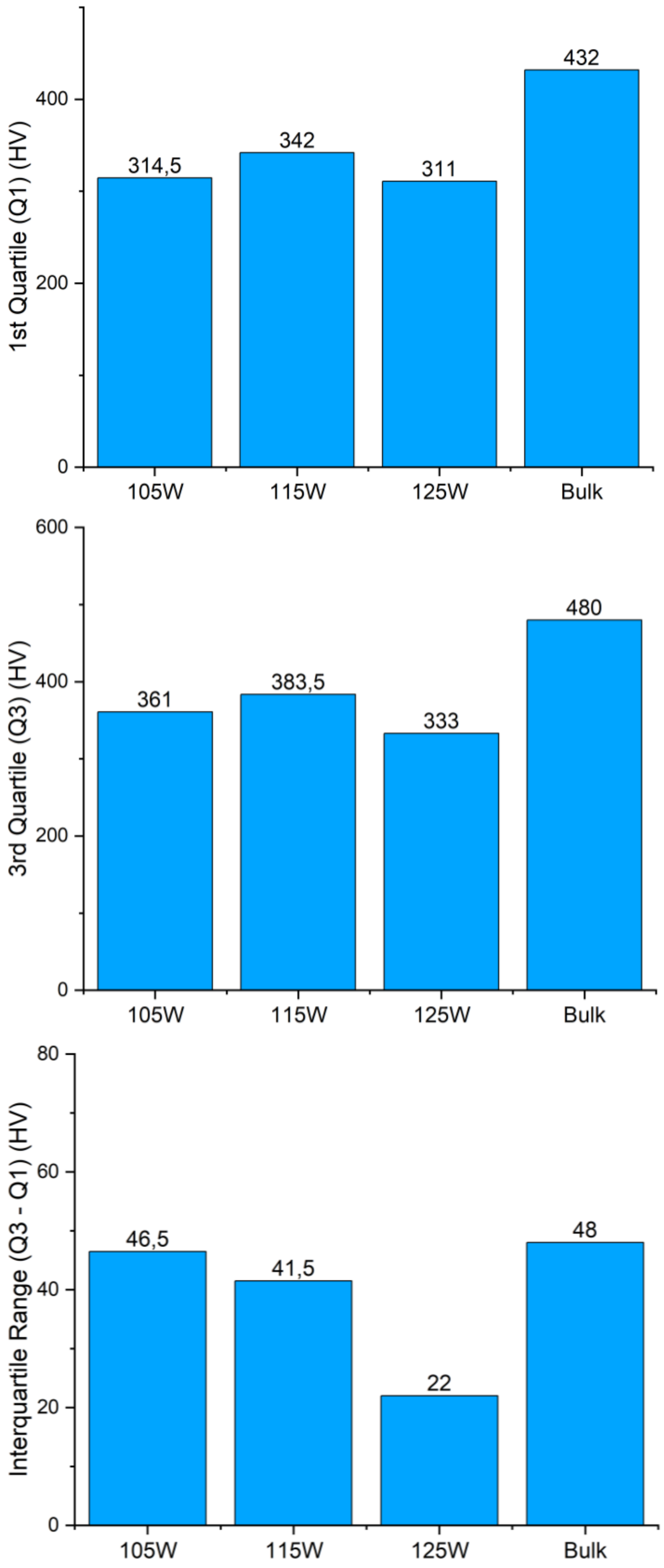

Figure 4.25: Comparison of the horizontal hardness data of the samples produced with different laser power.

Table 4.6: Data relating to the horizontal hardness of the samples produced with different laser power and their statistical analysis.

Data	N° measurements	Mean	Standard Deviation	Sum	Minimum
		HV	HV	HV	HV
Bulk_horizontal hardness	31	458,48387	33,89678	14213	396
105W_horizontal hardness	20	331,25	45,62649	6625	209
115W_horizontal hardness	20	358,6	23,81375	7172	323
125W_horizontal hardness	28	318,85714	25,76204	8928	209

Data	1st Quartile (Q1)	Median	3rd Quartile (Q3)	Maximum	Interquartile Range (Q3 - Q1)	Range (Maximum - Minimum)
	HV	HV	HV	HV	HV	HV
Bulk_horizontal hardness	432	470	480	512	48	116
105W_horizontal hardness	314,5	346	361	386	46,5	177
115W_horizontal hardness	342	354	383,5	399	41,5	76
125W_horizontal hardness	311	323	333	349	22	140

In this experience, the mean and the median show a ranking of the various materials valid for both, only the actual values of the two quantities vary slightly. Even considering the hardness along the vertical direction or the horizontal direction does not change the position of the different samples in the ranking. The bulk material is the one with the greatest hardness. The SLM samples have a significantly lower hardness than the reference samples. The 115W sample has a higher hardness value than all the other SLM samples, it is followed by the 105W sample. The power of 125W produced the material with the lowest hardness. The 115W sample has the right balance between scanning speed and power which leads to a peak of hardness, on the contrary, the 125W sample has a low hardness due to the excessive laser power used.

The hardness is influenced by the defects present in the samples and mainly by the microstructure that distinguishes them. The greater hardness of bulk materials is probably due to the ageing treatment undergone by the traditional sample which causes the precipitation of the reinforcing phases in small particles dispersed in the matrix. SLM samples have coarser precipitates placed between one dendrite and the other which can give rise to brittle fracture. The trend of the hardness is probably due to the trend in the defect density of the samples. The 115W sample is the one with the lowest pore density.

The interquartile value appears to follow the laser power. As laser power increases the interquartile decreases, indicating that the hardness distribution is smaller for the sample with higher laser power. This may be due to the more homogeneous distribution of pores in this sample.

Hardness distributions:

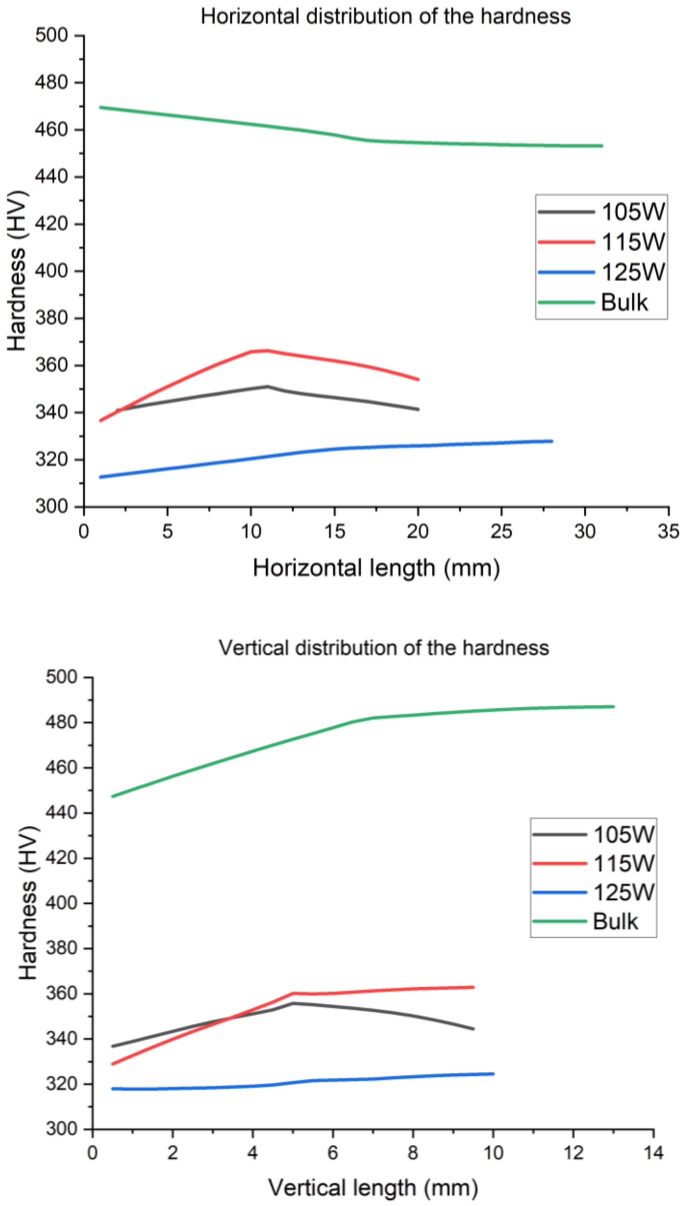

Figure 4.26: Comparison of the hardness distribution of the samples produced with different laser power, along the vertical and horizontal directions.

It can be seen that the distribution of hardness is not uniform. The values fluctuate around the average value with a difference of several tens of HV. This behaviour is observed both on bulk samples and SLM samples, probably due to the high sensitivity of the durometer to movements aimed at lifting the indenter tip. This procedure is carried out manually by turning a wheel connected directly to the tip, in this way every slight vibration is transmitted to the tip, which by moving, slightly deforms the impression left on the sample. Also due to the structure of the SLM samples, the hardness does not have a uniform distribution. The samples have areas of microstructural inhomogeneity such as the centre of the melt pools and their boundary. For this reason, many measurements were made on the sample.

Box Charts:

Vertical hardness:

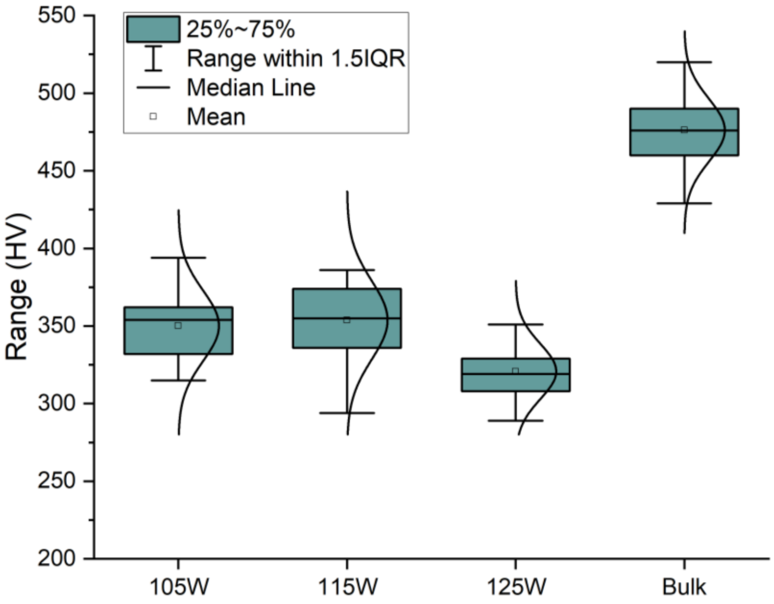

*Figure 4.27: Box chart showing the comparison of vertical hardness data of the samples produced with different laser power; the small square represents the mean, the line in the grey area represents the median, the grey area represents values in the range 25%~75%, the range delimited by the vertical line passing through the grey area contains the values within 1.5*Interquartile range.*

Horizontal hardness:

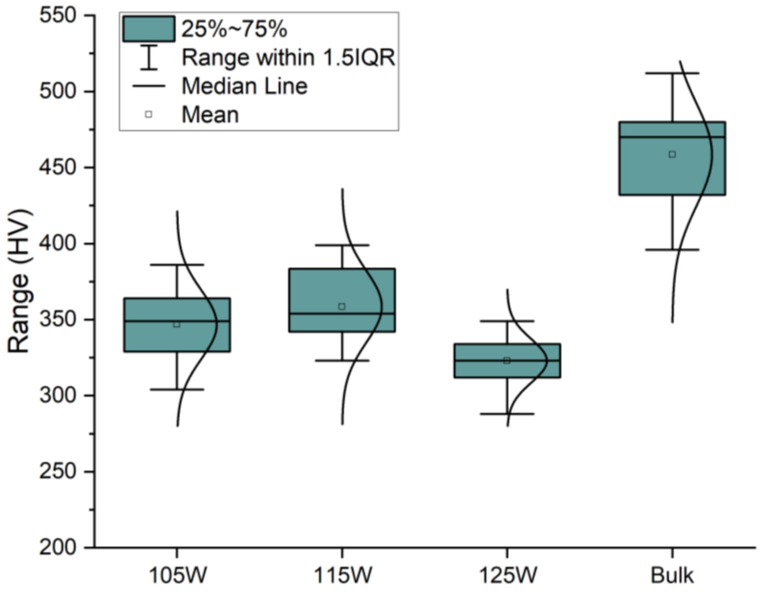

*Figure 4.28: Box chart showing the comparison of horizontal hardness data of the samples produced with different laser power; the small square represents the mean, the line in the grey area represents the median, the grey area represents values in the range 25%~75%, the range delimited by the vertical line passing through the grey area contains the values within 1.5*Interquartile range.*

4.4 Corrosion behaviour

4.4.1 Potentiodynamic polarization

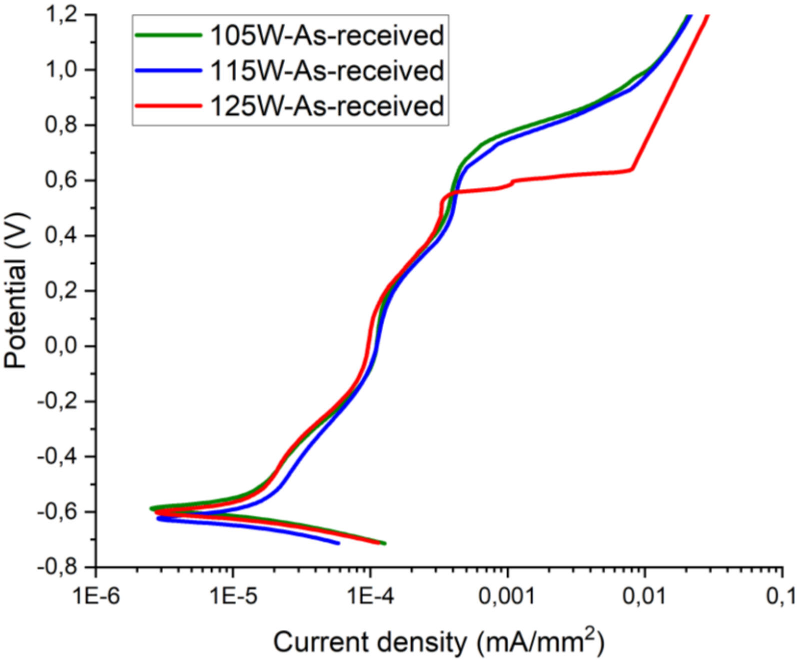

Figure 4.29: Potentiodynamic curves of the SLM samples produced with different laser power; As-received condition.

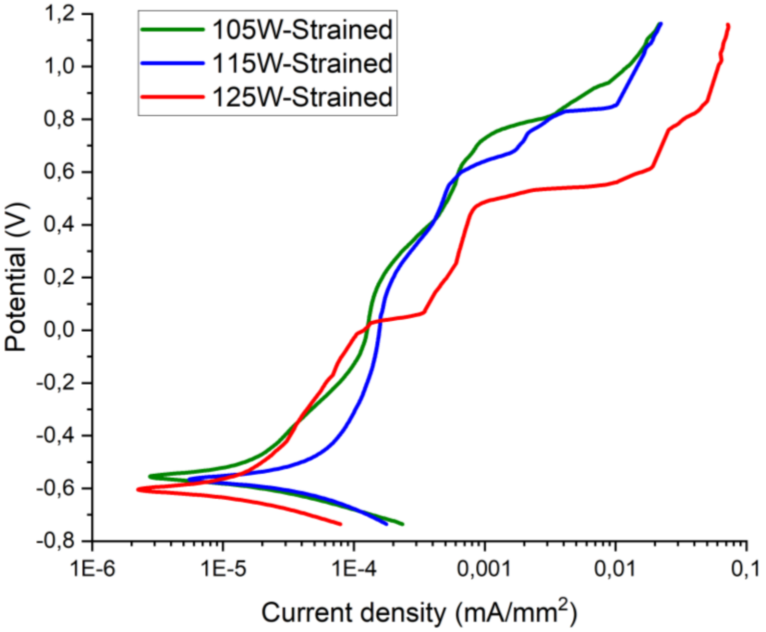

Figure 4.30: Potentiodynamic curves of the SLM samples produced with different laser power; Strained condition.

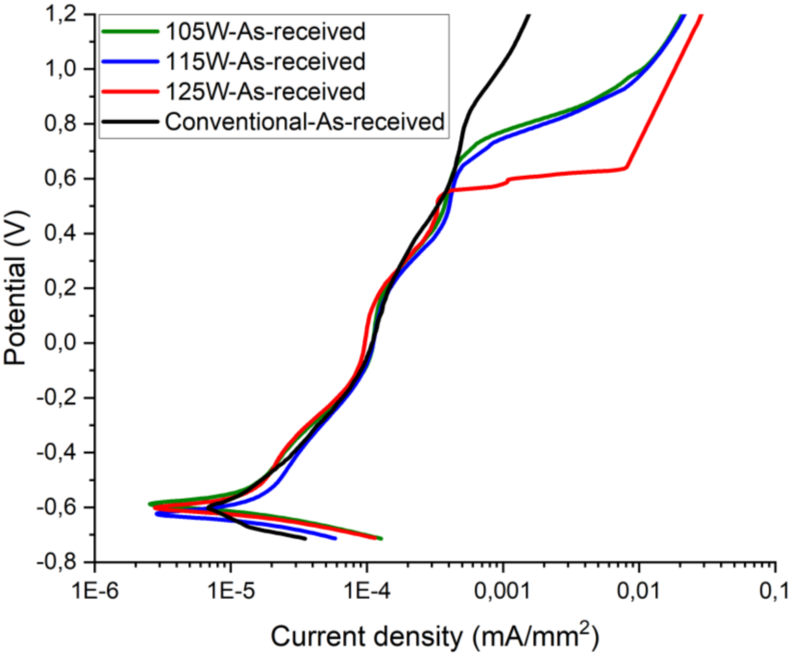

Figure 4.31: Comparison of potentiodynamic curves of all the samples; As-received condition.

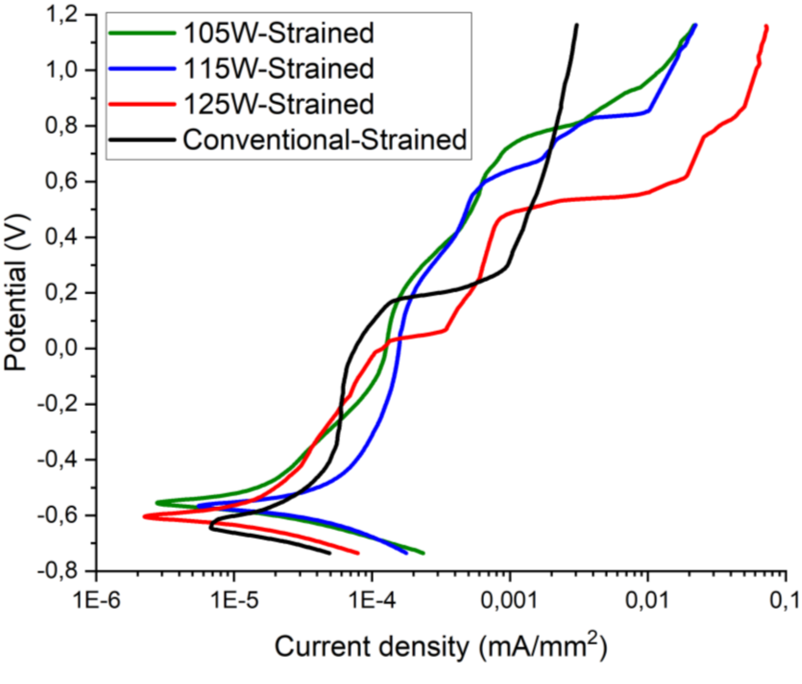

Figure 4.32: Comparison of potentiodynamic curves of all the samples; Strained condition.

Table 4.7: Data relating to the corrosion resistance of the samples, obtained by potentiodynamic tests.

	As-received				Strained			
	105W	**115W**	**125W**	**Conventional**	**105W**	**115W**	**125W**	**Conventional**
$E_{corrosion}$ (V)	-0,588	-0,624	-0,602	-0,602	-0,555	-0,597	-0,605	-0,629
$E_{pitting}$ (V)	0,670	0,649	0,523	0,834	0,708	0,599	0,447	0,162
i_{cor} (mA/mm^2)	2,54 E-06	2,84 E-06	2,76 E-06	6,81E-06	2,75 E-06	5,53 E-06	2,24 E-06	6,93E-06
i_{pit} (mA/mm^2)	4.87 E-04	5,11 E-04	3,34 E-04	5,58E-04	9,00 E-04	6,53 E-04	1,34 E-04	1,33E-04
Passive Range (V)	1,258	1,273	1,125	1,436	1,263	1,165	1,052	0,791

In these tests, the corrosion potential is identifiable as the point on the graph showing a negative current density peak. The passive region is noticeable due to the slight variation in current density with increasing potential. The pitting potential is identifiable as the point, after the passive region, where there is a rapid increase in current density with a slight increase in the potential. This leads to a noticeable change in the slope of the curve.

From the potentiodynamic measurements, it can be seen how the resistance to localized corrosion of the SLM samples is related to the laser power used. The sample 105W is the one showing the greatest resistance of the passive layer to pitting corrosion, represented by the greatest potential for pitting. The current density detected in the passive region, for this sample, is the lowest of all and this is another indicator of the greater compactness and strength of the passive layer. The 125W sample is the one showing the lowest resistance to localized corrosion, indeed, it has the lowest pitting potential evidenced by a surge in current density. The 115W sample has slightly less pitting potential than the 105W sample and a higher passive current density, indicating a less resistant and more defective passive film. This ranking is also repeated for champions under a tensile load. In practice, the greater the laser power, the greater the susceptibility of the material to localized corrosion. The difference between the pitting potential of 105W and 115W is not significant, indeed with the galvanostatic analysis, it is evident that the 115W sample has the most resistant passive film. In the as-received condition, the pitting potential of the conventional sample is the greatest of all, also showing a very slight change in the slope of the curve. Consequently, the passivity range of the material is also the largest. This indicates a high localized corrosion resistance of the conventional material in the tensile stress-free condition.

Deformation under tensile loading increased susceptibility to localized corrosion, decreasing the pitting potential compared to the as-received condition. The current density in the passive region also increased with the application of a tensile load. Furthermore, the corrosion potential has shifted to slightly less negative values. All this led to a reduction in the passive region of the graph, indicating that the passive layer has a potential range in which it is stable that has shrunk. In any case, the corrosion potential can be considered independent of the load conditions.

In conditions under tractive effort, the ranking is overturned, indeed, the conventional sample shows almost the lowest pitting potential, and only the 125W sample has a lower potential. In terms of potential drop, the conventional sample is the one showing the most drastic drop (678 mV). This indicates a low resistance of the passive layer to nucleation and propagation of SCC.

4.4.2 Galvanostatic test

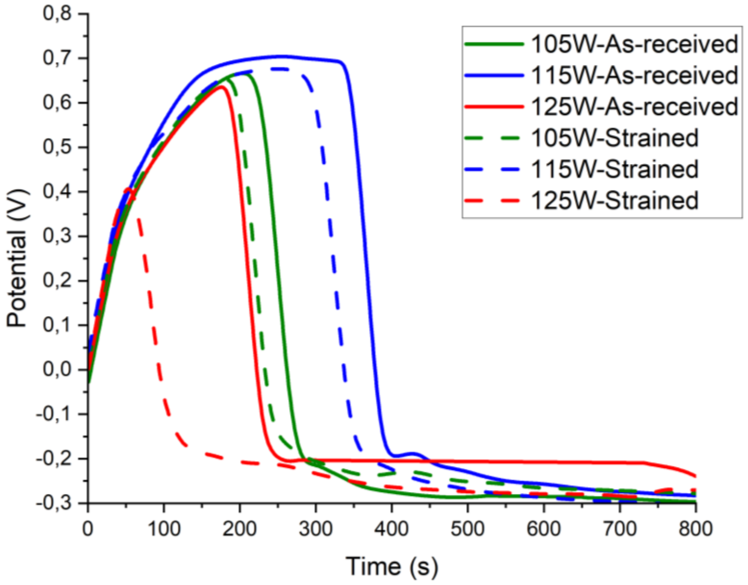

Figure 4.33: Galvanostatic curves of the SLM samples produced with different laser power; As-received condition compared to strained condition.

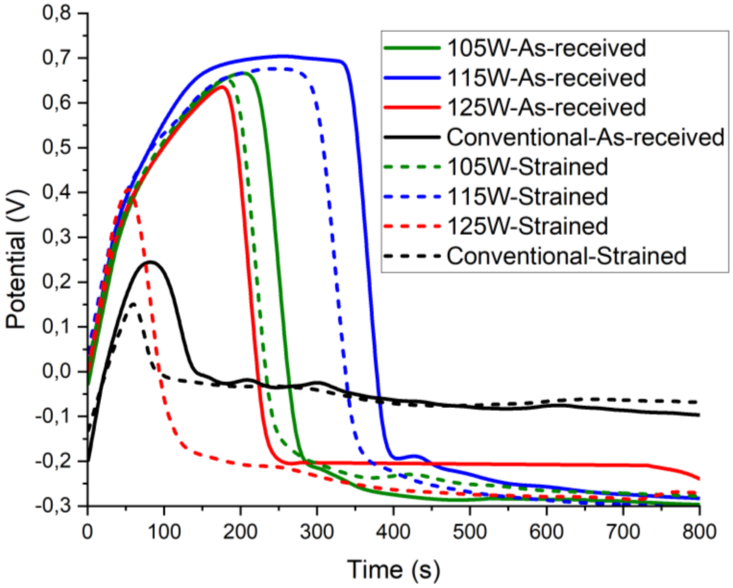

Figure 4.34: Galvanostatic curves of all the samples; As-received condition compared to strained condition.

Table 4.8: Data relating to the corrosion resistance of the samples, obtained by galvanostatic tests.

	As-received				Strained			
	105W	**115W**	**125W**	**Conventional**	**105W**	**115W**	**125W**	**Conventional**
$E_{breakdown}$ (V)	0,666	0,7	0,635	0,244	0,652	0,675	0,407	0,15
$T_{breakdown}$ (s)	286	401	250	143	259	370	128	97

In these tests, the breakdown potential of the passive layer is recognizable as the potential value at the top of the largest peak of a sample. Furthermore, it is possible to calculate the time necessary for the breakdown of the passive layer, measuring the seconds at the point where the potential peak has passed and reached a constant value.

The results of the galvanostatic tests show once again how there is a correlation between laser power and resistance of the passive layer. The 115W sample has the highest passive film breaking potential and breaking time. While the 125W sample has the lowest values. Sample 105W has intermediate values. This ranking is also repeated for the samples under tensile stress, even if the values of potential and time have been reduced. The 125W sample shows a dizzying drop in potential and time. This is because the tension causes the activation of the numerous pores which are present in this sample, and which were not yet classifiable as active sites without the imposition of tension. Conventional material exhibits the lowest rupture potential, both as-received and under tensile stress conditions. Also in this case, under stress, both the breaking potential and the breaking time are reduced. The fact that, under galvanostatic conditions, the resistance ranking has changed indicates that the SLM samples have greater resistance and, above all, greater integrity of the passive layer.

Galvanostatic tests show more accurately the sensitivity of the passive layer to localized corrosion. Since, in potentiodynamic tests, the continuous increase of the potential weakens the passive layer more severely. On the contrary, with the galvanostatic tests, it is possible to understand the behaviour of the passive layer in stationary conditions.

The property that has been found to vary between the SLM samples examined is porosity, which is closely related to the process parameters. In particular, both the surface area of the pores and the density of the pores, represented by their percentage on the surface, are the factors that determine the difference in the results obtained during the corrosion tests.

It is widely discussed in the literature that porosity plays an important role in determining the localized corrosion resistance of alloys obtained through additive manufacturing[91,92].

The 115W sample shows a higher localized corrosion resistance than the 105W sample due to its lower percentage of pores, leading to the presence of a smaller number of sites that are attacked and that will form stable pits. The 125W sample shows the lowest localized corrosion resistance because it has a high percentage of pores of considerable size, indeed, there is a dense network of large pores which are the main targets of localized corrosion.

The pore size is a very important factor, as there is a critical size above which the pore is a preferentially attackable site. This is precisely the reason that leads to the reduction of the corrosion resistance of the samples following the imposition of the tensile load. The tensile load makes the pores, which would normally be below the critical size, active sites because the tip of the pore inside the surface represents a zone of stress concentration that weakens the passive film formed inside and makes it vulnerable to breakage which consequently leads to the nucleation of an SCC, which tends to propagate more easily thanks to the traction tension on the tip.

4.5 SCC

105W:

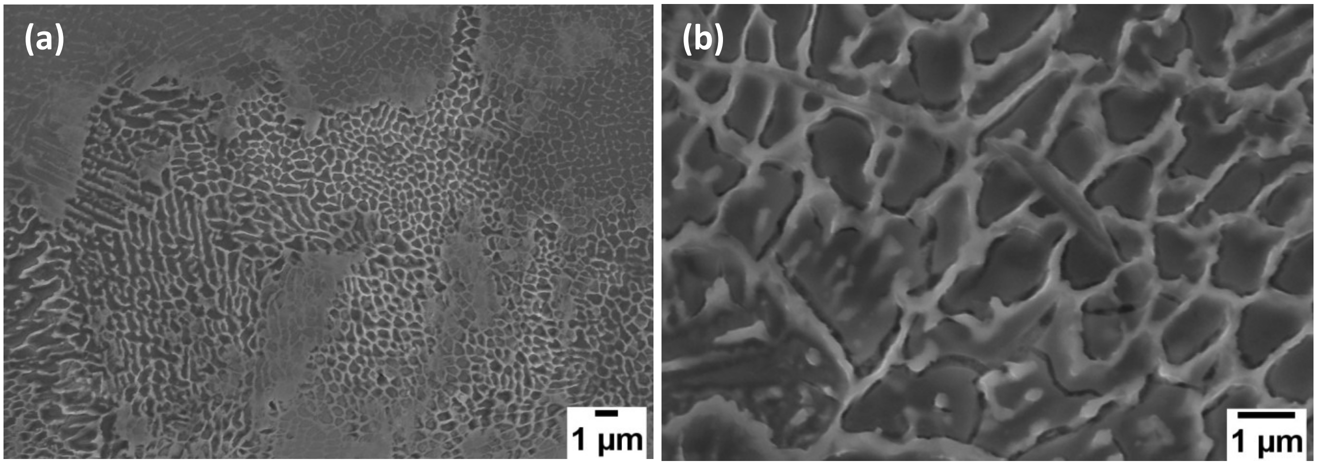

Figure 4.35: Pictures of the surface of the 105W sample, under the scanning electron microscope; (a) surface after galvanostatic test; (b) surface after galvanostatic test under tensile stress, on which stress corrosion cracks are noted.

115W:

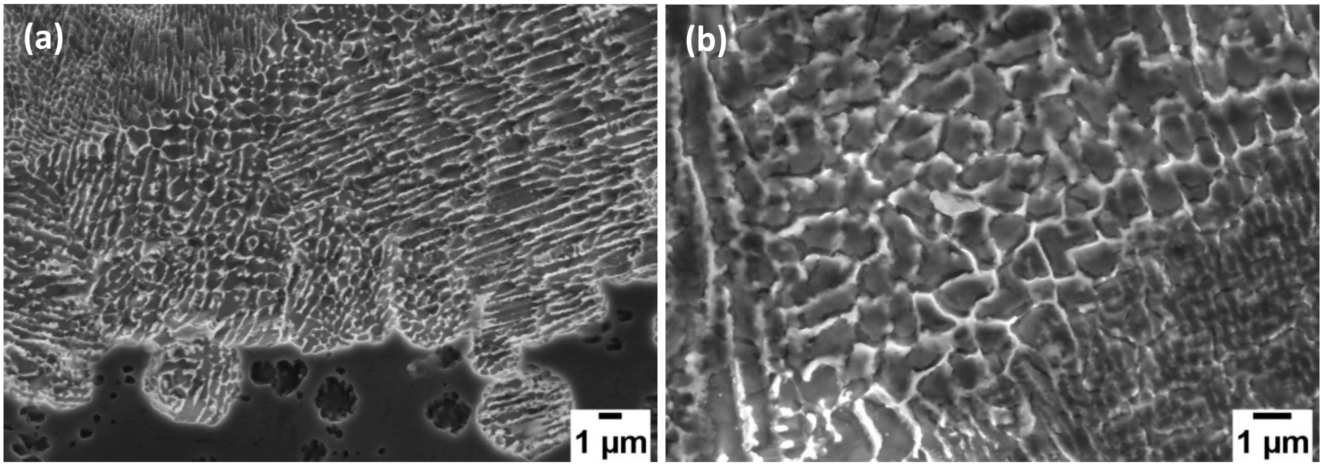

Figure 4.36: Pictures of the surface of the 115W sample, under the scanning electron microscope; (a) surface after galvanostatic test; (b) surface after galvanostatic test under tensile stress, on which stress corrosion cracks are noted.

125W:

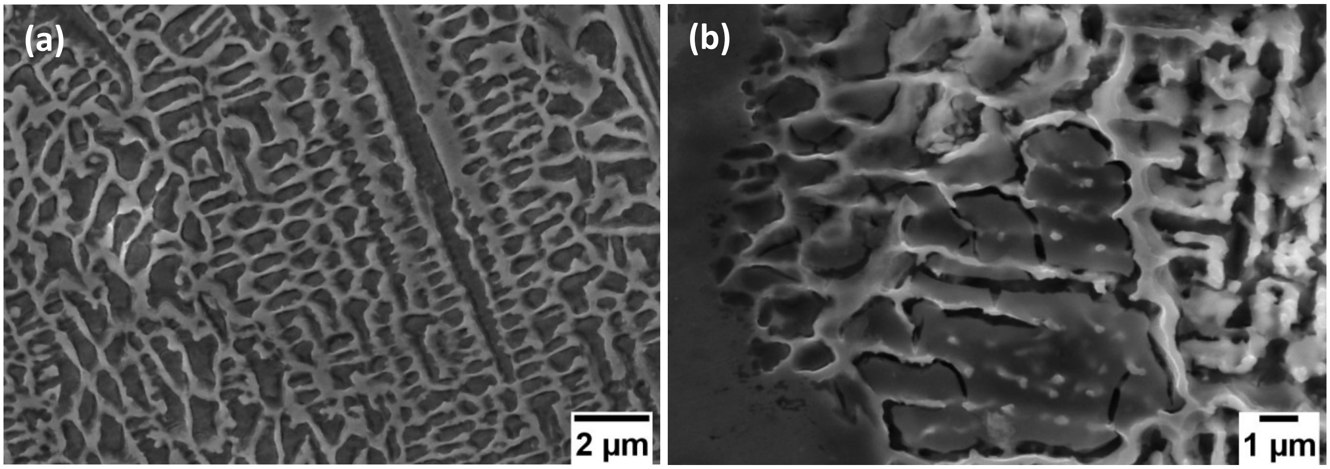

Figure 4.37: Pictures of the surface of the 125W sample, under the scanning electron microscope; (a) surface after galvanostatic test; (b) surface after galvanostatic test under tensile stress, on which stress corrosion cracks are noted.

Conventional material:

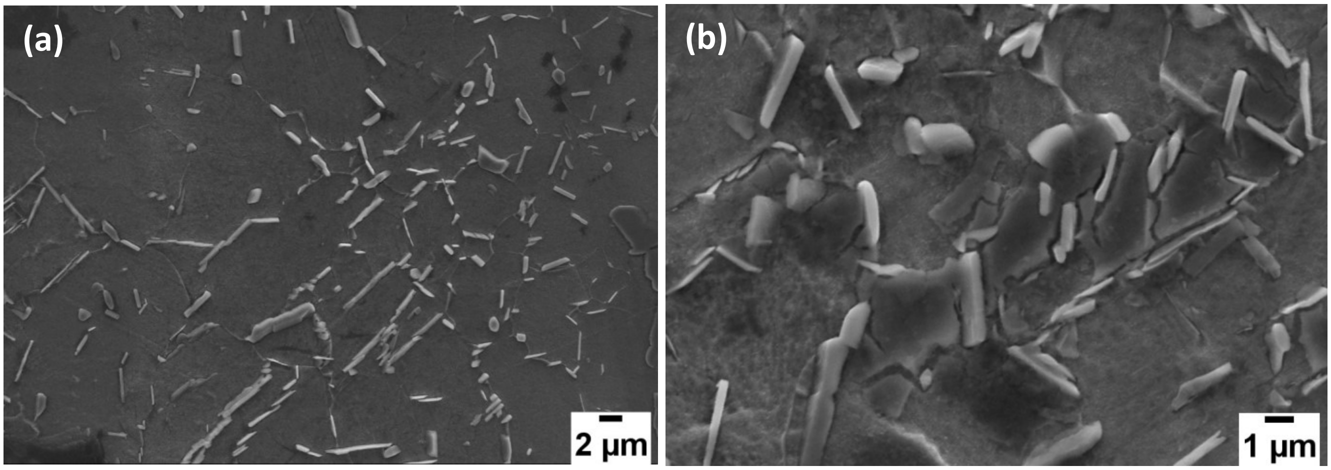

Figure 4.38: Pictures of the surface of the Bulk sample, under the scanning electron microscope; (a) surface after galvanostatic test; (b) surface after galvanostatic test under tensile stress, on which stress corrosion cracks are noted.

On the SLM samples under as-received conditions, after the galvanostatic test, selective dissolution of the matrix inside the subgrain is noted, with the grain boundary remaining intact and protruding from the surface. By applying the tensile stress, it was possible to initiate and nucleate the stress corrosion cracks, which are especially noticeable in the matrix immediately adjacent to the grain boundary, indicating that this is an area very susceptible to corrosive attack.

Conventional samples under as-received conditions, after the galvanostatic test, also showed a preferential dissolution of the matrix compared to that of the precipitates dispersed therein, which protrude from the metal surface. After the application of the tensile stress during the galvanostatic test, the presence of cracks originating in the matrix adjacent to the precipitates and propagating between one precipitate and another is noted.

The fact that the cracks in the SLM samples were mostly confined to the subgrains made these samples more resistant to localized corrosion, on the contrary, the fact that in the conventional samples the cracks were free to propagate in the matrix adjacent to the δ phase precipitates has made these samples less resistant. The precipitates and the boundaries of the subgrains appear to be much more corrosion-resistant than the matrix.

5 Discussion

The characteristic columnar dendritic microstructure is formed due to a very low undercooling that precedes the solidification front. This is possible due to the high rates of solidification. Specifically, the parameters that determine the formation of a given microstructure are the growth rate R (mm/s) and the temperature gradient G (°C/mm). These values make it possible to determine the mode of solidification and the size of the solidification structure. The solidification mode is a function of the G/R ratio. A low G/R ratio favours the formation of equiaxial grains while a high G/R ratio promotes planar growth. Intermediate values allow the formation of elongated structures towards the direction of solidification. This is the case with cellular dendrites and columnar grains. The product G x R allows the determination of the size and spacing of cells and dendrites. The higher the value of R, the smaller the size of the solidification structures.

In the work of Nadammal et al. [93], The length of the hatch was compared with the microstructure and residual stresses. Columnar dendrites were detected in both the short-hatch and long-hatch samples. Curves were detected in the grain boundaries, in the direction perpendicular to the building direction, in the region of overlap of two melt pools, due to the interaction between the newly created melt pool and the previously solidified melt pool, through the construction direction. The heat flow in the melt pool is maximum along the direction connecting the support plate with the newly built area of the workpiece. The overlapping of the melt pools in the marginal regions alters the heat flow in the pool and causes curvature during solidification.

In the case of a short hatch length, columnar grains are formed, due to the high temperatures and the higher temperature gradient that follows. Previously solidified layers act as a substrate for grain growth in subsequently deposited layers, inducing the formation of elongated grains. Short hatch lengths provide less time for the previously deposited substrate to cool down by inducing a greater thermal gradient along the construction direction. In the case of the sample with the longest hatch there is a situation in which the temperature is lower, and so is the thermal gradient, since the material has more time to cool down before the passage of the next layer. This is also thanks to the high thermal conductivity of Inconel 718. In this condition, there are finer structures and lower residual stress. The successive layers do not fuse, not inducing the growth of an elongated microstructure but rather of an equiaxed structure. The localized heat flow, due to a short hatch length, is therefore the cause of epitaxial growth parallel to the building direction.

The longitudinal component of residual stresses (RS) in the plane is compression for the sample with a longer hatch while it is traction for samples with a shorter hatch. Near the edges, both samples have residual compressive stresses. The shorter hatch sample has higher residual compressive stresses along the building direction. The tensile stress state present in the centre of the sample completely transformed into a compression stress state near the edges, for both samples. As for the RS in the transverse direction to the plane, it was noted that they are almost totally released in the case of the sample with the longest hatch, while they appear as compression RS in the case of the sample with the shorter hatch. This difference is based on the different thermal histories of the two samples. Shorter hatches are fused without significant remelting, which would allow the relaxation of stress. The compressive state on the edge of the sample with a shorter hatch length is caused by rapid cooling. This does not happen for the sample with a longer hatch since it already has a long cooling time for each hatch.

In practice, the adoption of a scanning pattern that uses a short length of the hatch, such as the checkerboard one used in the experiment described in this thesis, allows the reduction of the residual stresses that are generated because the previously built layer inhibits the free deformation of the one just deposited. In addition, the residual stresses are for the most part compression, therefore less burdensome for the formation of cracks. The state of tension found by Nadammal et al. [93] is therefore comparable to that present in the 718-SLM samples under examination. At the centre of the sample can be found residual tensile stresses that can cause increased susceptibility to corrosion.

Conventionally produced samples have undergone heat treatments at high temperatures, i.e. solubilization and hardening by ageing in two stages, which can significantly reduce the magnitude of RS and their anisotropy. Tensile corrosion resistance must be evaluated under tensile load conditions to consider the actual role of residual stresses on the resulting stress state.

The important role of compression RS on localized corrosion resistance is evident from the work of Cruz et al. [94]. Samples of 316L steel, produced with SLM technology, were used. It was noted that by increasing the heat treatment temperature and thus reducing more and more the residual stresses present in the sample as constructed, the pitting potential decreased towards less noble values. With the pitting potential, the passive window also decreases. Thus, mainly, anti-stress heat treatments appear to be harmful in the context of opening pits in SLM 316 L samples. The passive current shows the opposite trend, that is, it increases with the decrease of the compression stresses.

The current density detected during anodic polarization consists of the current relative to the formation reaction and the current relative to the passive film destruction reaction, which, according to the Point Defect Model (PDM), occur simultaneously when the metal is in the passive state. The kinetics of film growth is related to increased charge transport through the metal/film and film/electrolyte interfaces and through the film itself. The lower passive current density for samples with high compression RS values is probably due to the presence of a more compact passive film due to compression stresses that slightly shorten the interatomic distances in the metal lattice. The greater compactness of the film induces reduced kinetics of migration of point defects through the passive film, during the application of the potential, and this results in a low passive current. So, compression stress hinders the migration of point defects through the film, reducing the passive current generated and increasing the value of the pitting potential due to the increased resistance to charge transport.

The determination of the density of the donor species within the passive film is correlated with the residual stresses of the sample. It was found experimentally that the sample that underwent the greatest distension of RS has the highest donor density. In contrast, the SLM sample as constructed, with the higher compression RS, has a lower donor density. Considering a passive film, donors are point defects such as oxygen vacancies or metal interstitials, defined in the case of a semiconductor oxide layer of type n. The reduction of compression stresses, therefore, implies an increase in the concentration of point defects and therefore an increase in the kinetics of the interfacial reactions to the metal/film, film/solution interfaces and also within the passive film. This is the reason for the increase in passive current density. The Cl− ions at the film/electrolyte interface are adsorbed into the passive film, where they combine with oxygen vacancies. Higher concentrations of these defects can cause greater adsorption and greater penetration of Cl- ions into the passive layer. This destabilizes the film and induces the beginning of a pit.

On the contrary, compression RS seems to reduce the ability of the metal to repassivate. This is because RS, by reducing the concentration of defects in the passive film, decreases the growth kinetics of the oxide, also linked to the transport of species through the passive film.

From this work the beneficial properties of compression stresses on the localized corrosion susceptibility of samples produced by Selective laser melting are evident. Unfortunately, the different thermodynamic characteristics of Nickel-Iron superalloys compared to those of 316L steel lead to a tensile state in the centre of the sample. This causes the lower resistance to localized corrosion of alloy 718 compared to a condition of absence of stress as in the case of a piece produced with traditional methods and which has undergone heat treatments.

Unlike residual stresses, hardness is not a significant factor for resistance to the appearance of SCCs (stress corrosion cracks). Traditional samples have a greater hardness due to the presence of finely dispersed precipitates due to the ageing treatment, but this does not increase their resistance to stress corrosion. The predominant factor which determines the greater tensile corrosion resistance of SLM samples seems to be related to the microstructure characteristic of this process.

The stress corrosion cracking susceptibility of traditional 718 samples was studied by Wang et al. [95], taking into account the structure of the precipitates. Following annealing and double ageing treatments performed at different temperatures and for different times, the presence of the δ phase in various forms was detected. This phase was like platelets or similar to a film around the edges of grain boundaries, or in both forms. The time-temperature transformation (TTT) diagram of alloy 718 allows the prediction of the fact that below 1030 °C the δ phase is formed in a plate shape, also called the high-temperature δ phase. At 750 °C the film-like δ phase begins to form at the grain boundaries, and it is called the low-temperature δ phase. The platelet-shaped phase takes many hours while the film-shaped phase takes a few minutes to precipitate. Precipitation is also influenced by the magnitude of the cold work that the material undergoes between the various heat treatments. In addition, the presence of the reinforcement phases γ′ and γ″ was detected, which came in the form of larger precipitates, the higher the ageing temperature. While the ratio γ′/γ″ is influenced exclusively by the chemical composition, influencing the mechanical properties.

Precipitates γ' and γ" are called reinforcement phases because they act as barriers for the movement of dislocations during plastic deformation. Once a sliding band has formed during deformation, it creates an easier path for subsequent dislocations. The planar sliding due to the dislocations limited to the bands is dominant, and this induces greater local stress at the intersection of the sliding band with the grain boundaries. The greater the sliding in the bands (channels), the greater the number of intergranular cracks. Thus, widely separated bands will contain greater deformation per band and impose greater stress on the channel. Intersections between the band and the grain boundaries that do not allow the transfer of flow to the next grain have a much greater probability of forming intergranular cracks. The size of the precipitates γ′ and γ" is the factor that determines the localization of the deformation and therefore the susceptibility to cracking. The smaller the precipitates, the greater the sliding systems, therefore the lower the susceptibility.

The sample with the high-temperature δ phase located on the grain boundary and in the matrix had the highest susceptibility to SCC; The sample with the mixed δ phase, high-temperature and low-temperature, had the intermediate SCC susceptibility, the same happened for the sample with only the low-temperature δ phase; The sample with no δ phase was the one with the lowest SCC susceptibility. It has been noted that the platelet-shaped δ phase, deposited on the grain boundary, is the one that has the greatest ability to induce the generation of intergranular cracks.

A surface oxide analysis was also performed, and it was found that the δ phase can be oxidized under primary water conditions, forming a fragile niobium oxide. This oxide is separated from the matrix by chromium oxide, which surrounds the δ phase. This oxide facilitates the detachment of the precipitate from the matrix. As the applied stress increases, the oxide is broken and exposes the internal matrix to the corrosive environment generating an initiation site for intergranular cracks.

Therefore, the density, shape, and size of the γ′, γ", and in particular of the δ phase are dominant factors for the susceptibility of the alloy 718 produced by traditional methods. To determine, however, the strength of a piece of alloy 718 obtained by additive manufacturing, several microstructural and electrochemical factors must be considered.

Based on the PDM model illustrated above, the passive film is characterized by the balance between the formation reactions and the dissolution reactions in which point defects such as interstitials, cation vacancies and anion vacancies participate. The rupture of the passive film and the activation of localized corrosion sites are due to the disturbance of this equilibrium, which is shifted towards higher dissolution rates.

Dissolution of the passive layer of chromium oxide was studied on pure chromium in a solution of NaCl 0.1 M by Choudhary et al. [96]. In the passive region, it has been found that the thickness of the passive film increases linearly with the increase in the applied potential and increases logarithmically with the increase in the duration of exposure. The oxide film has a predominance of metal cation vacancies, and it is therefore classified as a p-type semiconductor film. Because of this data, it has been assumed that it is the movement and annihilation of the cation vacancies at the metal-film interface that controls the growth of the film. The vacancies go inward the film as the chromium cations diffuse outward and react with oxygen anions. In this way, a layer of chromium oxide is formed at the film-electrolyte interface.

The oxidation rate increases exponentially as the applied potential and pH increase, while it decreases exponentially as the thickness of the film increases. The rate of dissolution is independent of the applied potential and the thickness of the film; however, it increases with the decrease in interfacial pH in the passive region. From this fact, it can be deduced that the chromium oxide film dissolves by a chemical reaction in the passive region independently of the applied potential.

In the non-stationary region of the passive film, at a higher potential than that of its formation, the interfacial hydrogen ions increase in concentration as the oxidation rate increases, this may subsequently increase the rate of dissolution of the oxide layer. As the thickness of the film increases, the oxidation rate decreases and therefore also the rate of generation of H^+ ions. This causes the rate of dissolution of the film to decrease as the thickness of the film increases. After a certain potential value, the film enters the transpassive region, where the dissolution rate increases exponentially, which, however, is still lower than the oxidation rate. In this way, the passive film is not completely dissolved at the entrance to the transpassive region. Indeed, in this early transpassive region, the growth rate of the film increases despite accelerated dissolution. Transpassive dissolution causes an increase in the rate of generation of cation vacancies on the film-solution interface, in this way the density of the punctual defects in the barrier layer increases and with it also the growth rate of the film, thanks to the reactions that involve the defects.

When the dissolution rate becomes identical to the oxidation rate there is the complete dissolution of the film, this happens when the potential increases further, entering the stable transpassive zone. The oxidation rate increases exponentially with the applied potential due to the absence of the protective film. The mechanism that can justify these measurements in the transpassive zone can be described as a two-step mechanism. A thin layer of chromium oxide is quickly formed on the surface of the metal and just as quickly dissolved.

Analyzing alloys that contain chromium by anodic polarization, such as nickel-based Inconel alloys, it was observed that chromium enrichment occurs on the surface due to a high rate of dissolution of the other alloying elements. Chromium enrichment allows the formation of an increasingly thick layer of chromium oxide (Cr_2O_3). Thickening causes a decrease in the oxidation rate and dissolution rate of the other elements over time. This trend follows the evolution of the interfacial pH as in the case of pure Cr. Then the dependence between oxidation and dissolution that determine the resistance of the passive layer and therefore the corrosion resistance of an alloy containing chromium is further demonstrated. The growth kinetics of the passive film is direct logarithmic. However, the passive films that form on the surface of the alloys are semiconductors of type n, in the passive region. This indicates that the growth of the passive layer is dominated by the transport of oxygen vacancies. This causes the oxide layer to grow at the metal/film interface, then inwards. When the potential increases, reaching the transpassive region, the fraction of metal cations in the film also increases. This leads to the transformation of the film into a p-type semiconductor. Interfacial acidification, upon entry into the transpassive region, causes the oxidation rate to increase during the dissolution of chromium oxide. Subsequently, the presence of other stable oxides and the increase in the thickness of the film can cause the oxidation rate and the subsequent dissolution rate of the alloy to decrease. This mechanism causes secondary passivation in the transpassive region of chromium-containing alloys after chromium has dissolved. The increase in the thickness of this film follows the increase in the applied potential.

This study highlights the dependence of corrosion resistance of Inconel alloys on oxidation and dissolution of chromium. The dissolution of the alloying elements causes the enrichment of chromium on the surface and its oxidation allows the formation of a thick layer of chromium oxide, increasing the corrosion resistance of chromium-containing alloys such as Inconel 718. The importance of chromium and its concentration is also confirmed by the study of A. Yazdanpanah et al. [97].

The composition of the passivating oxide layer on Nickel-based Inconel alloys was studied by Zhong et al. [98]. Alloy 690, immersed in supercritical water, was used in the study. A fluctuating change in weight was detected. The behaviour of the weight change may be due to the coincidence between oxidation and pitting/dissolution of the oxide film. The first phenomenon determines weight gain, while the second determines mass loss.

It was observed that the oxide film formed on the samples had a duplex structure, divided into a poorly compact outer layer consisting of large polyhedral crystallites and a denser inner layer consisting of fine oxide particles. Observing the distribution of the alloy elements it was noted that the outer layer is rich in Ni and consists of nickel ferrite crystallites while the inner layer is rich in Cr. In addition, platelet oxides and faceted oxide particles are also noted on the surface layer.

Platelet oxide had a hexagonal crystal structure corresponding to $Ni(OH)_2$. Iron hydroxide was also detected in the outer layer. Not being stable, it reacts with nickel hydroxide and produces $NiFe_2O_4$ spinel. In contrast to hydroxides, NiO and Cr_2O_3 are chemically stable oxides in the test environment. Comparing the stability of all the oxides present we obtain the following classification: $Cr_2O_3 > FeCr_2O_4 > NiCr_2O_4 > NiFe_2O_4 > NiO$. So, nickel oxide is less stable than $NiCr_2O_4$ spinel. Indeed, it is observed, thanks to XRD analysis, that the content of NiO is low. This could be due to the reaction of NiO with iron hydroxide, which causes the generation of $NiFe_2O_4$, while the reaction between NiO and Cr_2O_3 generates $NiCr_2O_4$. Then the species present in the oxide film are divided between the outer layer and the inner layer in the following way: The outer layer consists of $Ni(OH)_2$, NiO and $NiFe_2O_4$. While the inner layer consists of Cr_2O_3 and $NiCr_2O_4$. The transport of iron through the chromium oxide layer ensures the formation of complex oxides containing this element.

From the composition of the different layers, it can be deduced that the outer layer grows by the dissolution of the metal and the precipitation of corrosion products on the surface, while the inner layer is developed by the solid-state growth mechanism, directly on the surface of the material. Thus, the following mechanism for the formation of the passive film was proposed: The first element to oxidize is chromium which immediately forms a layer of Cr_2O_3. At the same time, the elements that dissolve more easily, i.e. Fe and Ni, pass into the solution. These positive ions react with the anions present in the solution and precipitate on the surface of the metal as oxides and hydroxides. In this way, the outer layer of $Ni(OH)_2$ and $Fe(OH)_2$ develops. These species react with each other to form a more stable species, that is the $NiFe_2O_4$, that dominates in the composition of the outer layer. The low coefficient of reticular diffusion of chromium causes the enrichment of this element in the inner layer. In contrast, nickel and iron spread more easily to the outer layer. The chromium present in high quantities in the inner layer reacts with oxygen ions, which diffuse towards the metal/film interface through facilitated pathways such as micro-pores and grain edges. This further oxidation that takes place directly in the inner layer causes its compaction. Through the diffusion of Ni^{2+} ions towards the film/solution interface, the oxidation of this species can take place and form NiO, which reacts in part with the iron hydroxide to form further $NiFe_2O_4$. A small amount of nickel oxide reacts with chromium oxide and causes the formation of $NiCr_2O_4$.

The chromium oxide layer being the most compact and most stable is the one responsible for the corrosion resistance of nickel-based alloys. A greater diffusion of chromium towards the metal/film interface is a factor that could improve the quality and strength of the passive chromium oxide layer. A higher flow of Cr would lead to a higher passive film formation rate.

The size of the grain is an important factor that determines the kinetics of the formation of the passive layer because a greater amount of grain boundaries leads to a greater number of sites through which chromium can diffuse to the surface and thus increase the rate of formation of the chromium oxide film and its compactness. The investigation carried out by L. Jinlong et al. [99] on a coarse-grained 304 steel (CG) and a nano/ultrafine-grained 304 steel (NUG) demonstrates the fact that the smaller the grain size and the higher the corrosion resistance of the metal.

CG 304 stainless steel had a particle size of about 55 µm, while NUG 304 stainless steel showed an average grain size of 230 nm. Performing potentiodynamic tests, it was found that the passivation current decreases due to the refinement of the grain. From the impedance measurements, the charge transfer resistance of the passive film was calculated, which increases with the increase in the passivated potential. This resistance was higher for the NUG sample than for the CG sample. The difference between the resistances of the two samples increases as the passivated potential increases. This can be attributed to the faster diffusion rate of the NUG stainless steel element.

The concentrations of donors and acceptors (anion vacancies and cation vacancies) in the passive film were calculated. The donor's concentration decreased with the increase in passivated potential in a borate buffer solution. Grain refining resulted in a more pronounced decrease in donor and acceptor concentrations with increased passivated potential. An increased concentration of acceptors leads to a decrease in corrosion resistance. Thus, a finer particle size leads to an improvement in corrosion resistance, especially at a higher passivated potential.

The growth and rupture of the passive film are possible by transporting point defects into the passive film. A stable passive film is possible when a balance is established between at least two non-conservative reactions since only a non-conservative reaction will lead to monotonous growth or thinning of the passive film. A very important value for the formation of this balance is the diffusivity of cation vacancies, cationic interstitials, and oxygen vacancies.

The dominant defects turned out to be oxygen vacancies and cation vacancies. The NUG sample showed a greater diffusivity of defects in the passive film, while still having higher corrosion resistance. A low amount of oxygen vacancies can inhibit passive film growth, but the increased diffusivity of oxygen vacancies in the NUG sample accelerates the formation of the film.

In an environment where chloride ions are present, their higher concentration leads to an easier formation of oxygen vacancies in the passive layer. In addition, chloride ions can fill oxygen vacancies, and this causes the system to generate cation vacancies to maintain electrical neutrality. To do this, the system generates oxygen-cation vacancy pairs. In this way, oxygen vacancies also increase and are further occupied by chloride ions. The formation of cation vacancies is therefore an autocatalytic process. A greater number of oxygen vacancies leads to the formation of a greater number of cation vacancies which cause the passive film to break at the metal/film interface. The NUG sample has the lowest concentration of donors and acceptors, as well as having the greatest resistance to charge transfer of the passive film and it is, therefore, more resistant to this phenomenon.

Fine grain size has been observed to promote the growth of chromium oxide Cr_2O_3 and inhibit the formation of $Cr(OH)_3$. It is, therefore, most likely to imply the greater resistance of the passive film on the NUG sample to the greater amount of chromium oxide. In addition, iron oxides were favoured and ferrous oxides were disadvantaged. The reduction of the presence of chromium hydroxides implies the reduction of point defects in the passive film. Ultimately, a finer particle size promotes corrosion resistance because it increases the dynamics of layer formation and reduces the density of defects in the barrier layer.

The greater resistance to localized corrosion of the laser power bed fusion (L-PBF) 718 samples under tensile load is therefore most likely to be attributed to the submicronic ultrafine structure due to the production method, which allows the formation of a passive layer less defective and therefore more resistant than the samples conventionally produced with coarse grain.

Another microstructural factor that must be taken into account is the phenomenon of localized segregation of alloying elements. The rapid thermal cycles that the material undergoes during production by SLM allow the avoiding of macro-segregation altogether. On the contrary, it is impossible to avoid submicron precipitation in cellular/columnar subgrains.

The work done by W.M. Tucho et al. [90] has made it possible to identify the phases that precipitate on the grain boundaries of an SLM processed alloy 718 as well as identify its composition.

Irregularly shaped precipitates, rich in Nb, have been identified along the grain boundaries and the cellular subgrain boundaries. The analysis of the composition of these precipitates, performed by EDS, allowed the identification of them as a Laves phase with $(Cr, Fe, Ni)_2(Nb, Mo, Ti)$ as the general formula. The subgrain boundaries are enriched up to 10 % by weight of Nb and 7 % by weight of Mo and depleted in Fe, Ni and to a lesser extent in Cr, compared to the nominal composition. Further analysis of the composition of many of the precipitates along the boundaries of the subgrain reveals 6–35 % by weight of Nb, 3.8–7.4% by weight of Mo and 0.9–1.4% by weight of Ti. Precipitates are between 10 and 300 nm in size, with some of them showing an elongated shape. The Laves phase has been recognized by the high concentration of Nb which must be at least 10% by weight.

The formation of the Laves phase consumes a lot of Nb by decreasing its concentration in the matrix. For this reason, it has been found that the region of the subgrain matrix is depleted in Nb.

Also, within the matrix was detected the presence of the Laves phase with dimensions between 100 and 200 nm. Particles smaller than 100 nm rich in (Nb, Ti) have been detected and are enriched in C, they also contain N, and therefore could be precipitates of TiC and TiN. Disc-shaped particles with a diameter of up to a few microns rich in aluminium and oxygen have been identified as possible aluminium oxides. The precipitation of most of these phases is due to the presence of Nb in the solution since, together with Mo and Ti, it is an element known to be strongly segregating. During the cooling of the metal, a series of phase transformations occur induced by the segregation and depletion of the alloying elements that produce the observed microstructure. The solidification of the liquid forms the austenitic phase of the matrix, during this process the solid expels alloying elements into the liquid due to the lower solubility. In this way, the remaining liquid is enriched with Nb and C. As the temperature decreases, the precipitation of NbC occurs with a eutectic transformation that causes the depletion of carbon in the liquid that leads to the precipitation of the Laves phase through a second eutectic reaction.

This analysis provides an important result, namely that the area of the boundary of the subgrain is enriched in Mo which is a very important element for the corrosion resistance of alloys.

The study carried out by G.O. Ilevbare et al. [100] demonstrates how molybdenum is an alloying element that significantly improves the resistance to localized corrosion of alloys. The study was carried out on samples of stainless steel 304 and 316 (which has as an addition about 2% of Mo) immersed in a solution of HCl 1M. Potentiostatic and potentiodynamic analyses were performed to detect current transients that corresponded to the nucleation of pits.

It was observed that nucleation events occurred in greater numbers and faster in sample 304 than in sample 316. The fact that nucleation occurred more rapidly in sample 304 indicates that the oxide film was more prone to breakage than in the sample containing Mo. Sample 304 also showed larger nucleations, which are more likely to generate more metastable pits. In addition to size, the mere fact that more nucleations occur increases the probability of generating metastable pits. Five times more pits are generated on the 304 samples than on the 316 samples.

A possible mechanism that explains the nucleation of the pits is constituted by the migration of Cl- ions through the passive film until reaching the metal surface. The chloride ions react to form metal chloride which, by increasing the volume, causes the oxide film to break at the interface. According to this mechanism, the initial lower nucleation rate on sample 316 may indicate that the Cl^- ions find the oxide film more difficult to penetrate and that the passive layer, therefore, has better strength.

Mo can improve the oxide film by forming molybdates and increasing the compactness and thickness of the film. In addition, the presence of molybdenum can change the electronic properties of the oxide film, reversing ionic selectivity, and making it more difficult for Cl^- ions to migrate.

The generation of metastable pits is only possible if enough Cl^- is present in the cavity to prevent the repassification of the broken area and to support the continuous dissolution of the metal. In addition to the fact that there must be a barrier to the diffusion of Cl^- ions to prevent them from being washed away. This barrier can be made up of the residual passive film in the pit and the size and depth of the nucleation site, such as non-metallic inclusions on the surface.

Nucleations occurred on sample 304 and this increased the probability of generating metastable pits. The percentage of nucleations that turn into metastable pits at low current ranges is consistently higher for sample 304. So, when the nucleations are small, and therefore when it should be more difficult to generate metastable pits, on sample 304 this happens more easily. On the 316 samples, not only do fewer nucleations occur, but it is also more difficult for them to become metastable.

Mo helps repassivation of the bare metal, avoiding a prolonged dissolution of the metal, to prevent the formation of metastable pits.

The time constant τ describes the velocity of electrochemical micro-processes that cause the formation of a metastable pit. The higher the τ, the greater the dissolution rate in the pit. The slower this process is,

the more repassivation is favoured. Indeed, in sample 316 metastable pits are generated 14 times slower. This is also indicated by the lower current density detected during their generation.
Simple or complex insoluble molybdates are thought to be formed with metal cations in the pits of sample 316, due to the dissolution of molybdenum and the acidic environment present in the pit. The resistance to pitting increases due to the insolubility of these compounds which causes a slowing down of the dissolution of the alloy and a reduction in the released metal ions, leading to a decrease in the diffusion of Cl^- in the pit. The lower the dissolution rate the smaller the size of the pits. Indeed, it has been observed that on sample 304 much larger metastable pits are generated. Furthermore, in sample 316, thanks to molybdenum, the achievement of the critical concentration of metal ions required for the transition from metastability to stability is prevented. The same happens for the pit stability product (Pit radius*Current density).
The largest pits on sample 316 have a diameter of about 4 μm while those on sample 304 have a diameter of about 15 μm. This is almost a difference of 4 times. As the pit grows, the metal ion saturation concentration is created. The pits on 304, being larger, will more easily reach the product of stability due to the increase in current density and radius.
It was found that the concentration of metal ions in the wells is 4.1 and 0.13 M for 304 and 316 respectively. The critical saturation concentration (3.6 M) is therefore easily reached by 304. Therefore, on steel 316 there was no stable pitting due to the low currents, even at a high potential, which do not allow the enlargement of the pits and the achievement of the probability product.
The probability of stable pitting depends on the probability of activating sites capable of metastable pit growth and the probability that these metastable pits will achieve stability. These probabilities were higher in Mo-free steel, demonstrating the important role of this element in localized corrosion resistance. From this research it can be deduced that the enrichment of Mo that can be found in subgrain boundaries of SLM processed alloy 718 could increase the resistance to corrosion in this region, leading to a greater susceptibility of the matrix to localized forms of corrosion.

The compositional variation between the grain edge and the adjacent area results in a galvanic coupling which is an additional factor that facilitates the selective dissolution of the subgrains matrix. The mechanism related to SCC nucleation in L-PBF samples is the selective dissolution of the subgrains and the subsequent mechanical rupture of the intact subgrain boundaries. Selective corrosion attack was also detected for conventional 718 on a larger scale adjacent to precipitates that show greater resistance of these phases to corrosion attack.

The conditions for the appearance and propagation of SCC are described based on the differential aeration hypothesis (DAH) and the coupled environment model (CEFM) developed by MacDonald[101].

The DAH is based on the fact that the local anode and the local cathode, present on the surface of the metal, are separated. Indeed, the anode is located on the tip and sides of the crack, while the cathode is located on the outer surface near the mouth of the crack, where oxygen is more easily accessible. The accumulation of positive ions at the tip of the crack, due to the dissolution of the metal, causes the transport and accumulation of negative ions such as the Cl^- ion in the cavity of the crack to maintain charge neutrality. Positive ions tend to exit the crack generating a charge transport that is counterbalanced by the transport of electrons from the tip of the crack to the outer surface that generates a current that is consumed by the reduction of hydrogen ions, water, and oxygen. The internal and external environments of the crack are therefore strongly coupled. The annihilation of currents through a charge transfer reaction implies that the kinetics of this reaction are decisive for deriving the crack growth rate (CGR).

The electron current is known as the "coupling current". The generation of a cathode and an anode allows the maintenance of neutrality, but the passage of the coupling current also guarantees the maintenance of an aggressive environment inside the crack that prevents repassification and guarantees the continuation of localized corrosion. In an environment containing chloride ions, an aggressive environment is generated in the crack due to the generation of H^+ ions which, joining the Cl^- ions, form hydrochloric acid very concentrated in the tip of the pit.

The coupling current, being closely linked to the coupling force between the anode and cathode, is very important for the assessment of the severity of localized corrosion.

Maintaining the separation between the anode and the cathode is the necessary factor for the continuation of localized corrosion. This is because, as long as separation exists, the tip of the crack is in a semi-depassivated state. If maintenance is not possible then the crack "dies" and localized corrosion stops. This happens when the surface of the metal is coated with insulating paint.

By analyzing the corrosion of 304 steel in aqueous solutions at high temperatures it was possible to determine the existence of a critical potential for crack propagation. This happens for all localized corrosion phenomena, such as pitting. Corrosion, therefore, occurs only at potentials greater than the critical potential. The critical potential corresponds to the lowest observable CGR at which the occurrence of an environmentally induced intergranular fragile fracture is negligible compared to the ductile fracture.

The progress of the crack is determined by a mechanism divided into three phases that are repeated cyclically: mechanical sliding / electrochemical dissolution / repassivation. The CGR is directly proportional to the coupling current except when the potential is sufficiently negative to make the growth of the sliding cracks the control factor. Since the transport of ions is the factor that determines the maintenance of the anode-cathode pair, which is counteracted by the diffusion of ions out of the crack, there is a minimum coupling current below which the intergranular SCC (IGSCC) is negligible compared to the purely mechanical fracture. The minimum current is thus linked to the critical potential, which is the potential on the outer surface that does not allow the maintenance of the anode-cathode pair. On 304 it was found that until the stress intensity factor reached a value, no coupling current was detected. Subsequently, the current increased with the intensity of the stress and then stabilized at a constant value. When the tensile voltage was discharged, the current dropped to zero, indicating the closure of the crack. On surfaces catalyzed with Pt, a current 50 times greater than on non-catalyzed surfaces was detected. This indicates that the coupling current is closely linked to the oxygen reduction kinetics on the outer surface. So, inhibiting this reaction would greatly reduce CGR.

The coupling current had fluctuations with amplitude less than the average of the current. These fluctuations represent the periodic fracturing at the apex of the crack. While there is a time-dependent corrosion and independent of SCC. The absence of current is therefore an indication of the absence of periodic break and closure of the crack.

The increase in the intensity factor of the stress increases the CGR because it causes the frequency of microfracture events at the apex of the crack to increase. It has been found that most of the coupling current comes from the apex of the crack. On the contrary, with catalyzed cathodes, it was found that the coupling current derives from the flanks of the cracks. This fact once again confirms the impact of the external surface on the growth dynamics of the SCCs.

The low pH at the apex of the crack causes hydrogen to evolve, consuming part of the coupling current. The newly generated hydrogen penetrates the matrix and embrittles it, favouring microfrantumation and crack growth. The frequency with which microfracture events occur is determined by the rate of deformation of the crack tip.

Stress corrosion cracks can be described using two characteristic lengths: the mechanical crack length (MCL), which together with the applied mechanical load defines the mechanical state of the crack tip in terms of the stress intensity factor, and the electrochemical crack length (ECL), which determines the coupling current and its dependencies on independent electrochemical variables (potential, conductivity, etc.). The ECL represents the distance that the current must travel to meet less resistance, from the tip of the crack to the surface. In contrast, the MCL is the distance between the apex of the crack and the mechanical load line.

For any given corrosion potential in which environmental effects predominate (i.e., for E greater than critical E), the CGR decreases as the ECL increases, or a higher E must be applied to produce the same CGR as the ECL increases. The critical potential becomes more positive, as the size of the crack increases, so the driving force for crack propagation, $E_{critical}$ - E, decreases. This causes the CGR to decrease and become zero at $E_{critical}$=E. At this point, the crack is electrochemically "dead" and will not propagate further, unless E becomes more positive, although it will continue to propagate by sliding. So, the theory predicts that all cracks reach a limiting depth, above which they do not propagate.

The coupling current tends to travel the shortest possible distance to reduce the resistance to the passage of charge. In the case of this thesis, the shortest distance that the current could travel during the experiments is the distance between the subgrains. Indeed, coupling occurs between the matrix of the subgrain, which behaves as an anode, and the edge of the subgrain which behaves as a cathode. The nucleation and propagation of the crack are kept active by the presence of residual tensile stresses and further amplified by the applied tensile stress.

The work of M. Laleh et al. [92] demonstrates the harmful effect of the lack of fusion pores on localized corrosion resistance, highlighting how these pores are the preferred sites of pit nucleation.

Samples of 316L stainless steel were produced via Selective Laser Melting with different combinations of laser power and scanning speed. These samples showed different percentages of porosity, depending on the parameters chosen. Potentiodynamic tests were carried out on them in a solution of NaCl 0.06 M. This analysis revealed that samples with higher densities showed higher pitting potential values than those with lower densities. The samples had both spherical pores, which were caused by the entrapment of gases in the molten metal, and irregular pores which were caused by non-melting. Spherical pores were ubiquitous, while the lack of fusion pores increased as the percentage of porosity increased. This work focuses on the role of LOF (lack of fusion) pores on susceptibility to pitting corrosion, as other work shows that spherical pores have a lower impact[102].

The samples examined had a density between 97.3% and 99.5%. The high-density samples had almost exclusively spherical pores, while on the low-density samples, LOF pores were predominant in which pits were seen to be formed inside them and in the adjacent area. In contrast, no pits were noted on the high-density samples.

Polarization curves show how different types of pores affect corrosion resistance differently. Regions, where more spherical pores are present, show nobler pitting potentials, while regions that contain more LOF pores show much lower pitting potentials. This demonstrates that it is mainly LOF pores that significantly reduce the localized corrosion resistance of the SLM material.

X-ray computed tomography combined with Data Constrained Modeling was used to obtain 3D models of the samples, revealing the network of LOF pores within them. Observing the sample with lower density, the pores were characterized by a semicontinuous oxide film on the metal exposed inside the LOF pores. In addition, these pores form vertical structures in the building direction.

After corrosion in a 6 % by-weight ferric chloride solution, it can be seen how the specimen is almost completely dissolved, with the LOF zones enlarged out of all proportion. The presence of vertical structures consisting of LOF could indicate that there is a certain degree of connectivity between the pores that leads to a preferential path for the penetration of the corrosive solution. The pores that were previously isolated now have junction channels that highlight the penetration of the solution into these areas.

Taking into account a sample with greater density, the presence of layered LOF structures not in contact between one layer and another is observed. This means that a slower scanning speed allowed for greater melting of the material. LOF structures after corrosion do not show connectivity between them.

Considering a sample with intermediate porosity, the authors focused on observing two LOF structures that were separated before corrosion and joined together after corrosion. The corrosion followed the direction that allowed the connection of the two pores making it presume that there is a susceptible microstructural path that facilitates the dissolution of that area. In addition to the union of the LOF structures, the enlargement of the pores exposed to the solution was detected, indicating more generalized corrosion to the entire surface of the pore.

The high weight loss of the samples suggests that corrosion also occurs on the surface where LOF pores are not present, but in them, the nucleation of the pits is certainly favoured. Once the pits penetrate the internal structure of the material following the LOF structures, localized corrosion also develops on the healthy surface.

In essence, the severity of corrosion is greater in less dense samples. This is because numerous large LOF structures within the sample facilitate the creation of very deep pits due to the preferential corrosion of the material present between the pores. In the densest samples, these structures are not present and therefore the pit must propagate through a normal process. However, for the pit developed in the higher-density sample, there are far fewer LOF structures adjacent to the pit start site; therefore, pitting must proceed simply without the assistance of internal voids that facilitate internal attachment. So, in both cases propagation is probably a combination of grain attack and grain boundary attack, but in the case of lower-density samples, there is also the contribution of LOF structures to its total volume.

The mechanism leading to the preferential corrosion of pores is described below:

Surface defects including spherical pores and LOF pores are filled with electrolyte. The spherical pores having a large and uniform surface exposed to the solution reach the critical conditions for the triggering of the crack with more difficulty. In the LOF pores having an irregular surface with very narrow areas, as a result of corrosion of the surface, the accumulation of metal ions occurs; indeed, the path to reach the bulk electrolyte is too long. These, to maintain the neutrality of the solution, attract CL^- ions, which are concentrated in the area of the pore anomaly. This high concentration of anions causes the pit to nucleate. Thus, the presence of occluded regions within irregularly shaped pores can have a strong influence on the susceptibility to localized corrosion of 316 L SS produced by SLM.

The greater influence of lack of fusion pores on the resistance to localized corrosion of a material processed by laser powder bed fusion is also confirmed by the study of A. Yazdanpanah[103].

The work of G. Sander et al. [102] highlights the fact that pores under a certain diameter and spherical in shape do not affect the localized corrosion resistance of the material in an evident way, confirming the fact that a critical pore surface is needed to trigger a stable pit and thereby increase the susceptibility of the material to the corrosive environment.

In this work, 316L steel specimens produced by SLM were tested employing potentiodynamic tests in a NaCl 0.1M solution, varying the process parameters. The maximum porosity measured was 0.4%, while the minimum was less than 0.02%. The corrosion potential and corrosion current density values of the 3D printed samples were independent of the porosity of the sample. In addition, pitting potential values showed no statistically significant correlation with the porosity of the sample. Only the repassivation potential showed a correlation with porosity, decreasing as the density of the sample decreased. The most porous sample had a repassivation potential (-0.1 V SCE) significantly lower than that of the densest sample (0.035 V SCE). Porosity adversely affects the repassivation of the material but not necessarily the resistance of the passive layer to pitting. Once stable pitting has occurred, its cessation is more difficult in the presence of increasing porosity.

Porosity also influences the nucleation of metastable pits. Indeed, it was found that the least dense sample showed the highest metastable pit frequency (5.04 cm -2*s -1), while the sample with the highest density had one of the lowest metastable pit frequencies (2.18 cm -2*s -1). It seems that the metastable pits most present on the more porous sample do not necessarily turn into a greater number of stable pits, since there is no lowering of the pitting potential.

Deriving the cumulative charge passed through the metastable pits of each sample, it is observed that the most porous sample showed the highest cumulative charge (3.67 mC/cm 2) while the least porous sample showed the lowest cumulative charge (0.10 mC/cm 2). This indicates that in addition to being more susceptible to the appearance of metastable pits, the more porous sample also suffers more damage during these events (greater dissolution).

The results obtained indicate that the passive film protects the surface of the metal even at the pores. Passive film is more susceptible to rupture at the pores, and this induces the appearance of numerous metastable pits. The film can regenerate spontaneously and prevents these sites from turning into stable pits. The most difficult repassivation with the increase in porosity could be due to the presence of pores below the surface that would join the pits during their propagation, making it more difficult to regenerate the oxide film. Another contribution that makes it more difficult to repassive into the pores is the presence of a rougher surface than the polished one.

From this study, it is noted that the conditions found did not directly affect the resistance to the appearance of stable pits on the samples. Given that in other studies, such as the previous one, the determining role of porosity on susceptibility to localized corrosion has been demonstrated, it can be deduced that the shape of the pores and their size are the dominant factors that discriminate a porous SLM material susceptible from a more resistant one.

A study that highlights how the size of the pores is an important factor to consider excluding their shape is that of A. Yazdanpanah et al. [91]. In this study, samples of 316L stainless steel produced by SLM are examined, varying the process parameters, to obtain materials with different porosity and residual stress of different magnitudes. In this study, the surface area of the pores, and therefore their size, was taken into account. From potentiodynamic polarization tests in a solution of sodium chloride at 3.5% by weight, it was possible to see how the pitting potential decreased as the PSA (pore surface area) increased. As the magnitude of the residual stresses increased, even the samples with the smallest pores had a significant decrease in pitting potential. The residual stresses, and in general tensile forces are therefore able to make active sites more easily attackable even the smallest pores facilitating the break of the passive layer.

The mechanism that could link pore size with localized susceptibility to corrosion is as follows:

The key factor is the migration and accumulation of Cl^- ions. Pores smaller than a critical size will be less likely to accumulate chloride ions, and this leads to greater resistance to pitting. On the contrary, pores larger than a critical size possess the ideal conditions for easy migration of chloride ions into the pore cavity, attracted by an accumulation of metal cations, making the accumulation of ions more likely, establishing a more aggressive local condition that induces the rupture of the passive layer.

The previously presented studies confirm the harmful role of porosity and allow affirming that the difference in the resistance to localized corrosion shown by the specimens in the polarization tests is due to a different porosity, both in terms of % of surface area occupied by the pores and in terms of pore size. The higher the laser power used, the greater the porosity found, and consequently, the greater the susceptibility to localized corrosion of the samples. The 115 W sample has the least porosity due to having the best balance between laser power and scanning speed and therefore is excluded from this rule.

The structure of metallic materials has different types of defects, which are mainly concentrated in the inconsistent interface between the phases due to the random arrangement of atoms. The most observed defect in L-PBF materials is a line defect, dislocation entanglement, which was observed predominantly at the boundaries of the columnar subgrain. Considering the alloy 718 L-PBF, The presence of a high density of dislocations at the boundaries of the subgrain is due to the inconsistency between the matrix and the precipitated phases combined with extreme solidification cycles[90].

The investigation carried out by L. Liu et al. [104] on the behaviour of dislocations on a sample of 316L steel produced by SLM allows the understanding of the arrangement and movement of dislocations in the subgrain network.

The sample observed at SEM reveals a structure consisting of columnar grains ranging in thickness from a few to tens of micrometres and length up to hundreds of micrometres. Analyzing the sample at TEM, a network of dislocations embedded in the individual grains is observed. Dislocations are concentrated on the wall of columnar cells. Dislocation cells are often aligned with the direction of the temperature gradient that occurs during the process of solidification of the molten metal.

Quantitative EDS analysis allowed the identification of a higher concentration of Mo, Mn, Cr and Ni, compared to the matrix, in the dislocation network. The simultaneous formation of the dislocation network and the segregation of the elements are both due to cell growth due to the high-temperature gradient. The fact that dendritic subgrains grow with a slightly different orientation than each other in a single grain, causes the formation of dense dislocation walls. At the same time, the alloying elements are expelled from the solidified metal and segregate between the subgrains. Dislocation cells can also form as a result of plastic deformation. In addition, the smaller the size of the dislocation cells, the greater the flow stress of the material. Therefore, the presence of small cells confined in the subgrain of the SLM material allows a better mechanical strength of the steel produced with this method compared to one with greater grain size.

By performing mechanical tests at TEM it was observed that partial dislocations were the main vector of plastic deformation, which were hindered by the network of dislocations but not completely blocked. Indeed, dislocations dissociated into partial dislocations with jerky motion when temporarily trapped by the dislocation walls. As stress increased, the movement of dislocations continued. A sufficiently high stress induces the emission of a leading partial that moves from a cell wall to a nearby one where it blocks. As the stress increases further, even the trailing partial, which was still on the previous wall, manages to pass to the wall where the leading partial was stuck but at the same time, the latter manages to move to the next wall. The cell walls, therefore, hinder the movement of dislocations by increasing the necessary stress, improving mechanical properties.

The impediment imposed on partial dislocations can induce the separation of the leading-tailing pair and allow the coupling of two partial dislocations of the same type leading to the formation of nano-twins. Clusters of nano-twins have been detected on cell walls. Nano-twins also influence the motion of dislocations, leading to stable deformation and hardening.

The 316L SLM material has a good combination of mechanical strength and ductility thanks to its structure and network of dislocations. The dislocation network hinders the movement of dislocations thus increasing yield strength. With the increase in stress the dislocations move but thanks to the pinning effect of the segregated atoms the dislocation network is stabilized while maintaining its size during plastic deformation, increasing the ductility of the material. Disorientation between cells also has a stabilizing effect on the dislocation network. Meanwhile, the formation of nano-twins promoted by the dislocation network also contributes to hardening.

The size of the cells and the morphology of the dislocation network are regulated by the cooling rate and temperature gradient. Indeed, by decreasing the scanning speed, larger dislocation network cells were produced. Thus, an adjustment of the process parameters allows the obtaining of an SLM material with the desired mechanical properties, also considering the network of dislocations.

This study allows knowing the arrangement and behaviour of dislocations in an SLM material such as 718 L-PBF samples. The impediment of the movement of dislocations on the subgrain boundaries induces an increase in energy at these sites. Even if sufficient stress has been applied, the dislocations move but pass to the boundary of the next subgrain, indicating that the boundaries always retain more energy than the matrix and are therefore active sites. Sites with higher energy levels induce the formation of a greater number of point defects in the structure of the overlying passive film, according to the PDM theory. This reduces the resistance of the passive film at these sites and thus increases the susceptibility to localized corrosion and the appearance of SCC as a result of the imposition of tensile stress.

The importance of dislocations at the subgrain boundaries is further confirmed by the nucleation of the cracks preferred over their union and propagation. The presence of dislocations entanglement, combined with the shorter distance travelled by the coupling current and the ions, makes the area adjacent to subgrain boundaries very active and therefore highly susceptible to the beginning of the SCC cracks in high numbers, disadvantaging the propagation of a small number of cracks. This behaviour could lead to an increase in the time it takes for the crack to grow until it reaches the length value that can be classified as a high risk of component fracture. This fact makes the alloy 718 L-PBF less susceptible to severe stress corrosion cracking making it stronger than conventional alloy 718 and compensating for the lower mechanical strength.

6 Conclusion

The investigation carried out in this thesis aimed to compare the electrochemical behaviour and the susceptibility to stress corrosion of alloy 718, produced using different laser powers by additive manufacturing, with the conventional alloy produced by two-stage ageing. The microcapillary method was used, which allowed the investigation of the initial phases of the appearance of stress corrosion cracks, i.e. incubation and nucleation, avoiding overlapping with the propagation phase.

The microstructural characteristics of the 718 L-PBF alloy are strictly connected with the method used for their production and with the process parameters used. It has been observed that the size of the melt pools is related to the laser power used. Overall, as the laser power increased, the depth and width of the pools increased. The laser power of 115W made it possible to obtain the most optimal combination of the two properties, confirmed by the fact that the depth of the pools at this laser power was found to be the smallest, despite having the greatest width. Too great height would induce the formation of porosity due to gas trapping, while a high width allows a better overlap of the pools of the same layer, decreasing the porosity due to lack of fusion.

The porosity of the material reflected the behaviour of the melt pools, indeed, the power of 115W made it possible to obtain a material with the lowest density of the pores and the smaller pore surface area. On the contrary, the laser power of 125W is the one that showed the highest pore density, having both a high number of small pores and a considerable number of large pores that follow the scanning pattern. This behaviour is due to the excessive laser power used which increased the energy density that hit the material and led to a large number of pores due to gas trapping.

The hardness followed the trend imposed by the density of the pores but on the contrary. The higher the density of the pores, the lower the hardness of the material. So, this mechanical feature was also influenced by laser power. The 115W sample showed the highest hardness, while the 125W sample had the lowest. Conventional samples were those that had the greatest hardness, due to the two-step ageing treatment which has the objective of increasing the mechanical strength of the material through the precipitation of fine particles in the matrix.

The potentiodynamic polarization tests allowed the creation of a general picture of the corrosion behaviour of the samples. The real results, however, were determined thanks to galvanostatic tests, which showed that taking into consideration the under tensile load conditions, on SLM samples the appearance of SCC, and therefore localized corrosion, is delayed compared to traditional material. This indicates a better resistance of the SLM processed alloy 718 to crack incubation and nucleation. This is further confirmed by the high breaking potential of the materials produced by additive manufacturing.

Corrosion resistance is not directly related to the hardness and size of the melt pools, since the hardest samples were also the ones most prone to stress corrosion cracking. On the contrary, in the SLM samples, it seems that the hardness is proportional to the corrosion resistance, but this is mainly due to the porosity.

It is this characteristic that determines both the hardness and the resistance to localized corrosion. Samples with a lower pore density, and therefore a higher hardness, have the best resistance of the passive layer to corrosion. Thus, the laser power of 115W produced the most resistant material, while the power of 125W produced the most attackable material. The pores behave as active sites, more subject to corrosion attack, due to the greater ease of accumulating aggressive species within them, such as Cl- ions. The larger the pore size and the greater their density, the lower the corrosion resistance of the material.

The presence of a state of tensile stress is closely linked to the corrosion resistance of the material. It was noted that the load was essential for the appearance of the SCCs and that this greatly decreased the potential necessary for the breakdown of the passive layer.

In SLM samples, cracks were detected in the area adjacent to the boundaries of the cellular / columnar subgrain, while in conventional samples they appear adjacent to the precipitates, even within the matrix. The cracks of the SLM samples, being confined to the subgrains, were much smaller than those of the conventional material. This is a visual confirmation of the increased stress corrosion cracking resistance of the material produced by additive manufacturing.

The particular nucleation of SCCs that occurred in the SLM samples is due to several factors. The boundary of the subgrain is enriched in elements that increase its resistance to corrosion, such as Nb and Mo, on the contrary, the matrix is depleted of these elements. This produced galvanic coupling between the subgrain boundary and the adjacent matrix, causing greater dissolution of the metal in that area. Furthermore, the presence of a dense network of dislocations in the area adjacent to the subgrain boundary makes this area more vulnerable due to the formation of a more defective passive film and a greater stress concentration that causes the breakdown of the passive film and the advancement of the crack. In the presence of tensile stress, the galvanic micro-coupling in the subgrains is more favoured than the coupling between the bottom of the pore and the metal surface, due to the shorter distance that the electron current must travel.

7 References

1. Mars Fontana Corrosion Engineering (Mcgraw-Hill International Edition); McGraw-Hill Companies, 1986;
2. A.J de Bethune and N.A.S Loud Standard Aqueous Electrode Potentials and Temperature Coefficients at 25°C; Clifford A.Hampel,Skokie, III.; 1964;
3. O. L. Riggs, J. D. Sudbury, and M. Hutchinson Corrosion, 16:94-98; 1960;
4. U. R. Evans Corrosion, 7:238; 1951;
5. S. J. Hudak and R. A. Page Analysis of Oxide Wedging During Environment Assisted Crack Growth, Corrosion, 285-290; 1983;
6. E. N. Pugh, W. G. Montague, A. R. C. Westwood Corrosion Sci., 6:345; 1966;
7. D. K. Priest, F. H. Beck, and M. G. Fontana Trans. Am. Soc. Metals, 47:473-492; 1955;
8. Blaine Geddes, Hugo Leon, and Xiao Huang Superalloys_ Alloying and Performance; ASM International, 2010;
9. R.T. Holt and W. Wallace, Impurities and Trace Elements in Nickel-Base Superalloys, Int. Met. Rev., Vol 21; 1976;
10. J.M. Poole, J.J. Fischer, G.A.J. Hack, and G.M. McColvin, The Development, Performance and Future of the Mechanical Alloying Pro Cess and Oxide Dispersion Strengthened Alloys, Advances in High Temperature Structural Materials and Protective Coatings, A.K. Koul, Ed., National Research Council of Canada, Ottawa, p 34–53; 1994;
11. M.J. Donachie and S.J. Donachie, Superalloys: A Technical Guide, 2nd Ed., ASM International; 2002;
12. M. Durand-Charre, The Microstructure of Superalloys, Gordon and Breach Science Publishers, Amsterdam,p 1–124; 1997;
13. N.S. Stoloff, Fundamentals of Strengthening, Superalloys II, C.T. Sims, N.S. Stoloff, and W.C. Hagel, Ed., John Wiley & Sons, p 61–96; 1987;
14. E. Orowan, in Dislocations in Metals, M. Cohen, Ed., AIME, New York; 1954;
15. H.S. Ko, K.W. Paik, L.J. Park, Y.G. Kim, and J.H. Tundermann, Influence of Rhenium on the Microstructures and Mechanical Properties of a Mechanically Alloyed Oxide Dispersion-Strengthened Nickel-Base Superalloy, J. Mater. Sci., Vol 33, p 3361–3370; 1998;
16. P. Kumar, The Role of Niobium and Tantalum in Superalloys, Advances in High Temperature Structural Materials and Protective Coatings, A.K. Koul, Ed., National Research Council of Canada, Ottawa,p 34–53; 1994;
17. L. Liu, T. Huang, et al., Grain Refinement of Superalloy K4169 by Addition of Refiners: Cast Structure and Refinement Mechanisms, Mater. Sci. Eng. A, Vol 394, p 1; 2005;

18. C.T. Sims, Superalloys: Genesis and Character, Superalloys II, C.T. Sims, N.S. Stoloff, and W.C. Hagel, Ed., John Wiley & Sons, p 3–26; 1987;
19. E.W. Ross and C.T. Sims, Nickel-Base Alloys, Superalloys II, C.T. Sims, N.S. Stoloff, and W.C. Hagel, Ed., John Wiley & Sons, p 97–133; 1987;
20. Metallography and Microstructures, Vol 9, ASM Handbook, ASM International; 2004;
21. R.A. McKay, M.V. Nathal, and D.D. Pearson, Influence of Molybde Num on the Creep Properties of Nickel-Base Superalloy Single Crys Tals, Metall. Trans. A, Vol 21 (No. 2), p 3; 1990;
22. J.A. Manriquez, P.L. Bretz, L. Rabenberg, and J.K. Tien, The High Temperature Stability of IN718 Derivative Alloys, Superalloys 1992, S.D. Antolovich et al., Ed., TMS, p 507–516; 1992;
23. A.M. Beltran, Cobalt-Base Alloys, Superalloys II, C.T. Sims, N.S. Stoloff, and W.C. Hagel, Ed., John Wiley & Sons, p 135–163; 1987;
24. W.H. Jiang, X.D. Yao, H.R. Guan, and Z.Q. Hu, Secondary M6C Precipitation in a Cobalt-Base Superalloy, J. Mater. Sci. Lett., Vol 18, p 303–305; 1999;
25. Y. Murata, K. Suga, and N. Yukawa, Effects of Transition Elements on the Properties of MCrAlY Carbides in IN-100 Nickel-Based Superalloy, J. Mater. Sci., Vol 21 (No. 10), p 3653–; 1986;
26. J.R. Mihalisin and D.L. Pasquine, Phase Transformations in NickelBase Superalloys, Superalloys 1968, TMS, p 134–1; 1968;
27. M. Kamaraj, Rafting in Single Crystal Nickel-Base Superalloys—An Overview, Sadhana, Vol 28 (Parts 1 and 2), p 115–128; 2003;
28. Sander G, Tan J, Balan P, Gharbi O, Feenstra D, Singer L, Thomas S, Kelly R, Scully J, Birbilis N; Corrosion of Additively Manufactured Alloys: A Review. Corrosion 74(12):1318–1350; 2018;
29. C. Y. Chao, L. F. Lin, and D. D. Macdonald, A Point Defect Model for Anodic Passive Films, Department of Metallurgical Engineering, The Ohio State University, Columbus, Ohio 43210, 1981;
30. C. Chao and S. Smialowska, Sur. Sci., 96, 426.; 1980;
31. N. F. Mott, Trans. Faraday Soc., 43, 429 (1947); J. Chim. Phys., 44, 172; 1947;
32. N. Sato and M. Cohen, This Journal, 111, 512; 1964;
33. F. P. Fehlner and N. F. Mott, Oxid. Met., 2, 59; 1970;
34. C. L. McBee and J. Kruger, in “Localized Corrosion,” R. W. Staehle et al., Editors, p. 252, NACE, Houston; 1974;
35. C. Y. Chao, L. F. Lin, and D. D. Macdonald, A Point Defect Model for Anodic Passive Films III. Impedance Response, Department of Metallurgical Engineering, The Ohio State University, Columbus, Ohio 43210; 1982;

36. I.. F. Lin, C. Y. Chao, and D. D. Macdonald, A Point Defect Model for Anodic Passive Films II. Chemical Breakdown and Pit Initiation, Department of Metallurgical Engineering, The Ohio State University, Columbus, Ohio 43210, 1981;
37. C. Y. Chao and D. D. Macdonald, EPRI Report July 1-December 31, 1980;
38. W. Paik and Z. Szklarska-Smialowska, Surf. Sci., 96, 401; 1980;
39. Digby D. Macdonald, The Point Defect Model for the Passive State, Center for Advanced Materials, The Pennsylvania State University, University Park, Pennsylvania 16802; 1992;
40. C. B. Bargeron and R. B. Givens, Corrosion, 36, 618; 1980;
41. H. J. Engell, EIectrochim. Acta, 22, 987.; 1977;
42. Digby D. Macdonald, A Review of the Point Defect Model for Film Growth, 2011;
43. Macdonald, D., J. Electrochem. Soc., Vol. 153, p. B213; 2006;
44. Macdonald, D.D., AlRafaie, M., and Engelhardt, G.R., J. Electrochem. Soc., Vol. 148, p. B343.; 2001;
45. Rosas-Camacho, O., Urquidi -Macdonald, M., and Macdonald, D.D., ECS Trans, Vol. 19, No. 29, p. 143; 2009;
46. Macdonald, D.D., Pure Appl. Chem., Vol. 71, p. 951.; 1999;
47. A. Fattah-Alhossein, F. Soltani, F. Shirsalimi, B. Ezadi, N. Attarzadeh, The Semiconducting Properties of Passive Films Formed on AISI 316 L and AISI 321 Stainless Steels: A Test of the Point Defect Model (PDM), Faculty of Engineering, Bu-Ali Sina University, Hamedan 65178-38695, Iran, 2011;
48. Mickaël Payet , Loïc Marchetti, Michel Tabarant , Jean-Pierre Chevalier; Corrosion Mechanism of a Ni-Based Alloy in Supercritical Water: Impact of Surface Plastic Deformation; Elsevier Ltd. ; Corrosion Science 100, 47–56,; 2015;
49. H. Bohni, T. Suter and A. Schreyer; MICRO- AND NANOTECHNIQUES TO STUDY LOCALIZED CORROSION; Elsevier Science Ltd. ; Electrochimica Acta, Vol. 40. No. 10. Pp. 1361-1368,; 1995;
50. Tanja Trosch, Johannes Strößner, Rainer Völkl, Uwe Glatzel; Microstructure and Mechanical Properties of Selective Laser Melted Inconel 718 Compared to Forging and Casting; Elsevier B.V. ; Materials Letters 164, 428–431,; 2016;
51. Mohamed Balbaa, Sameh Mekhiel, Mohamed Elbestawi, Jeff McIsaac; On Selective Laser Melting of Inconel 718: Densification, Surface Roughness, and Residual Stresses; Elsevier Ltd. ; Materials and Design 193, 108818, 2020;
52. A. Machet, A. Galtayries, S. Zanna, L. Klein, V. Maurice, P. Jolivet b, M. Foucault, P. Combrade, P. Scott, P. Marcus; XPS and STM Study of the Growth and Structure of Passive Films in High Temperature Water on a Nickel-Base Alloy; Elsevier Ltd. ; Electrochimica Acta 49, 3957–3964, 2004;

53. Arshad Yazdanpanah, Mattia Franceschi, Gianluca Bergamo, Massimiliano Bonesso, Manuele Dabala`; On the Exceptional Stress Corrosion Cracking Susceptibility of Selective Laser Melted 316L Stainless Steel under the Individual Effect of Surface Residual Stresses; Elsevier Ltd. ; Engineering Failure Analysis 136, 106192, 2022;
54. Arshad Yazdanpanah, Farid Reza Biglari, Alireza Fallahi Arezoodar & Manuele Dabalà ; Role of Grinding Induced Surface Residual Stress on Probability of Stress Corrosion Cracks Initiation in 316L Austenitic Stainless Steel in 3.5% Sodium Chloride Aqueous Solution; CORROSION ENGINEERING, SCIENCE AND TECHNOLOGY; Taylor & Francis, 2020;
55. Arshad Yazdanpanah, Mattia Lago, Claudio Gennari and Manuele Dabalà; Stress Corrosion Cracking Probability of Selective Laser Melted 316L Austenitic Stainless Steel under the Effect of Grinding Induced Residual Stresses; MDPI, Basel, Switzerland; Metals, 11, 327, 2021;
56. Baicheng Zhanga, Mingzhen Xiub, Yong Teck Tanc, Jun Wei, Pei Wangd; Pitting Corrosion of SLM Inconel 718 Sample under Surface and Heat Treatments; Elsevier B.V. ; Applied Surface Science Volume 490, Pages 556-567, 2019;
57. Xingying Tang, Shuzhong Wang, Lili Qian, Yanhui Li, Zonghu Lin, Donghai Xu, Yupeng Zhang; Corrosion Behavior of Nickel Base Alloys, Stainless Steel and Titanium Alloy in Supercritical Water Containing Chloride, Phosphate and Oxygen; Elsevier B.V. ; Chemical Engineering Research and Design 100,530–541, 2015;
58. J.P. Oliveira, A.D. LaLonde, J. Ma; Processing Parameters in Laser Powder Bed Fusion Metal Additive Manufacturing; Elsevier Ltd. ; Materials and Design 193, 108762,; 2020;
59. Shuwei Guo, Donghai Xua, Yanhui Lia, Yang Guo, Shuzhong Wanga, Digby D. Macdonald; Corrosion Characteristics and Mechanisms of Typical Ni-Based Corrosion-Resistant Alloys in Sub- and Supercritical Water; Elsevier B.V. ; The Journal of Supercritical Fluids 170, 105138, 2021;
60. J.P. Oliveira, T.G. Santos, R.M. Miranda; Revisiting Fundamental Welding Concepts to Improve Additive Manufacturing: From Theory to Practice; Elsevier Ltd. ; Progress in Materials Science Volume 107, 100590, 2020;
61. Dafan Dua, Anping Donga, Da Shua, Guoliang Zhua, Baode Suna, Xi Lic, Enrique Lavernia; Influence of Build Orientation on Microstructure, Mechanical and Corrosion Behavior of Inconel 718 Processed by Selective Laser Melting; Elsevier B.V. ; Materials Science & Engineering A 760, Pp. 469-480,; 2019;
62. Qingbo Jia, Dongdong Gu; Selective Laser Melting Additive Manufacturing of Inconel 718 Superalloy Parts: Densification, Microstructure and Properties; Elsevier B.V. ; Journal of Alloys and Compounds 585, Pp. 713–721,; 2014;

63. Luying Wang, Heping Li, Qingyou Liu, Liping Xu, Sen Lin, Kai Zheng; Effect of Sodium Chloride on the Electrochemical Corrosion of Inconel 625 at High Temperature and Pressure; Elsevier B.V. ; Journal of Alloys and Compounds 703, Pp. 523-529,; 2017;
64. Huihui Yang, Liang Meng, Shuncun Luo, Zemin Wang; Microstructural Evolution and Mechanical Performances of Selective Laser Melting Inconel 718 from Low to High Laser Power; Elsevier B.V. ; Journal of Alloys and Compounds 828, 154473, 2020;
65. G.H. Cao, T.Y. Suna, C.H. Wanga, Xing Lia, M. Liu, Z.X. Zhanga, P.F. Hua, A.M. Russell, R. Schneider, D. Gerthsenc, Z.J. Zhou, C.P. Lid, G.F. Chend; Investigations of Γ′, Γ″ and δ Precipitates in Heat-Treated Inconel 718 Alloy Fabricated by Selective Laser Melting; Elsevier Inc. ; Materials Characterization 136, Pp. 398-406,; 2018;
66. Tyler Moss, Wenjun Kuang, Gary S Was; Stress Corrosion Crack Initiation in Alloy 690 in High Temperature Water; Elsevier Ltd. ; Current Opinion in Solid State and Materials Science 22, Pp. 16–25,; 2018;
67. K. Lutton Cwalina, C.R. Demarest, A.Y. Gerard, J.R. Scully; Revisiting the Effects of Molybdenum and Tungsten Alloying on Corrosion Behavior of Nickel-Chromium Alloys in Aqueous Corrosion; Elsevier Ltd. ; Current Opinion in Solid State & Materials Science 23, Pp. 129-141,; 2019;
68. K.N. Amato, S.M. Gaytan, L.E. Murr, E. Martinez, P.W. Shindo, J. Hernandez, S. Collins, F. Medina; Microstructures and Mechanical Behavior of Inconel 718 Fabricated by Selective Laser Melting; Elsevier Ltd. ; Acta Materialia 60, Pp. 2229-2239,; 2012;
69. Dongyun Zhanga, Pudan Zhanga, Zhen Liua, Zhe Fenga, Chengjie Wanga, Yanwu Guoa; Thermofluid Field of Molten Pool and Its Effects during Selective Laser Melting (SLM) of Inconel 718 Alloy; Elsevier B.V. ; Additive Manufacturing 21, Pp. 567-578,; 2018;
70. Xiaoqing Wang, Kevin Chou; Effects of Thermal Cycles on the Microstructure Evolution of Inconel 718 during Selective Laser Melting Process; Elsevier B.V. ; Additive Manufacturing 18, Pp. 1–14,; 2017;
71. Shuncun Luo, Wenpu Huang, Huihui Yang, Jingjing Yang, Zemin Wang, Xiaoyan Zeng; Microstructural Evolution and Corrosion Behaviors of Inconel 718 Alloy Produced by Selective Laser Melting Following Different Heat Treatments; Elsevier B.V. ; Additive Manufacturing 30, 100875, 2019;
72. P. Kritzer, N. Boukis, and E. Dinjus; Corrosion of Alloy 625 in Aqueous Solutions Containing Chloride and Oxygen; NACE International; 1998;
73. J.T. Ho and G.P. Yu; Pitting Corrosion of Inconel 600 in Chloride and Thiosulfate Anion Solutions at Low Temperature; National Association of Corrosion Engineers; 1992;

74. W. D. FRANCE, JR.; Effects of Stress and Plastic Deformation on the Corrosion of Steel; Chemistry Department, Research Laboratories, General Motors Corp., Warren; Michigan.; Vol. 26, No. 5,; 1970;
75. Hiroyuki Miyamoto; Corrosion of Ultrafine Grained Materials by Severe Plastic Deformation, an Overview; Department of Mechanical Engineering, Doshisha University, Kyotanabe 610–0394, Japan, 2016;
76. S.M. Bruemmer, M.J. Olszta, M.B. Toloczko, and L.E. Thomas; Linking Grain Boundary Microstructure to Stress Corrosion Cracking of Cold-Rolled Alloy 690 in Pressurized Water Reactor Primary Water; NACE International, 2013;
77. Koji Arioka, Takuyo Yamada, Tomoki Miyamoto and Masanori Aoki; Intergranular Stress Corrosion Cracking Growth Behavior of Ni-Cr-Fe Alloys in Pressurized Water Reactor Primary Water; NACE International, 2014;
78. Yanbing Tang, Xinwang Shen, Yanxin Qiao , Lanlan Yang, Jian Chen, Daohua Lu, and Zhongyu Zhang; Corrosion Behavior of a Selective Laser Melted Inconel 718 Alloy in a 3.5 Wt.% NaCl Solution; ASM International; Journal of Materials Engineering and Performance; 5506—Volume 30(7),; 2021;
79. Shuwei Guo, Donghai Xu, Yu Liang, Yanhui Li, Jianqiao Yang, Gang Chen, and Digby D. Macdonald; Corrosion Characteristics of Typical Ni−Cr Alloys and Ni−Cr−Mo Alloys in Supercritical Water: A Review; American Chemical Society; Ind. Eng. Chem. Res. 2020, 59, 18727−18739; 2020;
80. Parag M. Ahmedabadi, Vivekanand Kain, and Ashika Agrawal; Effect of Plastic Deformation on Passivation Characteristics of Type 304 Stainless Steel; ASM International; Journal of Materials Engineering and Performance; 7036—Volume 28(11),; 2019;
81. Lin Liu and Jun Zhang, Cheng Ai; Nickel-Based Superalloys; Elsevier Inc.; Encyclopedia of Materials: Metals and Alloys Doi:10.1016/B978-0-12-803581-8.12093-4; 2020;
82. Helmuth Sarmiento Klapper, Nikolay Molodtsov, Madison Burns, Christoph Wangenheim; Critical Factors Affecting the Pitting Corrosion Resistance of Additively Manufactured Nickel Alloy in Chloride Containing Environments; American Petroleum Institute, Washington, D.C. USA; 2017;
83. M. C.Chaturvedi and Va-Fang Han; Strengthening Mechanisms in Inconel 718 Superalloy; The Metals Society; Metal Science Vol. 17,; 1983;
84. Xingying Tang, Shuzhong Wang, Donghai Xu, Yanmeng Gong, Jie Zhang, and Yuzhen Wang; Corrosion Behavior of Ni-Based Alloys in Supercritical Water Containing High Concentrations of Salt and Oxygen; American Chemical Society; Ind. Eng. Chem. Res. 52, 18241−18250; 2013;

85. Le Zhou, Abhishek Mehta, Brandon McWilliams, Kyu Cho, Yongho Sohn; Microstructure, Precipitates and Mechanical Properties of Powder Bed Fused Inconel 718 before and after Heat Treatment; Journal of Materials Science and Amp; Technology; 2018;
86. Helmuth Sarmiento Klapper, Natalia S. Zadorozne, Raul B. Rebak; Localized Corrosion Characteristics of Nickel Alloys: A Review; The Chinese Society for Metals and Springer-Verlag Berlin Heidelberg; Acta Metall. Sin. (Engl. Lett.), 30(4), 296–305,; 2017;
87. K.V.U. PRAVEEN, G.V.S. SASTRY, and VAKIL SINGH; Work-Hardening Behavior of the Ni-Fe Based Superalloy IN718; The Minerals, Metals & Materials Society and ASM International; METALLURGICAL AND MATERIALS TRANSACTIONS A; VOLUME 39A,; 2008;
88. Yazdanpanah, A.; Franceschi, M.; Revilla, R.I.; Khademzadeh, S.; Graeve, I.D.; Dabalà, M. Revealing the Stress Corrosion Cracking Initiation Mechanism of Alloy 718 Prepared by Laser Powder Bed Fusion Assessed by Microcapillary Method. Corros. Sci., 208, 110642; 2022;
89. Bi Zhang, Yongtao Li, Qian Bai; Defect Formation Mechanisms in Selective Laser Melting: A Review; Chin. J. Mech. Eng. 30:515–527; 2017;
90. W.M. Tucho, P. Cuvillier, A. Sjolyst-Kverneland, V. Hansen; Microstructure and Hardness Studies of Inconel 718 Manufactured by Selective Laser Melting before and after Solution Heat Treatment; Mater. Sci. Eng.: A, 689, Pp. 220-232; 2017;
91. Arshad Yazdanpanah, Mattia Franceschi, Gianluca Bergamo, Massimiliano Bonesso, Manuele Dabala`; On the Exceptional Stress Corrosion Cracking Susceptibility of Selective Laser Melted 316L Stainless Steel under the Individual Effect of Surface Residual Stresses; Elsevier Ltd. ; Engineering Failure Analysis 136, 106192, 2022;
92. M. Laleh, A.E. Hughes, S. Yang, J. Li, W. Xu, I. Gibson, M.Y. Tan; Two and Three-Dimensional Characterisation of Localised Corrosion Affected by Lack-of-Fusion Pores in 316L Stainless Steel Produced by Selective Laser Melting; Corros. Sci., 165, Article 108394; 2020;
93. N. Nadammal, S. Cabeza, T. Mishurova, T. Thiede, A. Kromm, C. Seyfert, L. Farahbod, C. Haberland, JA Schneider, PD Portella, G. Bruno; Effect of Hatch Length on the Development of Microstructure, Texture and Residual Stresses in Selective Laser Melted Superalloy Inconel 718; Mater. Des., 134, Pp. 139-150; 2017;
94. V. Cruz, Q. Chao, N. Birbilis, D. Fabijanic, P.D. Hodgson, S. Thomas; Electrochemical Studies on the Effect of Residual Stress on the Corrosion of 316L Manufactured by Selective Laser Melting; Corros. Sci., 164, Article 108314; 2020;
95. M. Wang, M. Song, G.S. Was, J.L. Nelson; The Roles of Thermal Mechanical Treatment and δ Phase in the Stress Corrosion Cracking of Alloy 718 in Primary Water; Corros. Sci., 160, Article 108168; 2019;

96. S. Choudhary, S. Zhang, S. Thomas, N. Birbilis; A Closer Look at the Passivity and Transpassive Dissolution of Chromium Using Atomic Spectroelectrochemistry; ECS Adv.; 2020;
97. Yazdanpanah, A.; Pezzato, L.; Dabalà, M. Stress Corrosion Cracking of AISI 304 under Chromium Variation within the Standard Limits: Failure Analysis Implementing Microcapillary Method. Eng. Fail. Anal., 142, 106797; 2022;
98. X. Zhong, E.-H. Han, X. Wu; Corrosion Behavior of Alloy 690 in Aerated Supercritical Water; Corros. Sci., 66, Pp. 369-379; 2013;
99. L. Jinlong, L. Hongyun; The Effects of Grain Refinement and Deformation on Corrosion Resistance of Passive Film Formed on the Surface of 304 Stainless Steels; Mater. Res. Bull., 70, Pp. 896-907; 2015;
100. G.O. Ilevbare, G.T. Burstein; The Role of Alloyed Molybdenum in the Inhibition of Pitting Corrosion in Stainless Steels; Corros. Sci., 43, Pp. 485-513; 2001;
101. D.D. Macdonald; The Electrochemical Nature of Stress Corrosion Cracking; Stress Corrosion Cracking of Nickel Based Alloys in Water-Cooled Nuclear Reactors, Elsevier, Pp. 239-294; 2016;
102. G. Sander, S. Thomas, V. Cruz, M. Jurg, N. Birbilis, X. Gao, M. Brameld, C.R. Hutchinson; On the Corrosion and Metastable Pitting Characteristics of 316L Stainless Steel Produced by Selective Laser Melting; J. Electrochem. Soc., 164 (6), Pp. C250-C257; 2017;
103. Yazdanpanah, A.; Franceschi, M.; Rebesan, P.; Dabalà, M. Correlation of Lack of Fusion Pores with Stress Corrosion Cracking Susceptibility of L-PBF 316L: Effect of Surface Residual Stresses. Materials, 15, 7151; 2022;
104. L. Liu, Q. Ding, Y. Zhong, J. Zou, J. Wu, Y.-L. Chiu, J. Li, Z. Zhang, Q. Yu, Z. Shen; Dislocation Network in Additive Manufactured Steel Breaks Strength–Ductility Trade-off; Mater. Today, 21, Pp. 354-361; 2018.